

Effect of Metal-Alkyl Components  
on the Formation of Active Sites  
in Chromium-Based  
Ethylene Polymerization

Maarten K. Jongkind

# **Effect of Metal-Alkyl Components on the Formation of Active Sites in Chromium-Based Ethylene Polymerization**

**Effect van Metaal-Alkyl Verbindingen op de Vorming van de Actieve Plaats in Chroom-gebaseerde Polymerisatie van Ethyleen  
(met een samenvatting in het Nederlands)**

## **Proefschrift**

ter verkrijging van de graad van doctor aan de Universiteit Utrecht op gezag van de rector magnificus, prof. dr. H. R. B. M. Kummeling, ingevolge het besluit van het college voor promoties in het openbaar te verdedigen op

woensdag 27 oktober 2021 des middags te 2.15 uur

door

**Maarten Klaas-Jan Jongkind**  
geboren op 18 februari 1993  
te Amstelveen

**Promotor:**

Prof. dr. ir. B. M. Weckhuysen

This **Ph.D. Thesis** was accomplished with financial support from SABIC, TKI Chemistry (Topconsortium voor Kennis en Innovatieve Chemie), as well as funding from the European Union Horizon 2020 research innovation program under the Marie-Sklodowska-Curie grant agreement Marie-Sklodowska-Curie grant 641886.

Cover Design: Thomas Hartman | [www.thisillustrations.com](http://www.thisillustrations.com)

Printing: Ridderprint | [www.ridderprint.nl](http://www.ridderprint.nl)

ISBN: 978-94-6416-785-6

# Table of Contents

<b>General Introduction.....</b>	<b>9</b>
1.1 Polymers and Plastics.....	10
1.2 Catalytic Olefin Polymerization.....	12
1.2.1 (Post-)Metallocene-type Catalysts.....	13
1.2.2 Ziegler-Natta-type Catalysts.....	14
1.2.3 Phillips-type Catalysts .....	14
1.2.4 Metal-Organic Framework Polymerization Platforms .....	15
1.3 Phillips Catalyst Preparation .....	16
1.4 Support Type and Promotor Effects.....	17
1.5 Active Site Origins .....	17
1.6 Effect of Co-catalysts.....	18
1.7 Ethylene Polymerization Mechanism.....	20
1.8 Active Site Formation and Initiation Pathways .....	22
1.9 Outline of the Ph.D. Thesis.....	24
1.10 References.....	26
<b>Tuning the Redox Chemistry of a Cr/SiO<sub>2</sub> Phillips Catalyst for Controlling Activity, Induction Period and Polymer Properties.....</b>	<b>31</b>
2.1 Introduction .....	32
2.2 Results and Discussion .....	33
2.3 Conclusions .....	50
2.4 Acknowledgements.....	51
2.5 Experimental Section .....	51
2.6 References.....	52
<b>Influence of Metal-Alkyls on Early-Stage Ethylene Polymerization over a Cr/SiO<sub>2</sub> Phillips Catalyst: A Bulk Characterization and X-ray Chemical Imaging Study.....</b>	<b>57</b>
3.1 Introduction .....	58
3.2 Results and Discussion .....	59
3.3 Conclusions .....	77

3.4 Acknowledgements.....	77
3.5 Experimental Section .....	78
3.6 References.....	80
<b>Redox Behavior of a Cr/SiO<sub>2</sub> Phillips Catalyst assessed by Raman Spectroscopy .....</b>	<b>85</b>
4.1 Introduction .....	86
4.2 Results and Discussion .....	88
4.3 Conclusions .....	100
4.4 Acknowledgements.....	100
4.5 Experimental Section .....	100
4.6 References.....	101
<b>Influence of Pore Structure and Metal-Node Geometry on the Polymerization of Ethylene over Cr-Based Metal Organic Frameworks .....</b>	<b>107</b>
5.1 Introduction .....	108
5.2 Results and Discussion .....	110
5.3 Conclusions .....	125
5.4 Acknowledgements.....	127
5.5 Experimental Section .....	127
5.6 References.....	132
<b>Summary, Outlook, and Conclusions.....</b>	<b>137</b>
6.1 Summary .....	138
6.2 Outlook.....	141
6.2.1 Phillips-type Ethylene Polymerization.....	141
6.2.2 Cr-based Metal-Organic Framework Ethylene Polymerization.....	142
6.3 References.....	143
<b>Nederlandse Samenvatting .....</b>	<b>144</b>
<b>Appendix A. List of Abbreviations .....</b>	<b>150</b>
<b>Appendix B. Additional Tables .....</b>	<b>151</b>
<b>Appendix C. List of Scientific Publications and Presentations .....</b>	<b>154</b>
<b>Acknowledgements .....</b>	<b>157</b>
<b>About the Author.....</b>	<b>162</b>





# Chapter 1

## General Introduction

### Abstract

Polyolefin-based materials have been deeply embedded in our living standards ever since their conception more than half a century ago and are nowadays produced with three grand catalytic workhorses. Furthermore, their versatility and relative ease of production ensure that the coming years will see a further increase in their global demand. The Cr/SiO<sub>2</sub> Phillips catalyst stands as one of the oldest workhorses in catalytic ethylene polymerization, and its working state remains elusive to date. The major advantage of the Cr/SiO<sub>2</sub> Phillips Catalyst is simultaneously its disadvantage, namely the large variety of active sites, producing the desirable multimodal Molecular Weight Distributions (MWDs) as well as being responsible for not yet completely understanding what composes the active site. This **Ph.D. Thesis** focuses on Cr-based ethylene polymerization in a two-pronged approach, first by investigating the effect of metal-alkyl co-catalysts on the Cr/SiO<sub>2</sub> Phillips catalyst, and second by investigating Cr-based ethylene polymerization Metal Organic Frameworks (MOFs). To appreciate the Phillips-type catalyst's delicate nature, this **Chapter** discusses the preparation of the Cr/SiO<sub>2</sub> Phillips-type catalyst, as well as the ways in which metal-alkyl components as co-catalysts can affect the Cr surface structures. Second, this chapter also gives a brief overview of MOFs in ethylene polymerization, including a rationale for the increased interest towards these compounds as polymerization catalyst, including the most relevant and recent showcase examples. Finally, the scope and outline of this **Ph.D. Thesis** will be discussed.

## 1.1 Polymers and Plastics

The word polymer is derived from the Greek words *poly* (more) and *meros* (parts), literally translating into “more-parts”. This word was used as early as 1833 by Jöns Jacob Berzelius to describe organic compounds sharing identical empirical formulas yet varying in their respective overall molecular weight. Nowadays it is clear that this description is insufficient since it does not account for compounds with identical molecular formulas, but different structures. Instead, this term is now used to describe (macro-)molecules, which are defined by a repetition of characteristic smaller building blocks.<sup>[1,2]</sup>

This point of view allows us to coin a wide variety of compounds as polymers, ranging from natural to synthetic products. The former being exemplified by DNA, which provides our genetic code, as well as by cellulose and lignin giving wood its rigidity and strength. On the other hand, examples of synthetic polymers are polyethylene (PE), which is used in many compounds such as pipelines, and, polyethylene terephthalate (PET), which is processed into bottles.

Application-wise, synthetic polymers nowadays find more widespread usage than their natural counterparts, which is in part due to the relative ease with which these synthetic polymers can be produced and the fact that they outperform natural counterparts in many ways. Synthetic polymers have many unique property combinations that are unparalleled by any other class of materials, examples being attractive cost/performance ratios, flexible base of raw materials and high energy contents (similar to that of oil, and far superior to that of wood).<sup>[3,4]</sup>

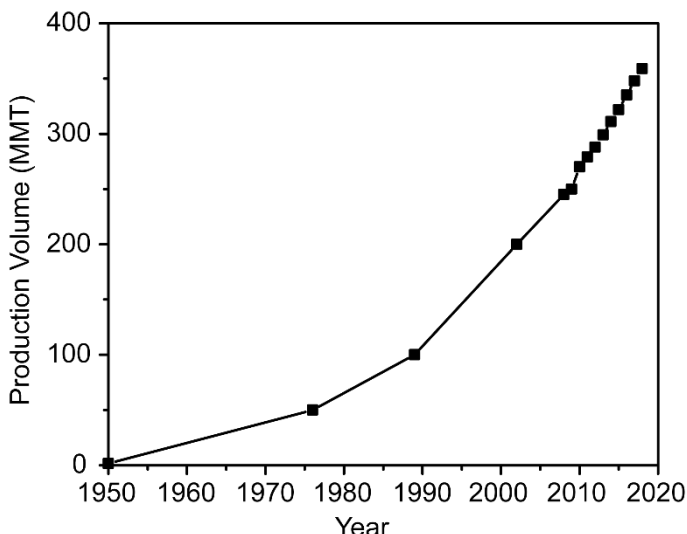


**Figure 1.1.** Global annual plastics production in million metric tons, also demonstrating the linear growth in the recent years.

**Table 1.1.** Schematic overview of the properties of High-Density Polyethylene (HDPE), Linear Low-Density Polyethylene (LLDPE) and Low-Density Polyethylene (LDPE), including their defining properties, such as density, structure, degree of Short Chain Branching (SCB), degree of Long Chain Branching (LCB) and degree of crosslinking.

	HDPE	LLDPE	LDPE
Density ( $\text{g cm}^{-3}$ )	0.945–0.975	0.925	0.915–0.935
Catalyst	Ziegler-Natta, Metallocene, Phillips	Ziegler-Natta, Metallocene, Phillips	Free radical, oxygen, peroxides
Structure			
Short-Chain Branches (SCB)	Little	Many	Many
Long-Chain Branches (LCB)	No	No	Yes
Crosslinking	No	No	Yes

At present, approximately 7% of the annual oil production is used to produce plastics, which in turn helps to save more than twice the amount of oil due to for example improving thermal insulation of houses, hereby circumventing the need for excessive heating and related fuel consumption. Besides, synthetic polymers now fulfil many basic needs, such as shelter, health-care equipment, communication equipment, electrical equipment, and protective equipment. At this moment, the polyolefin industry stands for one of the most effective and sustainable (and recyclable) uses of fossil as well as renewable feedstocks.<sup>[4]</sup> Furthermore, the trend in Figure 1.1 dictates that the demand for plastics will continue to increase in the coming years, which is mainly related to a higher demand in rapidly growing countries (Figure 1.2A).<sup>[5]</sup>

Figure 1.2B illustrates the importance of thermoplastics, with it being clear that PE has the largest market volume share, closely followed by polypropylene (PP). With respect to PE, although it is a relatively simple polymer consisting of repeating ethylene monomers, its versatility is enormous, as demonstrated in Table 1.1. This is predominantly caused by the ability to tailor the physicochemical properties by varying the PE properties in terms of Molecular Weight Distribution (MWD), Short-Chain Branches (SCB) and Long-Chain Branches (LCB). For example, a Low-Density Polyethylene (LDPE) material contains significant SCB, LCB and crosslinking, resulting in the low density. This combination of properties renders this material

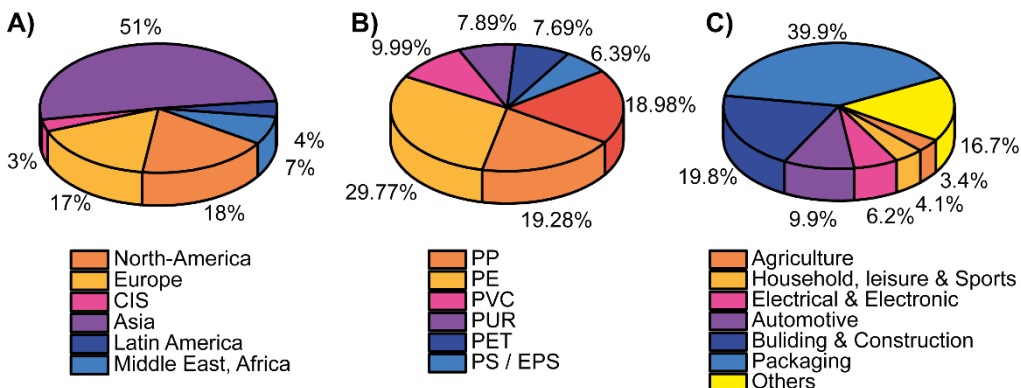


**Figure 1.2.** A) Global distribution of the annual production of plastics, demonstrating that Asia is the largest contributor. B) Distribution of individual types of plastics that make up the total annual plastics production including polypropylene (PP), polyethylene (PE), polyvinylchlorides (PVC), polyurethanes (PUR), polyethylene terephthalates (PET) and (expanded) polystyrenes (E-PS). C) The predominant applications that require usage of synthetic polymer materials.

rather flexible yet not particularly strong, ensuring that it is used to produce for example plastic bags. On the other hand, High-Density Polyethylene (HDPE) materials have small amounts of SCB, LCB and Crosslinking, hereby producing a material that lacks flexibility, while demonstrating superior rigidity, therefore finding applications in e.g., pipelines and sewage systems.

The versatility of these polymers is undeniably one of the driving factors in their annual growth. The possibility to finely tailor the product to precise specifications in terms of tensile strength, visco-elasticity and crystallinity is elegantly reflected in the wide variety of applications, ranging from construction applications to sterile hospital necessities, as shown in Figure 1.2C.<sup>[6-9]</sup> Despite all these benefits, recent years have seen a justified increase in plastic related environmental issues, with plastic waste standing at the center of public attention. Hereby even further driving research towards improved sustainability as well as efficiency.

## 1.2 Catalytic Olefin Polymerization

Catalytic ethylene polymerization marked a great improvement in comparison to the original radical and high-pressure ethylene polymerization,<sup>[10-12]</sup> since a larger variety of products could now be produced under significantly milder conditions. Nowadays, the industrial polymerization of ethylene revolves around three grand catalytic workhorses. Namely Cr/SiO<sub>2</sub>-type Phillips catalysts, with Cr as the active site, Ziegler-Natta-type catalysts, with Ti as the active site and lastly (post-)metallocene-type catalysts, with a variety of usable metal-centers, such as Zr and V. A schematic overview of the three catalytic systems is shown in Figure 1.3.

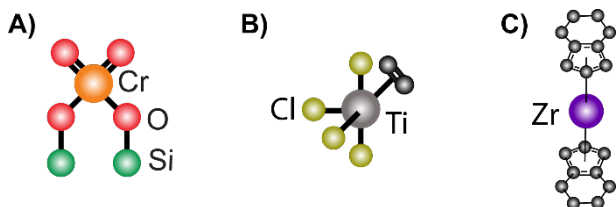


**Figure 1.3.** Illustrative representation of the three grand catalytic workhorses in olefin polymerization, namely **A)** Cr-based Phillips-type catalysts, **B)** Ti-based Ziegler-Natta-type catalysts and **C)** Zirconium-based metallocene-type catalysts.

Interestingly, two catalytic ethylene polymerization systems emerged almost simultaneously. It was John P. Hogan and Robert L. Banks at the Phillips Petroleum Company in 1951 that found that silica-supported chromium was able to both produce PP and HDPE.<sup>[13,14]</sup> In 1953 Karl Ziegler filed patents for a mixture of transition metal compounds and aluminum alkyls in the polymerization of ethylene. One year later, Giulio Natta's catalyst produced isotactic PP and elegantly demonstrated the possibility to perform stereospecific olefin polymerization.<sup>[15]</sup> The third workhorse is embodied by metallocene-type catalysts, which are significantly younger than the two others, and generally consist of supported bis-cyclopentadienyl derivatives of Group 4 transition-metals, combined with methylaluminoxane (MAO).<sup>[16,17]</sup>

### 1.2.1 (Post-)Metallocene-type Catalysts

As mentioned, (post-)metallocene type catalysts (Figure 1.3C) are the youngest of the ethylene polymerization catalysts. Metallocene-type catalysts are produced by the impregnation of a carrier material with MAO and the subsequent adsorption of the metallocene precursor, which is bound to the surface through electrostatic and Van der Waals interactions. In general, these catalysts are defined by excellent activities, higher than both Ziegler-Natta-type catalysts and Phillips-type catalysts. This category of ethylene polymerization catalysts is the only category that can be labeled as a single-site catalyst, with one well-defined type of active site being responsible for the polymerization of ethylene. In contrast to the other polymerization catalysts, this is directly reflected in the Dispersity Index ( $\mathcal{D}$ ) values in the range of 2-3, defined as the  $M_w$  (weight averaged molecular weight) of the PE divided by the  $M_n$  (number averaged molecular weight) of the PE, close to the theoretical value of 1-2 for true single-site catalysts.

One of the significant advantages of (post-)metallocenes is that the active site structure, in terms of geometry and electronic structure, is readily tailored by rational design of the bis-cyclopentadienyl ligand, which in turn results in an excellent controllability over the catalyst performances in terms of catalytic activity and final PE product properties, exemplified by controllable co-monomer incorporation (and thus stereospecificity)<sup>[16–18]</sup>

This ligand imposed stereospecificity means that the versatility of (post-)metallocenes can theoretically also be extended towards the polymerization of propylene. However, the first PP materials produced with (post-)metallocene catalysts were plagued by too-low melting temperatures as well as too-low Molecular Weights (MWs). Again, rational design of the ligands circumvented this, thereby resulting in (post-)metallocene systems also finding success in PP production.

### 1.2.2 Ziegler-Natta-type Catalysts

Ziegler-Natta-type catalysts have undergone the most distinct improvements starting from the original catalyst system.<sup>[15]</sup> Karl Ziegler found in 1950 that if either  $TiCl_4$  or  $TiCl_3$  was reacted with an organometallic compound, such as  $Et_3Al$  or  $Et_2AlCl$ , this reaction mixture could convert ethylene into high MW PE products.<sup>[19]</sup> The first breakthrough came in the early 1970s, when it was found that the efficiency of these catalysts is greatly improved if they are supported on certain magnesium compounds, such as  $MgCl_2$ , with activities of 100-1000 kg of PE per gram of Ti being reported.

Subsequent improvements were mainly in the form of Lewis base additives, such as di-ethers and phthalates, which act as ancillary ligands to the active site, hereby providing additional control over catalytic activity. Second, through their role as ancillary ligands, these additives also exert stereospecificity over (co-)monomer incorporation, which make it the grand catalytic workhorse in stereospecific propylene polymerization, with nowadays the ability to control the tacticity of the PP: resulting in the ability to produce either isotactic, syndiotactic or atactic PP. One additional, albeit less mentioned, advantage of Ziegler-Natta type catalysts is that they generally produce polymers with broad Molecular Weight Distributions (MWDs), which results in better physical product properties as well as better post-reaction processability.

### 1.2.3 Phillips-type Catalysts

The focus of this **Ph.D. Thesis** is on the  $Cr/SiO_2$  Phillips type catalyst, which is produced by the impregnation and subsequent calcination of a  $Cr^{3+}$  or  $Cr^{6+}$  precursor on an amorphous and porous carrier material such as silica. This catalyst distinguishes itself from the two other categories because it does not require the addition of a co-catalyst to attain catalytic activity: ethylene can fulfil the dual role of reductant and monomer source. However, co-catalysts in the form of metal-alkyls, can be added for several reasons: they scavenge poisons from the monomer feed, they reduce the induction period, they enhance the catalytic activity, and they are used to tailor the PE properties. These four reasons make that the usage of co-catalysts is common practice in industrial ethylene polymerization. To date, Phillips-type catalysts are responsible for

approximately 30% of the global HDPE production, with the ability to produce over 70 different types of HDPE.<sup>[20–24]</sup>

One of the major advantages of the Phillips catalyst is simultaneously the reason for its notoriety, namely the ability to produce multimodal HDPE materials, simply meaning that the active sites produce PE chains which differ from each other. This is reflected in broad MWDs as well as related large  $D$  values, which generally translate into easy post-reaction processability and superior physicochemical properties of the PE materials. However, this also implies that many different Cr active sites are responsible for ethylene polymerization.

The variety of active sites, the low viable catalytic weight-loading, and the even smaller number of Cr sites participating in ethylene polymerization, have also warranted strong academic interest into this catalyst system. Until date, numerous research efforts have delved into the catalyst activation mechanism as well as into the related polymerization mechanism, without reaching a full consensus. Some of the more relevant findings and challenges will be discussed later in this **Chapter**.

## 1.2.4 Metal-Organic Framework Polymerization Platforms

In addition to conventional heterogeneous systems, ethylene polymerization Metal-Organic Frameworks (MOFs) have seen a surge in interest in recent years. The reasoning includes the large degree of control over the metal-nodes and highly ordered pores, which ensures that all active sites are identical, a similarity shared with (post-)metallocene-type catalysts, and a direct testament to the potential of MOFs to act as single-site ethylene polymerization catalysts.<sup>[25–29]</sup> One of the major potential advantages of MOFs is the fact that their synthesis is often quite robust producing MOFs, which are intrinsically stable towards H<sub>2</sub>O and O<sub>2</sub>, whereas (post-) metallocene materials do have stability related issues for example.

Recent work in the literature comprises research from Lin *et al.*, demonstrating the possibility of polymerizing ethylene with a ZrCl<sub>2</sub>-BTC MOF, after activation with MMAO-12, hereby generating ZrMe-BTC as the active MOF.<sup>[30]</sup> Their work exemplified the usage of a MOF as a single-site ethylene polymerization catalyst, since the produced MWD of the PE was monomodal with a related  $D$  value of 2.6, being comparable to PEs produced by (post-)metallocene-type catalysts.

Second, Dincă, Roman-Leshkov and co-workers exploited a Cr<sup>3+</sup> ion-exchanged MFU-4I MOF in ethylene polymerization, finding that this MOF produced a PE with a  $D$  of 1.4, approaching a value of 1, which indicates that the polymers produced for each of the individual polymerization sites are identical. Additionally, they found that it is of paramount importance to accommodate appropriate coordination geometries for the Cr sites to be active in ethylene polymerization.<sup>[31]</sup>

Additionally, our group also studied the usage of several renowned Cr-based MOFs in ethylene polymerization, namely MIL-101(Cr), HKUST-1(Cr) and MIL-53(Cr). This work revealed

that additional parameters, such as the ability of the MOF to be activated, also performs a critical role in attaining polymerization activity with the MOFs that were readily activated by Et<sub>2</sub>AlCl as co-catalyst demonstrating polymerization activities and the MOF that was not demonstrated a poor catalytic activity. Furthermore, both spectroscopic experiments as well as analysis of the produced PE materials demonstrated that the active forms of these MOFs cannot be considered single-site polymerization catalysts since large  $\mathcal{D}$  polymer materials were obtained and a variety of active sites was observed. Furthermore, we found that selecting the appropriate MOF is of paramount importance for attaining desirable PE morphologies.<sup>[32,33]</sup>

### 1.3 Phillips Catalyst Preparation

The Cr Phillips type catalyst preparation is in principle relatively simple; however, reality is far from this. Either Cr<sup>6+</sup> or Cr<sup>3+</sup> precursors can be used, with increasing stringent environmental regulations ensuring the preferable use of Cr<sup>3+</sup> at the expense of Cr<sup>6+</sup> due to the significantly decreased carcinogenicity of Cr<sup>3+</sup> compared to Cr<sup>6+</sup>. A precursor solution is impregnated on a large surface area, large pore volume and wide pore size carrier, *e.g.* SiO<sub>2</sub> and Al<sub>2</sub>O<sub>3</sub>, before being calcined in dry air with specified temperature programs of at least 500 °C, producing the Cr<sup>6+</sup> precursors to the active site.<sup>[20]</sup> This calcination into the Cr<sup>6+</sup> active sites is a particularly delicate procedure and multiple types of active sites are potentially produced (Figure 1.4), predominantly depending on the applied calcination procedure as well as the Cr weight-loading, with higher weight-loadings favoring the formation of di-chromates and eventually poly-chromates. The dependency on desirable mono-chromate structures over di-chromates and poly-chromates impose restrictions on viable Cr weight-loadings, with preference for mono-chromate surface structures restricting the weight-loadings to values up until 1 wt% Cr, whereas higher weight-loadings favor the formation of the proposedly less-active/inactive di-chromates and eventually poly-chromates as well as Cr<sub>2</sub>O<sub>3</sub> formation.<sup>[34,35]</sup>

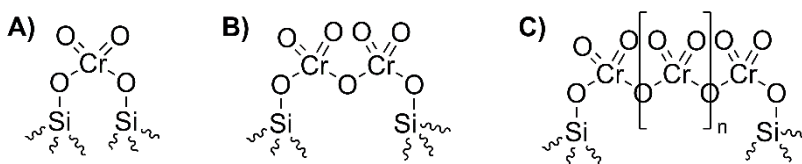


**Figure 1.4.** Schematic overview of the possible variety of surface structures including **A)** mono-chromates, **B)** di-chromates, and **C)** poly-chromates.

## 1.4 Support Type and Promotor Effects

A variety of high surface area and high pore volume supports are available for impregnation with Cr, with the support properties being critical for determining the final catalyst performances. The most common support remains  $\text{SiO}_2$ , which due to its tetrahedral geometry demonstrates excellent compatibility with the  $\text{Cr}^{6+}$  structure. Isostructural and isoelectronic to  $\text{SiO}_2$ ,  $\text{AlPO}_4$  also makes an excellent support material. The critical role of the support in olefin polymerization is exemplified by comparing PE materials produced over a  $\text{SiO}_2$  supported Phillips catalyst to PE materials produced over an  $\text{AlPO}_4$  supported Phillips catalyst. Their distinct differences are ascribed to unique Cr electronic structures originating from characteristic anchoring of the chromate, which is exclusively on Si-OH groups on a  $\text{SiO}_2$  support material and on both Al-OH and P-OH hydroxyls on an  $\text{AlPO}_4$  support material. While other supports, *e.g.*  $\text{TiO}_2$  and  $\text{Al}_2\text{O}_3$ , demonstrate excellent kinetic profiles in the earlier stages of olefin polymerization, they are prone to deactivation, resulting in an approximately 5 times lower catalytic activity over the entire duration as compared to conventional Cr/ $\text{SiO}_2$  Phillips catalysts.<sup>[20,34,36–40]</sup>

Secondly, promotor effects play a critical role in tailoring the support for desirable polymerization performances, which is attributed to enhancing the support acidity and related electron density withdrawal from the Cr site, rendering it more electrophilic. For example, if  $\text{Al}_2\text{O}_3$  is added in few weight-percentages to a  $\text{SiO}_2$  carrier it significantly promotes the activity, it enhances the reducibility of the Cr sites, and it broadens the MWD.<sup>[20,37]</sup> Additionally, the addition of a few weight-percentages of fluoride affects the catalyst performances similarly and also results in enhanced catalytic activities, broadened MWDs, and the ability to use lower calcination temperatures.<sup>[41]</sup> One last example from our group by Cicmil *et al.* included investigating a shell-titanated Cr/Ti/ $\text{SiO}_2$  Phillips catalyst and found enhanced catalyst activities and, probably more important, increased in-situ ethylene oligomerization, which resulted in the formation of LLDPE rather than a HDPE.<sup>[9,42,43]</sup> Conclusively, the common trend is enhanced support acidity through which the electrophilicity of the Cr sites is increased.

## 1.5 Active Site Origins

The plethora of active sites are illustrated in the multimodal MWD curve presented in Figure 1.5, explained by the fact that each unique polymerization site produces to-that-site distinct PE with specific properties in terms of MWD, SCB, and LCB, each uniquely contributing to the multimodal MWD trace.<sup>[7,39,44]</sup>

Until date, this challenge has resulted in methodologies often exploiting model-systems,<sup>[45–55]</sup> or catalyst systems with more defined site distribution, attained by *e.g.* CO reduction.<sup>[56–58]</sup> One specific example of a long-standing point of discussion is the oxidation state of the active site, which was determined to lie between 2 and 3 with a multitude of spectroscopic techniques,

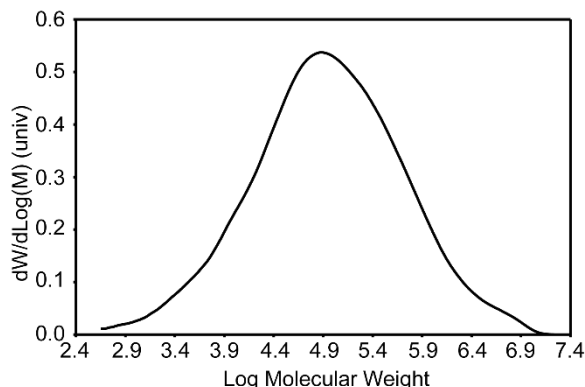


**Figure 1.5.** The Molecular Weight Distribution (MWD) of a polyethylene (PE) produced over a Cr/SiO<sub>2</sub> Phillips-type catalyst in a 5L semi-batch ethylene polymerization reactor at 99 °C and 33 bar without a co-catalyst.

including X-ray Absorption Near-Edge Structure (XANES), probe molecule Fourier Transform Infrared (FT-IR) spectroscopy and UV-Vis-NIR Diffuse Reflectance Spectroscopy (DRS). However, until date different groups still report varying insights, also including additional feasible oxidation states, which is in part attributed to different methodologies, reaction set-ups and catalyst materials.<sup>[22, 24, 47, 48, 51–53, 55–70]</sup>

The co-existence of multiple Cr sites was further exemplified by CO probe molecule FT-IR spectroscopy experiments on CO reduced Cr/SiO<sub>2</sub> catalyst materials, with which three different types of Cr surface sites could be disentangled on the basis of their (increasing) degree of coordinative saturation: Cr<sub>a</sub>, Cr<sub>b</sub> and Cr<sub>c</sub>.<sup>[22]</sup> This is, however, on the assumption that reduction with CO generates “naked” Cr sites, with CO<sub>2</sub> desorbing after the reaction. However, the reality is often far from this, since other reductants, in the form of C<sub>2</sub>H<sub>4</sub> or metal-alkyl co-catalysts (e.g., triethyl borane (TEB), and tri-ethyl aluminum (TEAl)), produce situations in which the reduction products remain intimate constituents of the active site throughout the entire olefin polymerization reaction.<sup>[71–74]</sup>

## 1.6 Effect of Co-catalysts

While ethylene can fulfil the dual role of reductant and monomer source, metal-alkyl co-catalysts are often added to improve the catalytic activity, to remove the induction period, to tailor PE properties, and to remove poisons from the reactor feed. Figure 1.6 schematically demonstrates how co-catalysts can affect the Cr surface sites. First, co-catalysts can abstract the terminal oxo-ligands from the Cr<sup>6+</sup> precursor to the active site. Take note that reduction by-products are only shown to be ancillary ligands in route 4. However, the situation is that the reduction by-products always remain in the coordination sphere of the Cr sites. Secondly, the co-catalyst can react with

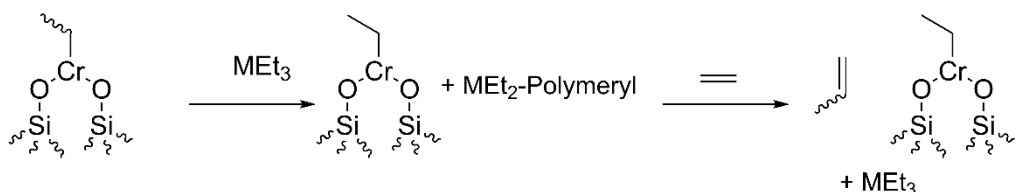
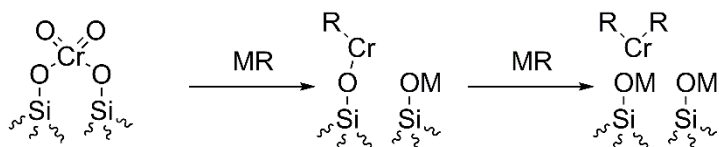
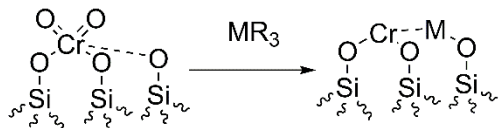
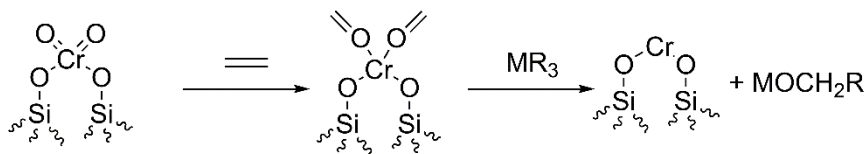
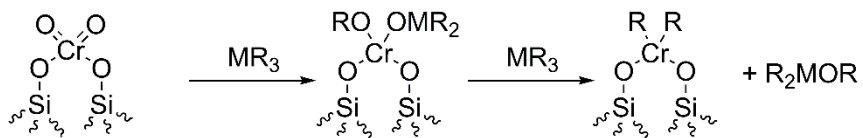
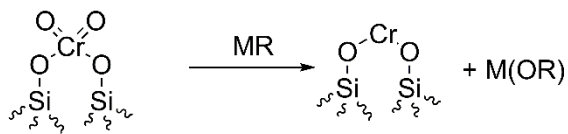


**Figure 1.6.** Schematic overview of the possible reaction routes metal-alkyl co-catalysts can undergo with the Cr surface sites on a Cr/ $\text{SiO}_2$  Phillips-type catalyst.

the terminal oxo-ligands without completely removing them, while subsequent ligand exchange produces bis-alkyl Cr sites, which hereafter participate in ethylene polymerization. The third route is an example of how formaldehyde, an ethylene reduction product, acts as a poison and is scavenged by the metal-alkyl co-catalyst. The fourth route demonstrates how, in addition to removing of the terminal oxo-ligands, the co-catalysts can also react with SiOH moieties in the vicinity of the active site, after which they can coordinate to the reduced active Cr site. The subsequent route starts to demonstrate the sensitivity of the Cr sites to excess metal-alkyl co-catalysts, which in this case can also result in an attack on the O-Cr anchoring bonds, producing mono-anchored species, and potentially eventually leaching of the Cr with even larger excesses of metal-alkyl co-catalyst. This illustrates the sensitivity of the Cr/SiO<sub>2</sub> Phillips catalyst and exemplifies how only narrow ranges of metal-alkyl co-catalyst amounts can be used, often in the range of 0-5 ppm based on reactor volume, with values exceeding these concentrations resulting in decreased catalyst performances and related catalyst deactivation. Last but not least, certain metal-alkyls are known to be chain-transfer reagents and can hereby help with elimination and re-alkylation of the active site, respectively producing an aluminum-polymer complex as well as freeing the Cr site for the formation of a new polymer.<sup>[20]</sup>

All these discussed effects uniquely affect the ethylene polymerization properties, with the common trend being that metal-alkyls directly alter the Cr active site in terms of electron density and coordination structure. These alterations result in significantly improved catalyst performances, such as increased activities as well as a strongly decreased induction period.<sup>[9,42,64,72,73,75]</sup> Additionally, and probably more importantly, the generation and alteration of a larger variety active Cr sites also translates into a large product pool of PE materials with characteristic properties in terms of MWD, SCB, and LCB.<sup>[42,43]</sup>

## 1.7 Ethylene Polymerization Mechanism

The ethylene polymerization and catalyst activation mechanism have been the subject of much controversy, with a more deconvoluted picture emerging in the recent years of both mechanisms, but more so for the ethylene polymerization mechanism. First, the polymerization is likely to occur via the Cossee-Arlman mechanism, which is depicted in Figure 1.7,<sup>[19]</sup> where we consider starting from a Cr-alkyl bond without commenting on the Cr oxidation state or additional ligands. In addition to this Cr-C bond, vacancies at the Cr site are also a prerequisite, to which incoming ethylene molecules coordinate. Subsequently, ethylene inserts into the Cr-C bond *via* a migratory insertion step, hereby growing the PE molecule for numerous steps until elimination occurs through  $\beta$ -hydrogen elimination, thereby yielding a Cr-hydride bond and a vinyl end-group. Subsequent coordination and migratory insertion of ethylene in this Cr-hydride bond then marks the birth of a new polyethylene molecule. While  $\beta$ -hydrogen elimination is

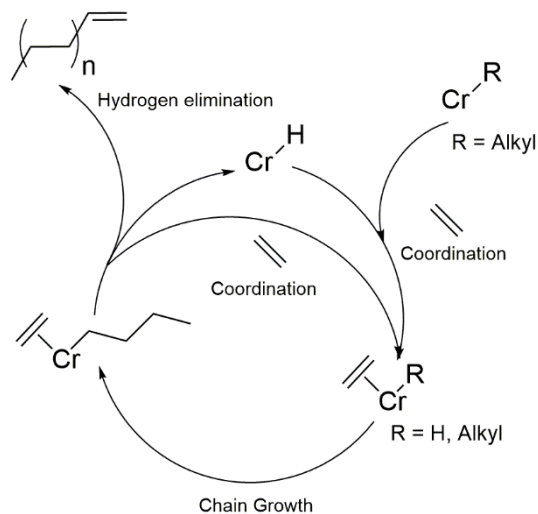


**Figure 1.7.** A schematic illustration of the Cossee-Arlman mechanism, which is the predominant pathway for chain elongation as well as chain elimination.

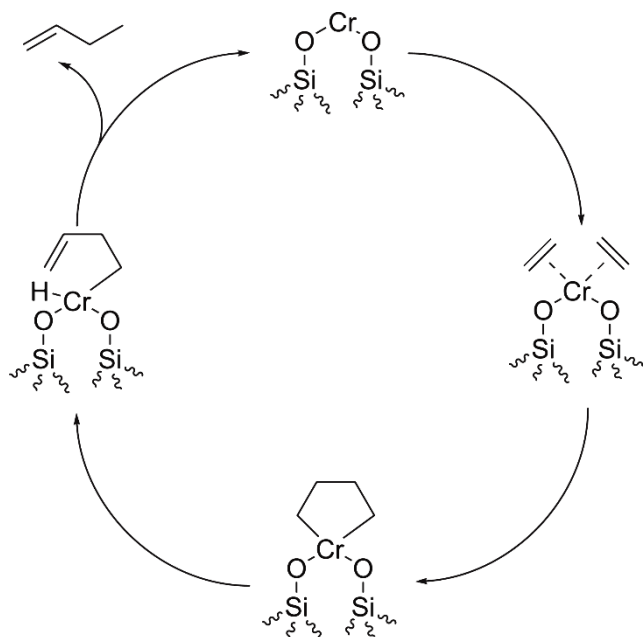


**Figure 1.8.** Ethylene oligomerization mechanism, which occurs through the metallacycle mechanism and is responsible for the in-situ generation of  $\alpha$ -oligomers.

likely prevalent, it is known that e.g., tri-ethyl aluminum acts as chain-transfer reagent and can enable an alternative elimination mechanism, for which the mechanism is shown in Figure 1.6.

The second suggested chain elongation involves a metallacycle mechanism, while it is unlikely that longer PE molecules are produced through this mechanism,  $\alpha$ -oligomers are likely produced via this route, which can subsequently insert in the growing PE chain, generating Short-Chain Branches. Recent research by Groppo *et al.*<sup>[72]</sup> has exemplified how treatment with TEAI resulted in the formation of mono-grafted Cr<sup>2+</sup> species on the catalyst surface, which are likely responsible for the oligomerization of ethylene. In any case, it is likely that oligomerization occurs through simultaneous oxidative addition of two ethylene molecules, creating a metallacycle. Hereafter additional ethylene molecules can either insert to increase the size of the metallacycle or elimination occurs through  $\beta$ -hydrogen elimination and subsequent reductive elimination that frees the  $\alpha$ -oligomer. Work from our group has shown that a LLDPE can be produced with a Cr/Ti/SiO<sub>2</sub> Phillips catalyst without co-feeding 1-hexene, attributed to the enhanced oligomerization properties of the Ti-rich region, resulting in a more branched PE, whereas the Ti-scarce region produced a more linear PE, which is more the norm for Phillips-type catalysts.<sup>[42,43]</sup>

## 1.8 Active Site Formation and Initiation Pathways

The active site formation and initiation pathways are still the reason for many heated debates with different groups reporting different pathways. As mentioned, this is in part caused by the different catalyst materials as well as reaction set-up. This section serves to illustrate and discuss some of the more recent investigated and proposed mechanisms on the formation of the active site upon reacting with C<sub>2</sub>H<sub>4</sub>.

Recent work by Groppo *et al.*, illustrated in Figure 1.9, has shown that formaldehyde is the predominant reduction by-product, which does not leave the active site but through a Tischenko reaction forms methyl-formate that ligates to the newly formed Cr<sup>2+</sup> active site.<sup>[74,76,77]</sup> Their research supports Cr<sup>2+</sup> as the active site in ethylene polymerization, where they found that these Cr<sup>2+</sup> sites were consumed by ethylene with the simultaneous formation of a white sticky product. With X- and Q-band EPR investigations they did observe Cr<sup>3+</sup> species, however found that these were derived from Cr<sup>5+</sup> precursors and found that these surface sites were inactive in ethylene

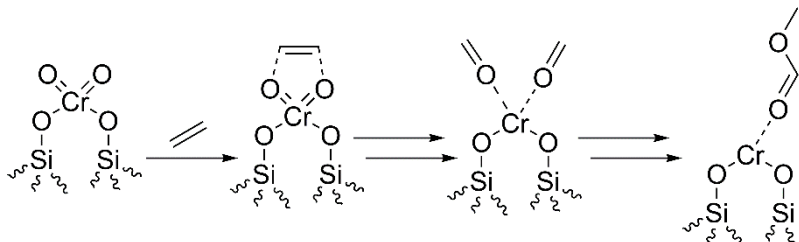


**Figure 1.9.** Activation of a Cr/SiO<sub>2</sub> Phillips-type catalyst with ethylene as reported by Groppo *et al.*<sup>[74,76,77]</sup>

polymerization.<sup>[78]</sup> Now, it is worth stating that here the formed Cr<sup>2+</sup> species are active in ethylene polymerization, however it does not (yet) show how the first Cr-C bond is formed or how polymerization occurs for that matter.

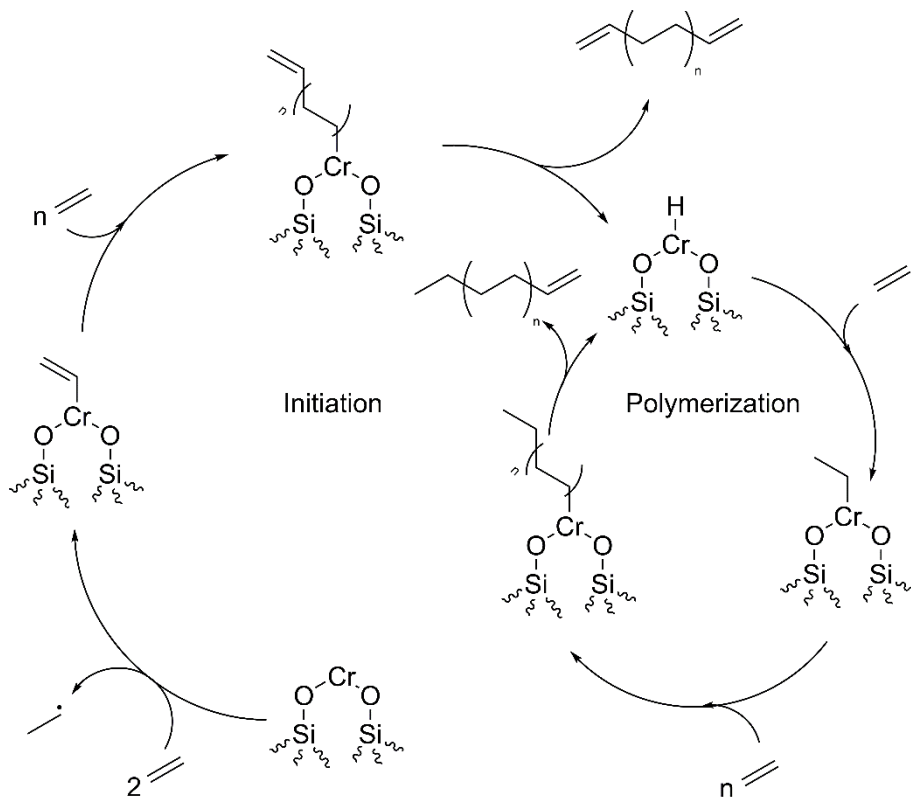


**Figure 1.10.** Activation of a Cr/SiO<sub>2</sub> Phillips-type catalyst with ethylene as reported by Scott *et al.*<sup>[61,79,80]</sup>

On the other hand, Scott *et al.* support Cr<sup>3+</sup> to be the active site for ethylene polymerization.<sup>[61,79,80]</sup> Their findings indicate the formation of an organo-Cr(III) complex after exposure of a Cr<sup>2+</sup> pre-reduced Phillips catalyst to ethylene. This occurs through a redox reaction, involving a one-electron oxidation of Cr<sup>2+</sup> via ethylene disproportionation, hereafter a Cr<sup>2+</sup>-CH=CH<sub>2</sub> complex is coordinated. Subsequent chain propagation occurs through the Cossee-Arlman mechanism with  $\beta$ -hydrogen elimination making up the final step: producing a first PE molecule with two vinyl end-groups. Subsequent polymerization takes place through coordination of ethylene, migratory insertion into the Cr-hydride, propagation through the Cossee-Arlman mechanism and  $\beta$ -hydrogen elimination.

A third proposed mechanism, postulated by Wachs *et al.* (Figure 1.11, route A), involves activation of an ethylene C-H bond over a Si-O-Cr bond through a oxochromacyclic intermediate

and hydrogen abstraction, hereby forming a Cr<sup>3+</sup>-vinyl complex as well as an additional Si-OH moiety.<sup>[68,81]</sup> Copéret *et al.* also investigated activation over a Si-O-Cr bond through a cyclic mechanism,<sup>[55,82,83]</sup> finding that highly strained Si-O-Cr bonds are producing the most active sites, over which activation occurs the easiest (Figure 1.11, route B). Furthermore, their research revealed that, through the use of model catalysts, di-nuclear Cr<sup>3+</sup> complexes were highly active in ethylene polymerization, whereas di-nuclear Cr<sup>2+</sup> complexes were inactive, hereby further complicating the debate on the active site oxidation state and molecular structure.<sup>[47,54,55]</sup>

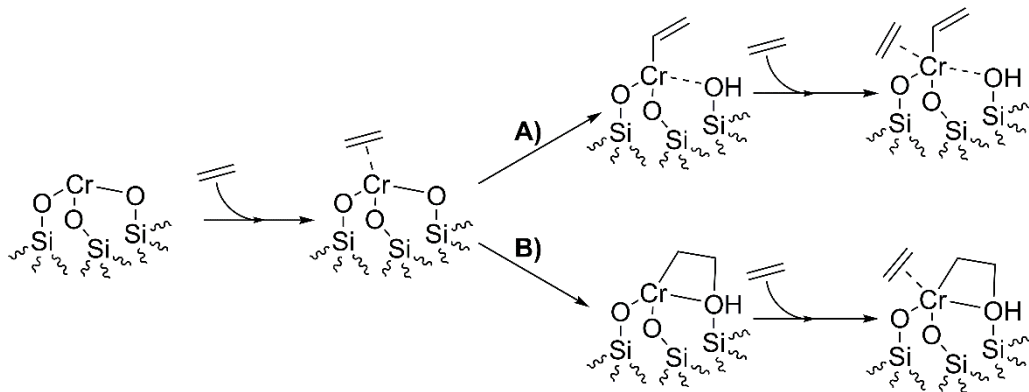


**Figure 1.11.** Activation of a Cr/SiO<sub>2</sub> Phillips-type catalyst by ethylene over a Si-O-Cr bond **A)** producing a Cr<sup>3+</sup>-vinyl complex according to Wachs *et al.*<sup>[68,81]</sup> or **B)** or through a cyclic activation mechanism according to Copéret *et al.*<sup>[55,82,83]</sup>

## 1.9 Outline of the Ph.D. Thesis

Cr-based ethylene polymerization catalysts take a prominent role in everyday life. While the field of Phillips-type ethylene polymerization is relatively mature, further developing spectroscopic and microscopic techniques allow us to approach this delicate catalyst system with new and refreshed mindsets, often studied under live (*operando*) conditions, which allows us to improve our understanding of this catalyst. This has enabled us to investigate the potential of rational co-catalyst selection as a strategy for exposing desirable catalyst performances and PE properties over one singular Cr/SiO<sub>2</sub> Phillips catalyst formula. Second, the knowledge gained in the field of Cr/SiO<sub>2</sub> Phillips-type ethylene polymerization was focused into investigating the potential of Cr-based MOFs in ethylene polymerization, which have the potential to act as heterogenized single-site polymerization catalysts. In what follows, we walk through the content of this **Ph.D. Thesis**, with a brief discussion on the highlights of each **Chapter**.

In **Chapter 2** we demonstrate the different effects of tri-ethyl borane (TEB) and tri-ethyl aluminum (TEAl) on the Cr/SiO<sub>2</sub> catalyst's performances. Despite an overall decreased induction period as well as increased activity, we found that TEB enhanced the catalytic activity more significantly than TEAl did. On the other hand, if excess amounts of TEB were used the catalyst started to deactivate, a phenomenon which was absent while using TEAl. Additionally, analysis of the PE materials revealed that by selecting the appropriate amount of TEB or TEAl the density could be tailored around a benchmark value obtained for the PE produced without a co-catalyst, inferring that selection of the proper type and amount of co-catalyst can be considered a viable strategy for obtaining the desirable PE features. UV-Vis-NIR diffuse reflectance spectroscopy (DRS) experiments revealed that indeed the co-catalysts enabled different activation pathways. TEAl reduced the Cr<sup>6+</sup> surface sites to a mixture of bis-grafted bis-alkyl Cr<sup>4+</sup>, mono-grafted mono-alkyl Cr<sup>2+</sup> and inaccessible Cr<sup>3+</sup> sites. Excesses of TEAl resulted in overreduction of the active Cr<sup>4+</sup> polymerization sites into either the Cr<sup>2+</sup> sites or the inaccessible Cr<sup>2+</sup> sites. On the other hand, TEB generated Cr<sup>2+</sup> sites and Cr<sup>3+</sup> sites, with excesses resulting in the conversion of these Cr<sup>2+</sup> sites into the Cr<sup>3+</sup> sites, possibly explaining the decreasing catalyst activity at higher amounts of TEB.

In **Chapter 3** we expand on the observed differences in polyethylene properties and have found, with <sup>13</sup>C Nuclear Magnetic Resonance (NMR) and GPC, how PE properties can indeed be tailored by strategically selecting the appropriate type and amount of co-catalyst. In terms of MWD, this was broadened to a larger extent by TEB than by TEAl, which only broadened the MWD at higher amounts. Second, TEAl enhanced SCB to a larger extent than TEB, which in turn only enhanced the SCB at higher amounts. With the different effects on the PE properties being evident, the second part of this **Chapter** addresses the question as to whether these differences were already manifested at the early stages of polymerization. We have used Scanning Transmission X-ray Microscopy (STXM) to study the density at the nanometer scale of PE materials produced with 1.5 or 5.0 mol. eq. of either TEB or TEAl without exceeding catalyst yields of 1-2 g<sub>PEG<sub>cat</sub></sub><sup>-1</sup>, which are considered early-stage PE materials. Interestingly we found that the average densities of all early-stage PEs were lower than what was expected for bulk materials. Second, we found that the expected different PE properties in terms of MWD and SCB indeed produce early-stage PEs with different densities, with the trend being comparable to the different densities for the bulk PE materials. The early-stage PEs produced with TEAl portrayed lower densities than those produced with TEB.

In **Chapter 4** we discuss how Raman spectroscopy can be used to study the surface structures on the Cr/SiO<sub>2</sub> Phillips catalyst and the effect of different reduction gasses at various temperatures on these surface structure compositions. These experiments demonstrated the existence of two main types of surface sites contributing with Raman signals at 985 cm<sup>-1</sup> and 1005 cm<sup>-1</sup>, respectively attributed to Cr<sup>6+</sup><sub>di-oxo</sub> and Cr<sup>6+</sup><sub>mono-oxo</sub> surface structures. Furthermore, by performing the reductions at various temperatures we found that the surface sites related to the

former signal reduce with relatively greater ease. Additionally, it appeared that H<sub>2</sub> was also more proficient at reducing the Cr<sup>6+</sup> surface sites at lower temperatures than CO. Furthermore, in the experiments that used C<sub>2</sub>H<sub>4</sub> as reduction gas, we similarly found that a relatively larger part of the sites contributing to the 985 cm<sup>-1</sup> Raman signal was reduced than the surface sites contributing to the 1005 cm<sup>-1</sup> signal and the final end-point spectra were in this instance already attained within 6 min of the reaction.

In **Chapter 5** we have studied three renowned Cr based MOFs as ethylene polymerization catalysts. More specifically we have studied MIL-101(Cr)-NDC (NDC = 2,6-dicarboxynaphthalene), MIL-53(Cr) and HKUST-1(Cr) (MIL = Matérial Institut Lavoisier, HKUST = Hong Kong University of Science and Technology). With 100 mol. eq. Et<sub>2</sub>AlCl as activator, the attainable catalytic activities were different for each of the MOFs. Unfortunately, a minor amount of the activity could be ascribed to leached species with a maximum of 5% of all Cr sites being leached for HKUST-1(Cr) and less than 1% for both MIL-101(Cr)-NDC and MIL-53(Cr). Analysis of the PE materials revealed that the MOFs produced unique materials, with broad MWDs, which is particularly interesting since MOFs are considered single-site catalysts. However, our findings indicate that under the applied reaction conditions this is far from the reality. Additionally, we found that selection of the proper MOF as templating agent is critical for attaining desirable spherical PE material morphologies, which was only the case for MIL-101(Cr)-NDC. MIL-53(Cr) produced a worm-like PE morphology, which is an effect of the too-close active-site spacing, hereby hindering lateral PE growth, while growth perpendicular to the catalyst surface is unhampered. HKUST-1(Cr) demonstrated a morphology which demonstrated both PE fibers as well as spherical PE materials, illustrating the potential to produce PE with more desirable morphologies. In a second part, we have opted to explain the observed reactivities by investigating active site formation. We found that the catalytic activity was directly related to the activation of the MOF material by the Et<sub>2</sub>AlCl co-catalyst, while the total collapse of the MOF material was excluded.

Last, **Chapter 6** summarizes the findings of this **Ph.D. Thesis**, while also providing some prospects and perspectives on future research.

## 1.10 References

- [1] Jöns Jacob Berzelius, found under "[https://en.wikipedia.org/wiki/J%C3%BCns\\_Jacob\\_Berzelius](https://en.wikipedia.org/wiki/J%C3%BCns_Jacob_Berzelius)" accessed March **2021**.
- [2] Jöns Jacob Berzelius, found under: "<https://www.britannica.com/biography/Jons-Jacob-Berzelius>" accessed March **2021**.
- [3] *Polymers - Opportunities and Risks in The Handbook of Environmental Chemistry*, Springer-Verlag, Vol 12 (Ed.: P. Eyerer, M. Weller, C. Hübner), Berlin, Germany, **2010**, 1-299.
- [4] R. Mühlaupt, *Macromol. Chem. Phys.* **2013**, 214, 159–174.
- [5] PlasticsEurope, Plastics - The Facts 2020 An analysis of European plastics, production, demand and waste data, **2020**, 1-64.

- [6] R. H. Somani, L. Yang, L. Zhu, B. S. Hsiao, *Polymer* **2005**, *46*, 8587–8623.
- [7] J. S. Fodor, P. J. DesLauriers, M. J. Lamborn, S. U. Hamim, *Polymer* **2019**, *180*, 121730.
- [8] M. P. McDaniel, *J. Catal.* **2009**, *261*, 34–49.
- [9] D. Cicmil, J. Meeuwissen, A. Vantomme, B. M. Weckhuysen, *ChemCatChem* **2016**, *8*, 1937–1944.
- [10] J. C. Woodbrey, P. Ehrlich, *J. Am. Chem. Soc.* **1963**, *85*, 1580–1584.
- [11] R. O. Symcox, P. Ehrlich, *J. Am. Chem. Soc.* **1962**, *84*, 531–536.
- [12] M. G. Evans, M. Polanyi, *Trans. Faraday Soc.* **1935**, *31*, 875–894.
- [13] J. P. Hogan, R. L. Banks, *US Pat*, 2825721, **1958**.
- [14] J. P. Hogan, R. L. Banks, *US Pat*, 2951816, **1960**.
- [15] *Advances in Polymer Science*, Vol. 257 (Ed.: W. Kaminsky), Springer, Berlin, **2013**.
- [16] H. H. Brintzinger, D. Fischer, R. Mülhaupt, B. Rieger, R. M. Waymouth, *Angew. Chem. Int. Ed.* **1995**, *34*, 1143–1170.
- [17] R. Van Grieken, A. Carrero, I. Suarez, B. Paredes, *Eur. Polym. J.* **2007**, *43*, 1267–1277.
- [18] B. Paredes, R. Van Grieken, A. Carrero, I. Suarez, J. B. P. Soares, *Macromol. Chem. Phys.* **2011**, *212*, 1590–1599.
- [19] *Handbook of Transition Metal Polymerization Catalysts*, Vol. 1 (Ed.: R. Hoff), John Wiley & Sons, Inc., Hoboken, **2010**.
- [20] M. P. McDaniel, *Adv. Catal.* **2010**, *53*, 123–606.
- [21] R. Cheng, Z. Liu, X. He, P. Qui, M. Terano, M. S. Eisen, S. L. Scott, B. Liu, *Adv. Polym. Sci.* **2013**, *257*, 135–202.
- [22] A. Zecchina, E. Groppo, C. Lamberti, S. Bordiga, G. Spoto, *Chem. Rev.* **2005**, *105*, 115–184.
- [23] R. Ramachandra Rao, B. M. Weckhuysen, R. A. Schoonheydt, *Chem. Commun.* **1999**, 445–446.
- [24] B. M. Weckhuysen, I. E. Wachs, R. A. Schoonheydt, *Chem. Rev.* **1996**, *96*, 3327–3349.
- [25] S. M. J. Rogge, A. Bavykina, J. Hajek, H. Garcia, A. I. Olivos-Suarez, A. Sepúlveda-Escribano, A. Vimont, G. Clet, P. Bazin, F. Kapteijn, M. Daturi, E. V. Ramos-Fernandez, F. X. Llabrés i Xamena, V. Van Speybroeck, J. Gascon, *Chem. Soc. Rev.* **2017**, *46*, 3134–3184.
- [26] S. M. Cohen, Z. Zhang, J. A. Boissonnault, *Inorg. Chem.* **2016**, *55*, 7281–7290.
- [27] B. E. G. Lucier, S. Chen, Y. Huang, *Acc. Chem. Res.* **2018**, *51*, 319–330.
- [28] D. Beyermann, A. Hartwig, *Arch. Toxicol.* **2008**, *82*, 493–512.
- [29] K. J. Liu, X. Shi, *Mol. Cell. Biochem.* **2001**, *222*, 41–47.
- [30] P. Ji, J. B. Solomon, Z. Lin, A. Johnson, R. F. Jordan, W. Lin, *J. Am. Chem. Soc.* **2017**, *139*, 11325–11328.
- [31] H. D. Park, R. J. Comito, Z. Wu, G. Zhang, N. Ricke, C. Sun, T. Van Voorhis, J. T. Miller, Y. Román-Leshkov, M. Dincă, *ACS Catal.* **2020**, *10*, 3864–3870.
- [32] M. Rivera-Torrente, P. D. Pletcher, M. K. Jongkind, N. Nikolopoulos, B. M. Weckhuysen, *ACS Catal.* **2019**, *9*, 3059–3069.
- [33] M. K. Jongkind, M. Rivera-Torrente, N. Nikolopoulos, B. M. Weckhuysen, *Chem. Eur. J.* **2021**, *27*, 5769–5781.
- [34] M. P. McDaniel, M. B. Welch, M. J. Dreiling, *J. Catal.* **1983**, *82*, 118–126.
- [35] E. M. E. van Kimmenade, J. Loos, J. W. Niemantsverdriet, P. C. Thüne, *J. Catal.* **2006**, *240*, 39–46.
- [36] M. P. McDaniel, M. M. Johnson, *Macromolecules* **2005**, *20*, 773–778.
- [37] G. A. Martino, C. Barzan, A. Piovano, A. Budnyk, E. Groppo, *J. Catal.* **2018**, *357*, 206–212.

- [38] M. P. McDaniel, M. M. Johnson, *J. Catal.* **1986**, *101*, 446–457.
- [39] P. J. Deslauriers, C. Tso, Y. Yu, D. L. Rohlffing, M. P. McDaniel, *Appl. Catal. A Gen.* **2010**, *388*, 102–112.
- [40] B. Rebenstorf, T. C. Sheng, *Langmuir* **1991**, *7*, 2160–2165.
- [41] Q. Sun, R. Cheng, Z. Liu, X. He, N. Zhao, B. Liu, *ChemCatChem* **2017**, *9*, 3364–3373.
- [42] D. Cicmil, I. K. Van Ravenhorst, J. Meeuwissen, A. Vantomme, B. M. Weckhuysen, *Catal. Sci. Technol.* **2016**, *6*, 731–743.
- [43] D. Cicmil, J. Meeuwissen, A. Vantomme, J. Wang, I. K. Van Ravenhorst, H. E. Van Der Bij, A. Muñoz-Murillo, B. M. Weckhuysen, *Angew. Chem. Int. Ed.* **2015**, *54*, 13073–13079.
- [44] K. Tonosaki, T. Taniike, M. Terano, *J. Mol. Catal. A Chem.* **2011**, *340*, 33–38.
- [45] P. C. Thüne, C. P. J. Verhagen, M. J. G. van den Boer, J. W. Niemantsverdriet, *J. Phys. Chem. B* **2002**, *101*, 8559–8563.
- [46] E. M. E. Van Kimmenade, A. E. T. Kuiper, Y. Tamminga, P. C. Thüne, J. W. Niemantsverdriet, *J. Catal.* **2004**, *223*, 134–141.
- [47] C. Copéret, F. Allouche, K. W. Chan, M. P. Conley, M. F. Delley, A. Fedorov, I. B. Moroz, V. Mougel, M. Pucino, K. Searles, K. Yamamoto, P. A. Zhizko, *Angew. Chem. Int. Ed.* **2018**, *57*, 6398–6440.
- [48] A. Budnyk, A. Damin, C. Barzan, E. Groppo, C. Lamberti, S. Bordiga, A. Zecchina, *J. Catal.* **2013**, *308*, 319–327.
- [49] P. C. Thüne, R. Linke, W. J. H. van Gennip, A. M. de Jong, J. W. Niemantsverdriet, *J. Phys. Chem. B* **2002**, *105*, 3073–3078.
- [50] P. C. Thüne, J. Loos, X. Chen, E. M. E. van Kimmenade, B. Kong, J. W. Niemantsverdriet, *Top. Catal.* **2007**, *46*, 239–245.
- [51] M. F. Delley, C. S. Praveen, A. P. Borosy, F. Núñez-Zarur, A. Comas-Vives, C. Copéret, *J. Catal.* **2017**, *354*, 223–230.
- [52] L. Floryan, A. P. Borosy, F. Núñez-Zarur, A. Comas-Vives, C. Copéret, *J. Catal.* **2017**, *346*, 50–56.
- [53] C. Copéret, *Acc. Chem. Res.* **2019**, *52*, 1697–1708.
- [54] M. F. Delley, G. Lapadula, F. Núñez-Zarur, A. Comas-Vives, V. Kalendra, G. Jeschke, D. Baabe, M. D. Walter, A. J. Rossini, A. Lesage, L. Emsley, O. Maury, C. Copéret, *J. Am. Chem. Soc.* **2017**, *139*, 8855–8867.
- [55] M. P. Conley, M. F. Delley, G. Siddiqi, G. Lapadula, S. Norsic, V. Monteil, O. V. Safonova, C. Copéret, *Angew. Chem. Int. Ed.* **2014**, *53*, 1872–1876.
- [56] B. M. Weckhuysen, L. M. De Ridder, R. A. Schoonheydt, *J. Phys. Chem.* **1993**, *97*, 4756–4763.
- [57] B. M. Weckhuysen, A. A. Verberckmoes, A. L. Buttiens, R. A. Schoonheydt, *J. Phys. Chem.* **1994**, *98*, 579–584.
- [58] B. M. Weckhuysen, R. A. Schoonheydt, J.-M. Jehng, I. E. Wachs, S. J. Cho, R. Ryoo, S. Kijlstra, E. Poels, *J. Chem. Soc. Faraday Trans.* **1994**, *91*, 3245–3253.
- [59] Z. Hulvey, B. Vlaisavljevich, J. A. Mason, E. Tsivion, T. P. Dougherty, E. D. Bloch, M. Head-Gordon, B. Smit, J. R. Long, C. M. Brown, *J. Am. Chem. Soc.* **2015**, *137*, 10816–10825.
- [60] N. M. Peek, D. B. Jeffcoat, C. Moisii, L. Van De Burgt, S. Profeta, S. L. Scott, A. E. Stiegman, *J. Phys. Chem. C* **2018**, *122*, 4349–4358.
- [61] A. Fong, C. Vandervelden, S. L. Scott, B. Peters, *ACS Catal.* **2018**, *8*, 1728–1733.
- [62] L. Zhong, M. Y. Lee, Z. Liu, Y. J. Wanglee, B. Liu, S. L. Scott, *J. Catal.* **2012**, *293*, 1–12.

- [63] E. Groppo, C. Lamberti, S. Bordiga, G. Spoto, A. Zecchina, *J. Catal.* **2006**, *240*, 172–181.
- [64] E. Groppo, G. A. Martino, A. Piovano, C. Barzan, *ACS Catal.* **2018**, *8*, 10846–10863.
- [65] E. Groppo, C. Prestipino, F. Cesano, F. Bonino, S. Bordiga, C. Lamberti, P. C. Thüne, J. W. Niemantsverdriet, A. Zecchina, *J. Catal.* **2005**, *230*, 98–108.
- [66] L. Mino, C. Barzan, G. A. Martino, A. Piovano, G. Spoto, A. Zecchina, E. Groppo, *J. Phys. Chem. C* **2019**, *123*, 8145–8152.
- [67] B. M. Weckhuysen, L. M. De Ridder, P. J. Grobet, R. A. Schoonheydt, *J. Phys. Chem.* **1995**, *99*, 320–326.
- [68] A. Chakrabarti, I. E. Wachs, *Catal. Lett.* **2014**, *145*, 985–994.
- [69] A. Chakrabarti, M. Gierada, J. Handzlik, I. E. Wachs, *Top. Catal.* **2016**, *59*, 725–739.
- [70] B. M. Weckhuysen, R. A. Schoonheydt, *Catal. Today* **1999**, *49*, 441–451.
- [71] G. A. Martino, A. Piovano, C. Barzan, S. Bordiga, E. Groppo, *Top. Catal.* **2018**, *61*, 1465–1473.
- [72] G. A. Martino, A. Piovano, C. Barzan, J. Rabeah, G. Agostini, A. Bruekner, G. Leone, G. Zanchin, T. Monoi, E. Groppo, *ACS Catal.* **2020**, *10*, 2694–2706.
- [73] J. Joseph, K. C. Potter, M. J. Wulfers, E. Schwerdtfeger, M. P. McDaniel, F. C. Jentoft, *J. Catal.* **2019**, *377*, 550–564.
- [74] C. Barzan, A. Piovano, L. Braglia, G. A. Martino, C. Lamberti, S. Bordiga, E. Groppo, *J. Am. Chem. Soc.* **2017**, *139*, 17064–17073.
- [75] C. A. Cruz, M. M. Monwar, J. Barr, M. P. McDaniel, *Macromolecules* **2019**, *52*, 5750–5760.
- [76] T. Seki, T. Nakajo, M. Onaka, *Chem. Lett.* **2006**, *35*, 824–829.
- [77] A. M. P. Koskinen, A. O. Kataja, *Org. React.* **2015**, *86*, 105–409.
- [78] E. Morra, G. A. Martino, A. Piovano, C. Barzan, E. Groppo, M. Chiesa, *J. Phys. Chem. C* **2018**, *122*, 21531–21536.
- [79] C. Brown, J. Krzystek, R. Achey, A. Lita, R. Fu, R. W. Meulenberg, M. Polinski, N. Peek, Y. Wang L. J. van de Burgt, S. Profeta, A. E. Stiegman, S. L. Scott, *ACS Catal.* **2015**, *5*, 5574–5583
- [80] C. Brown, A. Lita, Y. Tao, N. Peek, M. Crosswhite, M. Mileham, J. Krzystek, R. Achey, R. Fu, J. K. Bindra, M. Polinski, Y. Wang, L. J. van de Burgt, D. Jeffcoat, S. Profeta Jr., A. E. Stiegman, S. L. Scott, *ACS Catal.* **2017**, *7*, 7442–7455.
- [81] A. Chakrabarti, M. Gierada, J. Handzlik, I. E. Wachs, *Top. Catal.* **2016**, *59*, 725–739.
- [82] M. F. Delley, M. P. Conley, C. Copéret, *Catal. Lett.* **2014**, *144*, 805–808.
- [83] M. F. Delley, F. Nunez-Zarur, M. P. Conley, A. Comas-Vives, G. Siddiqi, S. Norsic, V. Monteil, O. V. Safanova, C. Coperet, *Proc. Natl. Acad. Sci.* **2014**, *111*, 11624–11629.



## Chapter 2

# Tuning the Redox Chemistry of a Cr/SiO<sub>2</sub> Phillips Catalyst for Controlling Activity, Induction Period and Polymer Properties

### Abstract

The Cr/SiO<sub>2</sub> Phillips catalyst has taken a central role in ethylene polymerization ever since its discovery in 1951. This catalyst is unique compared to other ethylene polymerization catalysts since it is active without the addition of a metal-alkyl compound as co-catalyst. However, metal-alkyls can be added for scavenging poisons, enhancing the catalyst activity, reducing the induction period, and altering polymer characteristics. Despite extensive research into the working state of the catalyst, still no consensus has been reached. In this **Chapter**, we show that by varying the type of metal-alkyl co-catalyst and its amount, the Cr redox chemistry can be tailored, resulting in distinct catalyst activities, induction periods, and polymer characteristics. We have used in-situ UV-Vis-NIR diffuse reflectance spectroscopy (DRS) for studying the Cr oxidation state during the reduction by tri-ethyl borane (TEB) or tri-ethyl aluminum (TEAI) and during subsequent ethylene polymerization. The results showed that TEB primarily acts as a reductant and reduces Cr<sup>6+</sup> with subsequent ethylene polymerization resulting in rapid polyethylene formation. TEAI generated two unique types of Cr<sup>2+</sup> sites, inaccessible Cr<sup>3+</sup> sites, and active Cr<sup>4+</sup> sites. Subsequent addition of ethylene also revealed increased reducibility of residual Cr<sup>6+</sup> sites and resulted in rapid polyethylene formation. These results demonstrate the possibility of controlling the redox chemistry by adding the proper amount and type of metal-alkyl co-catalyst, which can be exploited as a strategy for tailoring the catalytic activity as well as for suppressing or enhancing desirable polyethylene characteristics.

*This Chapter is based on:*

M. K. Jongkind, T. van Kessel, M. E. Z. Velthoен, N. Friederichs, B. M. Weckhuysen, *ChemPhysChem* **2020**, 21, 1665-1674.

## 2.1 Introduction

Polyethylene (PE) is one of the most important polymers in today's society, with its annual production exceeding 100 million tons in 2020.<sup>[1]</sup> The catalytic production of PE heavily relies on three workhorses, namely Ziegler-Natta type catalysts<sup>[2,3]</sup>, (post-) metallocene-type catalysts<sup>[4]</sup> and Phillips-type catalysts.<sup>[1,5–8]</sup> The Cr/SiO<sub>2</sub> Phillips-type catalyst is uniquely positioned with respect to the two other ethylene polymerization catalysts. Whereas Ziegler-Natta and Group 4 transition metal-based (post-)metallocene catalyst types need to be activated by a metal-alkyl co-catalyst, this is not required for the Phillips catalyst. Here, ethylene can fulfill a dual role of activator and monomer source. On the other hand, metal-alkyls can be added to scavenge poisons, to decrease the induction period, to enhance the ethylene polymerization rate, and to control the polymer product characteristics. Another remarkable difference is that, in contrast to Ziegler-Natta and the (post-) metallocene catalysts, the chain termination/transfer in Phillips-type systems is only mildly sensitive to H<sub>2</sub>.<sup>[1]</sup>

Ever since its discovery by Hogan and Banks at Phillips Petroleum Company in 1951, and patenting in the following years, the Phillips catalyst is nowadays responsible for more than 30% of all High-Density Polyethylene (HDPE) produced worldwide.<sup>[9,10]</sup> Despite this catalyst's well-established importance, there still is no consensus on its working state and the related ethylene polymerization mechanism. Completely understanding the functioning of this catalyst is, however, of paramount importance for further fine-tuning catalyst properties as well as for defining product characteristics.

Numerous research efforts have focused on understanding the active site oxidation state and molecular structure of this catalyst, which to date remains a matter of debate.<sup>[11–17]</sup> Solving this problem remains challenging because of at least two reasons. First of all, only a very low Cr weight loading is viable for Phillips-type catalysts, while secondly, this system is defined by a large variety among Cr sites of which only a small portion (maximum of ~30%) is proposed to be active in ethylene polymerization.<sup>[18–22]</sup>

This has resulted in the use of various characterization approaches often avoiding high pressures and temperatures. Examples include model systems<sup>[22–28]</sup> or well-defined catalyst systems in which Cr<sup>6+</sup> is reduced by e.g. CO.<sup>[13,14,29,30]</sup> With an array of spectroscopic techniques revealing that the oxidation state of the Cr active site lies between 2 and 3.<sup>[13,14,20,31–44]</sup> However, assigning a definitive oxidation state number remains a matter of debate due to the various findings from different groups, although this could be in part explained due to different catalyst materials and reaction set-ups.<sup>[6,20,34–38,40–42,46–49]</sup> Fortunately, with the continuous development of advanced spectroscopic and microscopic techniques, the low Cr weight-loading and relatively small portion of active sites are becoming less of a problem, exemplified by elucidation of an ethylene reduced active site.<sup>[18]</sup> In addition to our increasing understanding of CO and ethylene reduced Cr/SiO<sub>2</sub> catalysts, research towards the effects of metal-alkyl co-catalysts on the active

site structure and oxidation state has also started to gain momentum. One showcase example reveals how TEAI as the co-catalyst material in Cr/SiO<sub>2</sub> Phillips-type ethylene polymerization generates a variety of Cr sites, including bis-grafted bis-alkyl Cr<sup>4+</sup> species that are active in polymerization, coordinatively saturated inaccessible Cr<sup>3+</sup> sites, and two types of mono-grafted mono-alkyl Cr<sup>2+</sup> sites.<sup>[49]</sup>

These recent findings were preceded by work from our group, more specifically, we have investigated the effect of TEAI on an industrial shell-titanated Cr/Ti/SiO<sub>2</sub> Phillips-type catalyst, also demonstrating the enhanced degree of  $\alpha$ -oligomer generation and incorporation<sup>[50]</sup> as well as a significantly enhanced polymerization activity.<sup>[51]</sup> In addition, Scanning Transmission X-ray Microscopy (STXM) was used to reveal two different types of active sites, namely an ethylene polymerizing active site, which polymerized ethylene following the Cossee-Arlman mechanism and ethylene oligomerizing sites, which produced ethylene oligomers via the metallocycle mechanism. The properties of the active sites being determined by either the titanium-rich environment in the shell or the titanium-lean inner environment: the former producing a more linear PE and the latter a more branched PE.<sup>[52]</sup> These examples from our group as well as those from Groppo *et al.* demonstrate that a lot of insights with respect to the effect of co-catalysts on the Cr/SiO<sub>2</sub> catalyst are to be gained and it is exactly this field of research that is paramount for optimizing existing ethylene polymerization processes and for finding new routes towards (new) polyethylene materials.

Continuing this research effort into investigating the influence of metal-alkyl co-catalysts on the surface chemistry, and the working state of the Cr/SiO<sub>2</sub> Phillips ethylene polymerization catalyst, we discuss in this **Chapter** the influence of tri-ethyl aluminum (TEAI) and tri-ethyl borane (TEB) on the oxidation state during reduction and during polymerization, on the induction period, on the catalyst activity and on the polymer characteristics. In a first series of experiments, we opted to investigate how TEB and TEAI affect bulk properties, such as the catalyst activity, induction period, and, polymer characteristics, on an industrial 1 wt% Cr/SiO<sub>2</sub> Phillips catalyst. Because of the observed unique catalytic performances, we have investigated how the different metal-alkyl co-catalysts affect the redox chemistry of the Cr/SiO<sub>2</sub> Phillips catalyst with in-situ UV-Vis-NIR DRS. The combination of experimental techniques revealed that TEB and TEAI uniquely interact with the Cr/SiO<sub>2</sub> Phillips catalyst, resulting in specific reduction pathways and bulk performances.

## 2.2 Results and Discussion

### 2.2.1 Metal-Alkyl Influence on Induction Period and Catalyst Activity

Figure 2.1 illustrates the influence of TEAI and TEB on the induction period and the catalyst activity during the performed semi-batch ethylene polymerization reactions, with ppm (wt/wt)

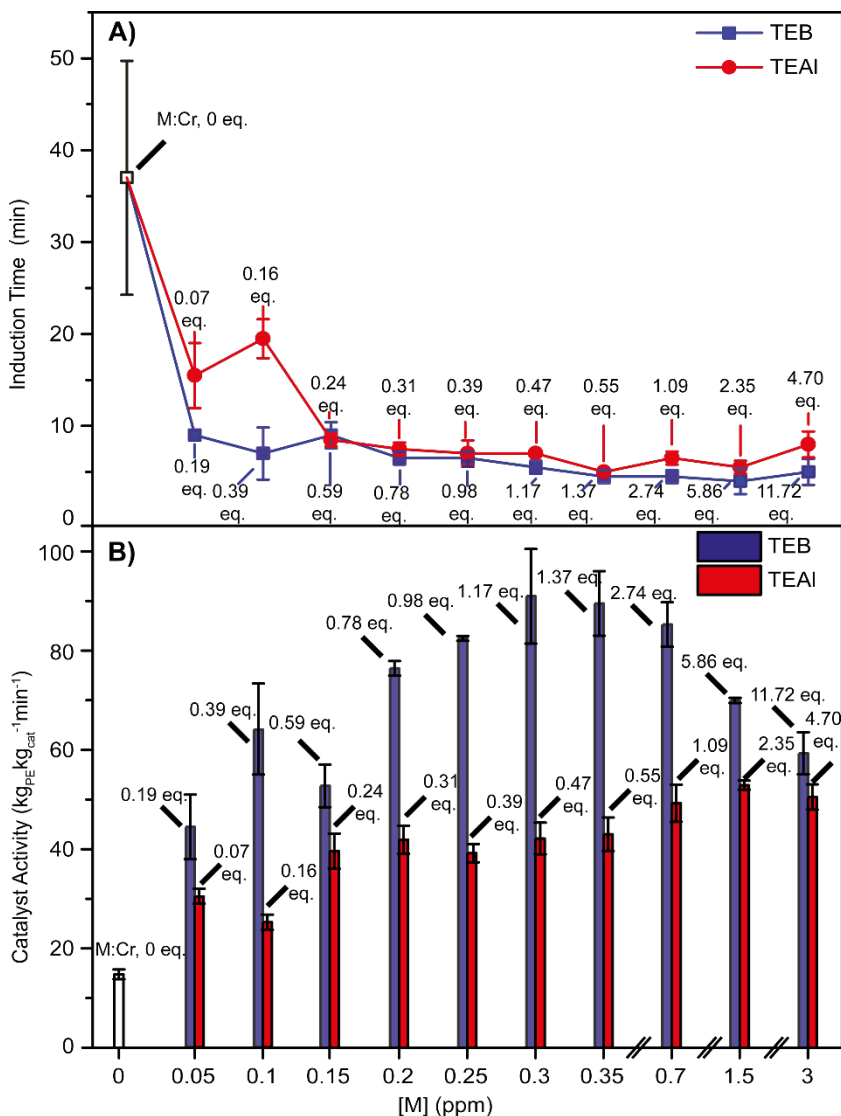


**Figure 2.1.** The effect of TEB (blue) or TEAI (Red) on **A**) the induction periods and **B**) the catalytic activities during the batch-ethylene polymerization reactions. All the reactions were performed in a 5 L semi-batch ethylene polymerization reactor, at 34 bar and 99 °C. The M:Cr (M = B/Al) mole ratios are given in both figures, with lower values for TEAI than for TEB due to the larger molecular weight for TEAI.

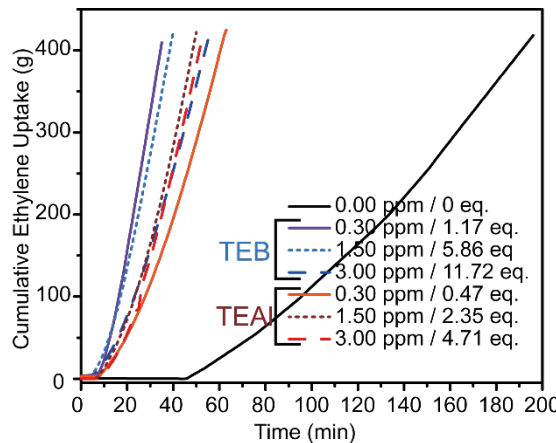
reflecting the added amount of the co-catalyst to the diluent. Prior to ethylene polymerization, the Cr<sup>6+</sup>/SiO<sub>2</sub> Phillips catalyst must be reduced to its active state, the duration of this process is defined as the induction period. Practically, the length of this period was determined as the time

between the first contact of the catalyst material with ethylene and the moment at which ethylene had to be actively added for maintaining the reactor pressure. One of the benefits of metal-alkyl co-catalysts is that they already reduce a number of the Cr<sup>6+</sup> surface sites and as a consequence partly remove the need for ethylene reduction, resulting in a strongly decreased induction period. In addition, poisonous oxygen-containing compounds, originating either from impurities in the gas feed or reduction by-products, are also removed by these co-catalysts, preventing the re-oxidation and/or poisoning of Cr active sites. These two features combined ensure a more reliable reduction process.

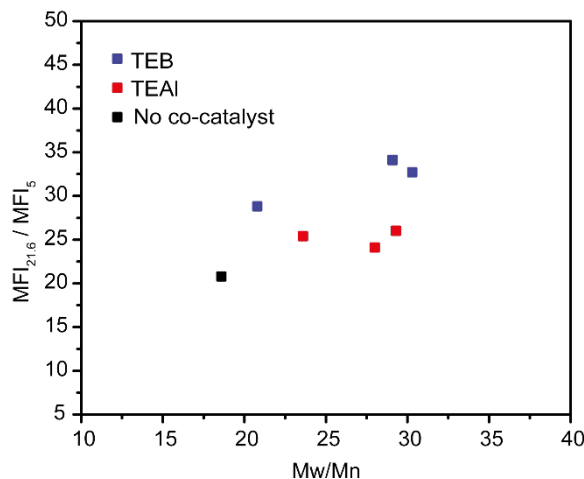
The importance of the co-catalyst in reducing the induction period is demonstrated in Figure 2.1A. In the presence of 0.05 ppm of TEB (0.19 B:Cr mole ratio), the induction period was decreased to 10 min and with 0.05 ppm of TEAI (0.07 Al:Cr mole ratio) it was decreased to 15 min. The induction period was decreased to a larger extent, until 0.15 ppm with TEB (0.59 B:Cr mole ratio) as compared to TEAI (0.24 Al:Cr mole ratio). However, beyond these co-catalyst amounts, the induction periods converged to a minimum of 8 min. Apparently, a smaller mole ratio is required to attain the minimum induction period of 8 min for TEAI as compared to TEB. The observed increase in induction period at 0.1 ppm TEAI (0.16 Al:Cr mole ratio) is attributed to an artefact in measuring the induction period.

Figure 2.1B illustrates how the incremental amounts of TEB and TEAI affect the catalytic activities. Addition of either co-catalyst is beneficial for the catalyst activity. However, TEB raises the activity to a larger extent than TEAI does, which is testified by the three-fold activity increase in the presence of TEB, whereas TEAI only results in an activity increase by a factor 2. The catalyst activity passes through a maximum of  $90 \text{ kg}_{\text{PE}} \text{kg}_{\text{cat}}^{-1} \text{min}^{-1}$  in the presence of 0.30 ppm TEB (1.17 B:Cr mole ratio), whereas the catalyst activity in the presence of 0.30 ppm TEAI (0.47 Al:Cr mole ratio) is  $40 \text{ kg}_{\text{PE}} \text{kg}_{\text{cat}}^{-1} \text{min}^{-1}$ . Interestingly, nearly equimolecular amount of TEB or TEAI (0.30 ppm, 1.17 B:Cr mole ratio; 1.09 Al:Cr mole ratio) did not result in converged catalyst activities, instead, the catalyst activity with TEAI was still approximately half the catalyst activity with TEB. By further increasing the amount of TEB the activity starts to decrease again. This is most evident with amounts of TEB above 1.50 ppm (5.86 B:Cr mole ratio). McDaniel *et al.* already reported that TEB amounts above 5.0 ppm negatively affect the catalyst activity and that this is most likely caused by over-reduction of the catalyst material.<sup>[1,53,54]</sup> On the other hand, the presence of TEAI does not seem to be disadvantageous for the catalyst activity for any of the used amounts, as is demonstrated by the relatively constant catalyst activity. However, a likely explanation is that we have not crossed the threshold for which catalyst performances start to decrease.

Figure 2.2 demonstrates a significantly enhanced kinetic profile in the presence of 0.30 ppm TEB (1.17 B:Cr mole ratio), whereas the polymerization rate decreases upon further increasing its amount. TEAI, on the other hand, results in an enhanced kinetic profile starting from 0.30 ppm (0.47 Al:Cr mole ratio) to 1.50 ppm (2.35 Al:Cr mole ratio) and 3.00 ppm (4.71 Al:Cr mole ratio), whereas the last two profiles are similar. These developments are in line with the similar trends



**Figure 2.2.** An overview of the kinetic profiles obtained by measuring the cumulative ethylene uptake during the semi batch ethylene polymerization reactions at 99 °C and 34 bar. The blue lines indicate the reactions performed with TEB and the red lines respectively the reactions with TEAI.



**Figure 2.3.** MFIR plotted versus the  $M_w/M_n$  for the materials from Table 1 after analysis of the Gel Permeation Chromatography (GPC) experiments. Higher values for the Melt Flow Index Ratio (MFIR) at a specific  $M_w/M_n$  indicate the possibility of Long-Chain Branching (LCB).

observed for the bulk activities. Furthermore, almost equal kinetic profiles are observed for 3.00 ppm of either co-catalyst material (11.72 B:Cr mole ratio; 4.71 Al:Cr mole ratio). By inspecting the kinetic profiles and the fragmentation patterns we observe that an increase in the former does not translate necessarily into an increase in the latter. Instead, fragmentation patterns are predominantly governed by the type of co-catalyst rather than the measured kinetic profile.

Table 2.1 gives an overview of the effects of TEB and TEAI on selected polymer characteristics and structural parameters of the PE products from the most relevant semi-batch ethylene polymerization reactions. Detailed information for all semi-batch ethylene polymerization experiments is provided in Tables 2.1, 2.2 and 2.3. The Melt Flow Index (MFI) represents the polymer molecular weight and gives an indication of the (weight averaged) molecular weight of the polyethylene, as further evidenced by the correlation between the MFI<sub>5</sub> and the M<sub>w</sub>. The Melt Flow Index Ratio (MFIR), defined as MFI<sub>21.6</sub>/MFI<sub>5</sub>, gives an indication of the rheological broadness of the polymer. Both co-catalyst materials lower the polymer MW and increase the rheological broadness of the produced PEs. However, TEB appears to do so more significantly, since the MFIR increased by over 50% already by the addition of only 0.30 ppm TEB (1.17 Cr:Cr Mole Ratio) whereas a 25% increase of the MFIR is observed in the presence of the same TEAI concentration (0.47 Al:Cr Mole Ratio). In terms of Long-Chain Branching (LCB) we see that for similar M<sub>w</sub>/M<sub>n</sub> values the MFIR (MFI<sub>21.6</sub>/MFI<sub>5</sub>) is higher for TEB than for TEAI, possibly indicating an enhanced degree of LCB for the polymers produced with TEB, where LCB is defined as a sidechain of more than 150 C atoms. For example, the MFIR at a D of ~29.3 is 28.8 for TEB and 26.0 for TEAI, further exemplified in Figure 2.3.

The obtained polymer densities give an indication of polymer crystallinity, which is predominantly governed by Short-Chain Branching (SCB) and molecular weight.<sup>[55]</sup> Interestingly,

**Table 2.1.** An overview of the polymer product ratios from the products obtained from the 5 L batch ethylene polymerization reactions. Analysis of the produced PE materials with Gel Permeation Chromatography (GPC) provided the M<sub>n</sub>, M<sub>w</sub>, M<sub>z</sub> structural parameters.

Exp.	M:Cr Mole Ratio	M <sub>n</sub> (kDa)	M <sub>w</sub> (kDa)	M <sub>z</sub> (kDa)	M <sub>w</sub> / M <sub>n</sub> (D)
Cr/SiO <sub>2</sub>	0	19	360	2600	18.6
<b>TEB</b>					
0.30 ppm	1.17	11	330	3000	30.3
1.50 ppm	5.86	11	220	1700	20.8
3.00 ppm	11.72	9	270	2400	29.1
<b>TEAI</b>					
0.30 ppm	0.47	16	370	2900	23.6
1.50 ppm	2.35	12	340	2900	29.3
3.00 ppm	4.71	12	320	2900	28.0

**Table 2.2.** Catalyst activity and product properties of the performed ethylene polymerization reactions in the presence of an increasing concentration of tri-ethyl borane (TEB). The induction time was the time ranging from the moment of catalyst injection to the moment of maintaining the reactor pressure by ethylene addition. The polymerization time is defined as the time it took to reach a Catalyst Yield of approximately 2700 kg/kg. The MFI 5 and MFI 21.6 Melt Flow Indices (MFI) were measured according to the ISO 1183 method and the Melt Flow Index Ratio (MFIR) is defined as  $MFI_{21.6}/MFI_5$ . D10, D50 and D90 Particle Size Distributions (PSD) were measured and from  $((D90-D10)/D50)$  the particle span was calculated.

TEB-Concentration (ppm)	Induction Time (min)	Polymerization Time (min)	Catalyst Yield ( $\text{g}_{\text{PE}}\text{g}_{\text{cat}}^{-1}$ )	MFI 5 (d <sub>g/mi</sub> )	MFI 21.6 (d <sub>g/mi</sub> )	MFIR	PBD (kg/m <sup>3</sup> )	PSD D10 ( $\mu\text{m}$ )	PSD D50 ( $\mu\text{m}$ )	PSD D90 ( $\mu\text{m}$ )	Span /D50
0.0	28	169	2649	0.13	2.7	19.8	442	336	636	889	0.87
0.0	46	197	2786	0.13	2.6	20.8	378	378	550	811	1.04
0.05	9	69	2744	0.11	3.1	28.2	347	239	550	793	1.00
0.05	9	55	2697	0.17	4.8	28.2	286	248	545	785	1.00
0.10	5	45	3174	0.15	5.0	33.3	310	246	535	801	1.04
0.10	9	51	2933	0.18	5.3	29.4	290	252	531	786	1.00
0.15	10	54	2686	0.19	5.3	27.9	285	255	534	786	1.00
0.15	8	48	2676	0.20	5.8	29.0	280	227	478	747	1.09
0.20	8	47	2626	0.22	7.0	31.8	290	229	484	745	1.07
0.20	6	39	2638	0.23	7.5	32.6	279	220	488	763	1.11
0.25	7	34	2793	0.26	8.2	31.6	274				
0.25	6	34	2815	0.29	9.2	31.7	256	222	467	741	1.11
0.30	6	38	1789	0.26	7.9	30.4	276	229	482	741	1.06
0.30	5	34	2712	0.26	8.5	32.7	268	216	464	728	1.10
0.35	4	30	2824	0.33	9.8	29.6	266	210	462	747	1.16
0.35	5	32	2717	0.30	10.7	35.7	251	221	458	724	1.10
0.70	4	32	2828	0.35	10.4	29.7	250	217	478	736	1.09
0.70	5	34	2793	0.35	10.9	31.1	241	235	510	776	1.06
1.50	5	39	2740	0.43	12.9	30.0	260	238	530	783	1.03
1.50	3	39	2714	0.43	12.4	28.8	254	203	504	766	1.12
3.00	4	43	2681	0.38	11.9	31.3	269	239	548	841	1.10
3.00	6	47	2747	0.32	10.9	34.3	271	241	582	802	0.96

**Table 2.3.** Catalyst activity and product properties of the performed ethylene polymerization reactions in the presence of an increasing concentration of tri-ethyl aluminum (TEAl). The induction time was the time ranging from the moment of catalyst injection to the moment of maintaining the reactor pressure by ethylene addition. The polymerization time is defined as the time it took to reach a Catalyst Yield of approximately 2700 kg/kg. The MFI 5 and MFI 21.6 Melt Flow Indices (MFI) were measured according to the ISO 1183 method and the Melt Flow Index Ratio (MFIR) is defined as  $MFI_{21.6}/MFI_5$ . D10, D50 and D90 Particle Size Distributions (PSD) were measured and from  $((D90-D10)/D50)$  the particle span was calculated.

TEA- Concentr- ation (ppm)	Inducti- on Time (min)	Polymeriz- ation Time (min)	Catalyst Yield (g <sub>PECat</sub> <sup>-1</sup> )	MFI 5 (d <sub>g/mi</sub> n)	MFI 21.6 (d <sub>g/mi</sub> n)	MFIR	PBD (kg/m <sup>3</sup> )	PSD D10 (μm)	PSD D50 (μm)	PSD D90 (μm)	Span D10- D50 (μm)
0.0	28	169	2649	0.13	2.7	19.8	442	336	636	889	0.87
0.0	46	197	2786	0.13	2.6	20.8	378	—	—	—	—
0.05	13	86	2707	0.10	2.5	25.0	509	189	493	760	1.16
0.05	18	98	2882	0.09	2.3	25.6	509	177	502	770	1.18
0.10	18	99	2606	0.11	2.3	20.9	510	211	553	872	1.19
0.10	21	113	2725	0.11	2.3	20.9	524	226	555	859	1.14
0.15	8	75	2782	0.11	2.8	25.5	444	130	446	745	1.38
0.15	9	70	2946	0.12	2.9	24.2	412	107	384	703	1.55
0.20	8	63	2769	0.12	3.2	26.7	420	167	513	816	1.27
0.20	7	68	2716	0.11	2.9	26.4	450	115	397	701	1.48
0.25	8	71	2695	0.12	2.8	23.3	405	186	497	766	1.17
0.25	6	66	2675	0.15	3.6	24.0	394	131	437	735	1.38
0.30	7	68	2719	0.13	3.2	24.6	410	—	—	—	—
0.30	7	62	2751	0.13	3.3	25.4	373	156	490	785	1.28
0.35	5	60	2723	0.15	3.7	24.7	376	142	463	716	1.24
0.35	5	66	2682	0.13	3.2	24.6	391	189	551	887	1.27
0.70	6	58	3012	0.15	3.9	26.0	362	173	549	857	1.25
0.70	7	58	2705	0.15	4.0	26.7	358	179	516	782	1.17
1.50	5	50	2673	0.25	6.5	26.0	380	165	472	750	1.24
1.50	6	51	2663	0.23	6.2	27.0	389	152	425	682	1.25
3.00	7	53	2770	0.32	7.7	24.1	362	161	401	685	1.31
3.00	9	55	2677	0.31	7.4	23.9	359	163	411	700	1.30

here we see that the presence of TEB resulted in a polymer with increased density in combination with an increased MFIR. Polymerization reactions in the presence of TEAI produced PEs with decreased density, while the MFIR still increased. This decreased polymer density infers the presence of SCB because of  $C_2H_4$  oligomerization and increased  $\alpha$ -olefin incorporation.

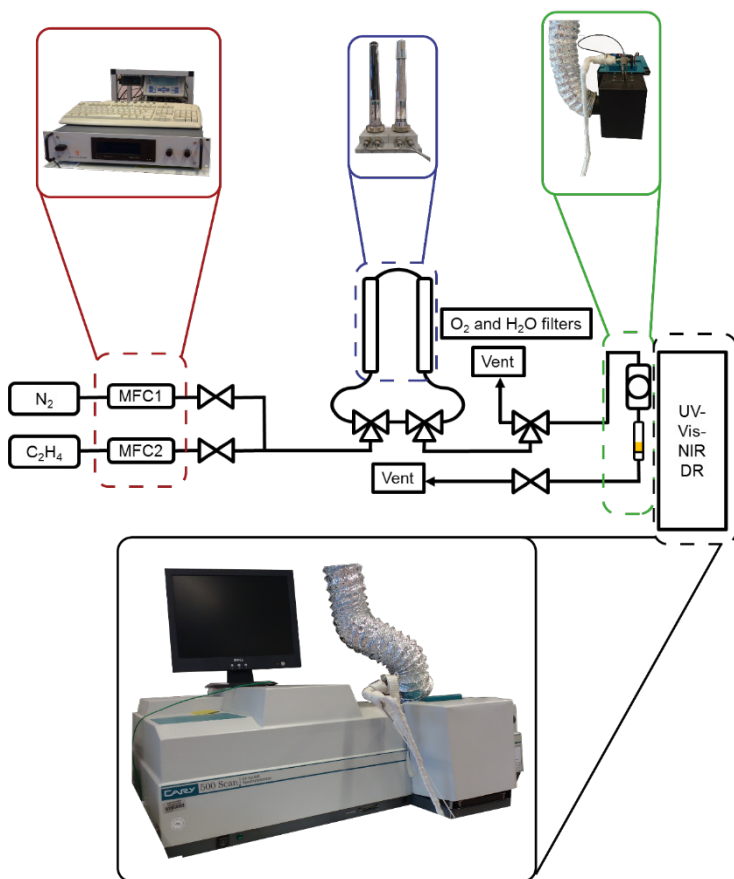
The Powder Bulk Density (PBD) is affected by the powder morphology, like for instance particle shape and particle size distribution. Tables **2.2** and **2.3** indicate that without a metal-alkyl co-catalyst a PBD of  $400\text{ kg/m}^3$  is obtained and that this value is highly dependent on the type of co-catalyst that is added and less so on the added amount. The addition of TEB resulted in a decreased PBD, with a minimum of  $257\text{ kg/m}^3$  in the presence of 1.50 ppm (5.86 B:Cr mole ratio). In contrast, with 3.00 ppm TEAI (4.71 Al:Cr mole ratio) a minimum PBD of  $360\text{ kg/m}^3$  was observed.

An increase of the particle size distribution broadness after ethylene polymerization, as compared to polymerization without co-catalyst, is an indication of increased particle fragmentation. Careful inspection of the PSE D50 and Span in Tables **2.2** and **2.3** reveals that the addition of either co-catalyst increases the span and PSE D50. However, the broadness is increased to a larger extent in the presence of TEAI than in the presence of TEB. In case the polymer powder particles obey the replication phenomenon, the average particle size (expressed as D50) is governed by the catalyst yield. In these experimental series, the catalyst yield was nearly constant, which allows a discussion on the effect of the co-catalyst on the particle size of the polymer. Quite interestingly, both co-catalysts cause an initial decrease in D50 and increase of the particle span compared to the polymer without TEB or TEAL. 0.30 ppm of TEB (1.17 B:Cr mole ratio) produces particles with a D50 of  $464\text{ }\mu\text{m}$  and a particle span of 1.10, which subsequently changes to a value of  $582\text{ }\mu\text{m}$  and a particle span of 0.96 with 3.00 ppm of TEB (11.72 B:Cr mole ratio). In the case of TEAL, however, the D50 decreases to a value of  $401\text{ }\mu\text{m}$  and a particle span of 1.31 with 3.00 ppm of TEAI (4.71 Al:Cr mole ratio). This infers that incremental amounts of TEAI enhance particle fragmentation, whereas incremental amounts of TEB suppress particle fragmentation.

## 2.2.2 Controlling the Cr Redox Chemistry by Rational Co-catalyst Selection

In a second series of experiments the influence of the type, and amount of metal-alkyl co-catalyst on the redox chemistry of Cr was investigated. For this purpose, UV-Vis-NIR DRS experiments were designed for studying oxidation state changes during reduction as well as subsequent polymerization with separation of these two stages in mind.

The in-situ set-up allowed for the reduction of the catalyst material by gaseous ethylene, or injection of a metal-alkyl co-catalyst solution into the  $N_2$  gas-stream *via* the septum. A detailed



**Scheme 2.1.** Overview of the in-situ UV-Vis-NIR Diffuse Reflectance Spectroscopy (DRS) setup, with the possibility of feeding respectively ethylene or nitrogen. The volume of gas per minute could be separately regulated with two mass flow controllers. After which they passed another two-way valve and the individual lines merged. Subsequently impurities were scrubbed from the gas-feed by  $O_2$  and  $H_2O$  filters, for circumventing contact of the catalyst material with atmospheric  $H_2O$  and  $O_2$ . After the two columns, the line passed a three-way valve either to a vent or to the catalyst material. The catalyst material was placed in a specially designed quartz cell on a frit, in each experiment 100 mg catalyst was used. The co-catalyst solution could be injected via the septum above the catalyst bed.

scheme of the experimental set-up is provided in Scheme 2.1. To investigate the effect of equimolar amounts of the different co-catalysts on the reduction chemistry, of which the results on the different reductants will be discussed as follows:

- 1.50 mole ratio of TEB (B:Cr)

- 1.50 mole ratio of TEAI (Al:Cr)
- 10.0 mole ratio of either co-catalyst (M:Cr)

Figure 2.4 is a collection of several of the relevant reference materials, including a Cr(ac)<sub>3</sub> complex, the Cr<sup>6+</sup>/SiO<sub>2</sub> catalyst reduced by CO, reduced by C<sub>2</sub>H<sub>4</sub>, and the materials reduced with 1.50 mol. eq. of the co-catalyst materials. Furthermore, the deconvolution parameters are given in two Tables in **Appendix B** separated on the respective co-catalysts. In any case, these reference materials elegantly illustrate the complex electronic transitions as well as the Charge Transfer (CT) transitions for different Cr/SiO<sub>2</sub> oxidation states, demonstrating that definitive assignment is challenging and the likeliness of multiple oxidation states in reduced catalyst materials.

### 2.2.3 Ethylene polymerization after pre-treatment with 1.50 molecular equivalents of tri-ethyl borane

Firstly, we have investigated the role of TEB, of which the results are shown in Figure 2.5. Figure 2.5A demonstrates the reduction at room temperature, where 1.50 mol. eq. TEB was added through the septum. Figure 2.5C illustrates ethylene polymerization while heating to 150 °C. While Figures 2.5B and 2.5D demonstrate respectively the deconvolution of the pristine catalyst material and the deconvolution of the material reduced with 1.50 mol. eq. TEB.

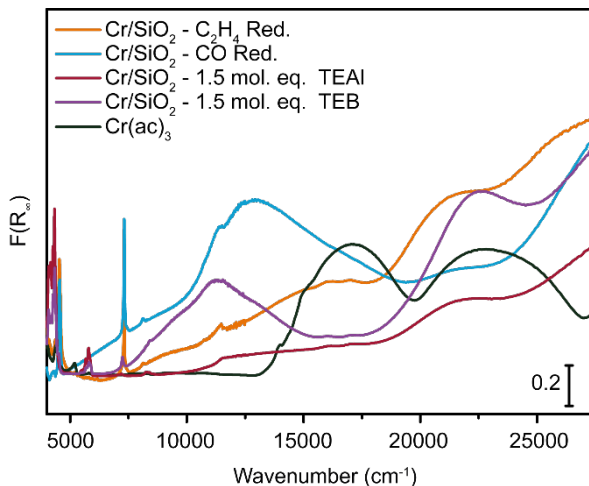


**Figure 2.4.** UV-Vis-NIR DRS spectra of the Cr/SiO<sub>2</sub> catalyst 20 min after reduction in a gas mixture of 10 mL/min ethylene and 10 mL/min N<sub>2</sub> at 150 °C and 1 bar (orange), by CO at 1 bar and a temperature of 350 °C (blue), by 1.50 eq. TEAI at 1 bar in 10 mL/min N<sub>2</sub> (red), by 1.5 eq. TEB at 1 bar in 10 mL/min N<sub>2</sub> (purple) as well as a Cr(III)acetate Cr<sup>3+</sup>(black) reference material.

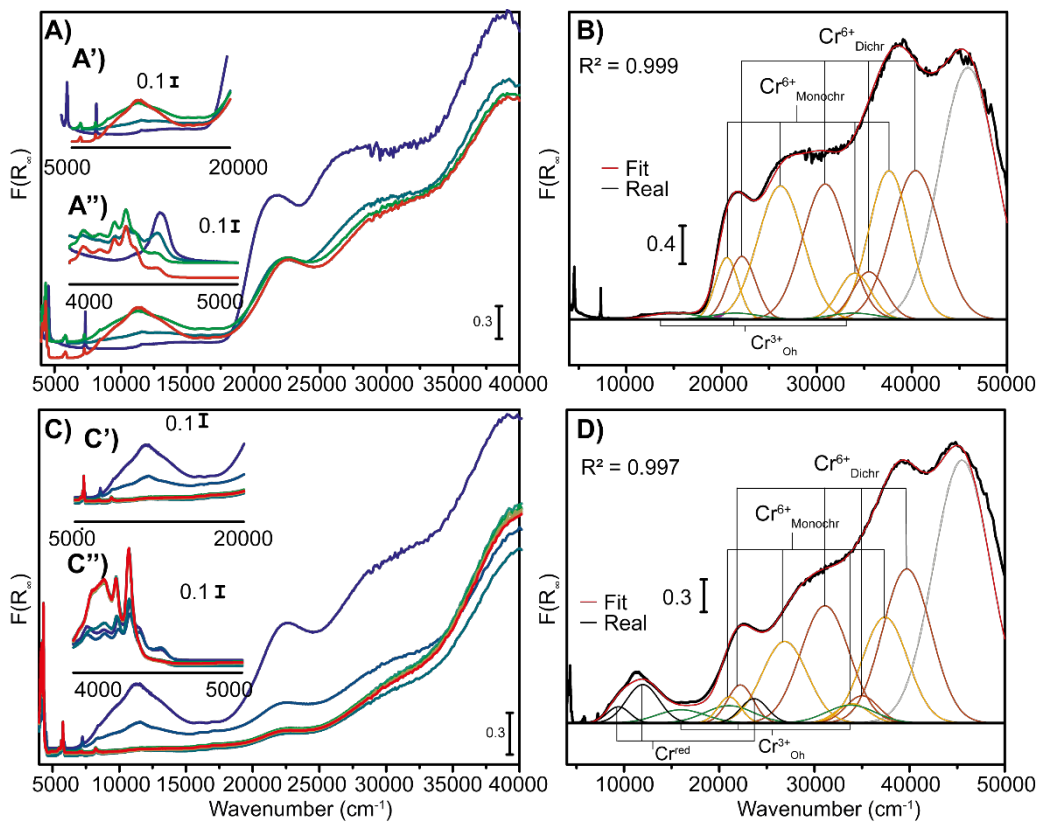


**Figure 2.5.** Spectroscopic developments for the UV-Vis-NIR DRS experiment with a B:Cr mole ratio of 1.50. **A)** The developments during pre-treatment of the catalyst with 1.50 molecular equivalents of TEB under an N<sub>2</sub> stream of 10 mL/min at room temperature and ambient pressure, aiming for a B:Cr mole ratio of 1.50. The spectra, from blue to red, are recorded with 5 min intervals. With the blue spectrum representing the pristine catalyst. **B)** Results from spectral deconvolution of the pristine Cr/SiO<sub>2</sub> Phillips catalyst material. **C)** Developments after the N<sub>2</sub> stream was switched to an ethylene stream of 10 mL/min, where the spectra were recorded at 20 °C intervals and the cell was heated to 150 °C with 5 °C/min. The spectra, from blue to red, are recorded with 5 min intervals. **D)** Results from the spectral deconvolution of the with 1.50 mol. eq. TEB reduced catalyst material, corresponding to the red trace in Figure 2.5A.

Directly after injection, a decrease in intensity of the Cr<sup>6+</sup> CT bands at ~37500, ~27500, and ~22500 cm<sup>-1</sup> is observed while a d-d transition band at 11000 cm<sup>-1</sup> developed. While the intensities of the O→Cr<sup>6+</sup> CT bands decrease over time, their characteristic fingerprint remains visible throughout the entire reduction stage, inferring that not every Cr<sup>6+</sup> site is reduced by TEB. The persistence of these bands makes it difficult to assign definitive oxidation state numbers.

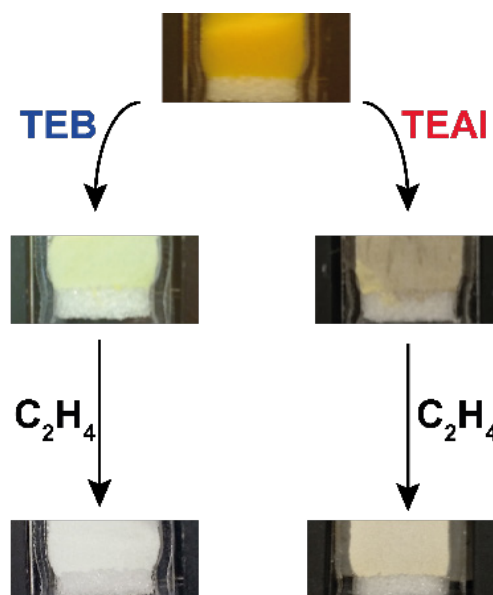


**Figure 2.6.** Photographs of the Cr/SiO<sub>2</sub> catalyst in the quartz reaction cell before reduction, after reduction with TEB or TEAI, and after ethylene polymerization.

The color change from orange to pale yellow/green, as shown in Figure 2.5, is a direct consequence of the present CT bands with the newly emerging band at 11000 cm<sup>-1</sup> [13–15,29]

The absence of an absorption band at 16000 cm<sup>-1</sup> might lead to the conclusion that no Cr<sup>3+</sup><sub>Oh</sub> species is formed, this is however rapidly dismissed by deconvoluted bands at 15500, 21500, and 33900 cm<sup>-1</sup> shown in Figure 2.5D. Furthermore, the d-d transition band at 11000 cm<sup>-1</sup> infers the presence of Cr<sup>2+</sup> centers, with deconvoluted bands contributing respectively at 9400 and 11900 cm<sup>-1</sup>. The maximum of this Cr<sup>2+</sup> d-d transition band is, however, blue-shifted in comparison to the d-d transfer band generated by CO reduction (Figure 2.4). This at least excludes the presence of naked Cr<sup>2+</sup> ions and indicates that reduction by-products remain in the proximity of the Cr active sites, hereby affecting the d-d transition and CT bands.<sup>[16,56–62]</sup> In order to ensure a proper fit, an additional band was required at 24000 cm<sup>-1</sup>, which is expected to be a CT band. This 24000 cm<sup>-1</sup> CT band, which is absent in the CO reduced material, can be explained by reduction by-products remaining in the coordination sphere of the Cr active site, thereby affecting the location of the d-d transition bands as well as the CT bands.

Subsequently, the gas stream was switched from N<sub>2</sub> to ethylene, followed by heating to 150 °C, with spectra being recorded at 20 °C intervals (5 min), as shown in Figure 2.5C. Changing the gas mixture resulted in an immediate decrease of the CT bands as well as the 11000 cm<sup>-1</sup> band, inferring that the latter band belongs to species participating in ethylene polymerization. Ethylene polymerization, in turn, was confirmed by the emerging PE fingerprint, the formation

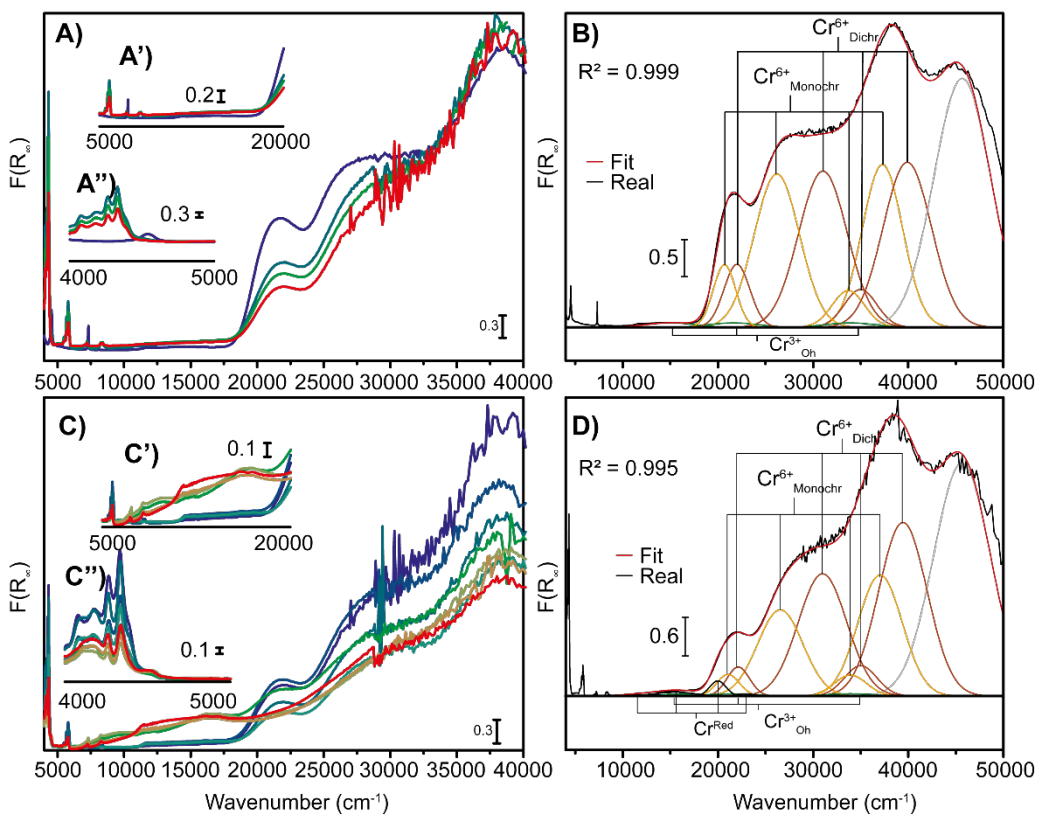


**Figure 2.7.** Spectroscopic developments for the UV-Vis-NIR DRS experiment with a Al:Cr mole ratio of 1.50. **A)** The UV-Vis-NIR DRS spectroscopic developments during pre-treatment of the catalyst with 1.50 molecular equivalents of TEB under an  $\text{N}_2$  stream of 10 mL/min at room temperature and ambient pressure, aiming for a Al:Cr mole ratio of 1.50. The spectra, from blue to red, are recorded with 5 min intervals. With the blue spectrum representing the pristine catalyst. **B)** Results from spectral deconvolution of the pristine  $\text{Cr}/\text{SiO}_2$  Phillips catalyst material. **C)** Developments after the  $\text{N}_2$  stream was switched to an ethylene stream of 10 mL/min, where the spectra were recorded at 20 °C intervals and the cell was heated to 150 °C with 5 °C/min. The spectra, from blue to red, are recorded with 5 min intervals. **D)** Results from the spectral deconvolution of the with 1.50 mol. eq. TEAI reduced catalyst material, corresponding to the red trace in Figure 2.7A.

of a white rubbery material (shown in Figure 2.6), and the loss of Cr related spectroscopic information due to the lack of diffuse scattered UV-Vis light caused by the PE layer around the Cr surface sites, thereby shielding them from detection.

#### 2.2.4 Ethylene polymerization after pre-treatment with 1.50 molecular equivalents of triethyl aluminum

The results of the experiments with 1.50 molecular equivalents of TEAI are shown in Figure 2.7. The most recent work by Groppe *et al.*<sup>[49]</sup> reported on the use of TEAI as a co-catalyst. Their work revealed the existence of bis-grafted bis-alkyl Cr<sup>4+</sup>, inaccessible Cr<sup>3+</sup>, and two mono-grafted mono-alkyl Cr<sup>2+</sup> surface sites. Moreover, it is worth stating that our findings on the UV-Vis-NIR DRS experiments match theirs, with (some) additional insights being provided due to the ability to perform reduction and polymerization in-situ.

Directly after injection, as seen in Figure 2.7A, the Cr<sup>6+</sup> CT bands decrease in intensity and a slight increase in intensity is observed from 20000 cm<sup>-1</sup> to lower wavenumbers. Figure 2.7A also demonstrates a slight shift of the 22500 cm<sup>-1</sup> band to lower wavenumbers, confirmed to be caused by the formation of the bis-grafted bis-alkyl Cr<sup>4+</sup> species, with deconvolution (Figure 2.7D) showing a contributing band at 19800 cm<sup>-1</sup>. Furthermore, the increase in the 20000 – 8000 cm<sup>-1</sup> region is attributed to the formation of two mono-grafted mono-alkyl Cr<sup>2+</sup> surface sites (band contributing at 11000 cm<sup>-1</sup>) and one inaccessible Cr<sup>3+</sup> site (band contributing at 15200 cm<sup>-1</sup>).<sup>[49]</sup>

One additional effect of TEAI is only revealed 15 min after exposure to ethylene, when bands at 9000 and 15500 cm<sup>-1</sup> rapidly emerge and then disappear, all while CT bands decrease in intensity. This event indicates the reduction of Cr<sup>6+</sup> species by ethylene, likely into Cr<sup>2+</sup>/Cr<sup>3+</sup> like those of the ethylene reduced system, considering the matching locations of their bands upon deconvolution. These results demonstrate that TEAI not only acts as a reductant but possibly also as a reducibility enhancer. Subsequent polymerization was evidenced by the loss of all Cr-related spectroscopic information, the emerging PE fingerprint in the NIR region, and the white reaction product, again demonstrated in Figure 2.6.

## 2.2.5 Ethylene polymerization after pre-treatment with 10 molecular equivalents of the co-catalysts

The bulk polymerization experiments revealed different catalyst performances if excesses of TEB or TEAI were used. Therefore, the experiments were repeated with 10 molecular equivalents co-catalyst, for which key-spectra are reported in Figure 2.8, including spectral deconvolution with similar peak parameters as in the previous discussions.

Interestingly, the addition of 10 molecular equivalents of TEB, shown in Figure 2.8A, appeared to alter the reduction pathway only to a small extent, as testified by the same trend where the CT bands decrease in intensity while a broad band at 11000 cm<sup>-1</sup> emerged, with deconvolution (Figure 2.8B) revealing bands contributing at 9400 and 11900 cm<sup>-1</sup>, all while retaining the CT fingerprint. Again, albeit Cr<sup>3+OH</sup> seems absent, its presence is confirmed by a band contributing at 16000 cm<sup>-1</sup>. A switch of the gas-feed to ethylene demonstrated the polymerization properties by the loss of all Cr-related spectroscopic information, the emerging PE fingerprint, and the formation of a white rubbery material.

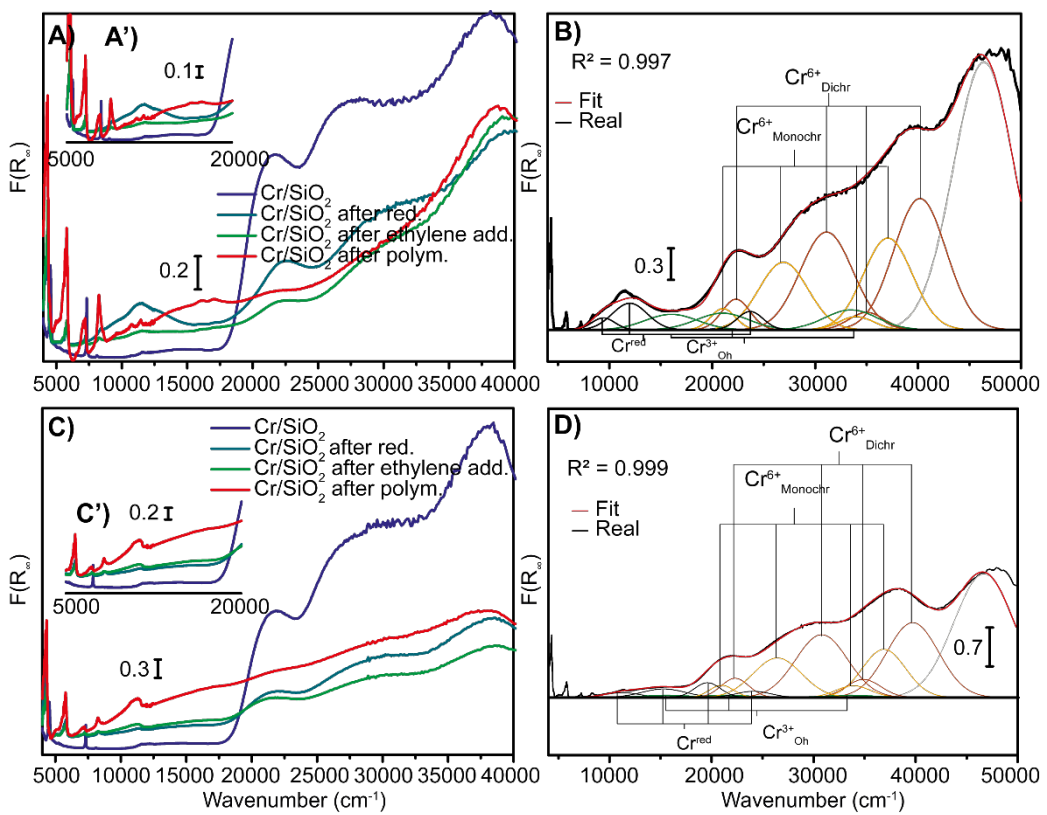


**Figure 2.8. A)** Highlights of the UV-Vis-NIR DRS experiments performed with a  $B:Cr$  ratio of 10.0. This figure shows the spectra of the pristine  $\text{Cr/SiO}_2$  catalyst (blue line), 10 min after addition reduction with TEB (blue-green line), 5 min after ethylene addition (green line) and after the complete polymerization process (red line). **B)** Deconvoluted spectrum of the with 10.0 mol. eq. TEB reduced  $\text{Cr/SiO}_2$  catalyst. **C)** Highlights of the UV-Vis-NIR DRS experiments performed with an  $A:Cr$  ratio of 10.0. This figure shows the spectra of the pristine  $\text{Cr/SiO}_2$  catalyst (blue line), 10 min after addition reduction with TEB (blue-green line), 5 min after ethylene addition (green line) and after the complete polymerization process (red line). **D)** Deconvoluted spectrum of the with 10.0 mol. eq. TEAI. reduced  $\text{Cr/SiO}_2$  catalyst.

On the other hand, an excess amount of TEAI did affect the UV-Vis-NIR DRS spectra, as shown in Figure 2.8C. The excess co-catalyst resulted in a more predominant increase in the  $20000 - 8000 \text{ cm}^{-1}$  region, with bands contributing at  $15200$  and  $11100 \text{ cm}^{-1}$  upon deconvolution (Figure 2.8D). Furthermore, the  $22500 \text{ cm}^{-1}$  band again shifted, caused by the formation of bis-grafted bis-alkyl  $\text{Cr}^{4+}$  surface sites, deconvolution demonstrating a band contributing at  $19800 \text{ cm}^{-1}$  (Figure 2.8D). These observations indicate the formation of additional  $\text{Cr}^{4+}$  sites from the reduction of  $\text{Cr}^{6+}$  sites, while simultaneously a larger number of  $\text{Cr}^{2+}$  and  $\text{Cr}^{3+}$  sites are formed from the over-reduction of these  $\text{Cr}^{4+}$  sites.<sup>[49]</sup> Lastly, changing the gas stream to ethylene

resulted in a small increase in intensity in the d-d transition region, combined with a decrease in intensity of the CT region. From the fit it is however clear that the larger amount of TEAI suppressed the subsequent ethylene reduction, likely due to fewer Cr<sup>6+</sup> sites being available for this. Eventually, all Cr spectroscopic features disappeared, until the UV-Vis-NIR DRS spectrum was completely dominated by the PE fingerprint region.

## 2.2.6 Semi-quantitative Analysis of the Effect of Co-catalysts on the Degree of Reduction

Deconvolution of the UV-Vis-NIR DR spectra was performed according to the same, proven, method reported by Weckhuysen *et al.*,<sup>[7,13,63]</sup> while refraining from commenting on the active site structure, since this would require the use of additional techniques such as NEXAFS, probe molecule FT-IR experiments, and Electron Paramagnetic Resonance (EPR) experiments. The established literature does allow for an in-depth and semi-quantitative discussion on the observed redox chemistry.

The consistency of band centers and HWHMs during deconvolution validated our approach, of which the deconvolution parameters can be found in **Appendix B**. Absolute quantification of the reduced Cr species in the UV-Vis-NIR DRS experiments is impossible for two reasons: **(1)** only for weight-loadings between 0 and 0.2 wt% a linear relationship between Cr<sup>6+</sup> band intensity and Cr<sup>6+</sup> concentration exists and **(2)** knowledge of the exact absorption coefficient is required.<sup>[13]</sup> However, equation **1** does show that semi-quantification is possible without knowing the exact extinction coefficients, since “ $\epsilon_{\text{reduced-species}} / \epsilon_{\text{chromate}}$ ” is reduced to a constant K. Therefore, the ratios between band intensities from reduced Cr species in the d-d transition region and from the 31000 cm<sup>-1</sup> Cr<sup>6+</sup> band remain a semi-quantitative measure of the reduction.

Consequently, Figure **2.9** shows how Cr<sub>reduced</sub> / Cr<sup>6+</sup><sub>dichromate</sub> band intensity ratios develop as a function of increasing TEB (**2.9A**) and TEAI (**2.9B**) amounts, with Cr<sub>reduced</sub> being reflected by the intensity at the maxima found for the deconvoluted bands. Lastly, Figure **2.9C** shows the development of the Cr<sup>6+</sup><sub>monochromate</sub> (27000 cm<sup>-1</sup>) / Cr<sup>6+</sup><sub>dichromate</sub> (31000 cm<sup>-1</sup>) ratio as a function of type and amount of co-catalyst.<sup>[13,14,63]</sup>

$$(2.1) \frac{I(11900 \text{ cm}^{-1})}{I(31000 \text{ cm}^{-1})} = \frac{\epsilon_{\text{reduced}} [C]_{\text{reduced}}}{\epsilon_{\text{chromate}} [C]_{\text{chromate}}} = K \frac{[C]_{\text{reduced}}}{[C]_{\text{chromate}}}$$

As discussed, larger amounts of TEB appeared to affect the reduction chemistry only to a small extent. However, Figure **2.9A** demonstrates an inverse relationship between relative amounts of Cr<sup>2+</sup> (11900 / 31000 cm<sup>-1</sup>) and Cr<sup>3+</sup> (16000 / 31000 cm<sup>-1</sup>) with increasing amounts of TEB. Furthermore, Figure **2.9C** demonstrates that predominantly the mono-chromates react with TEB, where the ratio appeared to be barely affected by the added amount. On the basis of these findings, it is likely that larger amounts of TEB enhance the formation of Cr<sup>3+</sup> at the expense

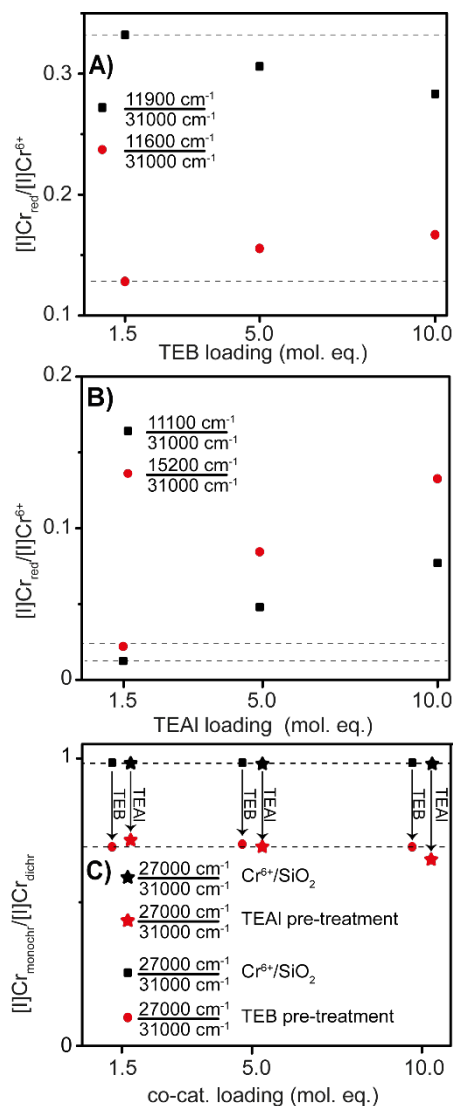


**Figure 2.9.** **A)** The band intensity ratios from the deconvoluted UV-Vis-NIR DRS spectra. The  $11900\text{ cm}^{-1}$  /  $31000\text{ cm}^{-1}$  band ratio and  $16000\text{ cm}^{-1}$  /  $31000\text{ cm}^{-1}$  band ratios are shown for the experiments with TEB. **B)** The band intensity ratios from the deconvoluted UV-Vis-NIR DRS spectra. The  $11100\text{ cm}^{-1}$  /  $31000\text{ cm}^{-1}$  band and  $15200\text{ cm}^{-1}$  /  $31000\text{ cm}^{-1}$  band ratios are shown for the experiments with TEAI. The  $19800\text{ cm}^{-1}$  /  $31000\text{ cm}^{-1}$  band ratios are omitted due to the overlap of the  $19800\text{ cm}^{-1}$  band with the  $21000$  and  $22000$  Cr<sup>6+</sup> bands. **C)** shows the intensity ratio of deconvoluted UV-Vis-NIR DRS bands of the Cr<sup>6+</sup><sub>monochromate</sub> band at  $27000\text{ cm}^{-1}$  to the Cr<sup>6+</sup><sub>dichromate</sub> band at  $31000\text{ cm}^{-1}$  before and after reduction with TEB or TEAI.

of  $\text{Cr}^{2+}$ , which explains, e.g., decreased catalyst activities of larger amounts, which in turn is rationalized by deactivation/destruction of otherwise active sites.

The more significant reduction with more TEAI was already discussed and is further illustrated in Figure 2.9B, where the increase of the  $11100\text{ cm}^{-1}$  band is explained by increasing amounts of two types of mono-grafted mono-alkyl  $\text{Cr}^{2+}$  sites and the increase of the  $15200\text{ cm}^{-1}$  is explained by an increase of inaccessible  $\text{Cr}^{3+}$  sites. It is likely that the increased formation of these species is due to over-reduction of the bis-grafted bis-alkyl  $\text{Cr}^{4+}$  sites contributing at  $19800\text{ cm}^{-1}$ . Interestingly, Figures 2.7D and 2.8D confirm increasing intensities for the band at  $19800\text{ cm}^{-1}$ , inferring relatively larger amounts of bis-grafted bis-alkyl  $\text{Cr}^{4+}$  sites, related to TEAI exploiting additional  $\text{Cr}^{6+}$  sites in the favor of active site formation. However, the bands do not increase thrice/twice in intensity if the added TEAI amount is tripled ( $1.5 \rightarrow 5.0$  mol. eq.) or doubled ( $5.0 \rightarrow 10.0$  mol. eq.). This is further supported by Figure 2.9C where a small, albeit continual, decrease of the  $27000 / 31000\text{ cm}^{-1}$  ratio is observed.

## 2.3 Conclusions

In this **Chapter** we found that careful selection of the type and amount of co-catalyst allows for uniquely tailoring  $\text{Cr/SiO}_2$  ethylene polymerization, with tunable catalyst activities, induction periods and polyethylene characteristics. Semi-batch ethylene polymerization experiments revealed that the added co-catalysts significantly enhanced the catalytic performance. TEB raised the catalyst activity to a larger extent, however, suffered from decreased catalyst performances at increased amounts. On the other hand, TEAI increased the catalyst activity to a smaller extent, however no decreasing catalyst activities were observed at the larger amounts, suggesting that we are working below the deactivation/destruction threshold. Addition of either co-catalyst greatly benefited the reduction of the induction period, in both instances a minimum of 8 min was attained.

Addition of the different types and amounts of co-catalyst materials allowed for finely tailoring the polymer product characteristics centered around a HDPE with a density of  $956\text{ kg/m}^3$ , which was produced in the absence of a co-catalyst. Addition of TEAI resulted in the production of HDPE with a decreased density, while TEB, on the other hand, produced HDPE with increased densities. The UV-Vis-NIR DRS experiments revealed that TEB and TEAI distinctly affected the redox chemistry of the  $\text{Cr/SiO}_2$  Phillips catalyst. TEB primarily reduced  $\text{Cr}^{6+}$  to  $\text{Cr}^{2+}_{\text{OH/Td}}$  and  $\text{Cr}^{3+}_{\text{OH}}$ , producing an active ethylene polymerization catalyst. Increased amounts of TEB resulted in the formation of  $\text{Cr}^{3+}_{\text{OH}}$ , at the expense of  $\text{Cr}^{2+}_{\text{OH/Td}}$ , indicating the potential of TEB to deactivate the catalyst while simultaneously inferring that the  $11000\text{ cm}^{-1}$  band is related to the species that participate in ethylene polymerization. The effect of TEAI was highly dependent on the added amount. With small amounts of TEAI producing bis-grafted bis-alkyl  $\text{Cr}^{4+}$  species and only minor amounts of  $\text{Cr}^{2+}$  and  $\text{Cr}^{3+}$ , while simultaneously enhancing the reducibility by

ethylene. Increased amounts of TEAI raised the reduction of Cr<sup>6+</sup> into bis-grafted bis-alkyl Cr<sup>4+</sup> species but also coincided with over-reduction of these Cr<sup>4+</sup> species to Cr<sup>2+</sup> and Cr<sup>3+</sup> species.

If anything, our results clearly confirm that the type and amount of co-catalyst is pivotal for controlling the Cr redox chemistries and as a result the active site formation. In addition, the results indicate that the co-catalyst remains a significant contributor to catalyst performances and bulk properties, even after the initial reduction stage.

## 2.4 Acknowledgements

O. Kerknaar (Utrecht University, UU), M. van Asselen (UU) and M. Krijnen (UU) are acknowledged for their support in constructing and optimizing the in-situ UV-Vis-NIR DRS setup as well as designing the quartz reactor for the experiments.

## 2.5 Experimental Section

### 2.5.1 Sample Preparation

The catalyst samples were provided by SABIC Geleen, the Netherlands. It is a silica Cr-catalyst with a ~1.0 wt% Cr loading, a surface area of 625 m<sup>2</sup>/g, a pore volume of 2.41 mL/g and a D50 particle size distribution of 52.8 µm. The catalyst was calcined at 650 °C via a SABIC-proprietary technique to yield the active CrO<sub>x</sub>/SiO<sub>2</sub> catalyst.

### 2.5.2 Batch-reactor Catalyst Testing

Slurry phase polymerization reactions were performed in a 5 L semi-batch reactor at SABIC Geleen, during which induction time, catalyst yield and total polymerization time were monitored. The batch reactor was loaded with 1071 g isobutane and heated to 99°C. 830 mg H<sub>2</sub> was added and subsequently the reactor was pressurized to 34 bar with C<sub>2</sub>H<sub>4</sub>. The diluent was loaded with 12 mol% C<sub>2</sub>H<sub>4</sub> and 1 mol% H<sub>2</sub>. Upon reaching the reaction conditions the co-catalyst was injected with 120 g of isobutane and subsequently the Cr/SiO<sub>2</sub> catalyst was injected with 180 g of isobutane. Ethylene was fed to the reactor to maintain constant pressure. A catalyst yield of 2700 g of polyethylene per g of catalyst was used as the reaction endpoint.

### 2.5.3 Density Measurements of the Polyethylene Products

The polymer Melt Flow Indices (MFI) were measured at 190 °C on a Zwick / Roell 4106 Extrusion Plastometer. Polymer amounts of 3.5 and 2.8 g were used for respectively measuring the MFI<sub>21.6</sub> and MFI<sub>5.0</sub>. Polymer densities were measured following the standardized ISO 1183 procedure.

#### **2.5.4 Gel Permeation Chromatography**

Gel permeation chromatography (GPC) was carried out on a PolymerChar GPC-IR system running at 160 °C equipped with a Polymer Char IR5 infrared detector and a PolymerChar viscometer. The column set consisted of three Polymer Laboratories 13 um PLgel Olexis 300 x 7.5 mm columns. PE molar mass calibration was performed with linear PE standards in the range of 0.5 – 2800 kg/mol ( $M_w/M_n = 4$  to 15).

#### **2.5.5 UV-Vis-NIR Diffuse Reflectance Spectroscopy**

The in-situ UV-Vis-NIR Diffuse Reflectance Spectroscopy (DRS) measurements were performed on a Varian Cary 500 Scan spectrophotometer with a DRS accessory. Measurements were performed in the spectroscopic range of 4000-45000 cm<sup>-1</sup> with 33 ms data point scan time and spectroscopic resolution of 17 cm<sup>-1</sup> and 7 cm<sup>-1</sup> in respectively the 12500-45000 cm<sup>-1</sup> and 4000-12500 cm<sup>-1</sup> range. Two artefacts in the measured spectra were corrected for the detector/grating and light source changeovers at 12500 cm<sup>-1</sup> and 28570 cm<sup>-1</sup>, while the spectroscopic feature appearing at 11250 cm<sup>-1</sup> is due to an instrumental artefact. For every measurement, the cell was loaded in a N<sub>2</sub> glovebox, preventing the samples from contact with atmospheric oxygen and water. The samples were measured against a Teflon-white measured in the same cell loaded with the same volume of 30 μm beads of Teflon powder. For measuring the catalyst materials, 100 mg of catalyst material was loaded in the specially designed cell. Subsequently, the desired volume of metal-alkyl co-catalyst was injected via the septum into the N<sub>2</sub> gas stream, in the form of tri-ethyl borane (Sigma-Aldrich, 1M in hexane), or a self-made solution of 1M tri-ethyl aluminum (Sigma-Aldrich, 93%) in hexane (dried over 4Å molsieves). After addition of the co-catalyst, spectra were recorded every 3 min for 15 min. Subsequently, the N<sub>2</sub> gas stream of 10 mL/min was switched to a gas stream of 10 mL/min C<sub>2</sub>H<sub>4</sub>. The system was heated to 150 °C with 5 °C/min, spectra were recorded at 40 °C, 60 °C, 80 °C, 100 °C, 120 °C and 150 °C.

### **2.6 References**

- [1] M. P. McDaniel, *Adv. Catal.* **2010**, *53*, 123-606.
- [2] L. L. Böhm, *Angew. Chem. Int. Ed.* **2003**, *42*, 5010–5030.
- [3] G. Wilke, *Angew. Chem. Int. Ed.* **2003**, *42*, 5000–5008.
- [4] H. H. Brintzinger, D. Fischer, R. Mülhaupt, B. Rieger, R. M. Waymouth, *Angew. Chem. Int. Ed.* **1995**, *34*, 1143–1170.
- [5] R. Cheng, Z. Liu, X. He, P. Qui, M. Terano, M. S. Eisen, S. L. Scott, B. Liu, *Adv Polym Sci* **2013**, *257*, 135–202.
- [6] A. Zecchina, E. Groppo, C. Lamberti, S. Bordiga, G. Spoto, *Chem. Rev.* **2005**, *105*, 115–184.

- [7] B. M. Weckhuysen, I. E. Wachs, R. A. Schoonheydt, *Chem. Rev.* **1996**, *96*, 3327–3349.
- [8] B. M. Weckhuysen, R. A. Schoonheydt, *Catal. Today* **1999**, *49*, 441–451.
- [9] J. P. Hogan, R. L. Banks, *US Pat.* 2825721, **1958**
- [10] J. P. Hogan, R. L. Banks, *US Pat.* 2951816, **1960**
- [11] R. Merryfield, M. McDaniel, G. Parks, *J. Catal.* **1982**, *77*, 348–359.
- [12] B. Liu, P. Šindelář, Y. Fang, K. Hasebe, M. Terano, *J. Mol. Catal. A Chem.* **2005**, *238*, 142–150.
- [13] B. M. Weckhuysen, L. M. De Ridder, R. A. Schoonheydt, *J. Phys. Chem.* **1993**, *97*, 4756–4763.
- [14] B. M. Weckhuysen, A. A. Verberckmoes, A. L. Buttiens, R. A. Schoonheydt, *J. Phys. Chem.* **1994**, *98*, 579–584.
- [15] E. Groppo, C. Lamberti, F. Cesano, A. Zecchina, *Phys. Chem. Chem. Phys.* **2006**, *8*, 2453–2456.
- [16] E. Groppo, G. A. Martino, A. Piovano, C. Barzan, *ACS Catal.* **2018**, *8*, 10846–10863.
- [17] G. A. Martino, C. Barzan, A. Piovano, A. Budnyk, E. Groppo, *J. Catal.* **2018**, *357*, 206–212.
- [18] M. Kantcheva, I. G. Dalla Lana, J. A. Szymura, *J. Catal.* **1995**, *154*, 329–334.
- [19] G. Ghiotti, E. Garrone, A. Zecchina, *J. Mol. Catal.* **1988**, *46*, 61–77.
- [20] C. Barzan, A. Piovano, L. Braglia, G. A. Martino, C. Lamberti, S. Bordiga, E. Groppo, *J. Am. Chem. Soc.* **2017**, *139*, 17064–17073.
- [21] C. Barzan, A. A. Damin, A. Budnyk, A. Zecchina, S. Bordiga, E. Groppo, *J. Catal.* **2016**, *337*, 45–51.
- [22] A. Budnyk, A. Damin, C. Barzan, E. Groppo, C. Lamberti, S. Bordiga, A. Zecchina, *J. Catal.* **2013**, *308*, 319–327.
- [23] V. J. Ruddick, J. P. S. Badyal, *J. Phys. Chem. B* **2002**, *101*, 1791–1793.
- [24] A. Budnyk, A. Damin, C. Barzan, E. Groppo, C. Lamberti, S. Bordiga, A. Zecchina, *J. Catal.* **2013**, *308*, 319–327.
- [25] P. C. Thüne, J. Loos, A. M. de Jong, P. J. Lemstra, J. W. Niemantsverdriet, *Top. Catal.* **2000**, *13*, 67–74.
- [26] E. M. E. van Kimmenade, J. Loos, J. W. Niemantsverdriet, P. C. Thüne, *J. Catal.* **2006**, *240*, 39–46.
- [27] P. C. Thüne, J. Loos, X. Chen, E. M. E. van Kimmenade, B. Kong, J. W. Niemantsverdriet, *Top. Catal.* **2007**, *46*, 239–245.
- [28] Q. Pan, L. Li, S. Shaikhutdinov, H. J. Freund, *J. Catal.* **2018**, *357*, 12–19.
- [29] E. Groppo, C. Prestipino, F. Cesano, F. Bonino, S. Bordiga, C. Lamberti, P. C. Thüne, J. W. Niemantsverdriet, A. Zecchina, *J. Catal.* **2005**, *230*, 98–108.
- [30] B. M. Weckhuysen, R. A. Schoonheydt, J. M. Jehng, I. E. Wachs, S. J. Cho, R. Ryoo, S. Kijlstra, E. Poels, *J. Chem. Soc. Faraday Trans.* **1995**, *91*, 3245–3253.
- [31] A. Zecchina, E. Garrone, G. Ghiotti, S. Coluccia, *J. Phys. Chem.* **1975**, *79*, 972–978.
- [32] A. Chakrabarti, I. E. Wachs, *Catal. Lett.* **2014**, *145*, 985–994.
- [33] C. Brown, A. Lita, Y. Tao, N. Peek, M. Crosswhite, M. Mileham, J. Krzystek, R. Achey, R. Fu, J. K. Bindra, M. Polinski, Y. Wang, L. J. Van De Burgt, D. Jeffcoat, S. Profeta, A. E. Stiegman, S. L. Scott, *ACS Catal.* **2017**, *7*, 7442–7455.
- [34] M. Gierada, P. Michorczyk, F. Tielens, J. Handzlik, *J. Catal.* **2016**, *340*, 122–135.
- [35] N. M. Peek, D. B. Jeffcoat, C. Moisii, L. Van De Burgt, S. Profeta, S. L. Scott, A. E. Stiegman, *J. Phys. Chem. C* **2018**, *122*, 4349–4358.
- [36] A. Fong, C. Vandervelden, S. L. Scott, B. Peters, *ACS Catal.* **2018**, *8*, 1728–1733.
- [37] C. Brown, J. Krzystek, R. Achey, A. Lita, R. Fu, R. W. Meulenberg, M. Polinski, N. Peek, Y. Wang, L.

- J. Van De Burgt, S. Profeta, E. E. Stiegman, S. L. Scott, *ACS Catal.* **2015**, *5*, 5574–5583.
- [38] L. Zhong, M. Y. Lee, Z. Liu, Y. J. Wanglee, B. Liu, S. L. Scott, *J. Catal.* **2012**, *293*, 1–12.
- [39] M. F. Delley, F. Nunez-Zarur, M. P. Conley, A. Comas-Vives, G. Siddiqi, S. Norsic, V. Monteil, O. V. Safonova, C. Copéret, *Proc. Natl. Acad. Sci.* **2014**, *111*, 11624–11629.
- [40] M. F. Delley, C. S. Praveen, A. P. Borosy, F. Núñez-Zarur, A. Comas-Vives, C. Copéret, *J. Catal.* **2017**, *354*, 223–230.
- [41] C. Copéret, *Acc. Chem. Res.* **2019**, *52*, 1697–1708.
- [42] B. Liu, M. Terano, *J. Mol. Catal. A Chem.* **2001**, *172*, 227–240.
- [43] B. Liu, H. Nakatani, M. Terano, *J. Mol. Catal. A Chem.* **2002**, *184*, 387–398.
- [44] B. M. Weckhuysen, L. M. De Ridder, P. J. Grobet, R. A. Schoonheydt, *J. Phys. Chem.* **1995**, *99*, 320–326.
- [45] M. F. Delley, M. P. Conley, C. Copéret, *Catal. Lett.* **2014**, *144*, 805–808.
- [46] M. F. Delley, G. Lapadula, F. Núñez-Zarur, A. Comas-Vives, V. Kalendra, G. Jeschke, D. Baabe, M. D. Walter, A. J. Rossini, A. Lesage, L. Emsley, O. Maury, C. Copéret, *J. Am. Chem. Soc.* **2017**, *139*, 8855–8867.
- [47] M. P. Conley, M. F. Delley, G. Siddiqi, G. Lapadula, S. Norsic, V. Monteil, O. V. Safonova, C. Copéret, *Angew. Chem. Int. Ed.* **2014**, *53*, 1872–1876.
- [48] E. Morra, G. A. Martino, A. Piovano, C. Barzan, E. Groppo, M. Chiesa, *J. Phys. Chem. C* **2018**, *122*, 21531–21536.
- [49] G. A. Martino, A. Piovano, C. Barzan, J. Rabeah, G. Agostini, A. Bruekner, G. Leone, G. Zanchin, T. Monoi, E. Groppo, *ACS Catal.* **2020**, *10*, 2694–2706.
- [50] D. Cicmil, I. K. Van Ravenhorst, J. Meeuwissen, A. Vantomme, B. M. Weckhuysen, *Catal. Sci. Technol.* **2016**, *6*, 731–743.
- [51] D. Cicmil, J. Meeuwissen, A. Vantomme, B. M. Weckhuysen, *ChemCatChem* **2016**, *8*, 1937–1944.
- [52] D. Cicmil, J. Meeuwissen, A. Vantomme, J. Wang, I. K. Van Ravenhorst, H. E. Van Der Bij, A. Muñoz-Murillo, B. M. Weckhuysen, *Angew. Chem. Int. Ed.* **2015**, *54*, 13073–13079.
- [53] T. W. Woo, S. I. Woo, *J. Catal.* **1990**, *123*, 215–227.
- [54] M. P. McDaniel, M. M. Johnson, *J. Catal.* **1986**, *101*, 446–457.
- [55] P. J. Deslauriers, D. C. Rohlfing, *Macromol. Symp.* **2009**, *282*, 136–149.
- [56] E. Groppo, A. Damin, C. Otero Arean, A. Zecchina, *Chem. Eur. J.* **2011**, *17*, 11110–11114.
- [57] W. Mowat, A. J. Shortland, N. J. Hill, G. Wilkinson, *J. C. S. Dalt.* **1972**, *3*, 770–778.
- [58] J. Amor Nait Ajjou, S. L. Scott, *Organometallics* **1997**, *16*, 86–92.
- [59] C. A. Cruz, M. M. Monwar, J. Barr, M. P. McDaniel, *Macromolecules* **2019**, *52*, 5750–5760.
- [60] G. A. Martino, A. Piovano, C. Barzan, S. Bordiga, E. Groppo, *Top. Catal.* **2018**, *61*, 1465–1473.
- [61] Z. Qin-Hui, Y. Fang, X. Wei, L. Chenguang, *Pet. Sci.* **2013**, *10*, 577–583.
- [62] J. Joseph, K. C. Potter, M. J. Wulfers, E. Schwerdtfeger, M. P. McDaniel, F. C. Jentoft, *J. Catal.* **2019**, *377*, 550–564.
- [63] R. A. Schoonheydt, *Chem. Soc. Rev.* **2010**, *39*, 5051–5066.





## Chapter 3

# Influence of Metal-Alkyls on Early-Stage Ethylene Polymerization over a Cr/SiO<sub>2</sub> Phillips Catalyst: A Bulk Characterization and X-ray Chemical Imaging Study

### Abstract

The Cr/SiO<sub>2</sub> Phillips catalyst has taken a central role in ethylene polymerization since its invention in 1951. The uniqueness of this catalyst is related to its ability to produce broad Molecular Weight Distribution (MWD) polyethylene (PE) materials as well as that no co-catalysts are required to attain activity. Nonetheless, co-catalysts in the form of metal-alkyls can be added for scavenging poisons, enhancing catalyst activity, reducing the induction period, and tailoring polymer characteristics. The activation mechanism and related polymerization mechanism remain elusive, despite extensive industrial and academic research. In this **Chapter**, we show that by varying the type and amount of metal-alkyl co-catalyst, we can tailor polymer properties around a single Cr/SiO<sub>2</sub> Phillips catalyst formulation. Furthermore, we show that these different polymer properties exist in the early stages of ethylene polymerization. We have used conventional polymer characterization techniques, such as Gel Permeation Chromatography (GPC) and <sup>13</sup>C Nuclear Magnetic Resonance (NMR), for studying the metal-alkyl co-catalyst effect on Short Chain Branching (SCB), Long Chain Branching (LCB), and MWD at the bulk scale. In addition, Scanning Transmission X-ray Microscopy (STXM) was used as a synchrotron technique to study the PE formation in the early stages. This method allowed us to investigate the produced type of early-stage PE within one particle cross-section with high energy resolution and nanometer-scale spatial resolution.

*This Chapter is based on:*

M. K. Jongkind, F. Meirer, K. W. Bossers, I. C. ten Have, T. van Kessel, N. Friederichs, B. Watts, H. Ohldag, B. M. Weckhuysen, *Chem. Eur. J.* **2021**, 27, 1688-1699.

### 3.1 Introduction

The production of polyethylene (PE) is estimated to increase to an annual production of over 100 million tons in 2020 and continues to be an important material in our society in the decades to come.<sup>[1]</sup> In the catalytic production of PE three main pillars can be identified, namely Ziegler-Natta catalysts<sup>[2,3]</sup>, (post-)metallocene catalysts<sup>[4]</sup>, and Phillips-type catalysts.<sup>[1,5–10]</sup>

Ever since its invention by Hogan and Banks at the Phillips Petroleum Company laboratories in 1951,<sup>[11,12]</sup> the Cr/SiO<sub>2</sub> Phillips catalyst has evolved to such an extent that nowadays it is responsible for approximately 30% of all High-Density Polyethylene (HDPE) manufactured worldwide. Due to the extensive industrial usage of the Cr/SiO<sub>2</sub> Phillips catalyst, it has received a lot of interest from both industrial and academic research. However, no consensus has been reached yet on the activation mechanism of this catalyst system, and the related ethylene polymerization mechanism.

The Cr/SiO<sub>2</sub> Phillips catalyst is unique in comparison to the other two ethylene polymerization catalysts. While Ziegler-Natta and Group 4 transition metal-based (post-) metallocene catalysts require the addition of a metal-alkyl as co-catalyst for activation, these compounds are not a necessity for the activation of Phillips-type ethylene polymerization catalysts. Here, ethylene can fulfill the dual role of activator and monomer source. However, metal-alkyls, often in the form of alkyl-boron or alkyl-aluminum compounds, can be added to scavenge poisons, reduce the induction period, enhance catalyst activity and tailor polyethylene product properties.<sup>[1]</sup>

A complete understanding of the activation mechanism and related ethylene polymerization mechanism is hindered by at least two reasons. Firstly, weight-loadings higher than 1 wt% are avoided due to a decrease in catalytic activity related to the formation of Cr clusters, or at least oligomeric species. Secondly, only a portion, proposedly a maximum of 30%, of the Cr sites is active in ethylene polymerization.<sup>[1]</sup> These two key-points made necessary the use of various powerful analytical approaches, often avoiding industrial conditions and/or catalyst materials by use of, for example, model systems<sup>[13–23]</sup> or well-defined catalysts in which Cr<sup>6+</sup> is reduced by e.g. CO. Both examples limit the heterogeneities of the surface sites: in the former case by rationally designing the Cr surface sites and in the latter case by quantitative reduction to isolated Cr<sup>2+</sup> surface sites.<sup>[24–32]</sup>

One such example of a long-standing discussion is the oxidation state of the Cr active site, which has been investigated with many different spectroscopic techniques, demonstrating that the active valency lies between 2 and 3, with the true value still being questioned by varying insights from different research groups. These differences, however, can in part be ascribed to different reaction set-ups and differently prepared catalyst materials.<sup>[33–46]</sup>

Another extraordinary aspect, and long-standing point of discussion, is the large variety of PEs that can be produced with the Phillips catalyst and the multitude of strategies, such as calcination temperature, support type, co-catalyst addition, and catalyst pre-treatment, one can

employ in tailoring the final PE product properties.<sup>[35,47–55]</sup> The diversity of produced PEs, in terms of PE-type as well as the broad Molecular Weight Distributions (MWD), is ascribed to the large variety of Cr surface sites and each surface site producing an average type of PE.<sup>[56–58]</sup> This is predominantly caused by the active sites not being naked Cr ions. Instead, reduction by-products remain important constituents of the active sites during polymerization and affect the active site properties.<sup>[27,36,57,59–61]</sup> For example, PE properties produced from an AlPO<sub>4</sub>-supported Cr catalyst can be controlled by the precise addition of tri-ethyl borane (TEB) to the polymerization process, whereas the SiO<sub>2</sub> counterparts were less sensitive to this metal-alkyl.<sup>[34,35,51,62–64]</sup> Despite the widespread industrial usage of metal-alkyl co-catalysts, such as TEB and tri-ethyl aluminum (TEAl), owing to their ability to increase control over PE product properties, they have only started to receive increased academic interest in recent years.<sup>[56,57,59,65–67]</sup>

One such example is a study from our group, where the influence of TEAl on the polymerization properties of a shell-titanated Phillips catalyst (i.e., Cr/Ti/SiO<sub>2</sub>) was investigated and demonstrated how the addition of TEAl as a co-catalyst increased the oligomerization of ethylene. Scanning Transmission X-ray Microscopy (STXM) was used to reveal that within one catalyst particle the titanium-rich shell-region produced a linear PE, while the titanium-poor center-region of the catalyst particle generated a Linear Low-Density Polyethylene (LLDPE), demonstrating how different PE materials can be distinguished at the nanometer-scale.<sup>[68–70]</sup>

This **Chapter** describes a study in which STXM offered the possibility to investigate the type of early-stage PE produced by a Cr/SiO<sub>2</sub> Phillips catalyst as a function of different amounts of TEB and TEAl.<sup>[71]</sup> Besides, semi-batch ethylene polymerization reactions at constant polymer yields allowed us to study catalyst activities as well as the resulting polymers, which were studied in terms of Molecular Weight ( $M_w$ ), MWD / Dispersity Index ( $D$ ,  $M_w/M_n$ ), Short-Chain Branching (SCB) and Long-Chain Branching (LCB) by bulk characterization techniques, namely Size Exclusion Chromatography (SEC) and <sup>13</sup>C-Nuclear Magnetic Resonance (NMR).<sup>[72,73]</sup> These data allowed us to correlate the type of PE produced at the level of a single catalyst particle cross-section with that of bulk PE.

## 3.2 Results and Discussion

For this work, we have selected a Cr/SiO<sub>2</sub> Phillips catalyst, consisting of 1 wt% Cr impregnated on a 625 m<sup>2</sup>/g SiO<sub>2</sub> porous support, activated via a proprietary calcination method at 650 °C. The ethylene polymerization performance of this catalyst in the presence of small amounts of TEB and TEAl as co-catalyst was investigated using a 5L semi-batch reactor, where the amount of co-catalyst was present in ppm (wt/wt) levels. The produced PE materials were subsequently characterized with SEC-DV-IR and <sup>13</sup>C-NMR.

In a second stage of our study, at key co-catalyst mole ratios of respectively 1.5 and 5.0 M:Cr (M = B/Al) of TEB and TEAl, the ethylene polymerization reactions over the Cr/SiO<sub>2</sub> Phillips

**Table 3.1.** Molecular structure parameters obtained from the Gel Permeation Chromatography (GPC) analysis of the polyethylene (PE) produced in a 5L semi-batch reactor during ethylene polymerization over a Cr/SiO<sub>2</sub> catalyst for various amounts of tri-ethyl borane (TEB) and tri-ethyl aluminum (TEAI) as co-catalysts. The molecular parameter structures include the number averaged Molecular Weight ( $M_n$ ), the weight averaged Molecular Weight ( $M_w$ ), the z-averaged Molecular Weight ( $M_z$ ), and the PE density

Sample	M:Cr Mole Ratio (M = B/Al)	$M_n$ (kDa)	$M_w$ (kDa)	$M_z$ (kDa)	$\mathcal{D}$	Density (kg/m <sup>3</sup> )	Averaged Catalyst Activity (Kg <sub>PE</sub> kg <sub>cat</sub> <sup>-1</sup> min <sup>-1</sup> )
0.00 ppm	0	19	360	2600	18.6	956.1	14.8
<b>TEB</b>							
0.05 ppm	0.19	15	380	2900	26.2	957.8	44.4
0.15 ppm	0.59	13	350	2900	25.9	959.4	52.8
0.30 ppm	1.17	11	330	3000	30.3	960.0	90.9
1.50 ppm	5.86	11	220	1700	20.8	958.8	69.9
3.00 ppm	11.72	9	270	2400	29.1	958.9	59.3
<b>TEAI</b>							
0.05 ppm	0.08	18	400	2900	22.1	956.4	30.5
0.15 ppm	0.23	19	370	2600	19.8	956.3	39.6
0.30 ppm	0.47	16	370	2900	23.6	954.6	42.2
1.50 ppm	2.35	12	340	2900	29.3	953.4	52.9
3.00 ppm	4.70	12	320	2900	28.0	953.5	50.5

catalyst were quenched before the onset of catalyst particle fragmentation. The produced catalyst-PE materials were cut into slices of ~100 nm by ultra-microtomy, after embedding in a hard immobilizing epoxy resin, and Scanning Transmission X-ray Microscopy (STXM) was used to study the type of PE produced while it was still largely dispersed within the Cr/SiO<sub>2</sub> catalyst phase, with polymer yields between 1-2 g<sub>PE</sub>kg<sub>cat</sub><sup>-1</sup>.

In the following, we will first present the ethylene polymerization results and the related characterization of the polyethylene produced by a Cr/SiO<sub>2</sub> Phillips catalyst as a function of the amount of TEB and TEAI. In the second part, we will focus on the STXM data of early-stage ethylene polymerization Cr/SiO<sub>2</sub> Phillips catalyst materials, which, in a final third part, will be compared to reference materials and rationalized with the bulk PE properties.

### 3.2.1 Effect of Metal-alkyls on the Bulk Polyethylene Properties

Two properties that govern a significant portion of the final PE characteristics are the MWD as well as branching, consisting SCB and LCB,<sup>[52,55,74]</sup> the latter being defined as a sidechain with over 150 carbon atoms. Table 3.1 illustrates how respectively TEB and TEAI affect the Mass Average Molar Mass ( $M_w$ ), the Number Average Molar Mass ( $M_n$ ), the z-average Molar Mass ( $M_z$ ), and

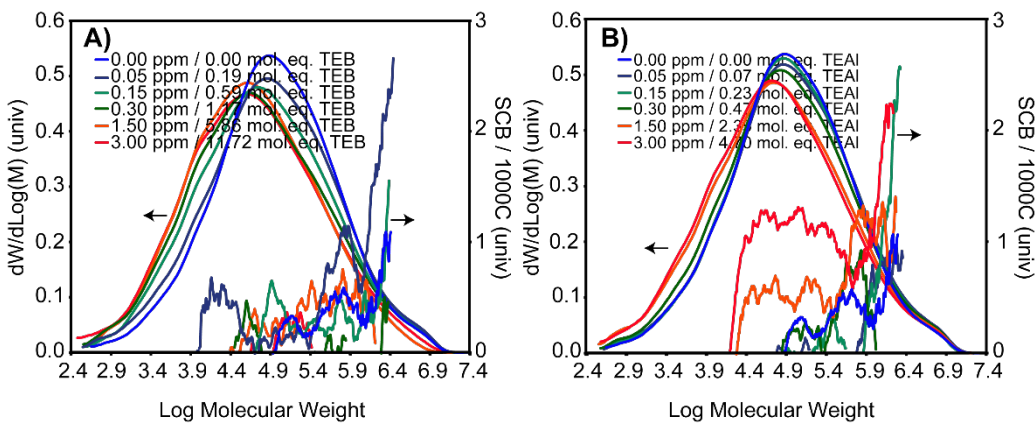


**Figure 3.1.** Results obtained from Gel Permeation Chromatography (GPC) measurements on the produced polymers with different amounts of **A)** tri-ethyl borane (TEB) and **B)** tri-ethyl aluminum (TEAI), demonstrating the Molecular Weight Distribution (MWD; arrow pointing left) as well as the degree and distribution of Short Chain Branching (SCB; arrow pointing right).

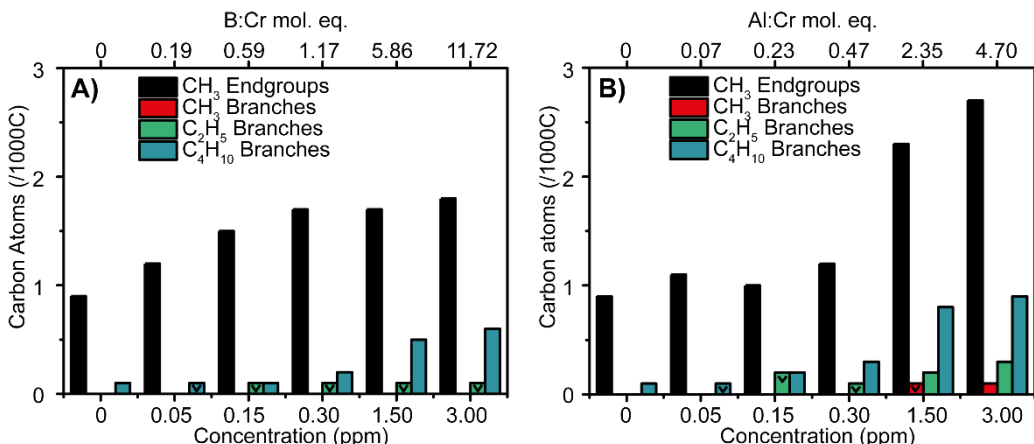


**Figure 3.2.** End-group analysis of the polymers produced with **A)** tri-ethyl borane (TEB) and **B)** tri-ethyl aluminum (TEAI) measured with <sup>13</sup>C Nuclear Magnetic Resonance (NMR) giving the number of methyl, ethyl, and butyl short chain branches (SCB) as well as methyl end-groups.

the Dispersity Index ( $D$ ,  $M_w/M_n$ ). TEB decreases the  $M_n$  after the addition of only 0.19 mol. eq. TEB (0.05 ppm) to 15 kDa and further to a minimum of 9 kDa in the presence of 11.72 mol. eq. TEB (3.00 ppm). The relative increase of shorter PE molecules is further corroborated by an increasing MWD, as demonstrated in Figure 3.1A. The  $M_w$  and  $M_z$  values reveal that the broadening MWD is mostly caused by a relatively larger number of low MW PE chains, since both the  $M_w$  and  $M_z$  take chain-length into account, with a stronger contribution of the larger PE molecules to the final value.<sup>[74]</sup> However, the  $M_w$  and  $M_z$  also start to decrease at amounts of

TEB larger than 5.86 mol. eq. (1.50 ppm), indicating that from here on a relatively smaller number of the higher MW fraction is observed, further corroborated in Figure 3.1A.

On the other hand, Table 3.1 and Figure 3.1B shows that TEAI affects the MWD to a smaller extent than TEB. Predominantly evidenced by a constant  $M_n$  up until TEAI amounts of 0.47 mol. eq. (0.30 ppm), and a relatively constant MWD trace as shown in Figure 3.1B. However, raising the used amount of TEAI to values above 2.35 mol. eq. (1.50 ppm) does broaden de MWD, albeit without altering the relative number of smaller PE chains.

The presence of TEB or TEAI also uniquely affects the degree of SCB, as is demonstrated in Figures 3.1 and 3.2, with the triangles in Figure 3.2 reflecting values “smaller than”. Firstly, it was found that the presence of TEAI is directly correlated to enhanced SCB, and, that this is predominantly observed for the PE produced in the presence of 2.35 and 4.70 mol. eq. TEAI (respectively 1.50 ppm and 3.00 ppm). All the short-chain branches reside on the longer chains if TEAI amounts up to 0.47 mol. eq. (0.30 ppm) were used. However, at values of 2.35 mol. eq. (1.50 ppm) and 4.70 (3.0 ppm) mol. eq. they also reside on the smaller PE chains. Enhanced  $\alpha$ -oligomer generation and incorporation is the underlying reason for this observation.

On the other hand, the presence of TEB has a less pronounced effect on the SCB. At TEB molecular equivalencies of 0.59 (0.15 ppm) and higher only minor amounts of butyl branches are detected, and ethyl branches are detected even less. Interestingly, increasing the amount of TEB to 5.86 mol. eq. (1.50 ppm) and higher resulted in a small increase of the butyl branches, however, there was no noticeable effect on the number of ethyl branches.

Furthermore, the in Table 3.1 presented densities are not just an effect of SCB and to a lesser extent by the  $M_w$ . Where the densities of the materials produced with TEB are higher than those produced with TEAI (Figure 3.3). Likely, this is caused by the lower  $M_n$  as well as the SCB distribution for the materials produced with TEB, with the SCB distribution demonstrating that

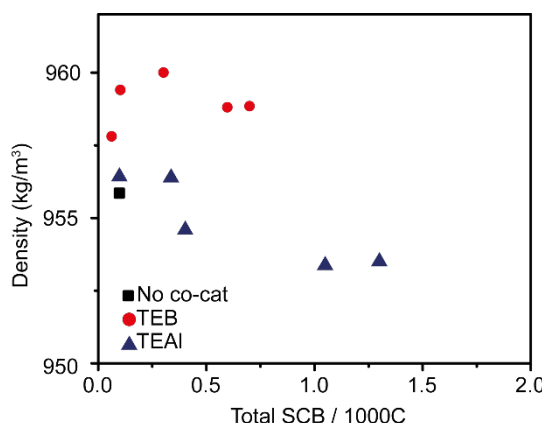


**Figure 3.3.** The densities of the produced PE materials plotted versus the cumulative number of Short Chain Branches (SCB).

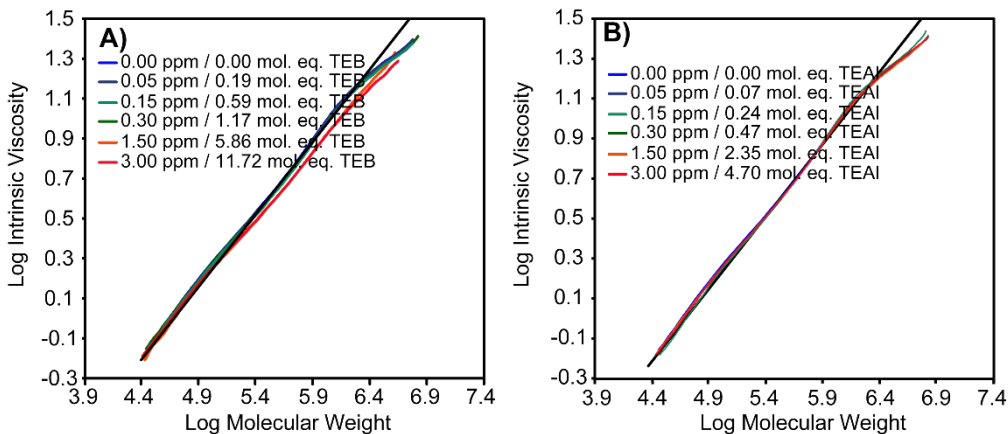


**Figure 3.4.** Mark-Houwink plots obtained from the Gel Permeation Chromatography (GPC) measurements for the polyethylene materials produced with **A)** TEB and **B)** TEAI, where the intrinsic viscosity of the produced PE materials was compared to those of linear PE materials. PE molar mass calibration was performed with linear PE standards in the range of 0.5 – 2800 kg/mol ( $M_w/M_n = 4$  to 15).

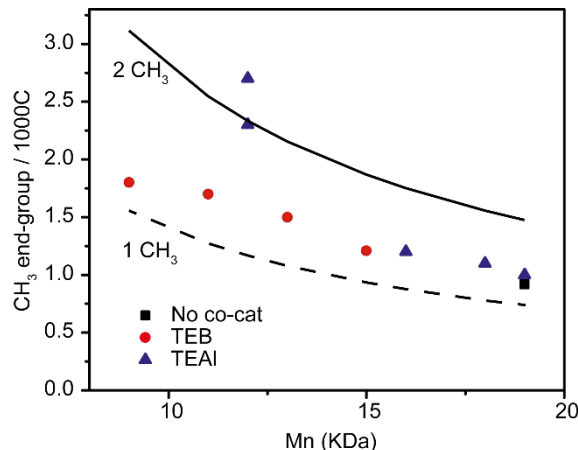


**Figure 3.5.** CH<sub>3</sub> end-groups plotted versus the  $M_n$ . The theoretical lines for 2 CH<sub>3</sub> end-group per PE chain and 1 CH<sub>3</sub> end-group per PE chain are plotted for assessing how much CH<sub>3</sub> groups per PE chains are present.

this does not occur on the smaller MW PE chains, in turn resulting in a high crystalline PE fraction. On the other hand, for TEAI there is initially little to no broadening of the MWD, thus these crystalline domains are absent: resulting in the overall lower densities of these PEs. In case the MWD does broaden, with amounts of 2.35 mol eq. and 4.70 mol. eq. TEAI (respectively 1.50 and 3.00 ppm), SCB is also observed at lower MWD chains, thus prohibiting the formation of high-crystalline domains.

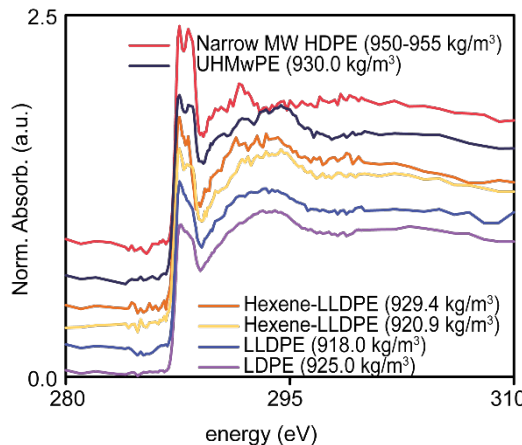


**Figure 3.6.** The results of the Scanning Transmission X-ray Microscopy (STXM) measurements at the reference materials on the C K-edge.

Both co-catalysts also have some effect on the presence, or absence, of LCB,<sup>[75,76]</sup> as shown in Figure 3.4, none of the materials perfectly fit the theoretical correlation for linear PE, however, it is only with increased amounts of TEB, 5.86 mol. eq. (1.50 ppm) and above, that the PEs deviate more significantly from the linear reference line.

If the  $M_n$  is used to calculate the theoretical number of  $\text{CH}_3$  end-groups per 1000 C atoms, illustrated in Figure 3.5, we see that in the case of 11.86 mol. eq. TEB (3.00 ppm),  $\sim 1.8$   $\text{CH}_3$  end-groups per 1000C are observed, which is close to the theoretical value of 1.55, under the assumption of 1  $\text{CH}_3$  end-group per PE chain. TEAI on the other hand, with an  $M_n$  of 12 should have a theoretical amount of  $\sim 1.2$   $\text{CH}_3$  end-group in the absence of LCB. However, the measured amount is closer to 2.75 with 4.70 mol. eq. (3.00 ppm). This value on its own might be interpreted as LCB, however, the Mark-Houwink plot in Figure 3.4 demonstrates only minor deviations from the linear references. In the case of TEB, an amount close to 1  $\text{CH}_3$  end-group per polymeric chain is observed. What is exactly responsible for this increased number of  $\text{CH}_3$  end-groups at relatively high amounts of TEAI remains elusive, but since TEAI is now present in excess, it might act now as a chain transfer agent as well. Possibly other elimination mechanisms from the aluminum-polymer complex proliferate, resulting in 2  $\text{CH}_3$  end-groups per chain.

### 3.2.2 Scanning Transmission X-ray Microscopy of Polyethylene Reference Materials

One of the key challenges is to compare the produced early-stage materials to bulk polymers. For this, a series of reference materials was investigated with STXM, their bulk C K-edge XANES, shown in Figure 3.6. These reference materials were rationally selected to cover a large variety of PE materials in terms of density.

Figure 3.6 illuminates the findings by Schöll *et al.*<sup>[77]</sup> who found that PE density, and related crystallinity, coincides with the line shape of the 287.4 and 287.8 eV  $\sigma^*_{\text{C-H}}$  transitions. Most importantly, Figure 3.6 shows that for a narrow MW HDPE, with a density of 950 – 955 kg/m<sup>3</sup>, the splitting of this signal is apparent, and the signals can be identified. The trend that emerges from Figure 3.6 is that upon decreasing the density, the splitting of the 287.4 and 287.8 eV  $\sigma^*_{\text{C-H}}$  transitions becomes more obscured, which also holds for the  $\sigma^*_{\text{C-C}}$  transitions. One exception is, however, the LDPE (925 kg/m<sup>3</sup>) reference material, for which the density was higher than two of the LLDPE (918 kg/m<sup>3</sup>, 920.9 kg/m<sup>3</sup>) references, nonetheless, the splitting was more obscured: this is likely due to LCB in this material, which was absent in all other instances.

### 3.2.3 Scanning Transmission X-ray Microscopy of the Early-Stage Ethylene Polymerization over Cr/SiO<sub>2</sub> Catalysts

The analysis of the bulk polymers has shown that it is possible to tailor the PE properties, in terms of predominantly the MWD and the SCB, with the proper selection of the type and amount of co-catalyst. However, it is still unclear how these differences affect early-stage PE materials. The fact that the C K-edge XANES line shape is directly related to the PE density allows us to correlate the type of early-stage PE to bulk PE references. STXM offers the opportunity to generate high spatial-resolution image-sequences at specified high-resolution X-ray energies ( $\Delta E \sim 0.1$  eV at edge-jump), allowing for the spatial correlation of different PE densities at the nanometer scale via their characteristic so-called X-ray Absorption Near-Edge Structure (XANES). However, individual PE crystallite domains (~27 nm) are below our used spatial resolution (100 nm<sup>2</sup>), as a consequence, each pixel is (possibly) a sum of multiple randomly oriented PE crystallites.<sup>[78]</sup> Improving the STXM technology further is technically possible, but also limited by the spectral signal to noise ratio when inspecting such small volumes containing tiny amounts of polymer, as is the case for these early-stage materials. To complement the spatially resolved STXM measurements, DSC was used as a tool to quantify the melting temperatures ( $T_m$ ) of these materials.

It is worth mentioning that Linear Dichroism can occur for crystalline PE materials in STXM measurements. However, this requires highly crystalline samples prepared with special methods and on special (poly-)crystalline substrates. The requirement of highly-ordered, preferably single-crystalline samples, is not fulfilled by our materials, since they show **1)** broad MWD, **2)** are grown randomly over **3)** a large variety of active sites, leading to azimuthally averaged distribution of early-stage PE materials, and **4)** are not grown on (poly-)crystalline substrates.<sup>[79]</sup>

We used equimolar amounts of TEB or TEAI in the preparation of the early-stage materials, to effectively compare their effects on the type of early-stage PE, and selected key amounts of 1.50 and 5.0 mol. eq. (M:Cr; M = B/Al). Firstly, 1.50 mol. eq. of TEB is expected to result in a broadened MWD, however should demonstrate very little SCB. By increasing the amount of TEB

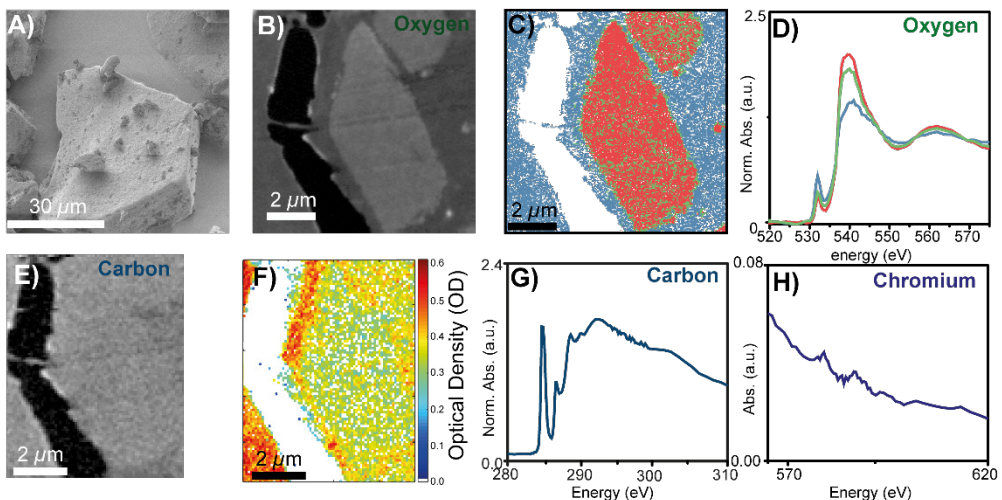


**Figure 3.7.** A schematic overview of the performed Scanning Transmission X-ray Microscopy (STXM) measurements on the Cr/SiO<sub>2</sub> Pristine catalyst. **A)** Scanning Electron Microscopy (SEM) image of the pristine catalyst. **B)** Optical Density (OD) image at the O K-edge (538 eV) of the microtomed cross-section of the pristine catalyst. **C)** Clustered image after Principal Component Analysis (PCA) at the O K-edge, showing three phases: oxygen from the Struers Epofix Epoxy resin and two mixed phases. **D)** O K-edge X-ray absorption near-edge spectra (XANES) prior to the linear subtraction of the epoxy reference O K-edge XANES from the combination spectra. **E)** STXM OD image at the C K-edge (280 eV) of the microtomed cross-section. **F)** Carbon K-edge edge-jump map of the OD image in Figure E. **G)** Bulk C K-edge XANES of the presented edge-jump map. **H)** Bulk XANES of the Cr L<sub>2</sub> and L<sub>3</sub> edge, extracted from Figure S2: PCA after removal of pixels with too much noise was impossible due to the low amount of Cr being atomically dispersed.

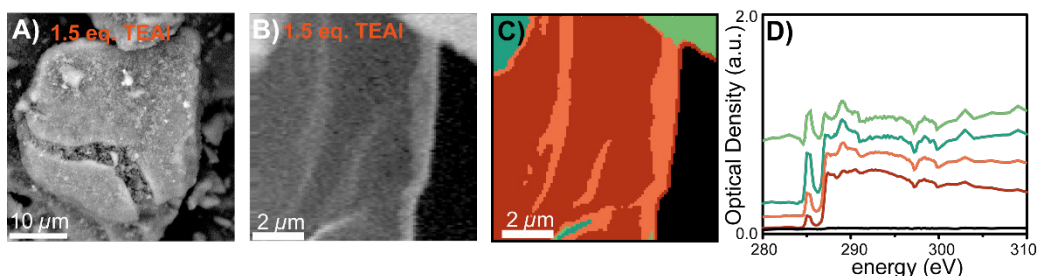
to 5.0 mol. eq., the expected degree of SCB was enhanced and the MWD is expected to broaden. Secondly, a comparison of the PE produced with 1.50 mol. eq. of TEAI shows, based on Figure 3.1, that almost no broadening of the MWD is expected, whereas the degree of SCB is expected to be larger. By raising the amount of TEAI to 5.0 mol. eq., the MWD is expected to broaden, while the degree of SCB is largely retained. In summary, we have 4 samples with the following characteristics: **1)** very small amounts of SCB (1.5 mol. eq. TEB), **2)** increased SCB (1.5 mol. eq. TEAI), **3)** significantly broadened MWD and a small amount of SCB (5.0 mol. eq. TEB) and **4)** broadened MWD with increased SCB (5 mol. eq. TEAI).

Figure 3.7A shows a Scanning Electron Microscopy (SEM) image of the pristine catalyst material, prior to treatment by a co-catalyst and subsequent ethylene polymerization. The OD image at the O K-edge (538 eV), in Figure 3.7B, shows features resembling the pristine material, and two clear phases are discerned: one corresponding to the SiO<sub>2</sub> framework and one to the embedding epoxy resin. Clustering after Principal Component Analysis (PCA) is reported in Figure 3.7C and confirms the presence of three characteristic clusters, that is, regions with distinctly different spectral features. The corresponding normalized XANES at the O K-edge of the clusters,

shown in Figure 3.7D, correspond to that of the epoxy resin and two clusters associated to the catalyst particle region of interest. In any case, the pre-edge feature infers infiltration of the catalyst particle with the epoxy resin since this feature should be absent in case of a pure SiO<sub>2</sub> phase. With respect to the pristine Cr/SiO<sub>2</sub> material, no carbonaceous material should be present within the catalyst, yet the carbon K-edge edge-jump map confirms its presence in the entire field of view, thus also the particle, with the corresponding carbon K-edge bulk XANES (Figure 3.7G) corresponding to the embedding epoxy resin.

In addition, Cr was found in the sample material, as demonstrated by the bulk XANES of the Cr L<sub>2,3</sub> edge in Figure 3.7H. The ΔOD of ~0.02 already corroborates the small amount of Cr atoms in the material cross-section. The discrepancy between the OD values reported in Figure 3.7H and the normalized absorption for the O K-edge (Figure 3.7D) comes from normalization of the XANES spectrum. Naturally, increasing the cross-section thickness would increase the ΔOD due to an increase in Cr atoms along the X-ray path. This would unfortunately coincide with a loss of spectroscopic information at the C K-edge due to absorption of nearly all the X-rays in this case as well as the too large signal offsets due to high absorption. Furthermore, even with increased S/N values, the Cr sites are expected to be isolated, and, at this cross-section thickness, the isolated sites or multi-atom ensembles are at least two orders of magnitude smaller than the spatial resolution of 100 nm.

Figure 3.8A shows the SEM image of the pre-polymerized catalyst particle, where the effect of polymerization on the particle morphology is visualized by the presence of extra surface features, attributed to PE, as well as by a significant crack formed due to disintegration of the SiO<sub>2</sub> support particle due to increasing internal stress caused by the growing PE. Still, the particle morphology in Figure 3.8A resembles that of the pristine material, thus confirming that fragmentation of the SiO<sub>2</sub> support has not yet occurred extensively, meaning that the PE is still largely dispersed within the support phase. Figure 3.8B reports an OD image at 280 eV of a cross-section of this pre-polymerized catalyst material. Where the top-right and top-left corners are



**Figure 3.8.** Results from the Scanning Transmission X-ray Microscopy (STXM) experiments before processing of the data. **A)** Scanning Electron Microscopy (SEM) image of the with 1.5 molecular equivalents TEAI pre-polymerized catalyst particle. **B)** STXM Optical Density (OD) image at 280 eV of the cross-section. **C)** Clustered image without applying edge-jump analysis and normalization of the OD reporting image and **D)** Carbon K-edge XANES of these clusters.

brighter than the center of this image. Subsequent alignment of the stack and sample/background selection was performed in aXis2000, with PCA and clustering (without filtering of pixels based on edge-jump analysis) being performed in TXM Wizard hereafter, the latter process producing the image in Figure 3.8C and corresponding raw XANES in Figure 3.8D. This shows five different regions, corresponding to in the OD image identifiable regions. Firstly, the top right corner is defined by absorption saturation, due to measuring very close (or partly on) the Cu TEM Grid. Secondly, the top-left corner is less affected by absorption saturation, confirmed by much larger contrast and a peak intensity of ~1 OD. The two residual clusters make up the center part of the OD image.<sup>[77]</sup> The pre-edge feature is attributed to the  $\pi^*_{\text{C}=\text{C}}$  transitions of the epoxy resin, whereas the features at 287.4 and 287.8 eV are attributed to PE  $\sigma^*_{\text{C}-\text{H}}$  transitions. This means that the top-left corner likely contains a larger contribution of the epoxy, whereas the center region contains less of this and is predominantly occupied by PE.<sup>[80]</sup>

Take note, that for some of the experiments, specifically in Figures 3.8D, 3.10D, 3.11D, 3.11H, 3.12, 3.13B, 3.14B, and 3.14D, there appears to be two dips in the C K-edge XANES at 297 and 300 eV, which are caused by the K 2p  $\rightarrow$  3d spin-orbit split transition. The materials produced with 1.5 and 5.0 mol. eq. of TEB and 1.5 mol. eq. of TEAI show these dips, whereas the sample with 5.0 mol. eq. TEAI does not. The latter was measured 9 months after the others, explaining why only one of the four signals does not contain the negative signals. However, the spectra are significantly like each other (and the reference materials) that it does not hamper analysis of the relevant signals at 287.4 and 287.8 eV.

To solve for the presence of mixed epoxy/PE phases (as shown in Figures 3.10 and 3.11), a method, illustrated in Figure 3.9, was developed that generated clustered images and C K-edge XANES without epoxy contributions. First, normal stack alignment and sample/background selection was performed using the aXis2000 software.<sup>[92]</sup> Subsequently, PCA and clustering was performed using the TXM Wizard software.<sup>[93]</sup> These two steps provided clustered images (with pixels pooled according to spectral similarity) and C K-edge XANES with the epoxy contributor still present. The C K-edge XANES of these materials show a pre-edge feature at 285 eV, which indicates the presence of epoxy (see the pure epoxy reference spectra in Figure 3.12). This feature is absent in the pure PE phase (see Figure 3.6) so it can be used as a quantitative marker for the presence of epoxy in each pixel by inspecting the magnitude of this feature in each normalized single-pixel XANES. This allowed to effectively remove the contribution of pure epoxy to each spectrum: after normalization of every single pixel XANES the normalized reference of epoxy was weighted by the magnitude of the feature at 285 eV and subtracted:

$$(3.1) \quad X_{i,corr} = X_i - w_i R_{epoxy}$$

Where index  $i$  indicates the pixel index,  $X_{i,corr}$  the corrected XANES,  $X_i$  the uncorrected XANES,  $R$  the epoxy reference, and  $w_i$  the weight for pixel  $i$  based on the magnitude of the 285 eV feature

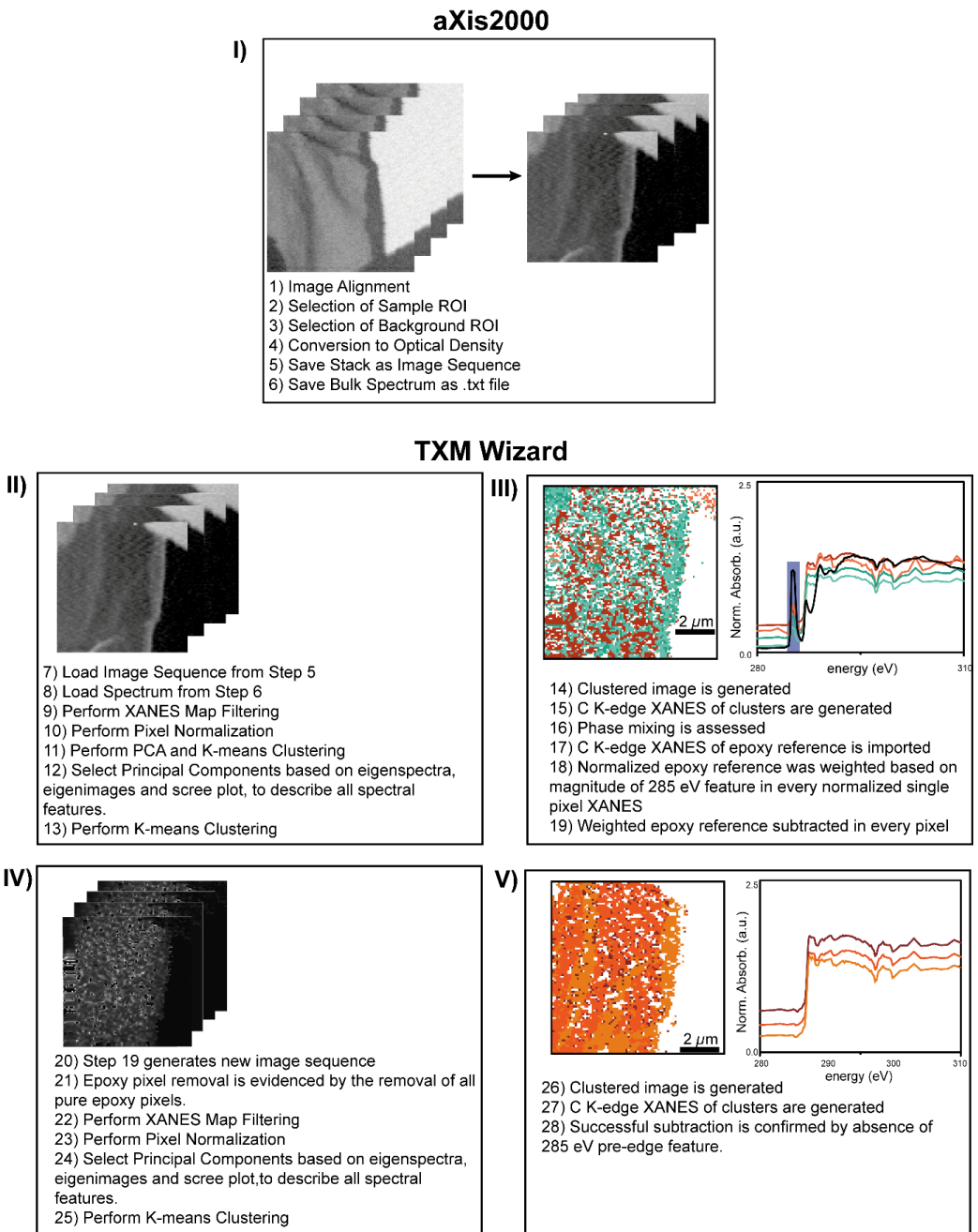


**Figure 3.9.** Schematic description of all individual steps of the Scanning Transmission X-ray Microscopy (STXM) data processing.

recorded for that pixel and scaled between 0 and 1;  $w_i = 1$  indicates a pure epoxy spectrum based on the magnitude of the 285 eV feature in the epoxy reference and  $w_i = 0$  the absence of any contribution from epoxy. The effectiveness of this method is nicely confirmed by the fact that all XANES of pixels containing pure epoxy have been reduced to their baseline and subsequently removed by the edge jump filter. After this removal of contributions from epoxy, PCA and clustering was again performed to group pixels according to their spectral similarity. The results are shown in Figures 3.13 for the materials pre-polymerized with TEAI and in Figure 3.14 for the materials pre-polymerized with TEB.

Figure 3.10E demonstrates the early-stage polymer materials with 5.0 mol. eq. of TEAI respectively. Again, this material is characterized by its largely intact original particle morphology in combination with starting cracks and surface features, with the original particle morphology being retained to a large extent: indicating that this particle is still in the early stages of disintegration.

The OD images are shown in Figures 3.8B, 3.10B, and 3.10F. In the case of the OD image shown in Figure 3.8B/3.10B, which was discussed before, one can differentiate between the

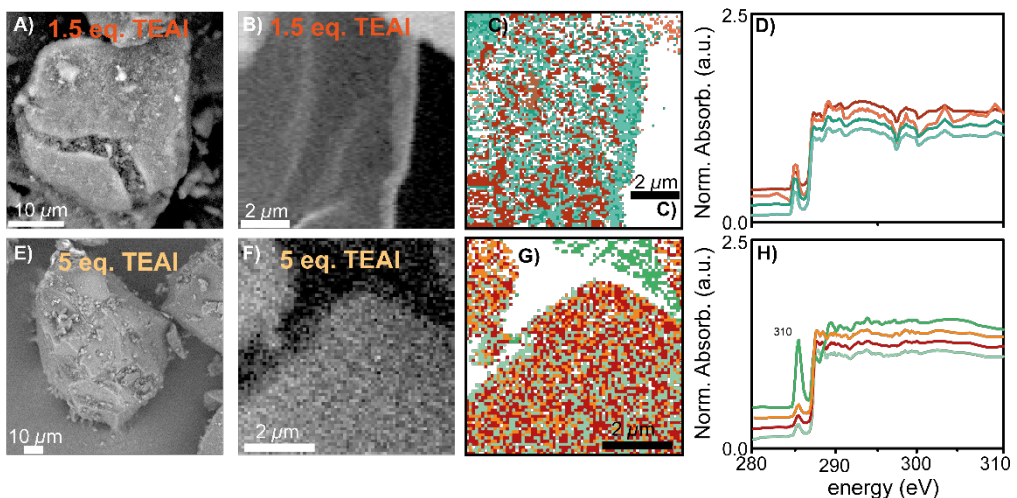


**Figure 3.10.** Overview of the Scanning Transmission X-ray Microscopy (STXM) measurement results on the with 1.5 and 5.0 mole equivalents of tri-ethyl aluminum (TEAI) pre-polymerized Cr/SiO<sub>2</sub> catalyst particles before linear subtraction of the epoxy reference C K-edge X-ray Absorption Near-Edge Spectra (XANES). **A**) and **E**) Scanning Electron Microscopy (SEM) images of the pre-polymerized catalyst materials with respectively 1.50 and 5.0 mole equivalents of tri-ethyl borane (TEB). **B**) and **F**) STXM Optical Density (OD) image at the C K-edge (280 eV) of the microtomed slice of the pre-polymerized material. **C**) and **G**) Clustered image after Principal Component Analysis (PCA) on the stacks obtained at the C K-edge, showing distinct phases: carbon from the Struers Epofix Epoxy resin and carbon from the polyethylene. **D**) and **H**) Obtained C K-edge XANES of the clustered images.

different regions in the catalyst material. The OD image of the cross-section with 5.0 mol. eq. of TEAl, shown in Figure 3.10F, only shows a minor an epoxy(-rich) region in the top, however, the pre-polymerized catalyst particle cross-section occupies most of the field of view. The image sequence in Figures 3.10F and thus also 3.13C was collected with a smaller field of view of 7x7  $\mu\text{m}$ , while maintaining the same pixel resolution of 100 nm.

Clustering after PCA with the epoxy removed by linear subtraction further confirmed the successful removal of the epoxy contributions, as shown in Figures 3.13A and 3.13C, which is further corroborated by the C K-edge XANES in Figures 3.13B and 3.13D, now free of epoxy contributions. The remaining clusters in Figure 3.13A now perfectly overlap with the early-stage catalyst materials as shown in the OD images in Figure 3.10. These clusters are internally characterized by similar 287.4 and 287.8 eV  $\sigma^*_{\text{C-H}}$  absorption features and 290-292 eV  $\sigma^*_{\text{C-C}}$  absorption feature at the C K-edge XANES, inferring only minor differences between the clusters. Interestingly, there appears to be at least some spatial correlation within this sample coinciding with the OD image, which is related to slight variations in sample thickness: the brighter parts corresponding to more absorption (more material) and the less bright residual volume of the catalyst cross-section is slightly less absorbing.

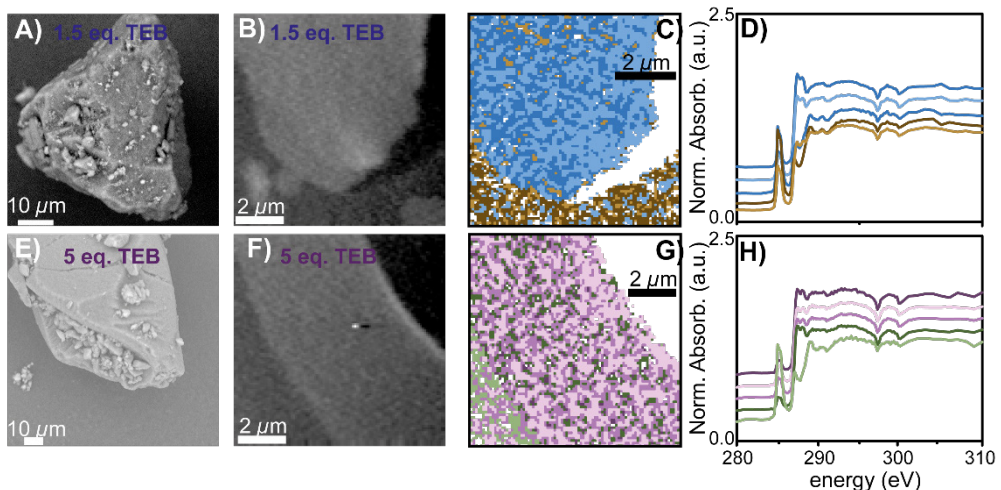


**Figure 3.11.** Overview of the Scanning Transmission X-ray Microscopy (STXM) measurement results on the with 1.5 and 5.0 mole equivalents of tri-ethyl borane (TEB) pre-polymerized Cr/SiO<sub>2</sub> catalyst particles before linear subtraction of the epoxy reference C K-edge X-ray Absorption Near-Edge Spectra (XANES). **A)** and **E)** Scanning Electron Microscopy (SEM) images of the pre-polymerized catalyst materials with respectively 1.50 and 5.0 mole equivalents of tri-ethyl borane (TEB). **B)** and **F)** STXM Optical Density (OD) image at the C K-edge (280 eV) of the microtomed slice of the pre-polymerized material. **C)** and **G)** Clustered image after Principal Component Analysis (PCA) on the stacks obtained at the C K-edge, showing distinct phases: carbon from the Struers Epofix Epoxy resin and carbon from the polyethylene. **D)** and **H)** Obtained C K-edge XANES of the clustered images

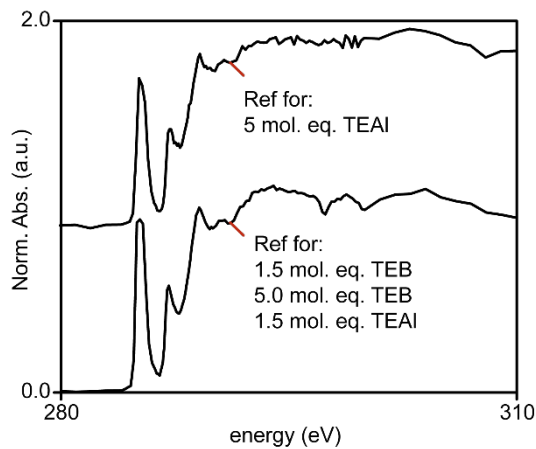


**Figure 3.12.** Normalized Epoxy reference XANES measured at ALS Beamline 11.0.2 that were used for subtraction from the combination XANES by LCA. The spectra are offset for clarity.

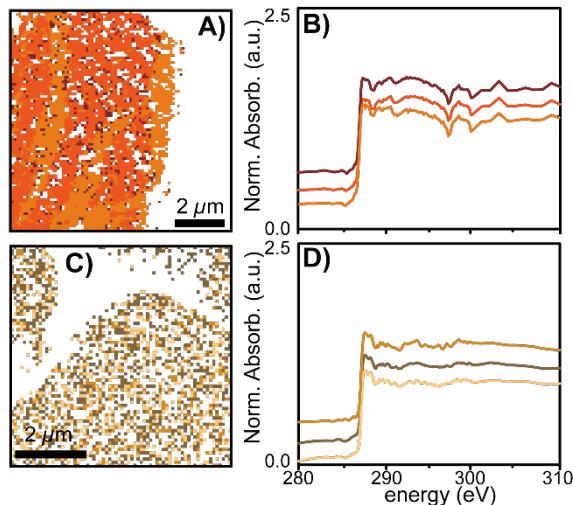


**Figure 3.13.** A) +B) Clustered image after Principal Component Analysis (PCA) of the with respectively 1.5 and 5.0 molecular equivalents TEAI pre-polymerized catalyst particle. The SEM image and Optical Density (OD) image are given in Figures 3.10A and 3.10B, respectively. C) + D) C K-edge X-ray Absorption Near-Edge Spectra (XANES) of clusters in the microtomed cross section of the pre-polymerized catalyst materials with respectively 1.5 and 5.0 molecular equivalents of TEAI. Modified from as-measured spectra of the indicated locations, by subtraction of the epoxy signal, according to the described procedure.

A comparison of the C K-edge XANES of the materials produced with 1.5 mol. eq. TEAI (Figure 3.13B) and 5.0 mol. eq. of TEAI (Fig 3.13D) demonstrates that the line shapes of the 287.4 and

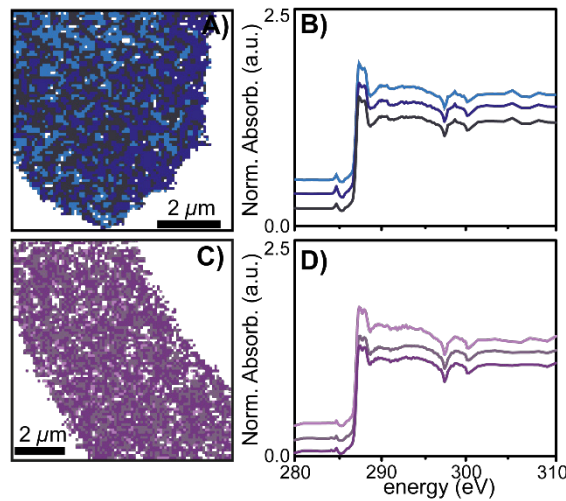


**Figure 3.14.** **A)** +**B)** Clustered image after Principal Component Analysis (PCA) of the with respectively 1.5 and 5.0 molecular equivalents TEB pre-polymerized catalyst particle. The SEM image and Optical Density (OD) image are given in Figures **3.11A** and **3.11B**, respectively. **C)** + **D)** C K-edge X-ray Absorption Near-Edge Spectra (XANES) of clusters in the microtomed cross section of the pre-polymerized catalyst materials with respectively 1.5 and 5.0 molecular equivalents of TEB. Modified from as-measured spectra of the indicated locations, by subtraction of the epoxy signal, according to the described procedure.

287.8 eV  $\sigma^*_{\text{C-H}}$  absorption features of these materials are relatively similar, with the individual transitions being slightly more obscured for the material produced with 1.5 mol. eq. TEAI. Furthermore, Figures **3.13B** and **3.13D** in both cases demonstrate similar  $\sigma^*_{\text{C-C}}$  absorption features in the 290 – 292 eV range. These observations show that these materials are similar in terms of density, albeit this likely being slightly lower for the material produced with 1.5 mol. eq. In accordance with the bulk-investigations, the larger density for the material with 5.0 mol. eq. TEAI is possibly explained by an expectedly relatively larger number of smaller PE molecules co-crystallizing between bigger PE chains.<sup>[78,81]</sup>

Figure **3.14** demonstrates the results of the STXM measurements with TEB as a co-catalyst, with the morphologies of the pre-polymerized materials being shown in Figures **3.11A** and **3.11E**, and the OD images being shown Figures **3.11B** and **3.11F**. The early stage of ethylene polymerization is confirmed by the presence of additional surface features and the absence of extensive catalyst fragmentation. The SEM images clearly show that the original particle morphology is largely retained.

Figures **3.11B** and **3.11F** show the OD images at the C K-edge. Clearly, the catalyst material can be discerned from the Struers Epofix epoxy resin in both cases: the darker areas corresponding to the epoxy resin and the lighter material to the pre-polymerized catalyst material. Clustering after PCA, as shown in Figures **3.14A** and **3.14C**, with three clusters

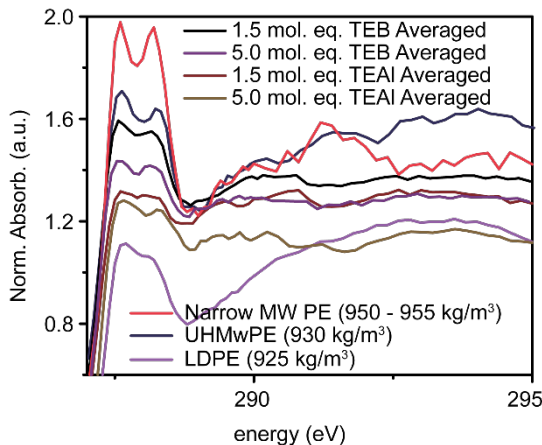


**Figure 3.15.** Magnification of the 287 – 295 eV region in the C K-edge X-ray Absorption Near-Edge Spectra (XANES) of the average spectra of the early-stage polyethylene (PE) materials as well as the spectra of three relevant reference materials. The C K-edge XANES are offset for clarity.

(corresponding XANES in Figure 3.14B and 3.14D) show that the regions attributed to epoxy are correctly subtracted, now revealing pure PE spectra.

First, the XANES of the early-stage PE material produced with 1.5 mol. eq. of TEB, shown in Figure 3.14B, is characterized by two distinct  $\sigma^*_{\text{C-H}}$  X-ray absorption features at 287.4 and 287.8 eV. In case 5.0 mol. eq. TEB was used, the produced XANES in Figure 3.14D, demonstrate a similar line shape: with clear and individual transitions at 287.4 and 287.8 eV.

At first sight, it appears that internally the growth of PE is homogeneous in each sample, testified by the similar XANES for the different clusters and further corroborated by Figures 3.14A-B and 3.14C-D that exhibit little spatial hierarchy. Having said this, Figure 3.14A appears to demonstrate some spatial hierarchy inferred by a larger concentration of “dark-blue” clusters at the right side and a larger concentration of “light-blue” clusters at the left side. However, as mentioned before, the C K-edges strongly resemble each other and likely infer homogeneous PE formation throughout the catalyst cross-section, thus if these PEs differ, it is only very minimally.

A quick comparison of the materials produced with TEB to those produced with TEAI (magnification shown in Figure 3.15), shows that splitting of the characteristic 287.4 and 287.8 eV  $\sigma^*_{\text{C-H}}$  X-ray absorption features is present for the materials produced with 1.5 mol. eq. and 5.0 mol. eq. TEB and for the material produced with 5.0 mol. eq. TEAI. The splitting can still be distinguished for the material produced with 1.5 mol. eq. TEAI, however, it can be argued that it is more obscured here. These results infer that the PE materials produced with 1.5 and 5.0 mol. eq. of TEB and the material produced with 5.0 mol. eq. of TEAI are very similar in terms of density, while the density of the material produced with 1.5 mol. eq. of TEAI is likely a bit lower.<sup>[77,82]</sup>

### 3.2.4. Relating Bulk Characterization Data to the X-ray Imaging Technique

Figure 3.15 also allows us to easily compare the C K-edge XANES of three reference materials, the two outliers (LDPE and Narrow MW PE) and the Ultra-High Molecular Weight PE (UHMwPE), with the averaged C K-edge XANES of the early-stage PE materials.

As mentioned, the early-stage PE are very similar in terms of density on basis of their 287.4 and 287.8 eV  $\sigma^*_{\text{C-H}}$  X-ray absorption features, which all show at least some splitting, with the splitting for the material produced with 1.5 mol. eq. TEAI being the most obscured of the four averages. One of the underlying reasons for this might be the increased SCB lowering the density. Figure 3.15 also shows that the early-stage PE produced with 5.0 mol. eq. of TEAI demonstrates a slightly more pronounced splitting of the 287.4 and 287.8 eV signals, likely due to the broader MWD: a relatively larger amount of small PE chains exist in this product, which can co-crystallize between the bigger chains, hereby increasing the PE density, also previously discussed.<sup>[81]</sup>

What is evident from Figure 3.15 is that the C K-edge XANES of none of the early-stage materials approaches the C K-edge XANES of the 950-955 kg/m<sup>3</sup> reference, instead, the materials are more comparable to the 930 kg/m<sup>3</sup> reference material. This indicates that the density of the early-stage materials is lower than what is to be expected for HDPE materials.

This finding coincides with findings by McKenna *et al.*, reporting that nascent early-stage PE materials demonstrated lower melting temperatures ( $T_m$ ) than was expected. This was attributed to the PE crystallite size dimensions being in line with the pore size dimensions of the original catalyst material, hereby confining polymer growth.<sup>[83-85]</sup> Similarly, we have used DSC (Table 3.2, Figure 3.16) to assess the  $T_m$  of the early-stage materials and in general found that these are lower than those of bulk PE materials (~135 °C). More specifically, the early-stage PE materials produced with 1.5 mol. eq. of TEAI demonstrate melting temperatures at 119.05 and 132.7 °C and for 5.0 mol. eq. TEAI melting temperatures of 120.9, 130.2, and 136.8 °C are measured. For TEB, the melting temperatures were 127.02 and 136.07 °C for the PE produced with 1.5 mol. eq.

**Table 3.2** Crystallinities and Melting Temperatures obtained with Differential Scanning Calorimetry (DSC) from the early-stage polyethylene (PE) materials.

Sample	X <sub>c</sub> (%)	T <sub>m1</sub> (°C)
<b>TEB</b>		
1.50 eq.	50.9	127.02; 136.07
5.00 eq.	48.4	121.12
<b>TEAL</b>		
1.50 eq.	44.3	119.05; 132.69
5.00 eq.	48.5	120.89; 130.15; 136.83

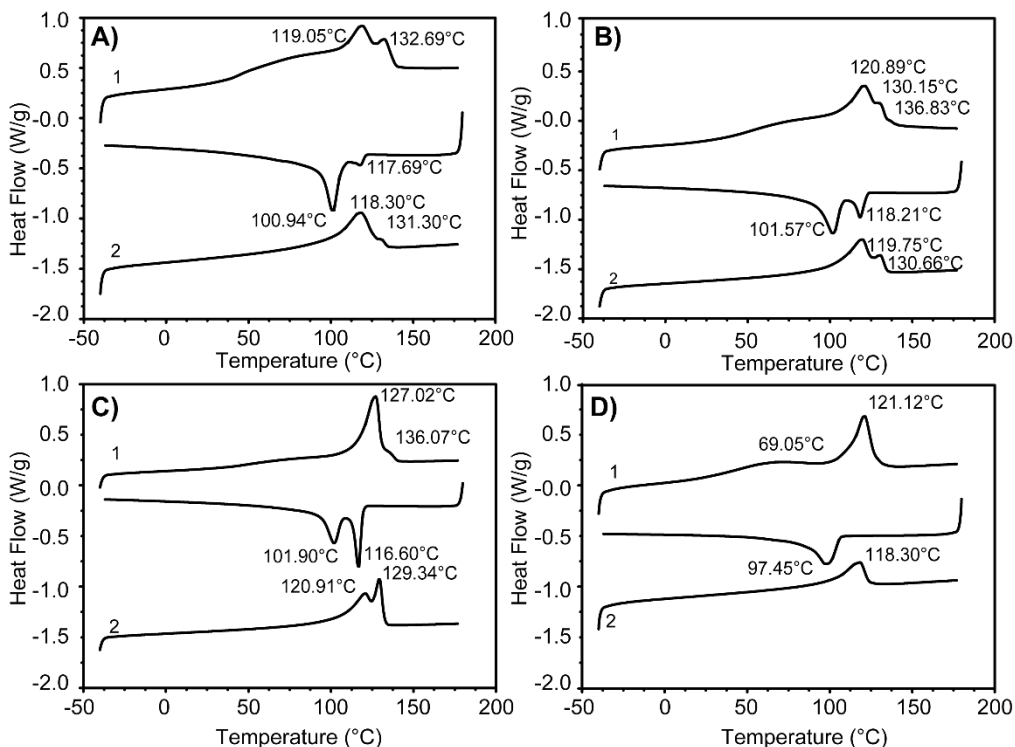


**Figure 3.16.** Differential Scanning Calorimetry (DSC) profiles for the early-stage polyethylene materials produced with **A)** 1.5 mole equivalents and **B)** 5.0 mole equivalents of tri-ethyl aluminum (TEAl) as well as **C)** 1.5 mole equivalents and **D)** 5.0 mole equivalents of tri-ethyl borane (TEB). The first heating ramp was from -40 °C to 180 °C with 10 °C/min, after which the temperature was kept constant at 180 °C to erase the thermal history. Subsequently the sample was cooled from 180 °C to -40 °C with a ramp of 10 °C/min and the second heating cycle was started from -40 °C to 180 °C with a 10 °C/min ramp.

TEB and 121.2 °C for the PE produced with 5.0 mol. eq. of TEB. The multiple melting temperatures for the materials produced with TEAl and 1.5 mol. eq. TEB are likely caused by the presence of different defective sequences, which constitute crystals of different thickness and is a testament to the presence of relatively larger amounts of SCB.<sup>[4,71,83–87]</sup>

The DSC results support the STXM results in the sense that indeed we see that the early-stage PE materials have lower densities than bulk HDPE materials, emphasizing the effect of the support matrix.<sup>[83,85]</sup> This is often explained due to PE materials with higher degrees of SCB being less crystalline while still dispersed in the SiO<sub>2</sub> framework and are proposed to be able to diffuse out of the SiO<sub>2</sub> pores, whereas the more crystalline and rigid PE materials are less able to do so.<sup>[84,86–88]</sup>

### **3.3 Conclusions**

In this **Chapter** we found that the properties of the polyethylene (PE) produced by a single Cr/SiO<sub>2</sub> Phillips catalyst formulation can be carefully tailored by selection of the proper type and amount of tri-ethyl borane (TEB) or tri-ethyl aluminum (TEAl). More specifically, PE properties in terms of molecular weight distribution (MWD), short-chain branching (SCB), and long-chain branching (LCB) were found to be sensitive to this and could be tuned. Both co-catalysts broadened the MWD, however, TEB did so to a greater extent than TEAl. TEAl, in turn, was more beneficial for SCB than TEB and exhibited more SCB. For both co-catalysts, only minor deviations from the theoretical linear reference in terms of viscosity are observed, excluding the PE materials produced with 4.86 mol. eq. and 11.72 mol. eq. TEB (respectively 1.50 and 3.00 ppm), here at least some deviations were observed.

Scanning transmission X-ray microscopy (STXM) measurements on the effect of TEB and TEAl on the nanometer-scale PE density and related crystallinity revealed that within one catalyst material the growth of PE is homogeneous, testified by only minor differences within the C K-edge XANES. Furthermore, we found that the densities of the early-stage materials were very similar. However, it could be argued that the densities for the early-stage materials produced with TEAl were slightly lower: the material produced with 1.5 mol. eq. of TEAl being the smallest. A comparison with the reference materials demonstrated overall smaller densities than what was to be expected for HDPE bulk materials, this being further corroborated by the  $T_m$  from the DSC measurements.

In summary, we have shown that STXM is a powerful tool in characterizing these early-stage PE materials. We have shown that both TEB and TEAl distinctly affect the early-stage PE and we have shown that the early-stage PE materials are, type-wise, different than their bulk variants, indicating the significance of the support in confining the early-stage PE by affecting the density and related crystallinity.

### **3.4 Acknowledgements**

H. Meeldijk (Utrecht University, UU) is acknowledged for his help in depositing the catalyst materials onto the TEM grids. E. Troisi (SABIC, Geleen) is acknowledged for his help with the DSC measurements. T. Schoffelen (SABIC, Geleen) is acknowledged for providing the reference PE materials. This research used resources of the Advanced Light Source, a U.S. DOE Office of Science User Facility under contract no. DE-AC02-05CH11231. The PolLux end station was financed by the German Ministerium für Bildung und Forschung (BMBF) through contracts 05K16WED and 05K19WE2.

## **3.5 Experimental Section**

### **3.5.1 Batch-reactor Catalyst Testing**

Slurry phase polymerization reactions with a Cr/SiO<sub>2</sub> Phillips-type catalyst were performed in a 5 L semi-batch reactor at SABIC Geleen, during which induction time, catalyst yield and total polymerization time were monitored. The batch reactor was loaded with 1071 g isobutane (SABIC, 96%, 4% n-butane) as diluent and heated to 99°C. 830 mg H<sub>2</sub> (SABIC, 99.9%) was added and subsequently the reactor was pressurized to 34 bar with C<sub>2</sub>H<sub>4</sub> (SABIC, 99.9%). Hence, the diluent was loaded with 12 mol% C<sub>2</sub>H<sub>4</sub> and 1 mol% H<sub>2</sub>. Upon reaching the reaction conditions, the co-catalyst was injected with 120 g of isobutane and subsequently the Cr/SiO<sub>2</sub> catalyst was injected with 180 g of isobutane. Ethylene was fed to the reactor to maintain constant pressure. A catalyst yield of approximately 2700 g of polyethylene per g of catalyst was used as an endpoint of the reaction. The co-catalysts under study are tri-ethylborane (TEB, SABIC, 99%) and tri-ethylaluminum (TEAl, SABIC, 99.0%). The Cr/SiO<sub>2</sub> is a silica Cr-catalyst with a ~1.0 wt% Cr loading, a surface area of 625 m<sup>2</sup>/g, a pore volume of 2.41 mL/g nad a D50 particle size distribution of 52.8 μm. The catalyst was calcined at 650 °C via a SABIC-propriety technique to yield the used CrO<sub>x</sub>/SiO<sub>2</sub> catalyst.

### **3.5.2 Nuclear Magnetic Resonance**

The samples were dissolved at 130 °C in C<sub>2</sub>D<sub>2</sub>Cl<sub>4</sub>-containing di-tert-butyl-p-cresol (DBPC, Sigma-Aldrich, >99%) as stabilizing agent. The <sup>13</sup>C-nuclear magnetic resonance (NMR) spectra were recorded on a Bruker Avance500 spectrometer with a cryogenically cooled probe operated at 125 °C.

### **3.5.3 Gel Permeation Chromatography**

Gel Permeation Chromatography (GPC) was carried out on a PolymerChar GPC-IR system running at 160 °C equipped with a Polymer Char IR5 infrared detector and a PolymerChar viscometer. The column set consisted of three Polymer Laboratories 13 um PLgel Olexis 300 x 7.5 mm columns. PE molar mass calibration was performed with linear PE standards in the range of 0.5 – 2800 kg/mol (Mw/Mn = 4 to 15).

### **3.5.4 Scanning Electron Microscopy**

Scanning electron microscopy (SEM) micrographs of the early-stage polyethylene materials were recorded on a PhenomPro X microscope (FEI Company, USA), equipped with a CsB detector for

backscattered electrons (BSE), operated at 10 kV. The samples were deposited onto Al stubs with carbon tape (Electron Microscopy Sciences, Hartfield, PA, USA) that were not coated prior to measurements.

### **3.5.5 Scanning Transmission X-ray Microscopy**

The sample preparation for the Scanning Transmission X-ray microscopy (STXM) experiments was performed by embedding product powders after polymerization in a quartz cell, pre-treated with either 1.50 and 5.00 mol. eq. of TEB or TEAI in a Struers Epofix Epoxy resin. The embedded material was ultra-microtomed with a Diatome Ultra 35° diamond knife on a Reichert-Jung Ultracut E into 100 nm slices and floated on a bath of water, after which they were placed on Transmission Electron Microscopy (TEM) grids and used as such for analysis. The STXM measurements were performed at the Advanced Light Source (ALS) beamline 11.0.2, USA, and at the PolLux STXM of the Swiss Light Source (SLS),<sup>[89–91]</sup> Paul Scherrer Institute, Switzerland. For the measurements across the C (275–320 eV), O (525–580 eV) and Cr (560–610 eV) edge a 45 nm Au zoneplate was used at the ALS and a 35 nm Au zoneplate was used at PolLux. The X-rays at the ALS were circularly polarized to avoid contrast from dichroism and the X-rays at the SLS are 80% horizontal linear polarization. The probed area of the particles varied between 50 and 100  $\mu\text{m}^2$  with a pixel size of 100 nm. The energy scan step size varied from 0.1 eV around the absorption edge to 1 eV in the pre-edge and post-edge regions.

### **3.5.6 Scanning Transmission X-ray Microscopy Data Analysis**

Data analysis was performed with the aXis2000<sup>[92]</sup> and TXM-XANES-Wizard<sup>[93]</sup> software. The alignment of the different image sequences was done in aXis2000, after which all spectra were converted to optical density (OD). Principal Component Analysis (PCA) and clustering was performed with the TXM-XANES-Wizard software. First, pixels with X-ray absorption edge jumps below a certain threshold were filtered out as they did not show sufficient S/N ration for further processing (especially normalization). After XANES normalization (here again single pixel spectra that showed insufficient quality for normalization were filtered) PCA and k-means clustering was performed keeping three Principal Components (PC) for clustering in PC space. The number of clusters was selected manually based upon inspection of the results from PCA (eigenspectra, eigenimages, and score plot). Subsequently, de-mixing of the XANES by removal of the contribution of the epoxy XANES was performed by subtracting an epoxy reference XANES from each single pixel XANES after weighting it by the peak area of the 285 eV X-ray absorption feature, a feature that is exclusively present in the epoxy XANES. The corrected data set was again processed as before (normalization, filtering, PCA, k-means clustering in 3-dimensional PC space with manually selected number of clusters (typically 3)).

### 3.5.7 Nitrogen Physisorption

$N_2$  adsorption isotherms were measured at 77 K on a Micromeritics TriStar 3000 instrument. Prior to all measurements, samples were dried at 423 K under dynamic vacuum. Specific surface areas (SSAs) were calculated using the multipoint BET method ( $0.05 < p/p_0 < 0.25$ ). Pore volumes ( $V_p$ ) were calculated by the t-plot method; pore size distributions (PSDs) were obtained by DFT using  $N_2$  and spherical pores in the package MicroActive 4.06 (Micromeritics).

### 3.5.8 Differential Scanning Calorimetry

Differential Scanning Calorimetry (DSC) was performed on a TA Instruments DSC Q20 with 1-2 mg of the nascent material. Each sample was heated from -40 °C to 200 °C at a rate of 10 °C min<sup>-1</sup> after which it was briefly held isothermally at 200 °C. Subsequently the cooling cycle was initiated to -40 °C at a rate of 10 °C/min followed by an additional heating cycle to 200 °C at a rate of 10 °C min<sup>-1</sup>. The crystallinities of the polyethylene materials were determined assuming  $\Delta H_m^0 = 293 \text{ J/g}$  for 100% crystalline polyethylene. The calculated crystallinities were not corrected for the residual amount of catalyst.

## 3.6 References

- [1] M. P. McDaniel, *Adv. Catal.* **2010**, *53*, 123–606.
- [2] G. Wilke, *Angew. Chem. Int. Ed.* **2003**, *42*, 5000–5008.
- [3] L. L. Böhm, *Angew. Chem. Int. Ed.* **2003**, *42*, 5010–5030.
- [4] H. H. Brintzinger, D. Fischer, R. Mülhaupt, B. Rieger, R. M. Waymouth, *Angew. Chem. Int. Ed.* **1995**, *34*, 1143–1170.
- [5] A. Zecchina, E. Groppo, C. Lamberti, S. Bordiga, G. Spoto, *Chem. Rev.* **2005**, *105*, 115–184.
- [6] B. M. Weckhuysen, R. A. Schoonheydt, *Catal. Today* **1999**, *51*, 223–232.
- [7] B. M. Weckhuysen, R. A. Schoonheydt, *Catal. Today* **1999**, *49*, 441–451.
- [8] B. M. Weckhuysen, I. E. Wachs, R. A. Schoonheydt, *Chem. Rev.* **1996**, *96*, 3327–3349.
- [9] B. M. Weckhuysen, L. M. De Ridder, R. A. Schoonheydt, *J. Phys. Chem.* **1993**, *97*, 4756–4763.
- [10] R. Cheng, Z. Liu, X. He, P. Qui, M. Terano, M. S. Eisen, S. L. Scott, B. Liu, *Adv Polym Sci* **2013**, *257*, 135–202.
- [11] J. P. Hogan, R. L. Banks, *US Pat*, 2824721, **1958**.
- [12] J. P. Hogan, R. L. Banks, *US Pat*, 2951816, **1960**.
- [13] A. Budnyk, A. Damin, C. Barzan, E. Groppo, C. Lamberti, S. Bordiga, A. Zecchina, *J. Catal.* **2013**, *308*, 319–327.
- [14] V. J. Ruddick, J. P. S. Badyal, *J. Phys. Chem. B* **2002**, *101*, 1791–1793.
- [15] Q. Pan, L. Li, S. Shaikhutdinov, H. J. Freund, *J. Catal.* **2018**, *357*, 12–19.
- [16] E. M. E. Van Kimmenade, A. E. T. Kuiper, Y. Tamminga, P. C. Thüne, J. W. Niemantsverdriet, *J. Catal.*

- 2004**, 223, 134–141.
- [17] P. C. Thüne, J. Loos, A. M. de Jong, P. J. Lemstra, J. W. Niemantsverdriet, *Top. Catal.* **2000**, 13, 67–74.
- [18] P. C. Thüne, J. Loos, X. Chen, E. M. E. van Kimmenade, B. Kong, J. W. Niemantsverdriet, *Top. Catal.* **2007**, 46, 239–245.
- [19] C. Copéret, *Acc. Chem. Res.* **2019**, 52, 1697–1708.
- [20] C. Copéret, F. Allouche, K. W. Chan, M. P. Conley, M. F. Delley, A. Fedorov, I. B. Moroz, V. Mougel, M. Pucino, K. Searles, K. Yamamoto, P. A. Zhizko, *Angew. Chem. Int. Ed.* **2018**, 57, 6398–6440.
- [21] M. F. Delley, C. S. Praveen, A. P. Borosy, F. Núñez-Zarur, A. Comas-Vives, C. Copéret, *J. Catal.* **2017**, 354, 223–230.
- [22] L. Floryan, A. P. Borosy, F. Núñez-Zarur, A. Comas-Vives, C. Copéret, *J. Catal.* **2017**, 346, 50–56.
- [23] Q. Pan, L. Li, S. Shaikhutdinov, Y. Fujimori, M. Hollerer, M. Sterrer, H. J. Freund, *Faraday Discuss.* **2018**, 208, 307–323.
- [24] B. M. Weckhuysen, L. M. De Ridder, P. J. Grobet, R. A. Schoonheydt, *J. Phys. Chem.* **1995**, 99, 320–326.
- [25] E. Groppo, C. Prestipino, F. Cesano, F. Bonino, S. Bordiga, C. Lamberti, P. C. Thüne, J. W. Niemantsverdriet, A. Zecchina, *J. Catal.* **2005**, 230, 98–108.
- [26] B. M. Weckhuysen, A. A. Verberckmoes, A. L. Buttiens, R. A. Schoonheydt, *J. Phys. Chem.* **1994**, 98, 579–584.
- [27] E. Groppo, A. Damin, C. Otero Arean, A. Zecchina, *Chem. Eur. J.* **2011**, 17, 11110–11114.
- [28] C. Barzan, A. Piovano, M. Botavina, G. A. Martino, G. Agostini, G. Martra, E. Groppo, *J. Catal.* **2019**, 373, 173–179.
- [29] L. Mino, C. Barzan, G. A. Martino, A. Piovano, G. Spoto, A. Zecchina, E. Groppo, *J. Phys. Chem. C* **2019**, 123, 8145–8152.
- [30] M. Gierada, J. Handzlik, *J. Catal.* **2018**, 359, 261–271.
- [31] C. Barzan, A. A. Damin, A. Budnyk, A. Zecchina, S. Bordiga, E. Groppo, *J. Catal.* **2016**, 337, 45–51.
- [32] L. Zhong, M. Y. Lee, Z. Liu, Y. J. Wanglee, B. Liu, S. L. Scott, *J. Catal.* **2012**, 293, 1–12.
- [33] R. Merryfield, M. McDaniel, G. Parks, *J. Catal.* **1982**, 77, 348–359.
- [34] M. P. McDaniel, M. M. Johnson, *J. Catal.* **1986**, 101, 446–457.
- [35] M. McDaniel, *Appl. Catal. A Gen.* **2017**, 542, 392–410.
- [36] C. A. Cruz, M. M. Monwar, J. Barr, M. P. McDaniel, *Macromolecules* **2019**, 52, 5750–5760.
- [37] E. Morra, G. A. Martino, A. Piovano, C. Barzan, E. Groppo, M. Chiesa, *J. Phys. Chem. C* **2018**, 122, 21531–21536.
- [38] N. M. Peek, D. B. Jeffcoat, C. Moisii, L. Van De Burgt, S. Profeta, S. L. Scott, A. E. Stiegman, *J. Phys. Chem. C* **2018**, 122, 4349–4358.
- [39] E. Groppo, C. Lamberti, S. Bordiga, G. Spoto, A. Zecchina, *J. Catal.* **2006**, 240, 172–181.
- [40] A. Damin, F. Bonino, S. Bordiga, E. Groppo, C. Lamberti, A. Zecchina, *ChemPhysChem* **2006**, 7, 342–344.
- [41] E. Groppo, C. Lamberti, F. Cesano, A. Zecchina, *Phys. Chem. Chem. Phys.* **2006**, 8, 2453–2456.
- [42] M. F. Delley, M. P. Conley, C. Copéret, *Catal. Lett.* **2014**, 144, 805–808.
- [43] C. Brown, J. Krzystek, R. Achey, A. Lita, R. Fu, R. W. Meulenberg, M. Polinski, N. Peek, Y. Wang, L. J. Van De Burgt, S. Profeta, A. E. Stiegman, S. L. Scott, *ACS Catal.* **2015**, 5, 5574–5583.

- [44] C. Brown, A. Lita, Y. Tao, N. Peek, M. Crosswhite, M. Mileham, J. Krzystek, R. Achey, R. Fu, J. K. Bindra, M. Polinski, Y. Wang, L. J. van de Burgt, D. Jeffcoat, S. Profeta, A. E. Stiegman, S. L. Scott, *ACS Catal.* **2017**, *7*, 7442–7455.
- [45] M. F. Delley, F. Nunez-Zarur, M. P. Conley, A. Comas-Vives, G. Siddiqi, S. Norsic, V. Monteil, O. V. Safonova, C. Coperet, *Proc. Natl. Acad. Sci.* **2014**, *111*, 11624–11629.
- [46] A. B. Gaspar, C. A. C. Perez, L. C. Dieguez, *Appl. Surf. Sci.* **2005**, *252*, 939–949.
- [47] Q. Sun, R. Cheng, Z. Liu, X. He, N. Zhao, B. Liu, *ChemCatChem* **2017**, *9*, 3364–3373.
- [48] M. P. McDaniel, K. S. Clear, *Appl. Catal. A Gen.* **2016**, *527*, 116–126.
- [49] G. A. Martino, C. Barzan, A. Piovano, A. Budnyk, E. Groppo, *J. Catal.* **2018**, *357*, 206–212.
- [50] A. Budnyk, A. Damin, E. Groppo, A. Zecchina, S. Bordiga, *J. Catal.* **2015**, *324*, 79–87.
- [51] M. P. McDaniel, *ACS Catal.* **2011**, *1*, 1394–1407.
- [52] P. J. Deslauriers, C. Tso, Y. Yu, D. L. Rohlfing, M. P. McDaniel, *Appl. Catal. A Gen.* **2010**, *388*, 102–112.
- [53] M. P. McDaniel, *J. Catal.* **2009**, *261*, 34–49.
- [54] M. P. McDaniel, K. S. Collins, *J. Polym. Sci. Part A Polym. Chem.* **2009**, *47*, 845–865.
- [55] P. J. DesLauriers, M. P. McDaniel, *J. Polym. Sci. Part A Polym. Chem.* **2007**, *45*, 3135–3149.
- [56] C. Barzan, A. Piovano, L. Braglia, G. A. Martino, C. Lamberti, S. Bordiga, E. Groppo, *J. Am. Chem. Soc.* **2017**, *139*, 17064–17073.
- [57] E. Groppo, G. A. Martino, A. Piovano, C. Barzan, *ACS Catal.* **2018**, *8*, 10846–10863.
- [58] K. Tonosaki, T. Taniike, M. Terano, *J. Mol. Catal. A Chem.* **2011**, *340*, 33–38.
- [59] G. A. Martino, A. Piovano, C. Barzan, S. Bordiga, E. Groppo, *Top. Catal.* **2018**, *61*, 1465–1473.
- [60] Z. Qin-Hui, Y. Fang, X. Wei, L. Chenguang, *Pet. Sci. Technol.* **2013**, *10*, 577–583.
- [61] J. Joseph, K. C. Potter, M. J. Wulfers, E. Schwerdtfeger, M. P. McDaniel, F. C. Jentoft, *J. Catal.* **2019**, *377*, 550–564.
- [62] M. P. McDaniel, M. M. Johnson, *Macromolecules* **1987**, *20*, 773–778.
- [63] E. M. E. van Kimmenade, J. Loos, J. W. Niemantsverdriet, P. C. Thüne, *J. Catal.* **2006**, *240*, 39–46.
- [64] M. P. McDaniel, D. C. Rohlfing, E. A. Benham, *Polym. React. Eng.* **2003**, *11*, 101–132.
- [65] A. Fong, C. Vandervelden, S. L. Scott, B. Peters, *ACS Catal.* **2018**, *8*, 1728–1733.
- [66] G. A. Martino, A. Piovano, C. Barzan, J. Rabeha, G. Agostini, A. Bruekner, G. Leone, G. Zanchin, T. Monoi, E. Groppo, *ACS Catal.* **2020**, *10*, 2694–2706.
- [67] M. K. Jongkind, T. Van Kessel, M. E. Z. Velthoen, N. Friederichs, B. M. Weckhuysen, *ChemPhysChem*, **2020**, *21*, 1665–1674.
- [68] D. Cicmil, J. Meeuwissen, A. Vantomme, J. Wang, I. K. Van Ravenhorst, H. E. Van Der Bij, A. Muñoz-Murillo, B. M. Weckhuysen, *Angew. Chem. Int. Ed.* **2015**, *54*, 13073–13079.
- [69] D. Cicmil, I. K. van Ravenhorst, J. Meeuwissen, A. Vantomme, B. M. Weckhuysen, *Catal. Sci. Technol.* **2016**, *6*, 731–743.
- [70] D. Cicmil, J. Meeuwissen, A. Vantomme, B. M. Weckhuysen, *ChemCatChem* **2016**, *8*, 1937–1944.
- [71] X. Zheng, J. Loos, *Macromol. Symp.* **2006**, *236*, 249–258.
- [72] M. E. A. Cudby, A. Bunn, *Polymer* **1976**, *17*, 345–347.
- [73] G. B. Galland, R. F. de Souza, R. S. Mauler, F. F. Nunes, *Macromolecules* **2007**, *32*, 1620–1625.
- [74] P. J. Deslauriers, D. C. Rohlfing, *Macromol. Symp.* **2009**, *282*, 136–149.
- [75] M. G. Neira-Velázquez, M. T. Rodríguez-Hernández, E. Hernández-Hernández, A. R. Y. Ruiz-

- Martínez, in *Handbook of Polymer Synthesis, Characterization, and Processing*, 1st ed., John Wiley & Sons, Inc., Hoboken, **2013**, pp. 355–366.
- [76] B. Erlandsson, A. C. Albertsson, S. Karlsson, *Polym. Degrad. Stab.* **1997**, *57*, 15–23.
- [77] A. Schöll, R. Fink, E. Umbach, G. E. Mitchell, S. G. Urquhart, H. Ade, *Chem. Phys. Lett.* **2003**, *370*, 834–841.
- [78] R. G. Alamo, L. Mandelkern, *Thermochim. Acta* **1994**, *238*, 155–201.
- [79] J. Fu, S. G. Urquhart, *J. Phys. Chem. A* **2005**, *109*, 11724–11732.
- [80] O. Dhez, H. Ade, S. G. Urquhart, *J. Electron Spectros. Relat. Phenomena* **2003**, *128*, 85–96.
- [81] L. L. Böhm, H. F. Enderle, M. Fleißner, *Adv. Mater.* **1992**, *4*, 234–238.
- [82] H. Ade, M. Rafailovich, G. Maron, A. Lustiger, J. Lüning, Y. Zou, J. Sokolov, S. Ge, Y. Wang, *Macromolecules* **2004**, *33*, 319–3327.
- [83] E. Tioni, V. Monteil, T. McKenna, *Macromolecules* **2013**, *46*, 335–343.
- [84] T. F. L. McKenna, A. Di Martino, G. Weickert, J. B. P. Soares, *Macromol. React. Eng.* **2010**, *4*, 40–64.
- [85] E. Tioni, J. P. Broyer, V. Monteil, T. McKenna, *Ind. Eng. Chem. Res.* **2012**, *51*, 14673–14684.
- [86] M. A. Ferrero, E. Koffi, R. Sommer, W. C. Conner, *J. Polym. Sci. Part A Polym. Chem.* **1992**, *30*, 2131–2141.
- [87] S. W. Webb, E. L. Weist, M. G. Chiovetta, R. L. Laurence, W. C. Conner, *Can. J. Chem. Eng.* **1991**, *69*, 665–681.
- [88] B. Paredes, R. Van Grieken, A. Carrero, I. Suarez, J. B. P. Soares, *Macromol. Chem. Phys.* **2011**, *212*, 1590–1599.
- [89] U. Flechsig, C. Quitmann, J. Raabe, M. Böge, R. Fink, H. Ade, *AIP Conf. Proc.* **2007**, *879*, 505–508.
- [90] U. Frommherz, J. Raabe, B. Watts, R. Stefani, U. Ellenberger, *AIP Conf. Proc.* **2010**, *1234*, 429–432.
- [91] J. Raabe, G. Tzvetkov, U. Flechsig, M. Böge, A. Jaggi, B. Sarafimov, M. G. C. Vernooij, T. Huthwelker, H. Ade, D. Kilcoyne, T. Tyliszczak, R. H. Fink, C. Quitmann, *Rev. Sci. Instrum.* **2008**, *79*, 113704–113714
- [92] A. P. Hitchcock, *J. Electron Spectros. Relat. Phenomena* **2015**, *200*, 49–63.
- [93] Y. Liu, F. Meirer, P. A. Williams, J. Wang, J. C. Andrews, P. Pianetta, *J. Synchrotron Radiat.* **2012**, *19*, 281–287.



## Chapter 4

# Redox Behavior of a Cr/SiO<sub>2</sub> Phillips Catalyst assessed by Raman Spectroscopy

### Abstract

The Cr/SiO<sub>2</sub> Phillips catalyst has been one of the three central workhorses in ethylene polymerization ever since its conception by Hogan and Banks at the Phillips Petroleum Company in 1951. Despite extensive academic and industrial research, the working state is not yet completely understood. With investigations into the exact working state being hindered by the low viable Cr weight-loadings, an even smaller portion of the total amount of these sites participating in ethylene polymerization, as well as the large variety between the surface sites. Yet, exactly understanding what composes the (precursors to the) active site is critical for further optimizing the catalyst materials, for finding new catalyst materials, and for optimizing routes towards (new) polyethylene (PE) materials. This **Chapter** describes the use of Raman spectroscopy to investigate the different types of surface structures on a Cr/SiO<sub>2</sub> Phillips ethylene polymerization catalyst, as well as the effects of CO, H<sub>2</sub> and C<sub>2</sub>H<sub>4</sub> as reducing agents on these surface structures at various temperatures. We found that two major types of surface sites exist, one contributing to the Raman spectrum at 983 cm<sup>-1</sup> and one at 1005 cm<sup>-1</sup>. Both surface sites portray different sensitivities to the reducing gases at the different temperatures. Both H<sub>2</sub> and CO revealed that the former type of surface structure was reduced with relative greater ease at temperatures of 250 and 300 °C, with H<sub>2</sub> portraying slightly better performances. In contrast, temperatures above 350 °C resulted in quantitatively reduced Cr surface structures, regardless of usage of CO or H<sub>2</sub>. Furthermore, C<sub>2</sub>H<sub>4</sub> was used at various temperatures and was found to exclusively produce partially reduced catalyst materials, with predominantly the surface sites related to the 985 cm<sup>-1</sup> Raman signal being reduced. The temperature affected the degree of reduction only minimally, and similar end-point Raman spectra were obtained at all reduction temperatures. Interestingly, the end-point Raman spectra were already obtained after approximately 6 min.

## 4.1 Introduction

The global annual plastics production is soon expected to exceed 400 million metric tons, with polyethylene (PE) having the largest market share volume.<sup>[1,2]</sup> Despite attention concerning environmental issues, their production stands as one of the most mature and sustainable uses of fossil as well as renewable feedstocks.<sup>[3]</sup> This ensures that these materials will remain essential products in our society in the coming years, further stimulating research towards even more efficient catalysts and production of (new) types of PE. The catalytic production of PE involves three main catalytic pillars, namely Ziegler-Natta catalysts,<sup>[4]</sup> (post-)Metallocene catalysts,<sup>[5]</sup> and Phillips-type catalysts.<sup>[6–15]</sup>

Ever since its invention by Hogan and Banks at the Phillips Petroleum Company, over half a century ago, the Phillips catalyst has been investigated,<sup>[6,7]</sup> modified, and improved to such an extent that nowadays it stands at the origin of approximately 30% of the global High-Density Polyethylene (HDPE) production.<sup>[1–3]</sup> This catalyst's widespread industrial usage has ensured significant research interest from both academic and industrial groups, unfortunately without reaching a consensus on the exact activation mechanism and the related polymerization mechanism.

The Cr/SiO<sub>2</sub> Phillips catalyst is unique, compared to the other catalytic systems, since it does not require the activation by a metal-alkyl co-catalyst.<sup>[8,16]</sup> However, these compounds can be added to reduce the induction time, to enhance the ethylene polymerization rate, to tailor the PE properties, and to scavenge poisons.<sup>[12,17–26]</sup> Specific gases (*i.e.*, CO, H<sub>2</sub>, and C<sub>2</sub>H<sub>4</sub>) can also act as reductant, with C<sub>2</sub>H<sub>4</sub> being unique since it acts as both the reductant and the monomer source.<sup>[27–43]</sup> One of the main advantages of these reduction gases, excluding C<sub>2</sub>H<sub>4</sub>, is that they produce a system in which the Cr<sup>6+</sup> surface sites are cleanly and quantitatively reduced to Cr<sup>2+</sup>, from which ethylene polymerization starts. Naturally, with C<sub>2</sub>H<sub>4</sub> the reduction stage is ill-separated from ethylene polymerization as these two phases overlap, with the onset of polymerization being delayed by the induction period, related to the slow reduction of the Cr<sup>6+</sup> active site precursors by C<sub>2</sub>H<sub>4</sub> and/or the subsequent first Cr-C bond formation.

A complete understanding of this catalyst system is hindered by at least two reasons. Firstly, the performance of the Cr/SiO<sub>2</sub> Phillips catalyst material is related to low Cr weight-loadings, maximally up to 1 wt% since higher loadings result in the formation of inactive oligomeric or polymeric chromate surface structures, which are easily converted into the inactive Cr<sub>2</sub>O<sub>3</sub> structure. Secondly, only a proposed one-third of the total Cr content (if not less) participates in the polymerization reaction, with the remainder acting as spectator species.<sup>[30]</sup> To avoid these challenges, research often focused on investigating well-defined catalyst materials, either by rationally producing specific surface sites or through the reduction of the Cr<sup>6+</sup> sites into well-defined Cr structures (*i.e.*, through using CO).<sup>[10,44–55]</sup> Recent years have, however, seen a surge

in researching industrially relevant catalyst materials, mostly attributed to ever improving spectroscopic and microscopic techniques.<sup>[17,19,20,27,56–58]</sup>

The large variety of active sites is simultaneously one of the advantages and disadvantages of Cr Phillips-type catalysts, since this active site distribution is responsible for both the favorable multimodal PE production,<sup>[59–63]</sup> as well as for heated discussions concerning the oxidation state and the structure of the (most) active site.<sup>[10,21,22,33,34,36,40,52,59,60,64–78]</sup> Current state-of-the-art investigations usually involve research into bulk catalyst systems, which has resulted in an increased understanding of the overall catalyst system, yet with different insights reported by different groups.<sup>[12,16,26,27,33–35,57]</sup>

Raman spectroscopy is not plagued by the normally overwhelming silica vibrations typically observed in FT-IR spectroscopy measurements, yet it is an excellent technique to investigate the surface structures.<sup>[31,76,78–87]</sup> In an early Raman spectroscopy study, Kim and Wachs found that 1 wt% CrO<sub>3</sub> deposited on SiO<sub>2</sub> gives rise to a Raman signal at 985 cm<sup>-1</sup>, which they attributed to the symmetric stretching frequency of the terminal Cr=O bonds based on similarities with the CrO<sub>2</sub>Cl<sub>2</sub> reference material, simultaneously indicating the likeliness that these structures possess a di-oxo nature. Furthermore, the absence of a band in the 800-900 cm<sup>-1</sup> region related to Cr-O-Cr bonds, resulted in the authors tentatively concluding that these di-oxo sites are monomeric

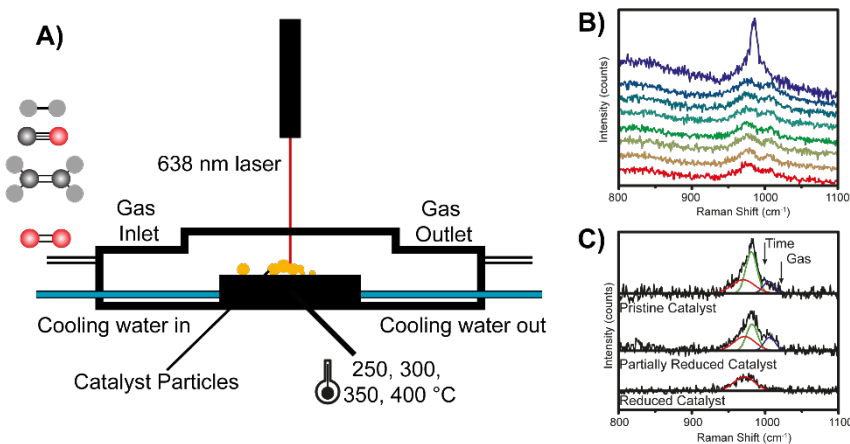


**Figure 4.1.** **A)** Schematic illustration of the performed experiments. The catalyst is loaded in a Linkam cell in an inert glovebox environment. Hereafter the cell is closed off from the outside environment and attached to a gas-feed system, which was purged at room temperature before opening the cell to either N<sub>2</sub> or Argon. In addition to N<sub>2</sub> and Ar, gases such as H<sub>2</sub>, CO, C<sub>2</sub>H<sub>4</sub>, and <sup>18</sup>O<sub>2</sub> could also be introduced in the cell. The catalyst temperature of the particle stage could be set by an external controller and controlled with cooling water. The objective, including the EMCCD detector, was positioned directly above the catalyst material and collected confocal images as well as elastically and inelastically scattered photons. **B)** This produced the (in-situ) Raman spectra. **C)** Spectral fitting was used to assess the developments of the Cr<sup>6+</sup>=O bonds during in-situ reduction conditions.

in nature.<sup>[82]</sup> This was followed up by several studies from Weckhuysen *et al.* in the following years, investigating CrO<sub>x</sub> deposited on a variety of oxide supports. The first Raman spectroscopy study focused on the understanding the surface structures of these materials under methanol oxidation and butane dehydrogenation reaction conditions, revealing that on SiO<sub>2</sub> and TiO<sub>2</sub>/SiO<sub>2</sub> supports the surface structures were predominantly isolated chromates, whereas mixtures of di-/polychromates and monochromates were obtained on supports, such as ZrO<sub>2</sub>, TiO<sub>2</sub>, and Al<sub>2</sub>O<sub>3</sub>. Unfortunately support induced fluorescence was observed under butane dehydrogenation and methanol oxidation conditions, complicating analysis of a SiO<sub>2</sub> and a TiO<sub>2</sub>/SiO<sub>2</sub> material.<sup>[76]</sup> Their second Raman spectroscopy study focused on disentangling the surface structure composition of these CrO<sub>x</sub> materials deposited on ZrO<sub>2</sub>, TiO<sub>2</sub>, and Al<sub>2</sub>O<sub>3</sub> supports, revealing that the surface structures on these supports predominantly possess mono-oxo character.<sup>[78]</sup> Research from the same authors around the same time exploited Raman spectroscopy to investigate the bond order and bond lengths of CrO<sub>x</sub> deposited on oxide supports and this research confirmed (amongst others) that the Cr=O bonds from SiO<sub>2</sub> supported chromates strongly resemble those on CrO<sub>2</sub>Cl<sub>2</sub>, indicating that these structures possess di-oxo character and confirming the earlier findings of Kim and Wachs.<sup>[11]</sup> Clearly, the situation was unsettled at these times.

Almost a decade later, Dines and Inglis used Raman spectroscopy in conjunction with computational methods to investigate the surface structures of various supported Cr catalysts, finding that at low weight-loadings the Cr is anchored mainly as monomeric Cr<sup>6+</sup><sub>di-oxo</sub> species on the SiO<sub>2</sub> carrier material, with respectively  $\nu_s(O=Cr=O)$  and  $\nu_{as}(O=Cr=O)$  Raman signals at 985 and 1015 cm<sup>-1</sup>, confirming previous findings by Kim *et al.* and Weckhuysen *et al.*<sup>[11,76,78,83]</sup> Work by Groppo *et al.* proceeded on these findings by depositing Cr on a Raman transparent silica aerogel, further corroborating that the 985 cm<sup>-1</sup> and 1015 cm<sup>-1</sup> Raman signals are indeed related to respectively  $\nu_s(O=Cr=O)$  an  $\nu_{as}(O=Cr=O)$ .<sup>[88]</sup> Later on, research by Wachs *et al.* on 3 wt% Cr/SiO<sub>2</sub> catalysts revealed a second contribution to the Raman signal at 1015 cm<sup>-1</sup> which was related to the Cr<sup>6+</sup><sub>mono-oxo</sub> surface structures in addition to the Cr<sup>6+</sup><sub>di-oxo</sub> signals contributing at 985 cm<sup>-1</sup>, as testified by independent developments of the two signals in reducing environments.<sup>[79,80,89,90]</sup>

This **Chapter** describes the use of Raman spectroscopy to exploit the polarizability of the Cr<sup>6+</sup>=O bond for investigating the Cr<sup>6+</sup> surface site composition on an industrially relevant 1 wt% Cr/SiO<sub>2</sub> Phillips-type ethylene polymerization catalyst. To that end, a series of in-situ Raman spectroscopy experiments are performed in which CO, H<sub>2</sub>, C<sub>2</sub>H<sub>4</sub> as reducing agents, and <sup>18</sup>O<sub>2</sub> as oxidation agent are used at various temperatures to study the development of the Cr<sup>6+</sup>=O surface structures. This allowed to assess the redox behavior of the Cr/SiO<sub>2</sub> Phillips catalyst.

## 4.2 Results and Discussion

Our experimental approach is illustrated in Figure 4.1 and demonstrates the ability to investigate individual catalyst particles, without invasive sample preparation. Additionally, the gas-feed

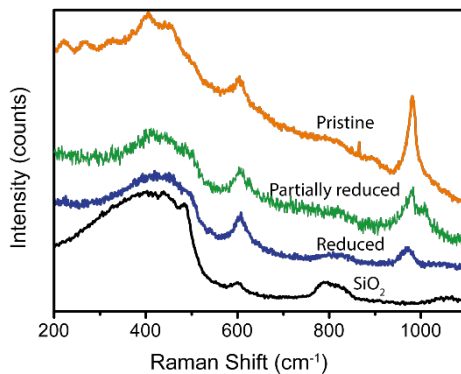


**Figure 4.2.** Raman spectra displaying the complete spectroscopic range of the pristine catalyst material, the at 250 °C with CO partially reduced catalyst material, the at 400 °C with CO quantitatively reduced catalyst material, and the  $\text{SiO}_2$  support material.

system enabled the possibility of feeding a variety of gases, including gases such as CO,  $\text{H}_2$ ,  $\text{C}_2\text{H}_4$ , and  $^{18}\text{O}_2$ , while the cooling water allowed for precise control over the temperature at which reactions were performed. Furthermore, usage of the 638 nm laser ensured that we are not entering resonant Raman conditions and seemingly also avoiding fluorescence emission interference.

#### 4.2.1 Investigating the Cr Surface Structure Composition of the Pristine Catalyst Material

Figure 4.2 shows Raman spectra of the  $\text{SiO}_2$  support material, the pristine Cr/ $\text{SiO}_2$  Phillips catalyst material, partially reduced catalyst material, and the fully reduced catalyst material. Interestingly, the Raman spectra demonstrate excellent overlap of the support related signals, with exception of the Raman signal at  $973 \text{ cm}^{-1}$ , which is attributed to unreacted surface Si-OH moieties.<sup>[89]</sup> These Si-OH moieties can completely convert during calcination in the absence of the Cr precursor. However, it seems that the presence of this precursor does prevent some of the isolated Si-OH moieties to react. The Raman spectrum of the pristine catalyst material demonstrates why Raman spectroscopy is particularly challenging on  $\text{SiO}_2$ -supported Phillips catalyst materials, mainly evidenced by the increasing baseline. However, the quality of the Raman spectra is good enough that in addition to the intense  $985 \text{ cm}^{-1}$  signal, a shoulder at  $1010 \text{ cm}^{-1}$  can be appreciated.

Despite the increasing baseline, a band with small intensity can be observed in the 820-880  $\text{cm}^{-1}$  region, indicating that at least some Cr-O-Cr bonds exist on the catalyst material under investigation.<sup>[76,78,88]</sup> Considering the higher weight-loading compared to the catalyst materials used in previous reports, this makes sense since higher weight-loadings usually favor increased dimeric and polymeric surface structure formation. However, the small intensity of this Raman

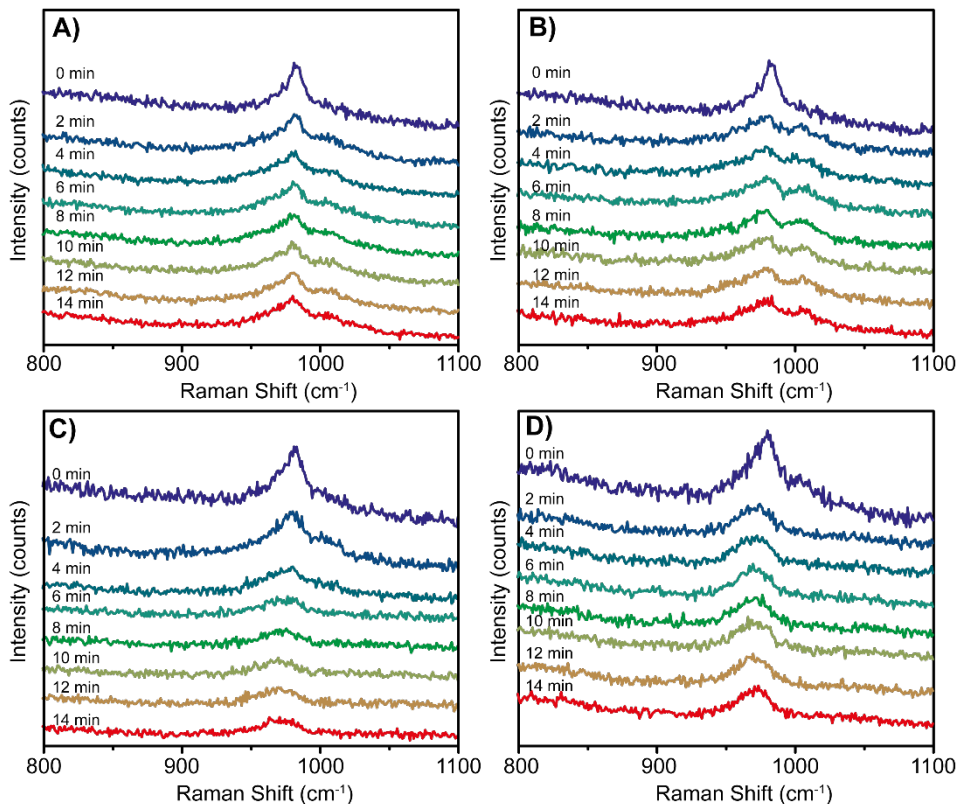


**Figure 4.3.** Raman spectra of the in-situ experiments performed in 10 mL CO / 40 mL Ar at **A)** 250 °C, **B)** 300 °C, **C)** 350 °C, and **D)** 400 °C. The spectra are offset for clarity and the first line in each of the figures represents the Raman spectrum of the pristine Cr<sup>6+</sup>/SiO<sub>2</sub> catalyst material.

signal testifies that only a relatively small amount of these Cr-O-Cr bond containing surface structures exists.

Secondly, reduction of the catalyst material goes hand in hand with disappearance of all non-support related Raman signals, as shown in Figure 4.2. For which the main reason is that the intensity of the Raman signals related to the Cr<sup>2+</sup> surface structures are significantly less intense and are not detected at this point.<sup>[76]</sup> These findings indicate that the surface structure composition of this industrial Cr/SiO<sub>2</sub> Phillips catalysts is complicated and that multiple surface structures exist. Completely disentangling the coordination geometries of all the contributing Cr surface sites is beyond the scope of this **Chapter** and would require a concerted effort with multiple complementary spectroscopic techniques, such as Fourier Transform Infrared (FTIR) spectroscopy, X-ray Absorption Spectroscopy (XAS), and UV-Vis-NIR diffuse reflectance spectroscopy (DRS).

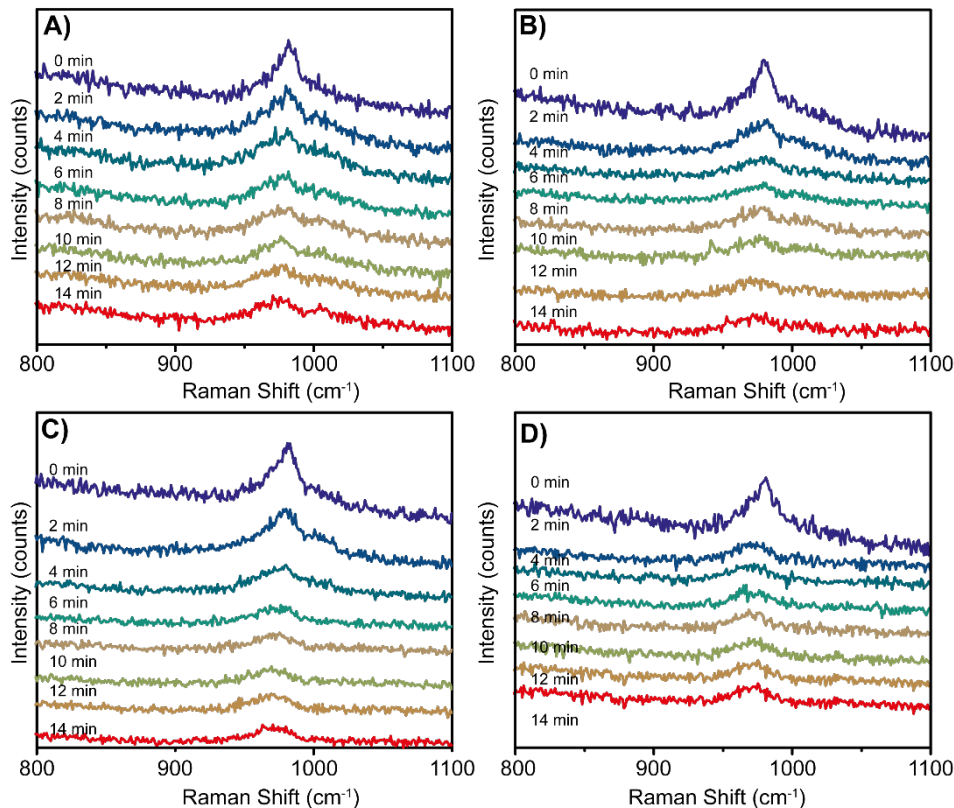


**Figure 4.4.** Raman spectra of the in-situ experiments performed in 10 mL H<sub>2</sub> / 40 mL Ar at **A)** 250 °C, **B)** 300 °C, **C)** 350 °C, and **D)** 400 °C. The spectra are offset for clarity and the first line in each of the figures represents the Raman spectrum of the pristine Cr<sup>6+</sup>/SiO<sub>2</sub> catalyst material.

#### 4.2.2 In-situ Reduction of Cr<sup>6+</sup> Surface Structures with CO, H<sub>2</sub> and C<sub>2</sub>H<sub>4</sub>

Figures 4.3, 4.4, and 4.5 demonstrate the in-situ experiments performed with respectively CO, H<sub>2</sub> and C<sub>2</sub>H<sub>4</sub> at various temperatures, with the Raman spectra being off-set for the sake of clarity. The experiments with all the reduction gases show the first 15 min of the reaction, while they were run until no further spectral changes were observed, which was consistently within the portrayed timeframe. Figure 4.3 gives an excellent overview of the effects of CO on reducing the catalyst material, related to the disappearance of the Cr<sup>6+</sup>=O signals at 983 cm<sup>-1</sup> and 1005 cm<sup>-1</sup>, as well as the effect that the temperature plays in this process. By performing the reactions at lower temperatures, the Cr<sup>6+</sup> signal at 1005 cm<sup>-1</sup> is revealed almost directly after introducing the

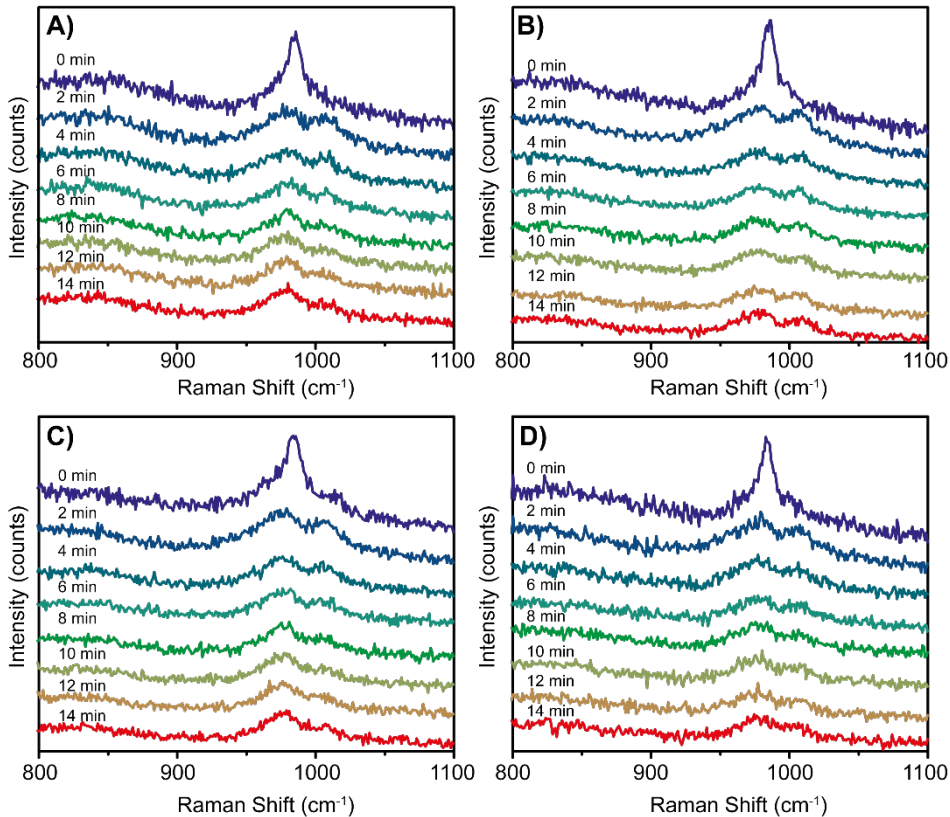


**Figure 4.5.** Raman spectra of the in-situ experiments performed in 20 N<sub>2</sub> / 20 mL C<sub>2</sub>H<sub>4</sub> at **A)** 90 °C, **B)** 110 °C, **C)** 130 °C, and **D)** 150 °C. The spectra are offset for clarity and the first line in each of the figures represents the Raman spectrum of the pristine Cr<sup>6+</sup>/SiO<sub>2</sub> catalyst material.

reducing gas. The independent developments of the two signals confirms the findings by Wachs *et al.* that two individual species contribute to the Raman signal in this region.<sup>[8,14,40,87,91]</sup>

Figure 4.3 does confirm that increased temperatures are in general more beneficial for the total degree of reduction as well as the rate at which the catalyst material is reduced, with temperatures of 350 °C (Figure 4.3C) and 400 °C (Figure 4.3D) showcasing quantitatively reduced catalyst materials, with the final spectrum only portraying the 970  $\text{cm}^{-1}$  Si-OH related signal. Naturally, the reduction occurs faster at a temperature of 400 °C and the material is already quantitatively reduced after recording the first Raman spectrum.

H<sub>2</sub> was used as the second reducing gas and acts similar as CO, with the exception that H<sub>2</sub>O is generated instead of CO<sub>2</sub>, which can be detrimental for the Cr surface structures due to the possibility of Si-O-Cr bond cleavage and the consequential leaching of the Cr sites. The results of these experiments are demonstrated in Figure 4.4 and they are almost identical to the

experiments performed with CO, except that H<sub>2</sub> appears to be more effective at reducing both types of Cr<sup>6+</sup> surface sites at lower temperatures, since a stronger decrease in intensity of both the 983 cm<sup>-1</sup> and 1005 cm<sup>-1</sup> signal is observed with H<sub>2</sub> until temperatures of 300 °C. Quantitative reduction is attained at the higher temperatures (350 °C in Figure 4.3C and 400 °C in Figure 4.3D). Conclusively, both CO and H<sub>2</sub> emphasize the independent development of the 1005 cm<sup>-1</sup> related Raman signal hereby confirming this second category of surface structures on industrial-type catalysts.

The last and (perhaps) most relevant reduction gas under investigation was C<sub>2</sub>H<sub>4</sub> (Figure 4.5), which is unique since it serves both as the monomer source and the reductant. One additional phenomenon related to the usage of C<sub>2</sub>H<sub>4</sub> is the so-called induction period, defined as the moment between the introduction of C<sub>2</sub>H<sub>4</sub> into the reaction vessel that contains the catalyst and the moment at which consumption of C<sub>2</sub>H<sub>4</sub> for polymer formation starts. This duration of this period is flexible and can vary between 30-60 min, resulting in ill-separated reduction and polymerization stages.<sup>[21]</sup> The simultaneous reduction and polymerization also limits the temperature working range to temperatures of approximately 100 °C. Therefore, to avoid working in the PE melt we performed our experiments at temperatures of 90 °C (Figure 4.5A), 110 °C (Figure 4.4B), 130 °C (Figure 4.5C), and 150 °C (Figure 4.5D).

Figure 4.5 infers that the temperature only minimally affects the reduction with C<sub>2</sub>H<sub>4</sub> since at all temperatures similar end-point Raman spectra are obtained, where neither the 983 cm<sup>-1</sup> signal nor the 1005 cm<sup>-1</sup> signal is completely removed. This is further confirmed in Figure 4.9

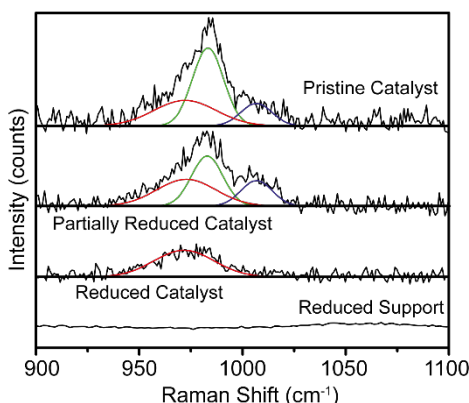


**Figure 4.6.** Spectral deconvolution of a set of representative reference spectra, related to the pristine Cr<sup>6+</sup>/SiO<sub>2</sub> material, a partially reduced Cr<sup>6+</sup>/SiO<sub>2</sub> material, and a quantitatively reduced Cr<sup>6+</sup>/SiO<sub>2</sub> catalyst material. The intensity of the 983 cm<sup>-1</sup> fitted band was used a measure for the degree of reduction. The Half-Widths at Half Maximum (HWHMs) were consistently 9 cm<sup>-1</sup> for the 983 and 1005 cm<sup>-1</sup> bands and 17 cm<sup>-1</sup> for the 973 cm<sup>-1</sup> band through all the experiments. Also, the band location was kept constant for both bands through all experiments.

showing that at 1 atm only a portion of the Cr<sup>6+</sup> surface sites is reduced with C<sub>2</sub>H<sub>4</sub>, while a significant portion remains unaffected.

A comparison of the three reduction gases definitively reveals the existence of two types of surface structures, with the definitive distinction between the two signals only being evidenced by their unique propensities to be reduced by the different reduction gases at various temperatures, with the 1005 cm<sup>-1</sup> related structures apparently reducing worse and slower than the 983 cm<sup>-1</sup> related structures.

Spectroscopic deconvolution served as a tool to further support these findings and was performed as illustrated by the representative reference spectra in Figure 4.6, as well as by the spectroscopic deconvolution of the first four and the final Raman spectra obtained in the in-situ

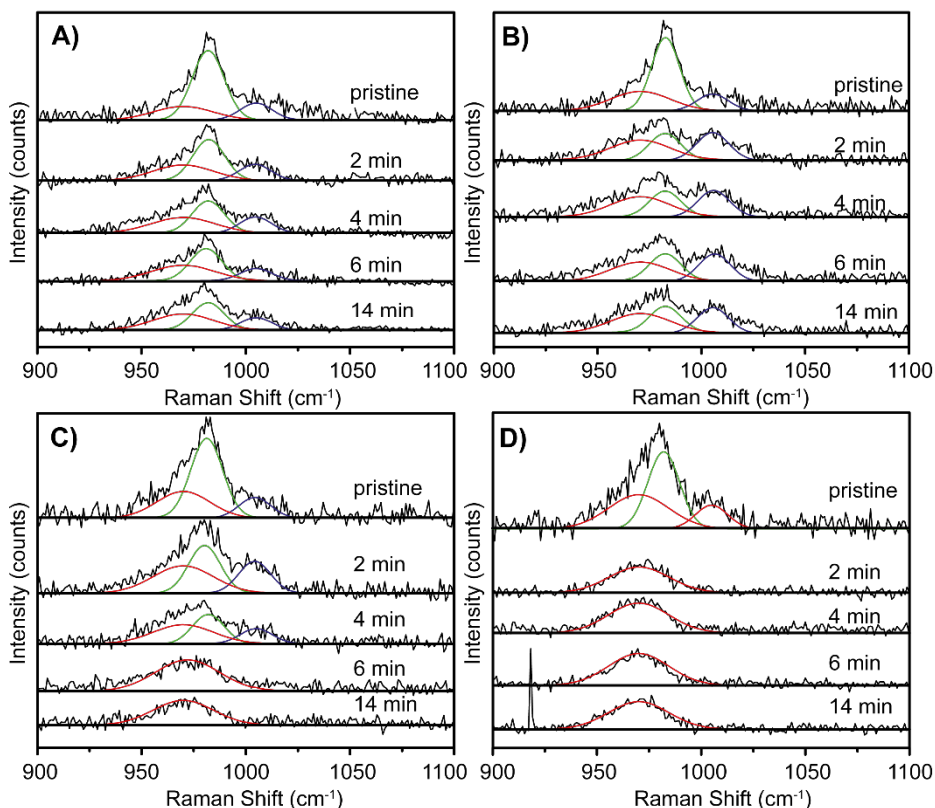


**Figure 4.7.** Results of the spectroscopic deconvolution of the Raman experiments performed with CO at respectively **A)** 250 °C, **B)** 300 °C, **C)** 350 °C and **D)** 400 °C. The results of the Deconvoluted Raman spectra for the first 6 min of the reaction as well as the last Raman spectrum of the reaction are shown for the sake of brevity. The deconvolution parameters of the bands were kept consistent throughout the different experiments.

Raman experiments, as illustrated in Figure 4.7, Figure 4.8, and Figure 4.9 for the experiments with respectively CO, H<sub>2</sub>, and C<sub>2</sub>H<sub>4</sub>. In all experiments the locations and the Half Widths at Half Maximum (HWHMs) were kept constant with values of 9 cm<sup>-1</sup> for the fitted bands at 983 cm<sup>-1</sup> and 1005 cm<sup>-1</sup>, and a HWHM of 17 cm<sup>-1</sup> for the SiO<sub>2</sub> band at 973 cm<sup>-1</sup>. The exact band locations and their corresponding HWHMs for all experiments can be found in Table B3. Furthermore, the developments of the normalized intensities of the 985 cm<sup>-1</sup> and the 1005 cm<sup>-1</sup> bands are illustrated in Figure 4.10, illustrating the reaction progress.

In any case, quantitative reduction was confirmed by the disappearing 983 cm<sup>-1</sup> fitted band as well as the disappearing 1005 cm<sup>-1</sup> band until neither could be fitted anymore, which is further emphasized by the consistent HWHM of the remaining Si-OH band at 973 cm<sup>-1</sup>. This is the case for the Cr/SiO<sub>2</sub> materials that were reduced with either CO or H<sub>2</sub> at temperatures of 350 and 400

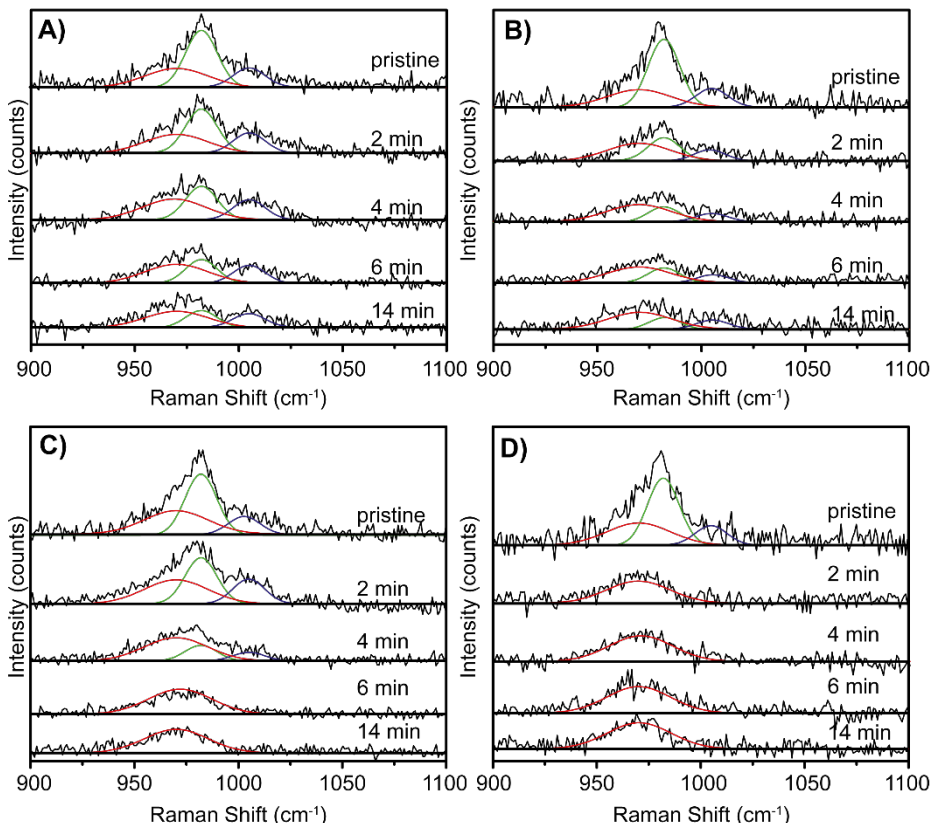


**Figure 4.8.** Results of the spectroscopic deconvolution of the Raman experiments performed with H<sub>2</sub> at respectively A) 250 °C, B) 300 °C, C) 350 °C and D) 400 °C. The results of the Deconvoluted Raman spectra for the first 6 min of the reaction as well as the last Raman spectrum of the reaction are shown for the sake of brevity. The deconvolution parameters of the bands were kept consistent throughout the different experiments.

°C, as is clear from Figures 4.7A and 4.7B for the former reducing gas and Figures 4.8A and 4.8B for the latter reducing gas. This is further testified by the straight lines in Figures 4.10A and 4.10B for the reactions with CO and Figures 4.10C and 4.10D for the reactions with H<sub>2</sub>. Interestingly, both reducing gases produced the final end-point spectrum already after 6 min at 350 °C and after 2 min at 400 °C, suggesting that their performances at these temperatures are very similar and that reduction occurs rapidly.

On the other hand, the reactions at 250 °C and 300 °C with either CO or H<sub>2</sub> do portray differences in the deepness of reduction. At these lower temperatures, H<sub>2</sub> outperforms CO as the reducing gas, testified by relatively lower ratios of the bands at 983 cm<sup>-1</sup> (Figure 4.7A and 4.8A) and 1005 cm<sup>-1</sup> (Figure 4.7B and 4.8B) compared to the support band at 973 cm<sup>-1</sup>. Quite interestingly, the 1005 cm<sup>-1</sup> signal appears to increase during the initial minutes of the reaction,

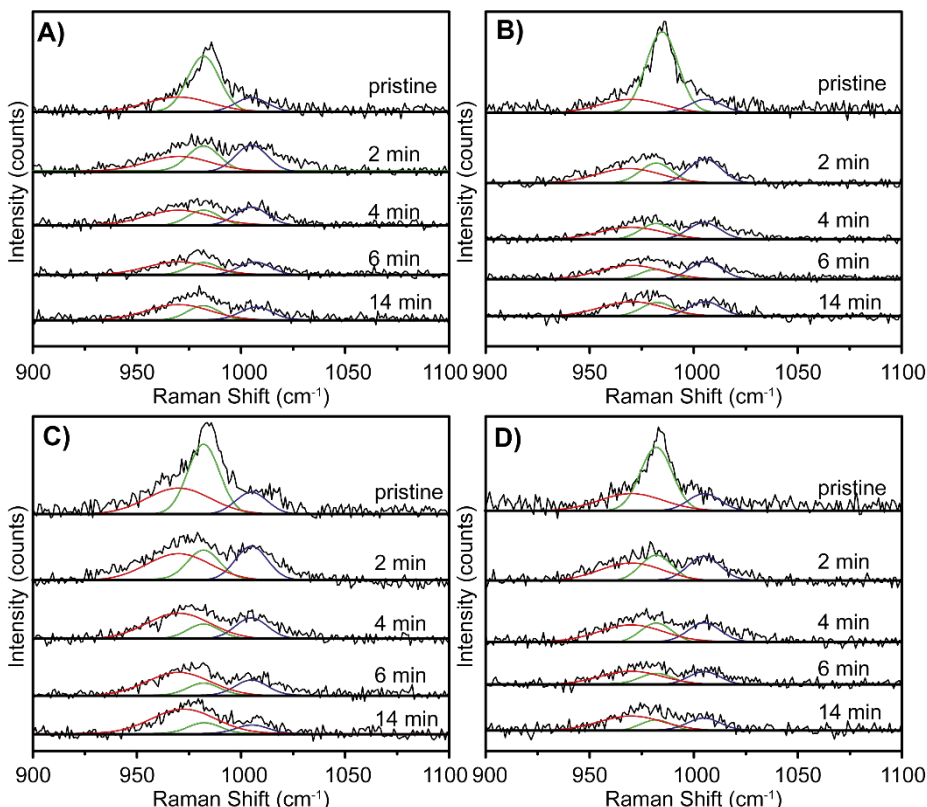


**Figure 4.9.** Results of the spectroscopic deconvolution of the experiments performed with C<sub>2</sub>H<sub>4</sub> at respectively **A)** 90 °C, **B)** 110 °C, **C)** 130 °C and **D)** 150 °C. The results of the Deconvoluted Raman spectra for the first 6 min of the reaction as well as the last Raman spectrum of the reaction are shown for the sake of brevity. The deconvolution parameters of the bands were kept consistent throughout the different experiments.

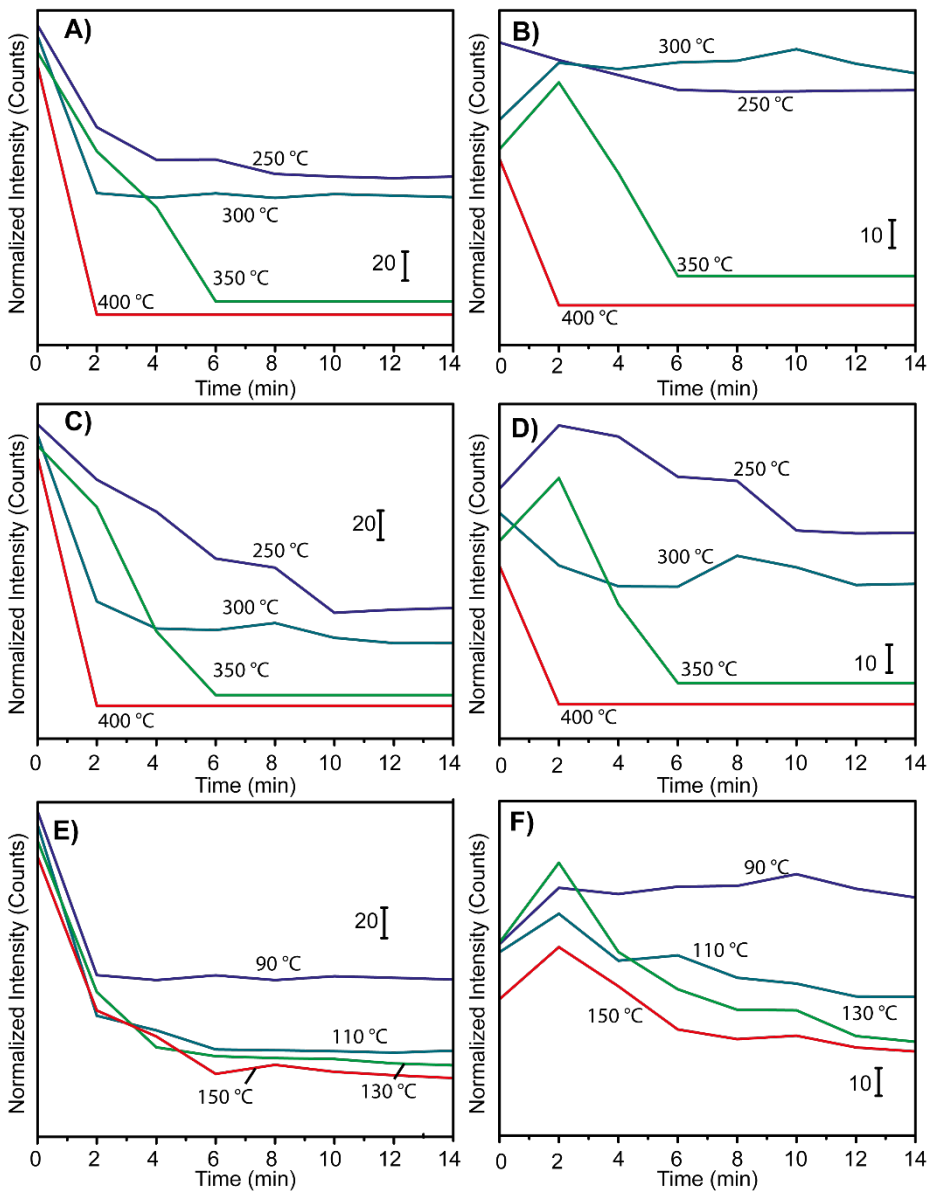


**Figure 4.10.** Developments of the intensities of the deconvoluted bands as a function of time at the used reduction temperatures for the **A**)  $983\text{ cm}^{-1}$  and **B**)  $1005\text{ cm}^{-1}$  band with CO, **C**) the  $983\text{ cm}^{-1}$  and **D**)  $1005\text{ cm}^{-1}$  band with  $\text{H}_2$ , and the **E**)  $983\text{ cm}^{-1}$  and **F**)  $1005\text{ cm}^{-1}$  band with  $\text{C}_2\text{H}_4$ . The lines are slightly off set for the sake of clarity. The bands were fitted according to the description in Figure 4.6.

after which it remains constant if CO is used (Figure 4.10A and Figure 4.10B), while it decreases slightly if H<sub>2</sub> is used (Figure 4.10C and Figure 4.10D). It is highly unlikely that this initial increase is related to the structures related to the 983 cm<sup>-1</sup> signal being converted and the intermediate structures, that now possibly possess mono-oxo character, contribute to the 1005 cm<sup>-1</sup> signal. The unlikeliness for this comes from the fact that the electronic structure of these intermediates is different from the electronic structure of the Cr<sup>6+</sup><sub>mono-oxo</sub> structures with the overall intensity of the Raman signals related to reduced Cr species overall being less intense. Conclusively, this confirms that the initial increase of the 1005 cm<sup>-1</sup> signal is caused by a decreasing contribution of the baseline.

With respect to C<sub>2</sub>H<sub>4</sub>, Figure 4.9 clearly confirms that in all instances partially reduced catalyst systems are produced with the possibility to always fit bands at 983 cm<sup>-1</sup> and 1005 cm<sup>-1</sup>. This confirms that at 1 atm of C<sub>2</sub>H<sub>4</sub> a part of the Cr surface sites remains unaltered. Interestingly, Figure 4.9 infers that reduction of the structures related to the 983 cm<sup>-1</sup> Raman signal is more pronounced than reduction of the structures related to the 1005 cm<sup>-1</sup> Raman signal. However, it is likely that the 1005 cm<sup>-1</sup> related band is slightly underestimated in the pristine material due to the increasing baseline. The effect of the decreasing baseline is which is evidenced by the initial increase of the 1005 cm<sup>-1</sup> signal in Figure 4.10F followed by the decrease until it stabilizes. Yet, the 1005 cm<sup>-1</sup> Raman signal remains relatively constant, indicating that predominantly the 983 cm<sup>-1</sup> related structures react with C<sub>2</sub>H<sub>4</sub>, at least at 1 atm pressure.

Figures 4.9, 4.10E, and 4.10F do confirm that the temperature does affect the degree of reduction, with a reaction temperature of 90 °C resulting in less deep reduction than the higher temperatures. However, beyond the temperature of 90 °C equally, albeit partially, reduced spectra are obtained, suggesting that beyond this initial threshold the effect of the temperature becomes less significant. With respect to end-point spectra, Figure 4.10 demonstrates that the final state of reduction with C<sub>2</sub>H<sub>4</sub> is already attained after 6 min into the reaction regardless of the used temperature, standing in contrast to the often long and variable induction period.

#### 4.2.3. <sup>18</sup>O<sub>2</sub> Isotopically Labeled Reduction-Oxidation Experiments

In addition to the previously discussed reduction experiments to assess the redox behavior of a Cr/SiO<sub>2</sub> Phillips catalyst, we have performed CO/<sup>18</sup>O<sub>2</sub> isotopically labeled reduction/re-oxidation experiments to further disentangle the contribution of the various Cr<sup>6+</sup> surface structures. Similar experiments by Weckhuysen *et al.* demonstrated that these types of experiments are a proficient tool to discriminate between the various surface structures over 6 wt% CrO<sub>x</sub> catalysts supported on various oxide supports, such as ZrO<sub>2</sub>.<sup>[78]</sup>

The outcomes of these experiments are shown in Figure 4.11. In this experiment the reduction was performed with CO at 400 °C, since at this temperature the catalyst material was quantitatively reduced and the reduction by-products readily desorb from the catalyst surface

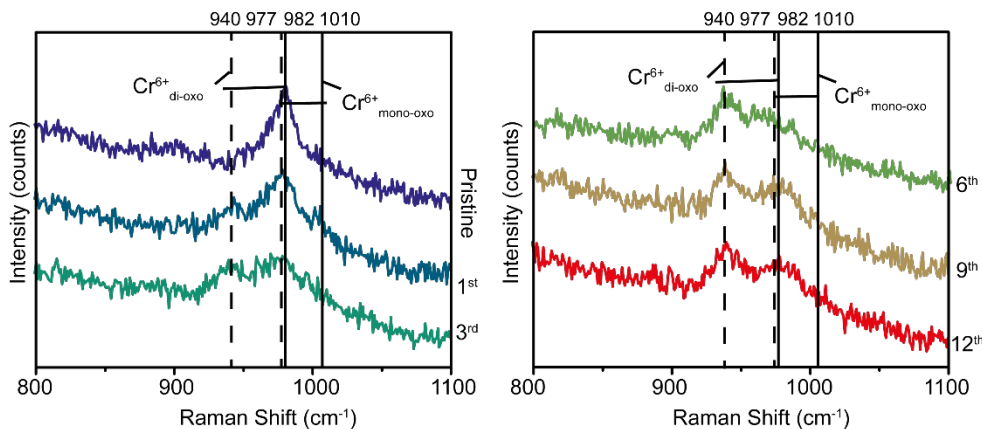


**Figure 4.11.** Raman spectra for the  $^{18}\text{O}$  isotopically labeled reduction/oxidation experiments at 400 °C. The reduction experiments were performed in 5 mL CO / 20 mL Ar and the re-oxidation experiments were performed in 5 mL  $^{18}\text{O}_2$  / 20 mL Ar.

without potential detrimental effects for the surface structures. Figure 4.11 shows that the final spectra was already attained after 6 reduction/re-oxidation cycles, which is significantly faster than reported for the other supports.<sup>[78]</sup> This further corroborates that reduction with CO is clean, producing exposed  $\text{Cr}^{2+}$  surface structures that instantaneously react with  $^{18}\text{O}_2$  to produce the re-oxidized  $\text{Cr}^{6+}/\text{SiO}_2$  catalyst again.

These results further strengthen the fact that the 983  $\text{cm}^{-1}$  Raman signal and 1005  $\text{cm}^{-1}$  Raman signal belong to different surface structures, since the two signals develop independently in these experiments. The 983  $\text{cm}^{-1}$  Raman signal is observed at a Raman shift of 940  $\text{cm}^{-1}$  and the 1005  $\text{cm}^{-1}$  Raman signal is now superimposed on the 975  $\text{cm}^{-1}$  Si-OH Raman signal. The shifts of the Raman signals are consistent with the theoretical isotopic shift of  $\sim 40 \text{ cm}^{-1}$ .

Figure 4.11 does not illustrate isotopically mixed moieties since if isotopically mixed  $\text{Cr}=\text{O}$  moieties were formed  $\text{Cr}^{6+}_{\text{di-oxo}}$  surface structures would give rise to three signals ( $^{16}\text{O}=\text{Cr}=\text{O}^{18}$ ,  $^{16}\text{O}=\text{Cr}=\text{O}^{16}$ , and  $^{18}\text{O}=\text{Cr}=\text{O}^{18}$ ) and  $\text{Cr}^{6+}_{\text{mono-oxo}}$  would give rise to two signals ( $^{18}\text{O}=\text{Cr}$  and  $^{16}\text{O}=\text{Cr}$ ). However, if taking isotopically exchanged  $\text{Cr}^{6+}_{\text{di-oxo}}$  surface structures as an example, which are related to the 940  $\text{cm}^{-1}$  signal, it might be that partially isotopically exchanged  $\text{Cr}^{6+}_{\text{di-oxo}}$  moieties do exist, but their existence is shrouded by overlap with other Raman signals as well as the sub-optimal S/N ratios. In conclusion it is clear that the isotopically exchanged  $\text{Cr}^{6+}$  sites match the earlier findings of Weckhuysen *et al.* and Wachs *et al.* in line with the existence of  $\text{Cr}^{6+}_{\text{di-oxo}}$  and  $\text{Cr}^{6+}_{\text{mono-oxo}}$  on this catalyst.<sup>[76,78,90]</sup>

## 4.3 Conclusions

This **Chapter** illustrates the usefulness of Raman spectroscopy in investigating inorganic catalyst systems, with the power of disentangling the reactivities of (potential) active sites towards various gases. The focus of this **Chapter** is on the reactivity of a Cr/SiO<sub>2</sub> Phillips catalyst with CO, H<sub>2</sub>, C<sub>2</sub>H<sub>4</sub>, as reducing gases and <sup>18</sup>O<sub>2</sub> as oxidizing gas at various temperatures.

The presented results confirm the existence of two types of surface structures, evidenced by the 983 cm<sup>-1</sup> and to the 1005 cm<sup>-1</sup> Raman signals, which are attributed to Cr surface structures possessing respectively a di-oxo and a mono-oxo character. Isotopically labeled CO/<sup>18</sup>O<sub>2</sub> reduction/re-oxidation experiments further confirmed the existence of these two surface sites, with experimental isotopic shifts corresponding to the expected theoretical values.

The experiments with CO or H<sub>2</sub> at various temperatures revealed the different sensitivities of the Cr surface sites to reduction, with the 985 cm<sup>-1</sup> related structures demonstrating easier reducibility at lower temperatures than the 1005 cm<sup>-1</sup> related structures. Furthermore, spectroscopic deconvolution revealed that H<sub>2</sub> is more proficient than CO at reducing the catalyst materials at these lower temperatures of 250 °C and 300 °C. However, higher temperatures produced fully reduced catalyst materials, regardless of the used reduction gas. We further pursued this research avenue by investigating the effect of C<sub>2</sub>H<sub>4</sub> at various temperatures, revealing that regardless of the temperature only partially reduced systems were produced, with the 985 cm<sup>-1</sup> related structures seemingly being easier reduced. Last but not least, the biggest increase of reducing efficiency was enabled by increasing the temperature from 90 to 110 °C, after which increasing the temperature apparently did not improve the reduction anymore.

## 4.4 Acknowledgements

The authors would like to thank J. Janssen (Utrecht University, UU), J. Wijten (UU), and P. Wijten (UU) for their help with developing the in-situ set-up.

## 4.5 Experimental Section

### 4.5.1 Sample Preparation

The catalyst samples were provided by SABIC Geleen, the Netherlands. It is a silica Cr-catalyst with a ~1.0wt% Cr loading, a surface area of 624 m<sup>2</sup>/g, a pore volume of 2.41 mL/g, and a d<sub>50</sub> particle size distribution of 52.8 µm. The catalyst was calcined at 650 °C via a SABIC-proprietary technique to yield the active CrO<sub>x</sub>/SiO<sub>2</sub> catalyst.

#### 4.5.2 Raman Spectroscopy

The Raman spectroscopy experiments were performed in a Linkam FTIR-600 cell, modified with additional three-way gas valves for closing off from ambient atmosphere. Before each experiment, the cell was loaded in an N<sub>2</sub> glovebox (O<sub>2</sub> < 1.2 ppm, H<sub>2</sub>O < 0.3 ppm). After loading the reactor, it was transferred to the Horiba Xploraplus Raman Microscope, where it was attached to the gas-feed and the lines were flushed for 30 min with Ar (30 mL/min) before opening the cell towards the gas-feed. Hereafter the temperature of the cell could be set to a specific temperature with a defined temperature program of 10 °C/min for all the performed experiments. All the experiments were performed with the 50x objective, a 638 nm laser, with a grating of 1800 mm<sup>-1</sup>, a hole size of 300 µm, a slit size of 100 µm, and a laser power varying between 10-50%, depending on the spectral quality. For the in-situ Raman spectroscopy experiments, a spot central on the catalyst surface was selected. For the measurements of the maps, a 12x12 µm grid was selected, containing 81 different points, with 1.5 µm spacing, at which spectra were recorded. For all experiments, the gas-feed compositions were as follows: H<sub>2</sub>/Ar (5 mL/40 mL), CO/Ar(5 mL/40 mL), and C<sub>2</sub>H<sub>4</sub>/Ar (20 mL / 20 mL). For H<sub>2</sub> and CO the temperatures at which the reductions were performed were 250, 300, 350, and 400 °C and the temperatures at which the reductions with C<sub>2</sub>H<sub>4</sub> were performed were 90, 110, 130, and 150 °C. After finding the areas for the map measurements and the spot for the in-situ spectroscopy measurement, one map of 81 data points was recorded. Hereafter, the reduction was started with the pre-set gas-flows and a spectral interval of 1.5 min per spectrum. For H<sub>2</sub> and CO this process was followed for 1 h and for C<sub>2</sub>H<sub>4</sub> we followed the reduction for 2 h. Hereafter, the cell was flushed with Argon for 5 min before measuring a map of 81 data points again at the previous location.

### 4.6 References

- [1] PlasticsEurope, Plastics - The Facts 2020 An analysis of European plastics, production, demand and waste data, **2020**, 1-64.
- [2] R. Geyer, J. Jambeck, K. Law, *Sci. Adv.* **2017**, 3, 25–29.
- [3] R. Mülhaupt, *Macromol. Chem. Phys.* **2013**, 214, 159–174.
- [4] *Advances in Polymer Science*, Vol. 257 (Ed.: W. Kaminsky), Springer, Berlin, **2013**, pp. 1-256
- [5] H. H. Brintzinger, D. Fischer, R. Mülhaupt, B. Rieger, R. M. Waymouth, *Angew. Chem. Int. Ed. English* **1995**, 34, 1143–1170.
- [6] J. P. Hogan, R. L. Banks, *US Pat*, 2825621, **1958**.
- [7] J. P. Hogan, R. L. Banks, *US Pat*, 2951816, **1960**.
- [8] M. P. McDaniel, *Adv. Catal.* **2010**, 53, 123-606.
- [9] R. Cheng, Z. Liu, X. He, P. Qui, M. Terano, M. S. Eisen, S. L. Scott, B. Liu, *Adv. Polym. Sci.* **2013**, 257, 135–202.
- [10] A. Zecchina, E. Groppo, C. Lamberti, S. Bordiga, G. Spoto, *Chem. Rev.* **2005**, 105, 115–184.

- [11] B. M. Weckhuysen, I. E. Wachs, R. A. Schoonheydt, *Chem. Rev.* **1996**, *96*, 3327–3349.
- [12] E. Groppo, G. A. Martino, A. Piovano, C. Barzan, *ACS Catal.* **2018**, *8*, 10846–10863.
- [13] M. P. McDaniel, *A Review of the Phillips Chromium Catalyst for Ethylene Polymerization in Handbook of Transition Metal Polymerization Catalysts*, 2<sup>nd</sup> ed (Ed.: R. Hoff), John Wiley & Sons, Inc., Hoboken, **2018**
- [14] M. P. McDaniel, *Adv. Catal.* **1985**, *33*, 47–98.
- [15] M. McDaniel, *MRS Bull.* **2013**, *38*, 234–238.
- [16] C. Barzan, A. Piovano, L. Braglia, G. A. Martino, C. Lamberti, S. Bordiga, E. Groppo, *J. Am. Chem. Soc.* **2017**, *139*, 17064–17073.
- [17] D. Cicmil, J. Meeuwissen, A. Vantomme, J. Wang, I. K. Van Ravenhorst, H. E. Van Der Bij, A. Muñoz-Murillo, B. M. Weckhuysen, *Angew. Chem. Int. Ed.* **2015**, *54*, 13073–13079.
- [18] Y. Zeng, P. Chammingskwan, R. Baba, T. Taniike, M. Terano, *Macromol. React. Eng.* **2017**, *11*, 1600046–1600051.
- [19] D. Cicmil, I. K. Van Ravenhorst, J. Meeuwissen, A. Vantomme, B. M. Weckhuysen, *Catal. Sci. Technol.* **2016**, *6*, 731–743.
- [20] D. Cicmil, J. Meeuwissen, A. Vantomme, B. M. Weckhuysen, *ChemCatChem* **2016**, *8*, 1937–1944.
- [21] M. K. Jongkind, T. van Kessel, M. E. Z. Velthoen, N. Friederichs, B. M. Weckhuysen, *ChemPhysChem* **2020**, *21*, 1665–1674.
- [22] M. K. Jongkind, F. Meirer, K. W. Bossers, I. C. ten Have, H. Ohldag, B. Watts, T. van Kessel, N. Friederichs, B. M. Weckhuysen, *Chem. Eur. J.* **2021**, *27*, 1688–1699.
- [23] W. Xia, B. Liu, Y. Fang, K. Hasebe, M. Terano, *J. Mol. Catal. A Chem.* **2006**, *256*, 301–308.
- [24] O. M. Bade, R. Blom, M. Ystenes, *J. Mol. Catal. A Chem.* **1998**, *135*, 163–179.
- [25] Z. Qin-Hui, Y. Fang, X. Wei, L. Chenguang, *Pet. Sci.* **2013**, *10*, 577–582.
- [26] G. A. Martino, A. Piovano, C. Barzan, J. Rabieah, G. Agostini, A. Bruekner, G. Leone, G. Zanchin, T. Monoi, E. Groppo, *ACS Catal.* **2020**, *10*, 2694–2706.
- [27] C. Barzan, A. Piovano, M. Botavina, G. A. Martino, G. Agostini, G. Martra, E. Groppo, *J. Catal.* **2019**, *373*, 173–179.
- [28] C. Barzan, S. Bordiga, E. Groppo, *ACS Catal.* **2016**, *6*, 2918–2922.
- [29] A. Zecchina, E. Garrone, C. Morterra, S. Coluccia, *J. Phys. Chem.* **1975**, *79*, 978–983.
- [30] E. Groppo, C. Lamberti, F. Cesano, A. Zecchina, *Phys. Chem. Chem. Phys.* **2006**, *8*, 2453–2456.
- [31] A. Damin, F. Bonino, S. Bordiga, E. Groppo, C. Lamberti, A. Zecchina, *ChemPhysChem* **2006**, *7*, 342–344.
- [32] E. Groppo, C. Lamberti, S. Bordiga, G. Spoto, A. Zecchina, *J. Catal.* **2006**, *240*, 172–181.
- [33] N. M. Peek, D. B. Jeffcoat, C. Moisii, L. Van De Burgt, S. Profeta, S. L. Scott, A. E. Stiegman, *J. Phys. Chem. C* **2018**, *122*, 4349–4358.
- [34] C. Brown, A. Lita, Y. Tao, N. Peek, M. Crosswhite, M. Mileham, J. Krzystek, R. Achey, R. Fu, J. K. Bindra, M. Polinski, Y. Wang, L. J. van de Burgt, D. Jeffcoat, S. Profeta, Jr., A. E. Stiegman, S. L. Scott, *ACS Catal.* **2017**, *7*, 7442–7455.
- [35] A. Fong, C. Vandervelden, S. L. Scott, B. Peters, *ACS Catal.* **2018**, *8*, 1728–1733.
- [36] L. Zhong, M. Y. Lee, Z. Liu, Y. J. Wanglee, B. Liu, S. L. Scott, *J. Catal.* **2012**, *293*, 1–12.
- [37] J. Joseph, K. C. Potter, M. J. Wulfers, E. Schwerdtfeger, M. P. McDaniel, F. C. Jentoft, *J. Catal.* **2019**, *377*, 550–564.

- [38] K. C. Potter, C. W. Beckerle, F. C. Jentoft, E. Schwerdtfeger, M. P. McDaniel, *J. Catal.* **2016**, *344*, 657–668.
- [39] R. Ramachandra Rao, B. M. Weckhuysen, R. A. Schoonheydt, *Chem. Commun.* **1999**, 445–446.
- [40] B. M. Weckhuysen, L. M. De Ridder, P. J. Grobet, R. A. Schoonheydt, *J. Phys. Chem.* **1995**, *99*, 320–326.
- [41] B. M. Weckhuysen, A. A. Verberckmoes, A. L. Buttiens, R. A. Schoonheydt, *J. Phys. Chem.* **1994**, *98*, 579–584.
- [42] B. M. Weckhuysen, L. M. De Ridder, R. A. Schoonheydt, *J. Phys. Chem.* **1993**, *97*, 4756–4763.
- [43] B. M. Weckhuysen, R. A. Schoonheydt, J.-M. Jehng, I. E. Wachs, S. J. Cho, R. Ryoo, S. Kijlstra, E. Poels, *J. Chem. Soc. Faraday Trans.* **1994**, *91*, 3245–3253.
- [44] P. C. Thüne, C. P. J. Verhagen, M. J. G. van den Boer, J. W. Niemantsverdriet, *J. Phys. Chem. B* **2002**, *101*, 8559–8563.
- [45] E. M. E. Van Kimmenade, A. E. T. Kuiper, Y. Tamminga, P. C. Thüne, J. W. Niemantsverdriet, *J. Catal.* **2004**, *223*, 134–141.
- [46] C. Copéret, F. Allouche, K. W. Chan, M. P. Conley, M. F. Delley, A. Fedorov, I. B. Moroz, V. Mougel, M. Pucino, K. Searles, K. Yamamoto, P. A. Zhizko., *Angew. Chem. Int. Ed.* **2018**, *57*, 6398–6440.
- [47] M. F. Delley, C. S. Praveen, A. P. Borosy, F. Núñez-Zarur, A. Comas-Vives, C. Copéret, *J. Catal.* **2017**, *354*, 223–230.
- [48] L. Floryan, A. P. Borosy, F. Núñez-Zarur, A. Comas-Vives, C. Copéret, *J. Catal.* **2017**, *346*, 50–56.
- [49] C. Copéret, *Acc. Chem. Res.* **2019**, *52*, 1697–1708.
- [50] M. F. Delley, G. Lapadula, F. Núñez-Zarur, A. Comas-Vives, V. Kalendra, G. Jeschke, D. Baabe, M. D. Walter, A. J. Rossini, A. Lesage, L. Emsley, O. Maury, C. Copéret, *J. Am. Chem. Soc.* **2017**, *139*, 8855–8867.
- [51] M. P. Conley, M. F. Delley, G. Siddiqi, G. Lapadula, S. Norsic, V. Monteil, O. V. Safanova, C. Copéret, *Angew. Chem. Int. Ed.* **2014**, *53*, 1872–1876.
- [52] B. M. Weckhuysen, R. A. Schoonheydt, *Catal. Today* **1999**, *49*, 441–451.
- [53] M. F. Delley, M. P. Conley, C. Copéret, *Catal. Lett.* **2014**, *144*, 805–808.
- [54] B. M. Weckhuysen, R. A. Schoonheydt, *Catal. Today* **1999**, *51*, 223–232.
- [55] A. Poater, X. Solans-Monfort, E. Clot, C. Copéret, O. Eisenstein, *J. Chem. Soc. Dalton Trans.* **2006**, 3077–3087.
- [56] G. A. Martino, C. Barzan, A. Piovano, A. Budnyk, E. Groppo, *J. Catal.* **2018**, *357*, 206–212.
- [57] G. A. Martino, A. Piovano, C. Barzan, S. Bordiga, E. Groppo, *Top. Catal.* **2018**, *61*, 1465–1473.
- [58] C. A. Cruz, M. M. Monwar, J. Barr, M. P. McDaniel, *Macromolecules* **2019**, *52*, 5750–5760.
- [59] P. J. Deslauriers, C. Tso, Y. Yu, D. L. Rohlffing, M. P. McDaniel, *Appl. Catal. A Gen.* **2010**, *388*, 102–112.
- [60] K. Tonosaki, T. Taniike, M. Terano, *J. Mol. Catal. A Chem.* **2011**, *340*, 33–38.
- [61] P. J. Deslauriers, D. C. Rohlffing, *Macromol. Symp.* **2009**, *282*, 136–149.
- [62] P. J. DesLauriers, M. P. McDaniel, *J. Polym. Sci. Part A Polym. Chem.* **2007**, *45*, 3135–3149.
- [63] M. P. McDaniel, M. M. Johnson, *Macromolecules* **1987**, *20*, 773–778.
- [64] *Multimodal Polymers with Supported Catalysts: Design and Production*, 1<sup>st</sup> ed. (Ed.: A. R. Albunia, F. Prades, D. Jeremic), Springer Nature, Cham, **2019**, pp. 1–276

- [65] M. P. McDaniel, D. C. Rohlfing, E. A. Benham, *Polym. React. Eng.* **2003**, *11*, 101–132.
- [66] M. P. McDaniel, K. S. Collins, *J. Polym. Sci. Part A Polym. Chem.* **2009**, *47*, 845–865.
- [67] M. P. McDaniel, *J. Catal.* **2009**, *261*, 34–49.
- [68] M. P. McDaniel, *ACS Catal.* **2011**, *1*, 1394–1407.
- [69] R. Merryfield, M. McDaniel, G. Parks, *J. Catal.* **1982**, *77*, 348–359.
- [70] G. Ghiotti, E. Garrone, A. Zecchina, *J. Mol. Catal.* **1991**, *65*, 73–83.
- [71] D. Scarano, G. Spoto, S. Bordiga, L. Carnelli, G. Ricchiardi, A. Zecchina, *Langmuir* **1994**, *10*, 3094–3104.
- [72] A. Zecchina, E. Garrone, G. Ghiotti, S. Coluccia, *J. Phys. Chem.* **1975**, *79*, 972–978.
- [73] A. Bensalem, B. M. Weckhuysen, R. A. Schoonheydt, *J. Phys. Chem. B* **1997**, *101*, 2824–2829.
- [74] B. M. Weckhuysen, I. E. Wachs, *J. Chem. Soc. Faraday Trans.* **1996**, *92*, 1969–1973.
- [75] R. L. Puurunen, B. G. Beheydt, B. M. Weckhuysen, *J. Catal.* **2001**, *204*, 253–257.
- [76] B. M. Weckhuysen, I. E. Wachs, *J. Phys. Chem.* **1996**, *100*, 14437–14442.
- [77] A. Bensalem, B. M. Weckhuysen, R. A. Schoonheydt, *J. Chem. Soc. Faraday Trans.* **1997**, *93*, 4065–4069.
- [78] B. M. Weckhuysen, I. E. Wachs, *J. Phys. Chem. B* **1997**, *101*, 2793–2796.
- [79] A. Chakrabarti, I. E. Wachs, *Catal. Lett.* **2014**, *145*, 985–994.
- [80] A. Chakrabarti, M. Gierada, J. Handzlik, I. E. Wachs, *Top. Catal.* **2016**, *59*, 725–739.
- [81] Y. T. Chua, P. C. Stair, I. E. Wachs, *J. Phys. Chem. B* **2001**, *105*, 8600–8606.
- [82] D. S. Kim, I. E. Wachs, *J. Catal.* **1993**, *142*, 166–171.
- [83] T. J. Dines, S. Inglis, *Phys. Chem. Chem. Phys.* **2003**, *5*, 1320–1328.
- [84] V. S. Sullivan, S. D. Jackson, P. C. Stair, *J. Phys. Chem. B* **2005**, *109*, 352–356.
- [85] B. Grzybowska, J. Śloczyński, R. Grabowski, K. Wcisło, A. Kozłowska, J. Stoch, J. Zieliński, *J. Catal.* **1998**, *178*, 687–700.
- [86] M. A. Vuurman, I. E. Wachs, D. J. Stufkens, A. Oskam, *J. Mol. Catal.* **1993**, *80*, 209–227.
- [87] M. A. Vuurman, D. J. Stufkens, A. Oskam, J. A. Moulijn, F. Kapteijn, *J. Mol. Catal.* **1990**, *60*, 83–98.
- [88] E. Groppo, A. Damin, F. Bonino, A. Zecchina, S. Bordiga, C. Lamberti, *Chem. Mater.* **2005**, *17*, 2019–2027.
- [89] E. L. Lee, I. E. Wachs, *J. Phys. Chem. C* **2007**, *111*, 14410–14425.
- [90] E. L. Lee, I. E. Wachs, *J. Phys. Chem. B* **2008**, *112*, 6487–6498.
- [91] B. M. Weckhuysen, A. A. Verberckmoes, A. R. De Baets, R. A. Schoonheydt, *J. Catal.* **1997**, *166*, 160–171.





## Chapter 5

# Influence of Pore Structure and Metal-Node Geometry on the Polymerization of Ethylene over Cr-Based Metal Organic Frameworks

### Abstract

Metal-Organic Frameworks (MOFs) have received increasing interest as solid single-site catalysts, owing to their tunable pore architecture and metal node geometry. The ability to exploit these modulators makes them prominent candidates for producing polyethylene materials with narrow dispersity index ( $\mathcal{D}$ ) values. In this **Chapter** we present a study in which we systematically investigated the ethylene polymerization properties, with Et<sub>2</sub>AlCl as the activator, of three renowned Cr-based MOFs: MIL-101(Cr)-NDC (NDC = 2,6-dicarboxynaphthalene), MIL-53(Cr), and HKUST-1(Cr). Ethylene polymerization reactions revealed varying catalytic activities, with MIL-101(Cr)-NDC and MIL-53(Cr) being significantly more active than HKUST-1(Cr). Analysis of the PE products revealed large  $\mathcal{D}$  values, demonstrating that ethylene polymerization occurs over a multitude of active Cr centers rather than a singular type of Cr site. Spectroscopic experiments, in the form of powder X-ray diffraction (pXRD), UV-Vis-NIR Diffuse Reflectance Spectroscopy (DRS), and CO Probe Molecule Fourier Transform (FTIR) corroborated these findings, indicating that indeed to each MOF unique active sites are generated, however without alteration of the original oxidation state. Furthermore, the pXRD experiments indicated that one major prerequisite for catalytic activity was the degree of MOF activation by the Et<sub>2</sub>AlCl co-catalyst.

*This Chapter is based on:*

M. K. Jongkind, M. Rivera-Torrente, N. Nikolopoulos, B. M. Weckhuysen, *Chem. Eur. J.* **2021**, 27, 5769 – 5781.

## 5.1 Introduction

The production processes of plastics, of which polyethylene (PE) has the largest market volume share, stand as one of the most mature, sustainable, and efficient technologies relying on fossil and, more recently, renewable feedstocks. Despite increased attention to the environmental issues that plastics cause, the broad range of applications ensures that the production of PE will continue to grow in the coming years.<sup>[1]</sup> These factors continue to drive research towards improved production of PE, as well as towards finding new types of PE.

Nowadays, polyethylene production is centered around three catalytic workhorses, namely Ziegler-Natta, (post-) Metallocene catalysts, and Cr/SiO<sub>2</sub> Phillips type catalysts, each catalyst producing a variety of PEs in terms of Molecular Weight Distribution (MWD), Short-Chain, and, Long-Chain Branching (SCB and LCB).<sup>[2–6]</sup> In addition to selecting the proper catalyst, reaction conditions and reactor configurations can be exploited to enhance or suppress specific PE properties.<sup>[7–11]</sup> However, as mentioned before, the discovery and development of new catalysts keep driving worldwide research efforts.

Metal-Organic Frameworks (MOFs) are defined by a high degree of ordering in terms of pore size and pore structure, as well as the possibility to exploit a wide variety of metal-sites, tailoring their activity by rational design.<sup>[12–17]</sup> This has been elegantly exemplified by the linear correlation between catalytic CO<sub>2</sub> photoreduction, as a model reaction, and the electronic structure of the linker, showing that functional groups on the organic linker directly affect the reactivity.<sup>[15–20]</sup> This method is comparable to conventional strategies for heterogenous catalyst design, such as using dopants (promoters) or tuning the support,<sup>[3,21–26]</sup> but with the added value of a straightforward characterization and understanding of the material. The ability to change the pore structure, metal-node, and electronic structure with relative ease, makes MOFs increasingly prominent candidates for heterogenized single-site catalysis.<sup>[27–29]</sup> Until now, they have been used as such in numerous reactions, *e.g.* alkene oligomerization reactions<sup>[30–39]</sup> as well as (olefin) polymerization reactions.<sup>[30,37,40–48]</sup>

Dincă, Roman-Leshkov, and coworkers investigated the ethylene polymerization properties of MFU-41 (MFU = Metal-Organic Framework Ulm-University) MOFs.<sup>[41,45]</sup> The gas-phase ethylene polymerization properties of Cr<sup>3+</sup> ion-exchanged MFU-41 MOF material were investigated, revealing a polymerization MOF that produced PE with a Dispersity Index ( $\mathcal{D}$ ) of ~1.4, the  $\mathcal{D}$  being defined as the M<sub>w</sub>/M<sub>n</sub>, with the M<sub>w</sub> representing the weight averaged molecular weight of the polymer and the M<sub>n</sub> representing the number averaged molecular weight of the polymer. This indicates that active sites are similar in nature and is an excellent example of a Cr-based MOF acting as a heterogenized single-site ethylene polymerization catalyst. However, in the case of MOFs, forming true single-site catalysts depends strongly on the material structure and its evolution upon reaction with co-catalyst species; and it merits detailed studies on a *per case* basis. Previous work from our group compared the polymerization

properties of MIL-101(Cr) vs. MIL-100(Cr) and revealed that the type of linker is of paramount importance for the ability, or inability, of the MOF to fragment. Here, the ability of the MOF (MIL-101(Cr)) to fragment was correlated to the ability to polymerize ethylene, whereas the inability to fragment (MIL-100(Cr)) was related to predominantly  $\alpha$ -oligomerization and negligible polymerization activity.<sup>[35,43]</sup>

Despite all these advantages and already numerous applications, one should be cautious in using Cr-based catalysts due to their toxicity as well as related environmental hazards. Fortunately, this is of no concern in olefin polymerization, since state-of-the-art catalysts portray such high activities that noncorrosive and nontoxic catalyst residues can be safely left in the PE product material in sub-ppb levels.<sup>[49,50]</sup>

Because of an increasing interest in the application of MOFs in ethylene polymerization, we opted in this **Chapter** to investigate several well renowned Cr-based MOFs in this reaction, their structures demonstrated in Figure 5.1, specifically: MIL-101(Cr)-NDC (NDC = 2,6-dicarboxynaphthalene),<sup>[17,51–54]</sup> MIL-53(Cr),<sup>[55–57]</sup> and HKUST-1(Cr).<sup>[58]</sup> To establish structure-activity relationships, this selection of MOFs comprises a variety of pore sizes, 3D-structures, and metal-node geometries. We have investigated the fate of these materials when reacting with Et<sub>2</sub>AlCl to activate the MOF towards ethylene polymerization in the slurry-phase. Two different hydrocarbon solvents: heptane and toluene, were studied as reaction media. The molecular

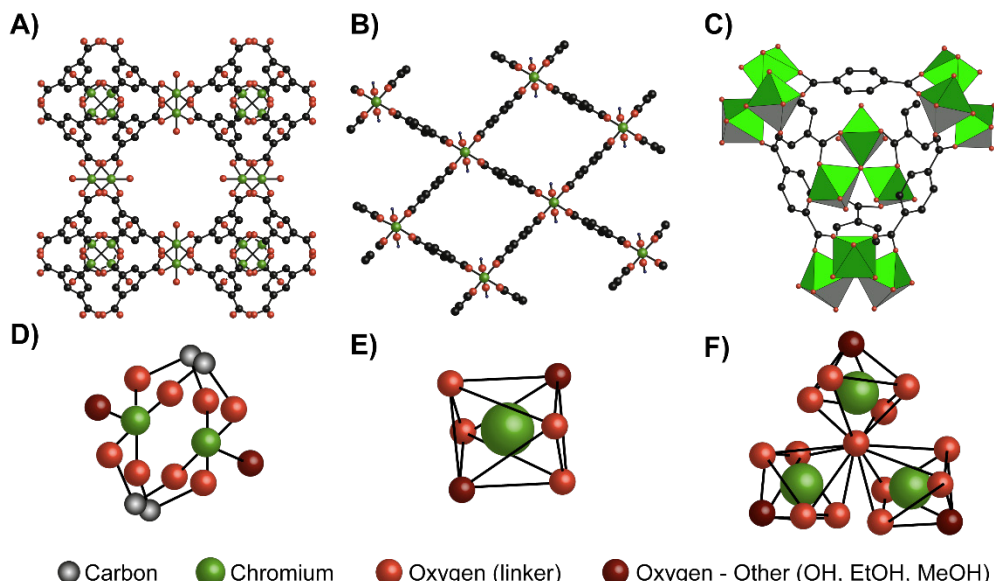


**Figure 5.1.** **A)** Overview of the HKUST-1(Cr) pore geometry and unit cell. **B)** Overview of the MIL-53(Cr) pore geometry and unit cell. **C)** Overview of the MIL-101(Cr) pore geometry and unit cell. **D)** Metal-node structure of HKUST-1(Cr). **E)** Metal-node structure of MIL-53(Cr). **F)** Metal-node structure of MIL-101(Cr).

architecture and morphology of the resulting polymers were respectively investigated with Gel Permeation Chromatography (GPC), Differential Scanning Calorimetry (DSC), and with Scanning Electron Microscopy (SEM). Moreover, we sought to understand the underlying mechanisms of how Et<sub>2</sub>AlCl activates the MOF in terms of crystallinity, surface area, Cr oxidation state, and surface site accessibility, using a broad array of tools including X-ray Diffraction (XRD), UV-Vis-NIR Diffuse Reflectance Spectroscopy (DRS), CO Probe Molecule Fourier Transform Infrared (FT-IR), N<sub>2</sub> Physisorption, Diffuse Reflectance Infrared Spectroscopy (DRIFTS) and Scanning Electron Microscopy (SEM).

## 5.2 Results and Discussion

The MOFs under investigation, MIL-101(Cr)-NDC,<sup>[51]</sup> MIL-53(Cr),<sup>[55]</sup> and HKUST-1(Cr)<sup>[58]</sup> were prepared in accordance to already reported procedures and their thermal stability was assessed with TGA, as reported in Figure 5.2.

### 5.2.1 Ethylene Polymerization Reactions

Table 5.1 shows the activity in ethylene polymerization of the different MOFs in both heptane and toluene as diluents. It is well known that the selected solvent can detrimentally affect ethylene polymerization/oligomerization properties, either due to coordination to the active site or decomposition of the active site.<sup>[59,60]</sup>

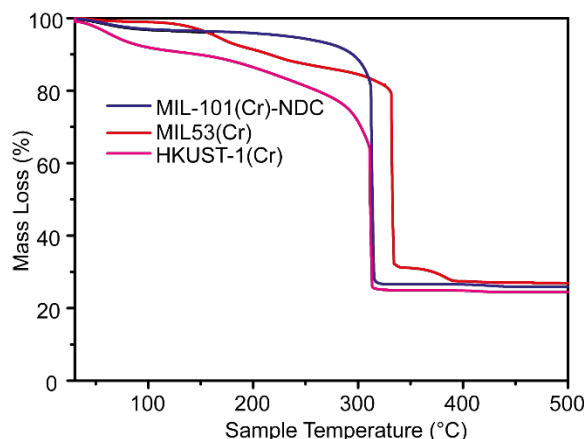


**Figure 5.2.** Thermogravimetric analysis of the thermal stability of the prepared Metal-Organic Frameworks (MOFs).

**Table 5.1.** Results of the ethylene polymerization reactions at 10 bar for the three Metal-Organic Frameworks (MOFs) under study.

MOF Activity ( $\text{kg}_{\text{PE}} \text{mol}_{\text{Cr}}^{-1} \text{h}^{-1} \text{bar}^{-1}$ )			
	MIL-101(Cr)-NDC	MIL-53(Cr)	HKUST-1(Cr)
Heptane	1.24	4.01	0.22
Filtrate <sup>a</sup>	0.08	1.19	0.089
%activity from leached Cr species	6.5	29.7	40.5
No Activator	<i>Inactive</i>	<i>Inactive</i>	<i>Inactive</i>
Toluene	0.87	0.39	0.11

*Reactions conditions unless specified otherwise: 10 bar  $\text{C}_2\text{H}_4$ ,  $T = 25^\circ\text{C}$ ,  $[\text{Cr}] = 5 \cdot 10^{-2} \text{ mmol}$  was used in 15 mL solvent with mol [Al]/[Cr] = 100 and  $\text{Et}_2\text{AlCl}$ . <sup>(a)</sup> A reaction mixture of the filtrate is produced by reacting  $[\text{Cr}] = 5 \cdot 10^{-2} \text{ mmol}$  MOF with 100 mol. eq.  $\text{Et}_2\text{AlCl}$  in 10 mL heptane. Then, the filtrate is collected, and the filter is washed twice with 2 mL heptane and once with 1 mL heptane, to add the leached Cr into the solution.*

All three MOF structures showed higher productivity in heptane, likely due to the absence of potential  $\text{Cr}^{3+}\text{-}\pi$  ring interactions which may be present when toluene is used.<sup>[59–61]</sup> The catalytic activities in Table 5.1 confirm that selection of the proper MOF precursor is of paramount importance and the topology plays a dominant role in polymerization activity. MIL-53(Cr) is the most active MOF, with an activity of  $4.01 \text{ kg}_{\text{PE}} \text{mol}_{\text{Cr}}^{-1} \text{h}^{-1} \text{bar}^{-1}$ , followed by MIL-101(Cr)-NDC with an activity of  $1.24 \text{ kg}_{\text{PE}} \text{mol}_{\text{Cr}}^{-1} \text{h}^{-1} \text{bar}^{-1}$ , and HKUST-1(Cr), exhibiting a poor activity of  $0.22 \text{ kg}_{\text{PE}} \text{mol}_{\text{Cr}}^{-1} \text{h}^{-1} \text{bar}^{-1}$ . Table 5.1 also clearly demonstrates the importance of selecting the proper reaction medium, since MIL-53(Cr) loses most of its activity upon switching to toluene. Similarly, HKUST-1(Cr) lost about 50% of its original activity and only MIL-101(Cr)-NDC appeared to be relatively unaffected by the change in the reaction medium, retaining about 75% of its original activity.

As already mentioned, current state-of-the-art polyolefin catalysts portray such activities that the catalyst residues can be harmlessly left in the PE material. The MOF residue percentages in the final PE products vary from 24wt% for HKUST-1(Cr) to 0.4wt% for MIL-53(Cr) in the here discussed polymerization reactions, which is not (yet) ideal. However, we were limited in terms of catalyst yields by the reaction vessel size. By simply increasing the reactor volume and

increasing the reaction time it is possible to increase the PE yield and lower related MOF contribution to the final product composition.

As shown in our previous efforts, Cr may partly leach from the MOFs into the solution.<sup>[43]</sup> Hence, to investigate the contribution of such species to polymer formation, the reactions were also performed after filtration of the MOFs after reaction with the co-catalyst, and labeled “Filtrate Reactions”. We found that for all the MOF topologies under study, residual activity was obtained from the liquid, indeed confirming that a certain fraction of polymer may be produced by species in solution instead of Cr sites on/in the MOF lattice. In the case of MIL-101(Cr)-NDC, an activity of  $0.08 \text{ kg}_{\text{PE}} \text{mol}_{\text{Cr}}^{-1} \text{h}^{-1} \text{bar}^{-1}$  is obtained, corresponding to 6.6% of its original activity, while the filtrates of MIL-53(Cr) and HKUST-(Cr) demonstrated higher activities with values of respectively 29.7% and 40.5%.

Inductively Coupled Plasma – Atomic Emission Spectroscopy (ICP-OES) was used to quantify the amount of Cr leached from the framework. These measurements revealed that for MIL-101(Cr)-NDC, MIL-53(Cr), and HKUST-1(Cr) respectively 1.02%, 4.96%, and 0.71% of the original Cr content leached into solution. However, these Cr species were responsible for a significant fraction of the polymer produced (6.5, 29.7, and 40.5%, respectively). This shows that although the MOF materials are relatively stable (<5% Cr leached) towards disintegration by the co-catalyst, the homogeneous compounds produced by the pre-treatment are very active in ethylene polymerization.

### 5.2.2 Polymer Analysis

The results of the Gel Permeation Chromatography (GPC) analysis on the PE materials are shown in Table 5.2, with the corresponding traces of the PE materials produced in the heterogeneous reactions being shown in Figure 5.3A and those produced in the homogeneous reactions demonstrated in Figure 5.3B.

The first observation is the broad MW curves in Figure 5.3, which coincidentally are also typical for high-density polyethylene materials produced by (ill-defined) Cr-based Phillips-type catalysts.<sup>[3,61]</sup> For instance, both MIL-101(Cr) and MIL-53(Cr) demonstrate a variety of peaks in their respective GPC curves. On the other hand, the MWD curve for HKUST-1(Cr) is a bit narrower, but still: multiple peaks are identifiable. These three curves gave rise to high  $\mathcal{D}$  values of 28.2, 16.9, and 9.8 for MIL-101(Cr)-NDC, MIL-53(Cr), and HKUST-1(Cr), respectively. While these results do reflect a narrowing MWD, they are still far from values usually observed for single-site catalysts, ultimately indicating the existence of a multitude of active sites on the MOFs, as was also the case for MIL-101(Cr).<sup>[43]</sup>

The GPC curves, and related  $\mathcal{D}$  values, are slightly different for the reactions performed with the filtrates. The traces of the PE obtained when using the Cr species filtered from MIL-101(Cr)-NDC and HKUST-1(Cr) are significantly skewed around  $\log \text{MW} \sim 6$ , suggesting that the number of

**Table 5.2.** Properties of the Polyethylene (PE) materials produced with the heterogeneous reactions and the filtrate reactions.

	$M_w^a$ (kDa)	$M_n^a$ (kDa)	$M_z^a$ (kDa)	$D$	$T_{m2}$ (°C) <sup>b</sup>	$X_{c2}$ (%) <sup>b</sup>
<b>Heterogeneous Reactions</b>						
MIL-101(Cr)-NDC	1100	39	3300	28.2	126.4	46.4
MIL-53(Cr)	759	45	3592	16.9	133.8	52.4
HKUST-1(Cr)	963	98	3466	9.8	133.8 (51.7) <sup>c</sup>	39.3
<b>Filtrate Reactions</b>						
MIL-101(Cr)-NDC	922	146	3077	6.3	134.5	49.1
MIL-53(Cr)	961	51	3467	18.8	134.2	57.0
HKUST-1(Cr)	1102	337	3026	3.2	134.3	48.1

<sup>a</sup>) Determined by GPC with PE and PP standards. <sup>b</sup>) Determined by the melting enthalpy calculated from DSC in comparison to  $\Delta H_m^0 = 293 \text{ J/g}$  for 100% crystalline UHMWPE. <sup>c</sup>This value is the crystallinity after correcting for the significant catalyst residue contribution in the final PE/HKUST-1(Cr) composition product.

active sites participating in polymer formation is smaller. This may be related to the Cr species in solution being Cr atoms with similar ligand coordination and no steric restrictions. Furthermore, and in contrast to the two other topologies, the  $D$  value obtained for the reaction performed with the filtrate of MIL-53(Cr) is very similar to that for the reaction performed with MIL-53(Cr) itself. Again, this finding shows that the number of Cr species generated from MIL-53(Cr) is larger than in the other two cases.

Additionally, the differences in polymer architecture are further manifested in the different crystallinities, shown in Table 5.2. The resulting PE materials demonstrate varying crystallinities: the lowest being that of the PE produced with HKUST-1(Cr) (39.3%) and the highest being that of MIL-53(Cr) (52.4%). Interestingly, the PEs produced in the filtrate reactions all demonstrate

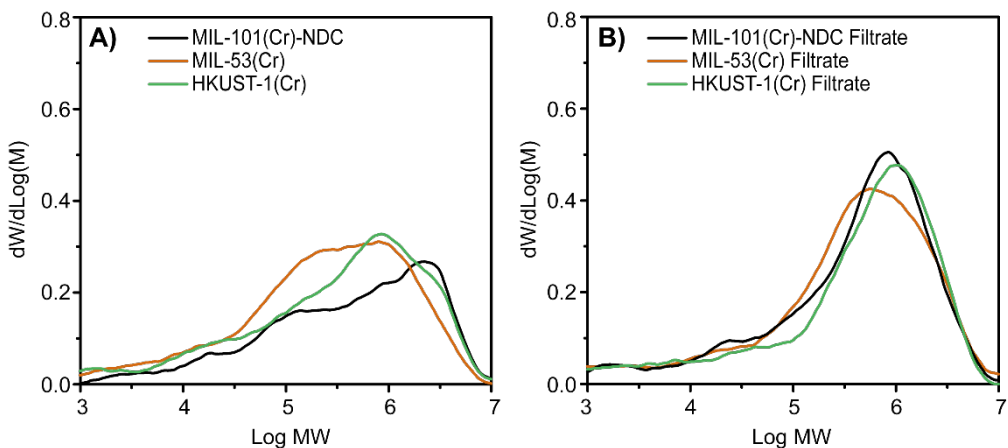


**Figure 5.3.** Gel Permeation Chromatography (GPC) traces of the polyethylene (PE) materials produced in the **A)** heterogeneous reactions and **B)** homogeneous reactions.

higher crystallinities than their heterogeneous counterparts. Perhaps the fact that the average increased  $M_n$  explains this, since this value infers an overall relative increase of average chain-length, which can be associated with the higher crystallinity of the materials. Take note that the calculated crystallinity of the PE/HKUST-1(Cr) material is underestimated due to the significant contribution of the HKUST-1(Cr) MOF residue. The likely PE crystallinity is higher and correcting for the MOF residue gives a value of 51.7%.

Conclusively, it is evident from Table 5.2 and Figure 5.3 that rational selection of the MOF is a valid strategy for exposing and/or attaining desirable PE properties.

### 5.2.3 Polyethylene Morphology

Naturally, the PE morphology is highly important for assessing post-reaction processability as well as preventing reactor fouling, often related to expensive reactor downtimes.<sup>[62]</sup> From an industrial point of view, “good” is considered spherical with narrow particle size distributions, which is directly related to high bulk density, controlled porosity, controlled internal composition, and high process flowability.<sup>[63,64]</sup>

Figure 5.4 shows the obtained PE materials obtained from the ethylene polymerization reactions with the MOFs and demonstrates that one can affect the final PE morphology by selecting the proper MOF polymerization template, at least under the here described reaction conditions.

First, Figure 5.4A shows that the PE produced by MIL-101(Cr)-NDC consists of spherical particles, where the inset shows sub-crystallites being tied together by PE molecules. This indicates that the MOF acts as a self-sacrificial template and disintegrates due to the increasing

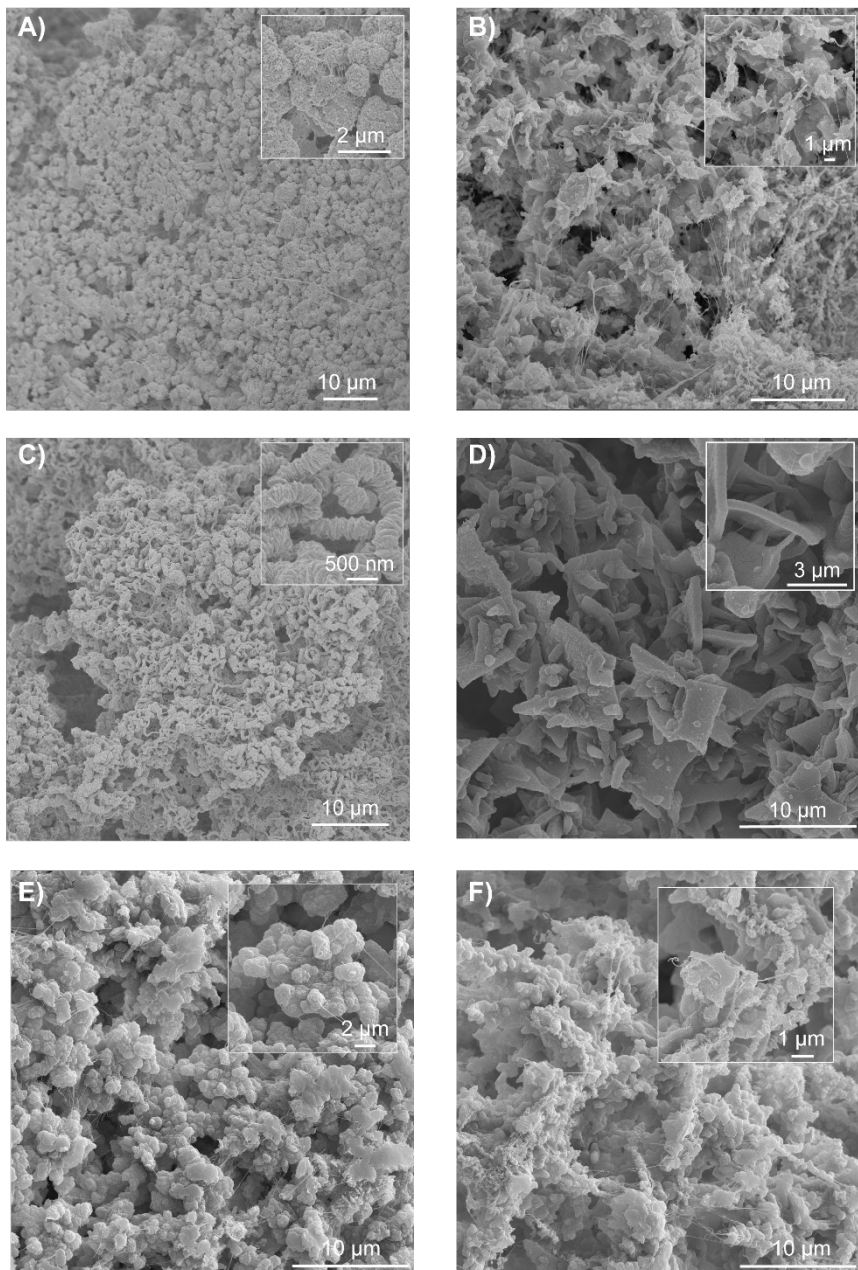


**Figure 5.4.** Scanning Electron Microscopy (SEM) images of the polyethylene (PE) materials produced with respectively **A**) MIL-101(Cr)-NDC, **B**) filtrate from MIL-101(Cr)-NDC, **C**) MIL-53(Cr), **D**) filtrate from MIL-53(Cr), **E**) HKUST-1(Cr), and **F**) the filtrate from HKUST-1(Cr).

stress generated by the growing polyethylene. Despite this fragmentation, it seems that the originally octahedral MOF morphology enforces a spherical morphology on the PE. Second, the obtained morphology from the reactions with MIL-53(Cr) is best described as a fibrous worm-like PE material.<sup>[65]</sup> Interestingly, Chanzy *et al.* attributed this mechanism of PE growth to active sites being in very close proximity, hereby hampering the PE growth in lateral directions while this is not the case perpendicular to the plane of active sites.<sup>[65]</sup> Thus, this indicates that factors such as active site spacing are also a highly important parameter to consider when using MOFs in ethylene polymerization.

Despite the low activity of HKUST-1(Cr), it mainly produced spherical PE beads, as shown in Figure 5.4E, with some PE fibers as well. The dual morphology is likely explained by the fact that a significant percentage of the catalytic activity originates from homogeneous Cr sites that produce the fibrous PE material. Interestingly, the amount of fibrous material is relatively small, and spherical particles are the predominant product. This indicates that even for the homogeneously polymerizing components, the MOF can act as the preferential growth template.

Figures 5.4B, 5.4D and 5.4F are a testament to the importance of the MOF's role as a structuring agent. In all instances, if this structuring agent is removed from the equation, a variety of structures (*e.g.*, platelets, spheroids, and fibers) is obtained. Irregularities on the reactor wall and/or stirrer now predominantly act as crystallization points for the (relatively small) waxes formed over the homogeneous Cr sites, after which PE continues growing.<sup>[62]</sup>

If anything, these SEM images highlight the importance of selecting the appropriate MOF as ethylene polymerization platform for attaining desirable PE morphologies. Additionally, and possibly more importantly, the simultaneous polymerization over heterogeneous Cr sites and homogeneous Cr sites is not detrimental for the final morphology, inferring that even for the dissolved active sites, and PE materials, the MOF crystallites act as crystallization point.

#### 5.2.4 Active Site Formation

The GPC results indicated the participation of a variety of active Cr sites in ethylene polymerization: both homogeneous and heterogeneous. Therefore, we opted to exploit an array of spectroscopic techniques such as XRD, CO probe molecule FTIR and UV-Vis-NIR DRS experiments to investigate the MOF activation stage. Additionally, investigating the morphology of the pristine and activated MOFs required the use of SEM as an imaging technique.

First, XRD serves as an excellent tool to investigate the effect of the co-catalyst on the MOF crystallinity, for which the results are shown in Figure 5.5. The X-ray diffractograms of the three pristine MOFs perfectly resemble those from the literature, although noteworthy: the x-ray diffractogram of MIL-53(Cr) resembles that of the solvated MOF.<sup>[51,55,58]</sup> Now, the effect of Et<sub>2</sub>AlCl on the crystallinity of each MOF was different and will be discussed hereafter. If

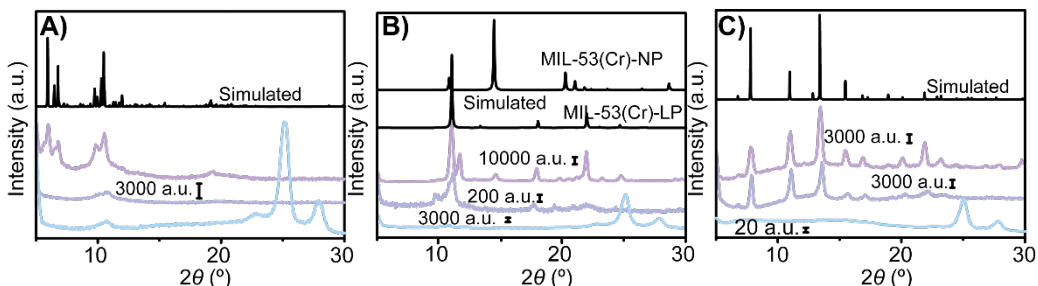


**Figure 5.5.** Results from the powder X-ray diffraction (XRD) experiments for **A)** MIL-101(Cr)-NDC, **B)** MIL-53(Cr) and **C)** HKUST-1(Cr). Purple, top line is the x-ray diffractogram of the pristine MOF. Dark-blue, middle-line, is the x-ray diffractogram of the MOF after activation with 100 mol. eq. co-catalyst. Light-blue, bottom line, after the ethylene polymerization reaction.

consumption of the MOF is to occur, this would coincide with a loss and/or broadening of the diffraction signals.

For both MIL-101(Cr)-NDC and MIL-53(Cr) this indeed occurs, as demonstrated in Figures **5.5A** and **5.5B**, respectively. Activation of MIL-101(Cr) is related to a disappearance of the signals below diffraction angles of  $10^\circ$ . It can be argued that the diffraction signals at  $10^\circ$  can still be identified, albeit less intense, inferring that at least some of the crystallinity is retained. In Figure **5.5B**, activation of MIL-53(Cr) is related to the disappearance of some of the diffraction peaks (most clearly the ones at  $2\theta = 13, 15, 23$ , and  $25^\circ$ ), indicating that the crystallinity of MIL-53(Cr) is severely disrupted. It is worth stating, that MIL-53(Cr) is known to undergo structural transitions and exhibits a so-called breathing effect, however, it is highly unlikely that such events occur here, since only some of the typical XRD reflections for large pore (LP) structures are visible in this case.<sup>[55,66,67]</sup>

Interestingly, the crystallinity of HKUST-1(Cr) is almost unaffected by the activation procedure with 100 mol. eq.  $\text{Et}_2\text{AlCl}$  since the original diffraction pattern is largely retained. The decrease in intensity of diffraction peaks above  $2\theta = 15^\circ$  does infer some minor disruption of the crystallinity, however, the severity is far from those found for MIL-101(Cr)-NDC and MIL-53(Cr). This observation might provide part of the explanation for the low activity of HKUST-1(Cr), since this MOF is activated to the least extent. Also, the X-ray diffractograms are a testament to the polymerization of ethylene over the MOFs, since instead of MOF-related reflections, only HDPE x-ray diffraction peaks are observed, specifically at  $23^\circ$ .

Furthermore, UV-Vis-NIR DRS served as a tool to investigate the effect of the co-catalyst on the oxidation state and coordination geometry of the Cr active sites. The spectra of the materials before and after reaction with the organo-aluminum co-catalysts are shown in Figure **5.6**. It is worth stating that the starting oxidation states of MIL-101(Cr)-NDC and MIL-53(Cr) are  $\text{Cr}^{3+}$ , demonstrated by the bands around  $16000$  and  $22000 \text{ cm}^{-1}$ . That of HKUST-1(Cr) is expected to be  $\text{Cr}^{2+}$  on basis of the original manuscript, which was also confirmed by the orange color of the

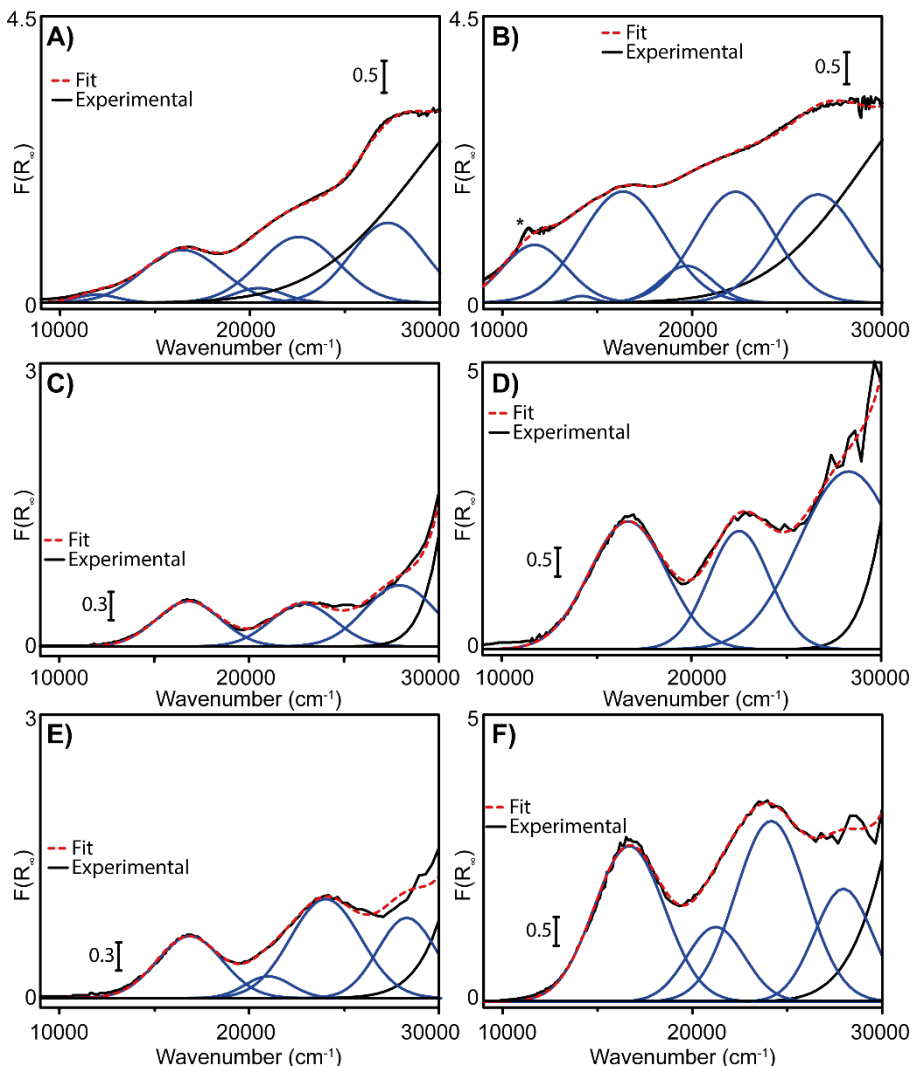


**Figure 5.6.** UV-Vis-NIR Diffuse Reflectance Spectroscopy (DRS) results of the Metal Organic Frameworks before and after activation with 100 mol. eq. Et<sub>2</sub>AlCl. **A) + B)** Respectively for MIL-101(Cr)-NDC, **C) + D)** respectively for MIL-53(Cr), and **E) + F)** respectively for HKUST-1(Cr).

material, consistent with the original report. If oxidation of HKUST-1(Cr) is to occur, a color change from orange to green would be observed, which was excluded. There are small variations from one MOF to another, due to the different electronic structures of the metal centers. The Charge Transfer (CT) bands above 30000 cm<sup>-1</sup> have been omitted for all MOFs, due to their extreme intensity that saturates the detector and therefore renders interpretation impossible.

Activation with the co-catalyst does affect the spectra to some extent. In each case, reacting the MOF materials with the co-catalyst resulted in a darkening of the powder material, which in the UV-Vis-NIR DRS spectra is directly related to an overall increase of intensity of these spectra.

Concerning the oxidation state, none of the UV-Vis-NIR DRS spectra give strong indications for the formation of any oxidation state besides  $\text{Cr}^{3+}$ , unlike the case of previously reported MIL-101(Cr).<sup>[43]</sup> This is surprising given the identical Cr trimer for MIL-101(Cr) and MIL-101(Cr)-NDC, with the pore size being the only difference between these two materials. It is worth stating that the  $16000\text{ cm}^{-1}$  band broadens significantly for MIL-101(Cr)-NDC after activation with the co-catalyst, with two possible chemical explanations. First, activation with the organo-aluminum complex was found to generate a large variety of active sites, naturally, this translates into a variety of UV-Vis-NIR absorptions and is related to the observed heterogeneous broadening. Second,  $\text{Et}_2\text{AlCl}$  in fact reduces some of the  $\text{Cr}^{3+}$  sites from the pristine MOFs to  $\text{Cr}^{2+}$ , which are known to absorb in the  $8000\text{-}12000\text{ cm}^{-1}$  region. In this case, the exact location is usually determined by the degree of coordinative saturation, and the fact that broadening is observed around  $10500\text{ cm}^{-1}$  infers that if reduction is occurring it is likely that  $\text{Cr}^{2+}\text{OH}$  is formed (*i.e.*, coordinatively more saturated  $\text{Cr}^{2+}$ ). With respect to the fitted bands, these only serve to emphasize broadening of the band at  $16000\text{ cm}^{-1}$  band, with its location and FWHM being identical in Figures 5.6A and 5.6B.<sup>[25,68–71]</sup>

The UV-Vis-NIR DRS spectra after activation for both MIL-53(Cr) (Figure 5.6D) and HKUST-1(Cr) (Figure 5.6F) only demonstrate increased intensities of the Cr bands,  $\text{Cr}^{3+}$  for MIL-53(Cr) and  $\text{Cr}^{2+}$  for HKUST-1(Cr). However, the width and location of these bands remain identical, indicating that activation with the co-catalyst does not particularly affect the oxidation state of the MOFs.

Next, CO probe molecule FTIR is an excellent tool to probe the Cr site accessibility, while simultaneously providing some information on the related oxidation state.<sup>[72]</sup> Similarly as in the previous section, CO probe molecule experiments were performed on the pristine MOF materials as well as MOF materials that were activated with 100 mol. eq.  $\text{Et}_2\text{AlCl}$ , the results of these experiments are shown in Figure 5.7.

Figures 5.7A and 5.7B respectively illustrate the results obtained for MIL-101(Cr) before and after activation with 100 mol. eq.  $\text{Et}_2\text{AlCl}$ . It is worth stating that the band at  $2137\text{ cm}^{-1}$  can exclusively be attributed to physisorbed CO on the MOF material. The second band, at  $2158\text{ cm}^{-1}$  can be attributed to CO coordinated to  $\text{H}_2\text{O}$  moieties still reminiscent from the hydrothermal synthesis. Additionally, two bands with low intensity at  $2198$  and  $2088\text{ cm}^{-1}$  are present in the spectra, which based on the literature can be attributed to minor amounts of respectively Lewis Acidic (LA)  $\text{Cr}^{3+}$  sites and extra-framework Cr (oxidation state 2+ or 3+). With the UV-Vis-NIR DRS spectra in mind, extra-framework  $\text{Cr}^{3+}$  is more likely since no hard evidence for  $\text{Cr}^{2+}$  in the pristine material was found. Activation with the co-catalyst, as seen in Figure 5.7B, results in a significant decrease of the  $2158\text{ cm}^{-1}$  band, likely due to scavenging of the coordinating  $\text{H}_2\text{O}$  moieties by

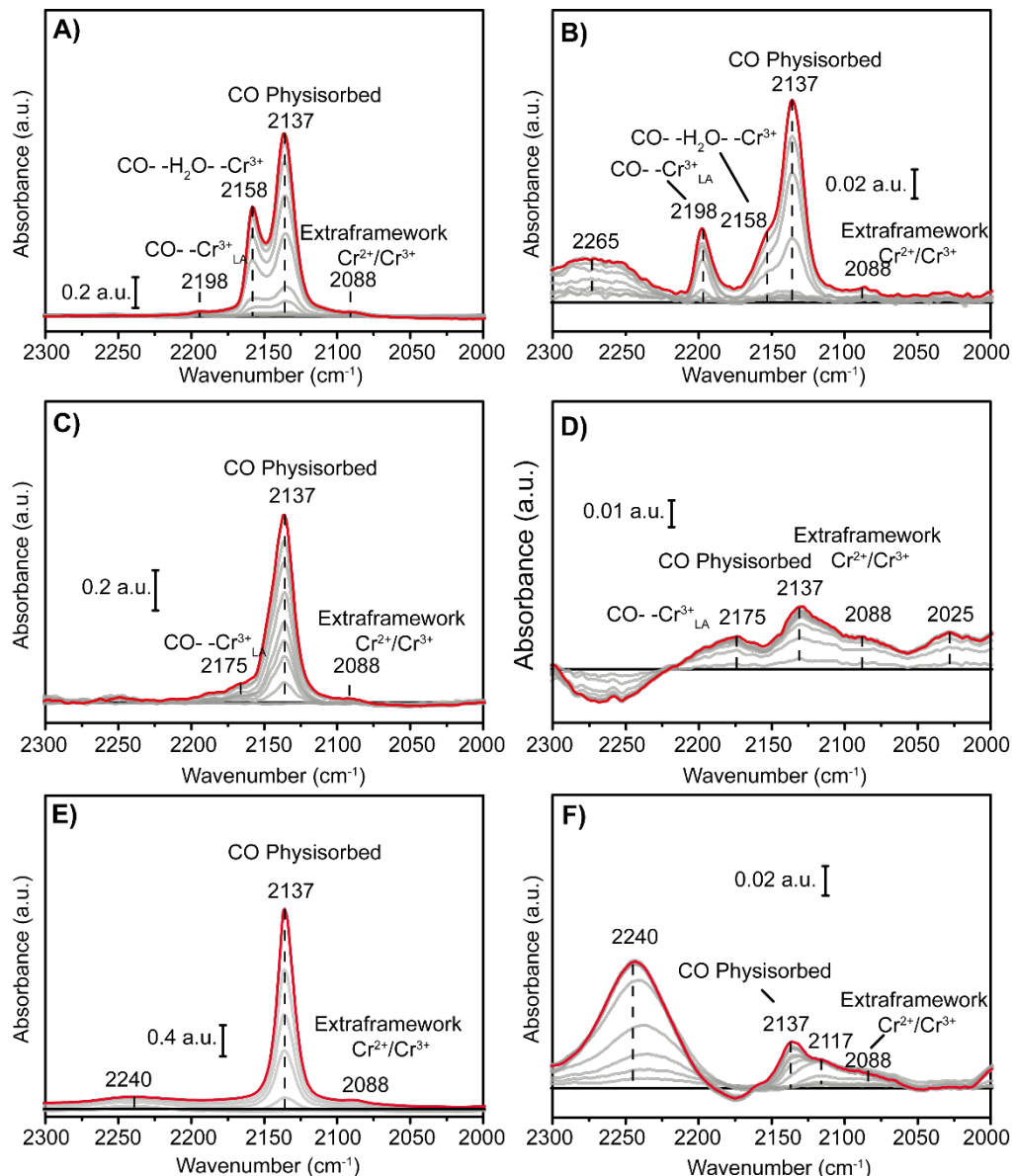


**Figure 5.7** CO probe molecule Fourier Transform Infrared (FTIR) experiment results of the Metal Organic Frameworks before and after activation with 100 mol. eq.  $\text{Et}_2\text{AlCl}$ . Respectively for **A) + B)** MIL-101(Cr)-NDC, **C) + D)** MIL-53(Cr), and **E) + F)** HKUST-1(Cr), respectively.

$\text{Et}_2\text{AlCl}$ . Second, the band at  $2088 \text{ cm}^{-1}$  is still similarly intense as before activation, suggesting that only little additional extra-framework Cr is formed, with both  $2+$  and  $3+$  oxidation states now being viable. However, the significant increase in  $\text{Cr}^{3+}$  LA species, testified by the  $2198 \text{ cm}^{-1}$

band, does infer that the heterogeneous broadening in Figure 5.6B is predominantly caused by the heterogenization of the Cr<sup>3+</sup> sites rather than the formation of Cr<sup>2+</sup> species. Last, a new band emerged at 2265 cm<sup>-1</sup>, which is possibly attributed to CO coordinated to Al<sup>3+</sup> from the co-catalyst material which is embedded/reacted with the MOF material and could not be washed away.

MIL-53(Cr) is defined by the ability to only physisorb CO, with its coordinative saturation being well demonstrated by the lack of any additional bands, with exception of the band at 2088 cm<sup>-1</sup> attributed to minor amounts of extra-framework Cr, likely oxidation state 3+, as well as the very small band at 2175 cm<sup>-1</sup> attributed to LA Cr<sup>3+</sup>. It is worth mentioning that in this case MIL-53(Cr)-np (np = narrow-porous) is likely the phase of MIL-53(Cr) under investigation. Performing the CO probe molecule FTIR experiments on the activated MIL-53(Cr) results produces a strongly changed spectrum. First, it appears that the ability to physisorb CO has significantly decreased. Now, the relative intensity of the LA Cr<sup>3+</sup> bands and extra-framework Cr bands is larger. However, one should take note that the absolute intensities of these bands remain very small. Additionally, one band at 2025 cm<sup>-1</sup> can now be discerned, which infers the possibility of few-atom Cr clusters.

Last, the CO probe molecule FTIR spectrum for HKUST-1(Cr), as shown in Figure 5.7E, is defined by only one major signal attributed to the physisorption of CO. This indicates the absence of coordinatively unsaturated sites (CUS) formed after evacuating/drying during the synthesis, suggesting that either dimethyl formamide (DMF) molecules from the synthesis or OH molecules from the solvent exchange remain coordinated to the Cr sites, even under the conditions used in this study. Apart from the band at 2137 cm<sup>-1</sup>, only minor bands are observed at 2088 and 2240 cm<sup>-1</sup>, the former is again attributed to extra-framework Cr<sup>2+</sup>. Performing the same activation procedure with Et<sub>2</sub>AlCl on HKUST-1(Cr) resulted in a band at 2240 cm<sup>-1</sup>, along with bands at 2117 and 2088 cm<sup>-1</sup>. Due to the unlikelihood of any other oxidation state than 2+, the latter signal is again attributed to extra-framework Cr<sup>2+</sup>. Interestingly, the 2117 cm<sup>-1</sup> band falls in the range where normally few-atom Cr clusters (either oxidation state 2+ or 3+) are observed, which considering the structure of the metal-node is not an unlikely explanation.<sup>[72]</sup> In any case, the fact that the intensity of this band is low is a testament to the stability of this MOF, indicating that only a small number of the original linker-Cr bonds is broken.

In summary, the x-ray diffraction experiments indicate that the more active MOFs are modified to a larger extent. The CO FTIR experiments further corroborate the generation of a variety of active sites, unique to each MOF, which retain the oxidation state of the pristine MOF.

### 5.2.5 Estimating Collapse

From the X-ray diffractograms and CO-FTIR spectra shown above, collapse of the framework may have occurred, affecting the catalytic properties of the MOFs by limiting accessibility of ethylene

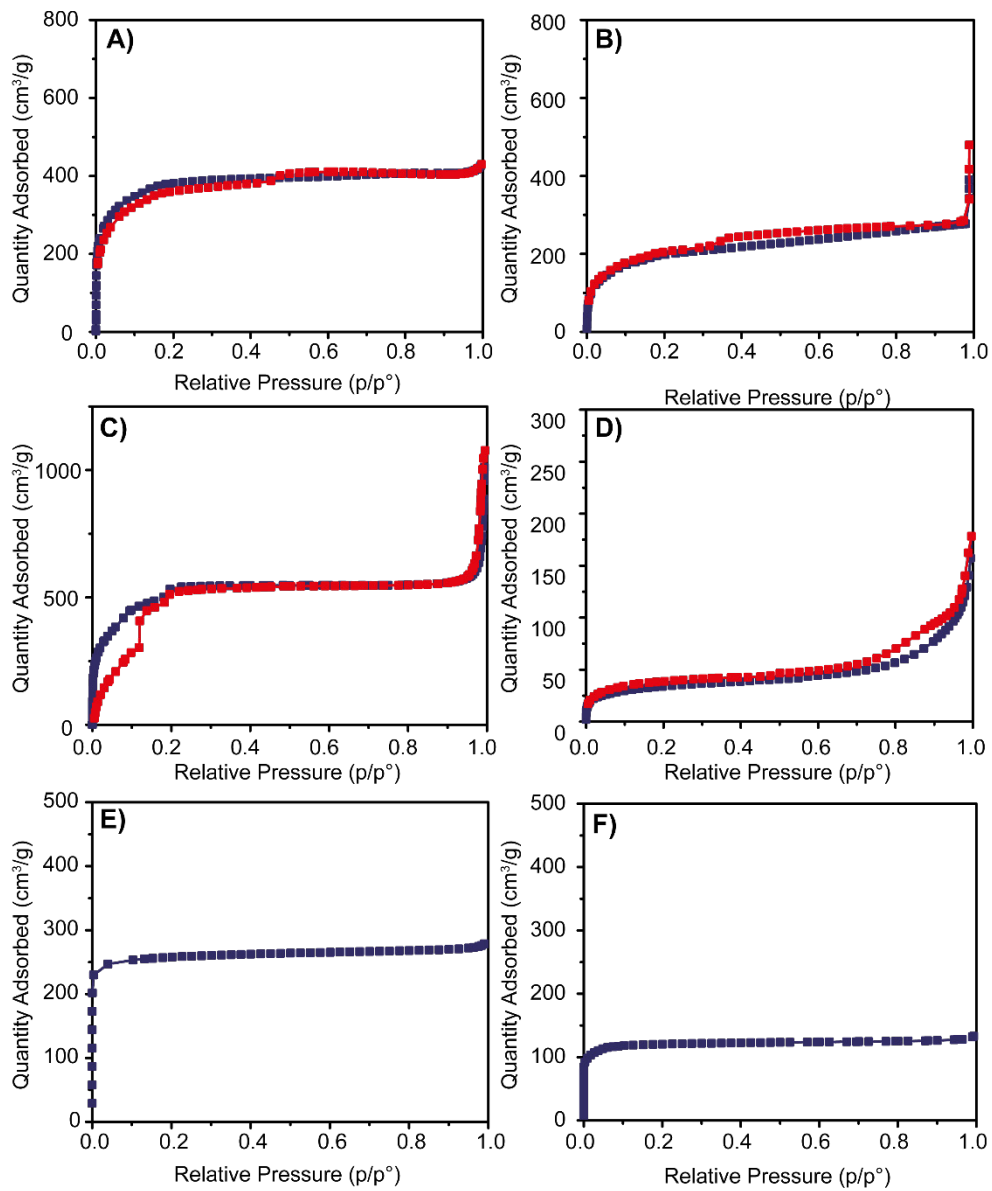


**Figure 5.8.** Nitrogen ( $N_2$ ) Physisorption measurements performed on the Metal Organic Frameworks before and after activation with the blue curves representing the adsorption curves and the red curves representing the desorption curves. **A)** + **B)** MIL-101(Cr)-NDC, **C)** + **D)** MIL-53(Cr), and **E)** + **F)** HKUST-1(Cr) respectively before and after activation with the co-catalyst.

or chain growth. We used N<sub>2</sub> physisorption at -196 °C to evaluate the porosity of the MOFs before and after activation with the co-catalyst. The respective isotherms of the pristine MIL-101(Cr)-NDC, MIL-53(Cr), and HKUST-1(Cr) are shown in Figures **5.8A-B**, **5.8C-D**, and **5.8E-F** with Brunauer-Emmett-Teller (BET) surface areas of 1419, 1531 and 1033 m<sup>2</sup>/g. In any case, Type I isotherms are observed for all the MOFs, confirming their porosity. Collapse of the MOF is likely related to a disappearance of the material's porosity as well as a potential change in the observed type of isotherm. While Figure **5.8** does confirm that part of the surface area is lost, apparent BET surface areas of 635, 124, and 468 m<sup>2</sup>/g, indicate that still a significant part of the porosity is retained. The largest drop is observed in case of MIL-53(Cr), suggesting that in this case porosity might not be correlated to catalytic activity. It is worth stating that drying of the pristine MOFs was performed under dynamic high-vacuum, while this is supposedly a safe possibility for these MOFs, it is important to consider that vacuum *might* have detrimental effects on the surface area, explaining the slightly lower value compared to those observed in the literature in case of MIL-101(Cr)-NDC.<sup>[73,74]</sup>

Second, the morphology of all the MOFs, as shown in Figure **5.9**, has been extensively described in the literature and matches the crystals observed in our case. For MIL-101(Cr)-NDC that means nanosized octahedral crystals clustered into larger structures, as shown in Figure **5.9A**.<sup>[75,76]</sup> For MIL-53(Cr) a crystalline material is obtained, which consists of exclusively needles (sized 5-10 µm). It is worth stating that MIL-53(Cr) is the thermodynamic product of MIL-101(Cr).<sup>[57,77-79]</sup> In the case of HKUST-1(Cr), a uniform powder consisting of the octahedral crystals in Figure **5.9E** is obtained. Again, this is perfectly in line with what is reported in the literature on the morphology of this MOF.<sup>[80-82]</sup> It is worth stating that our research does not provide a basis to comment on any potential MOF morphology/activity relations, due to the varying metal-nodes of the MOFs which in that case should have been constant. However, this does warrant further research where the metal-node structure is kept identical, and the particle size/shape is systematically varied.

The morphologies of the activated MOFs are shown in Figures **5.9B**, **5.9D**, and **5.9F**, in which no obvious changes are visible, confirmed by the preserved shapes and sizes of the MOF crystals. It is worth stating that no Al<sub>2</sub>O<sub>3</sub> is observed in the bright-field micrograph as a possible by-product originating from the activation procedure.

Diffuse Reflectance Infrared Spectroscopy (DRIFTS) was used to investigate whether the characteristic MOF fingerprint bands changed during activation with the co-catalyst. In the case of MIL-101(Cr)-NDC (Figure **5.10A**) the obtained DRIFTS spectrum is in line with reported spectra. Worth noting, our preparation of MIL-101(Cr)-NDC yielded a product without free 2,6-dicarboxynaphthalene, which may potentially block pores as well Cr<sup>3+</sup> CUS sites, testified by the absence of a  $\nu(\text{C=O})$  band at 1700 cm<sup>-1</sup>. Second, activation of the MOF, as shown in Figure **5.10B**, did not decrease the S/N ratio nor did it affect the MOF fingerprint. It is worth stating that newly

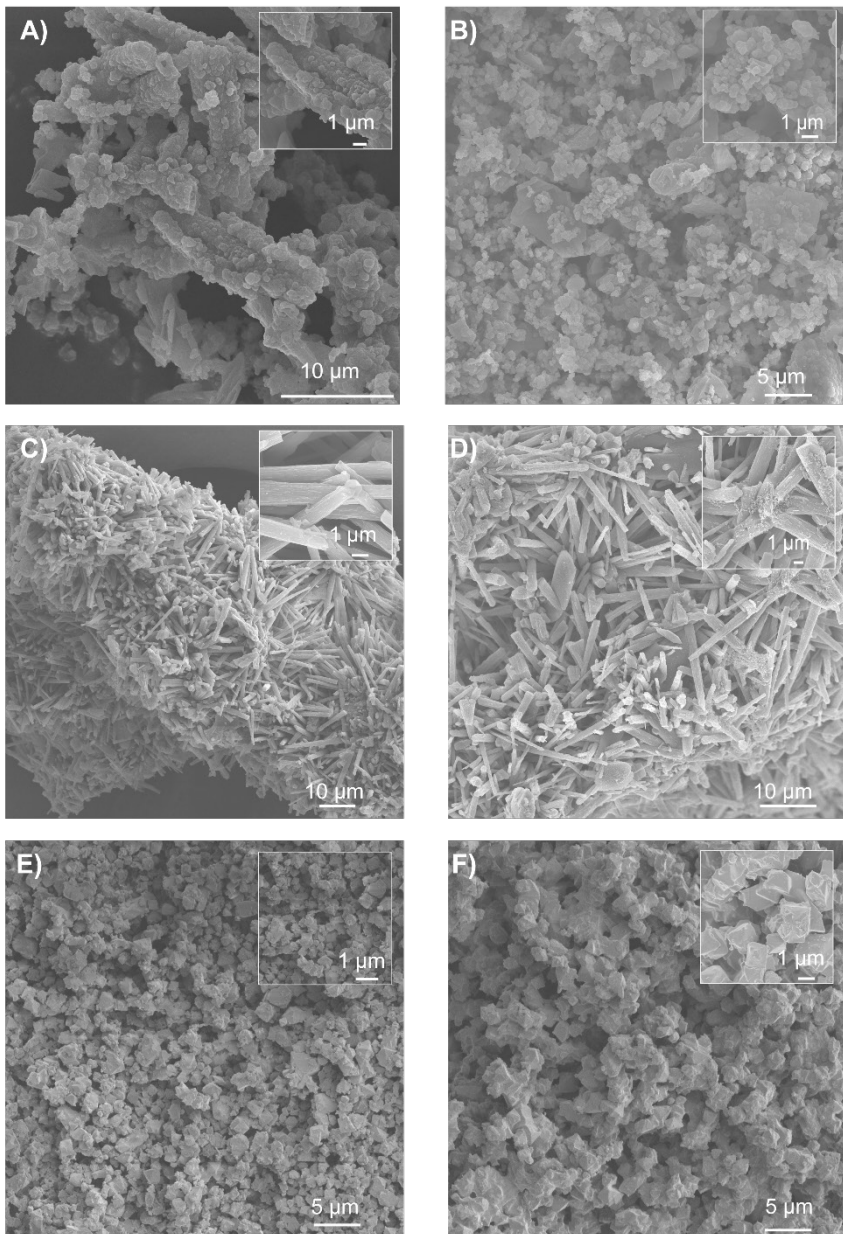


**Figure 5.9.** Scanning Electron Microscopy (SEM) images of the Metal Organic Frameworks before and after activation with 100 mol. eq. Et<sub>2</sub>AlCl. for **A) + B)** MIL-101(Cr)-NDC, **C) + D)** MIL-53(Cr), and **E) + F)** HKUST-1(Cr), respectively.

emerged bands at 2870 and 2950 cm<sup>-1</sup> can be assigned to alkylation of the MOF by the Et<sub>2</sub>AlCl co-catalyst, as they correspond to the stretching vibrations of the ethyl groups.

MIL-53(Cr) (shown in Figure 5.10C) is characterized by isolated Cr<sup>3+</sup><sub>oh</sub> metal centers, linked in infinite chains 1D by terephthalic acid with  $\mu_2$ -OH groups bridging the individual chains. These  $\mu_2$ -OH groups give rise to the characteristic 3600 cm<sup>-1</sup>  $\nu(OH)$  band. Again, only the newly emerged  $\nu_{as/s}(CH_2)$  and  $\nu_{as/s}(CH_3)$  bands are evident and the persistence of the  $\mu_2$ -OH indicates that the overall structure is largely untouched.

HKUST-1(Cr) behaves very similar, as shown in Figures 5.10E and 5.10F. The DRIFTS spectrum of pristine HKUST-1(Cr) testifies to the successful synthesis where no free trimesic acid is observed which might potentially block the pores and/or Cr<sup>3+</sup> sites. Interestingly, the 1640-1650 cm<sup>-1</sup> range shows two signals of one which likely belongs to bound DMF originating from the MOF synthesis. Activation with the co-catalyst resulted in the disappearance of this signal, related to the abstraction of DMF, while alkylation occurred simultaneously.

Despite the significant concern of MOF collapse after activation with the Et<sub>2</sub>AlCl co-catalyst, the above results show that the chemical bonds comprising the MOF seem to be unaffected. This points to the fact that, in terms of morphology and bonding, the MOF remains intact. While the loss of crystallinity is related to the observed loss in porosity, it is highly important to state that activation with Et<sub>2</sub>AlCl does not result in the total collapse of the MOF. This suggests that the resulting materials are partially disordered and porous Cr<sup>3+</sup> carboxylates with a variety of Cr<sup>3+</sup> embedded (and potentially extra-framework Cr<sup>3+</sup> and Cr<sup>2+</sup>) alkylated sites for MIL-101(Cr)-NDC and MIL-53(Cr), whereas this involves Cr<sup>2+</sup> sites for HKUST-1(Cr). From our study, it seems that more generated defects, *i.e.*, MIL-101(Cr)-NDC and MIL-53(Cr), is related to higher ethylene polymerization activity. The catalytic activity was related to large  $D$  values, confirming the presence of a variety of active Cr sites. However, further experiments are necessary to disentangle the contribution of each of the solid and/or homogeneous Cr compounds to the MWD. It is also clear that a larger percentage of PE produced over homogeneous Cr complexes leads to more fibrous HDPE, probably due to uncontrolled growth.

### 5.3 Conclusions

We have investigated the catalytic performance of MIL-101(Cr)-NDC, MIL-53(Cr) and HKUST-1(Cr) in ethylene polymerization. We have found that selecting the appropriate MOF as polymerization platform is of paramount importance for attaining desirable levels of activity: with MIL-53(Cr) being the most active, followed by MIL-101(Cr)-NDC and eventually HKUST-1(Cr). Although the three MOFs demonstrated activity, we found that some of the activity originated from leached Cr complexes.

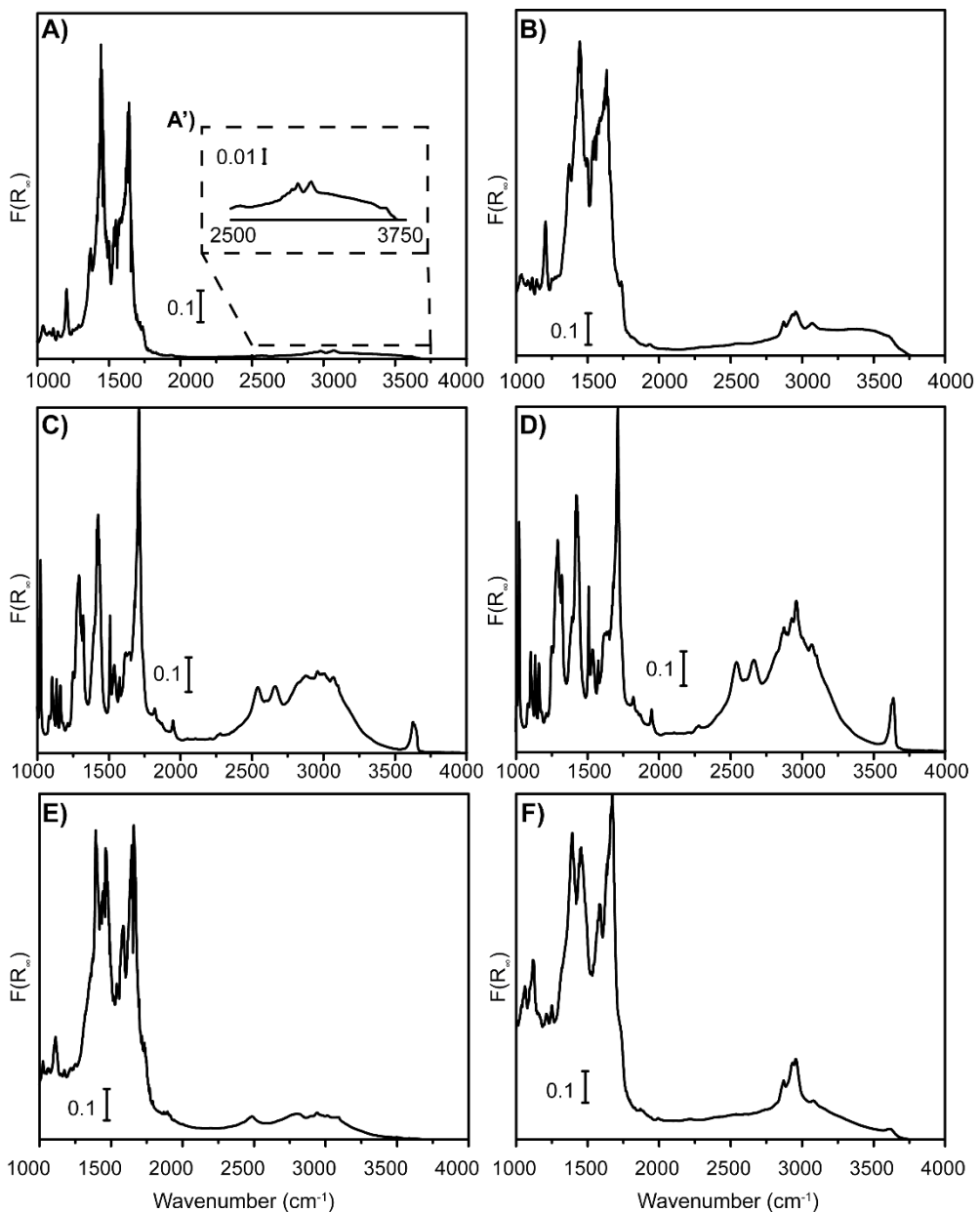


**Figure 5.10.** Diffuse Reflectance Infrared Spectroscopy (DRIFTS) spectra of the Metal Organic Frameworks before and after activation with 100 mol. eq.  $\text{Et}_2\text{AlCl}$ . **A)** + **B)** Respectively for MIL-101(Cr)-NDC, **C)** + **D)** respectively for MIL-53(Cr), and **E)** + **F)** respectively for HKUST-1(Cr)

Second, the PEs produced over the MOFs demonstrated large  $D$  values as well as varying crystallinities, indicating that ethylene polymerization occurs over a large variety of active sites. Furthermore, selection of the appropriate MOF was critical for templating the final PE morphology, with only MIL-101(Cr)-NDC producing favorable PE spheres and HKUST-1(Cr) demonstrating potential by predominantly producing spheres, however with some fibers.

Third, our spectroscopic investigations indeed confirmed that activation of the MOFs results in the generation of a variety of active sites, while retaining the oxidation state of the pristine MOF. Furthermore, we found that the MOFs which were the most modified were also the most active, indicating that proper activation of the MOFs is a prerequisite for ethylene polymerization.

Last, it was critical to exclude total collapse of the MOF, which on basis of the GPC and spectroscopic results was a likely event. Activation of the pristine MOFs indeed resulted in decreased BET surface areas, with porous materials (BET SA >400 m<sup>2</sup>/g) still being the predominant products. Furthermore, activation of the MOF neither affected the MOF morphology or the MOF DRIFTS fingerprint, indicating that activation does not result in cleavage of all the bonds constituting the MOF.

In summary, we have explored three well renowned Cr-based MOFs as ethylene polymerization platforms. In this work we have shown that selecting the appropriate MOF is critical for the activity, PE properties as well as PE morphologies. More importantly, we have also demonstrated that the active MOF cannot be considered a single site heterogenized ethylene polymerization catalyst. We believe that these findings can be helpful for the future development of heterogeneous Cr catalysts as well as Cr-based MOFs and their applications in the important ethylene polymerization reaction.

## 5.4 Acknowledgements

We thank N. Friederichs (Sabic), T. Schoffelen (Sabic) and E. Troisi (Sabic) for the GPC-SEC and DSC measurements.

## 5.5 Experimental Section

### 5.5.1 Catalyst Preparation

The synthesis of the MOFs MIL-101(Cr)-NDC<sup>[51]</sup>, MIL-53(Cr)<sup>[55]</sup> and HKUST-1(Cr)<sup>[58]</sup> was carried out according to previously published procedures. Dry glassware was kept in an oven at 120 °C prior to use and the Schlenk experiments were carried out under Ar using dry flasks and joints. In the case of HKUST-1(Cr), the solvents: DMF (anhydrous, 99.9%, Sigma-Aldrich) and MeOH

(anhydrous, 99.8%, Sigma-Aldrich) were kept in 3 Å mol sieves and degassed by sparging Ar for 2 h prior to use.

### a. Synthesis of MIL-101(Cr)-NDC

2,6-naphthalenedicarboxylic acid (430 mg, 2 mmol, Sigma-Aldrich, 95%), Cr(NO<sub>3</sub>)<sub>3</sub>·9H<sub>2</sub>O (800 mg, 2 mmol, Sigma-Aldrich, 98%), glacial acetic acid (23.8 mL, 4 mmol, Merck KgaA, +99%), and deionized H<sub>2</sub>O (9.54 mL) were introduced into a Teflon liner inserted into a stainless steel Parr autoclave and stirred for 20 min. The autoclave was then heated to 200 °C over the course of 3 h, then kept at 200 °C for 5 h, and finally cooled to room temperature over 3 h. The reaction product MIL-101(Cr)-NDC was recovered by centrifugation as a green powder, washed with water (50 mL), ethanol (50 mL) and soaked in ethanol at 60 °C for 24 h under stirring in a round bottom flask. Then, the powder was recovered and dried *in vacuo* at 150 °C for 24 h and subsequently introduced into a glovebox until further use.

### b. Synthesis of HKUST-1(Cr)

Cr(CO)<sub>6</sub> (8.2 g, 10 mmol), trimesic acid (H<sub>3</sub>BTC, 1.2 g, 6 mmol) and degassed (purged with Ar for 2 h and dried in 3 Å mol sieves) anhydrous DMF (80 mL) were introduced into a dry 250 mL Schlenk flask under Ar atmosphere. The mixture was refluxed (150 °C) for 3 days under Ar flow and then cooled to 25 RT. The violet suspended powder was isolated by Schlenk filtration and rinsed three times with anhydrous oxygen-free DMF. Then, the DMF was removed with a canula and the product soaked with 100 mL of degassed methanol. After 24 h, the methanol was decanted to afford a dark orange solid, and the product dried under vacuum at room temperature for 24 h and at 100 °C for 24 h before being introduced in the glovebox as an orange powder.

### c. Synthesis of MIL-53(Cr)

A mixture of chromium(III) nitrate Cr(NO<sub>3</sub>)<sub>3</sub>·9H<sub>2</sub>O (Sigma-Aldrich, 98%), terephthalic acid (Sigma-Aldrich, 98%), hydrofluoric acid (HF) (Sigma-Aldrich, solution 48-51% v/v), and H<sub>2</sub>O (20 mL) in the molar ratio 1:1:1:280; was introduced in a Teflon liner within a stainless steel Parr autoclave and introduced into an oven at 220 °C for 3 days, then cooled naturally to room temperature. A purple powder with long white needles of terephthalic acid was recovered by centrifugation. Then, the mixture was soaked in DMF at 90 °C under stirring for 24 h to dissolve the linker, then the purified MOF powder recovered. Thereafter, it was washed with EtOH (VWR International, technical, 98%) twice then soaked in DMF at 90 °C under stirring for 24 h, subsequently in ethanol

at 60 °C for 24 h, recovered by centrifugation, dried in air at room temperature and at vacuum at 150 °C for 12h.

### **5.5.2 Catalyst Testing**

In a typical polymerization experiment, an amount equivalent to 0.05 mmol of each MOF was suspended in 15 mL of anhydrous heptane (99.9% anhydrous, stored over molecular sieves, Sigma-Aldrich) or toluene (99.9% anhydrous, stored over molecular sieves, Sigma-Aldrich) in a stainless-steel Parr reactor, together with 100:1 (Al:Cr) molecular equivalents of Et<sub>2</sub>AlCl (97%, Sigma-Aldrich) in an N<sub>2</sub> filled glovebox (O<sub>2</sub> < 1.5 ppm and H<sub>2</sub>O < 0.6 ppm). Subsequently, the reactor was attached to an ethylene gas/vacuum system allowing the evacuation and flushing of the lines before ethylene (Linde AG, 99.9%) polymerization was performed at a constant pressure of 10 bar and a temperature of 23 °C. The reaction mixture was stirred at 1000 rpm. The reactor was depressurized after 30 min of polymerization and the residual Et<sub>2</sub>AlCl was quenched with 1 M HCl in ethanol. The solid product was copiously washed with 1M HCl in ethanol, followed by ethanol. The solid material was dried at 70 °C overnight and 3h under vacuum. The catalyst activity was based on the weight of the obtained polymer products. The polymerization reactions with the filtrates were performed as follows. 0.05 mmol of each MOF was suspended in 10 mL of anhydrous heptane (99.9% anhydrous, stored over molecular sieves, Sigma-Aldrich), stirred for 15 minutes and subsequently collected by filtration, the filter was washed twice with 2 mL of the heptane and once with 1 mL of the heptane to reach the desired diluent volume of 15 mL. Subsequently, ethylene polymerization was performed as described before.

### **5.5.3 Catalyst Characterization**

#### **a. X-ray Diffraction Experiments**

The X-ray diffraction (XRD) patterns were obtained with a Bruker-AXS D2 Phaser powder X-ray diffractometer in Bragg-Brentano geometry using Co K $\alpha$  = 1.78897 Å, operated at 30 kV. The measurements were carried out between 5 and 30 °, using a step-size of 0.05° and a scan speed of 1s with a 0.1 mm slit for the source. The activated MOF material was prepared as follows. 100 mg of MOF was distributed over a required number of vials so that each vial contained 0.05 mmol MOF. Subsequently, 15 mL of heptane was added and 100 mol. eq. of Et<sub>2</sub>AlCl and the mixture was homogenized for 15 minutes before collecting the powder by filtration. Hereafter it was washed thrice with 5 mL pentane. The MOF was carefully dried in N<sub>2</sub> atmosphere for 5 min before being brought outside and carefully exposed to ambient atmosphere. After this, the materials were measured.

### **b. CO Probe Molecule Fourier Transform Infrared Spectroscopy**

Fourier Transform Infrared (FT-IR) spectroscopy measurements with CO probe molecules were recorded on a PerkinElmer 2000 instrument, in a specially designed cell fitted with CaF<sub>2</sub> windows. The dried MOF materials were pressed into 5-7 mg wafers inside an N<sub>2</sub> glovebox (O<sub>2</sub> < 1.2 ppm and H<sub>2</sub>O < 0.6 ppm). The cell was sealed and connected to the gas/vacuum system. Subsequently, the cell was carefully evacuated to 10<sup>-5</sup> bar at 25 °C, after which the sample was cooled to liquid N<sub>2</sub> temperature. A mixture of 10% CO / 90% HE (v/v) was dosed with small increments while measuring FT-IR spectra 1 min after each CO dosing to ensure equilibration. Experiments performed on the activated materials were performed as follows: 5-7 mg of the pristine MOF was pressed in a self-supporting pellet, after which it was carefully suspended for 15 min in a mixture containing 15 mL heptane and 100 mol. eq. Et<sub>2</sub>AlCl. Subsequently, it was suspended in 15 mL pentane to wash away the excess Et<sub>2</sub>AlCl. Subsequently, the CO probe molecule experiments were performed as previously described. Extra care was taken to ensure that there were no cracks in the pellet after activation.

### **c. UV-Vis-NIR Diffuse Reflectance Spectroscopy**

These measurements were performed using a PerkinElmer Lambda950s spectrophotometer with a Praying Mantis DRS accessory. The measurements were performed in the 40000 – 4000 cm<sup>-1</sup> region with a 60 ms datapoint scan time and 4 nm spectral resolution. For every measurement, the Praying Mantis DRS was loaded with 10-20 mg of MOF inside an N<sub>2</sub> filled glovebox (O<sub>2</sub> < 1.2 ppm and H<sub>2</sub>O < 0.6 ppm). The samples were measured against a Teflon white, measured in the same cell, consisting of 30 µm Teflon beads. The activated MOFs were performed as follows: 0.05 mmol MOF was suspended in 15 mL heptane, to which 100 mol. eq. Et<sub>2</sub>AlCl was added. The mixture was stirred for 10 min, after which the powder was collected by filtration and washed twice with 5 mL heptane. The powder was dried in the atmosphere for an additional 10 min before being measured.

### **d. Inductively Coupled Plasma – Atomic Emission Spectroscopy**

0.05 mmol of the pristine MOF was weighed and suspended in 15 mL heptane to which 100 mol. eq. Et<sub>2</sub>AlCl was added. Subsequently, the liquid was collected by filtration and the filter was washed twice with 5 mL heptane. Subsequently, the diluents were removed by slow evaporation. The residue was then dissolved in a minimal amount of aqua regia before being diluted to the same pH as a 5% HNO<sub>3</sub> solution. 10 mL of the diluted samples were taken for measurements on a PerkinElmer Optima 8300 and an average of three samples was used. Cr (267.7, 205.6 and

283.6 nm) were measured and referenced to 0, 0.2, 0.4, 0.6, 0.8 and 1.0 mg/L were prepared of all the metals.

#### e. Scanning Electron Microscopy

Scanning Electron Microscopy (SEM) measurements were carried out with a FEI Helios NanoLab G3 UC (FEI Company) instrument equipped with a Silicon Drift Detector (SDD) at 10.0 kV acceleration voltage and a 0.10 nA current. The samples were dispersed on an aluminum SEM stub with a carbon sticker and were subsequently coated with a Pt layer.

#### f. Differential Scanning Calorimetry

DSC was performed on a TA Instruments DSC Q20 with 1-2 mg of the nascent material. Each sample was heated from -40 °C to 200 °C at a rate of 10 °C·min<sup>-1</sup> after which it was held isothermally at 200 °C to erase thermal history of the PE. Subsequently the cooling cycle was initiated to -40 °C at a rate of 10 °C·min<sup>-1</sup> followed by an additional heating cycle to 200 °C at a rate of 10 °C·min<sup>-1</sup>. The crystallinities of the polyethylene materials were determined assuming  $\Delta H_m^0 = 293 \text{ J} \cdot \text{g}^{-1}$  for 100% crystalline ultrahigh-molecular-weight polyethylene (UHMWPE).

#### g. Gel Permeation Chromatography

Gel Permeation Chromatography (GPC) was carried out on a Polymer Laboratories PL-GPC220 instrument in 1,2,4-trichlorobenzene at 160 °C, equipped with a PL BV-400 refractive index detector. The column set consisted of three Polymer Laboratories 13 µm PLgel Olexis 300 x 7.5 mm columns, and the calibration was performed with linear polyethylene (PE) and polypropylene (PP) standards.

#### h. N<sub>2</sub> Physisorption

N<sub>2</sub> adsorption measurements for MIL-101(Cr)-NDC and MIL-53(Cr) were measured at 77 K on a Micromeritics TriStar 3000 instrument. Prior to all measurements, samples were dried at 150 °C under dynamic vacuum. Specific surface areas (SSAs) were calculated using the multipoint BET method ( $0.05 < p/p_0 < 0.25$ ). N<sub>2</sub> measurements for HKUST-1(Cr) were performed as follows: high-resolution low-pressure adsorption measurements were measured on a Micromeritics ASAP2010 gas adsorption analyser equipped with additional 1 mmHg and 10 mmHg pressure transducers. A relative pressure range from  $p/p_0 = 10^{-7}$  to 0.99 has been applied. Before the actual measurements on this apparatus, the samples were degassed for 16h at 150 °C. Specific surface areas (SSAs) were calculated using the multipoint BET method ( $0.05 < p/p_0 < 0.25$ ).

## 5.6 References

- [1] R. Mülhaupt, *Macromol. Chem. Phys.* **2013**, *214*, 159–174.
- [2] P. J. Deslauriers, D. C. Rohlfing, *Macromol. Symp.* **2009**, *282*, 136–149.
- [3] M. P. McDaniel, *Adv. Catal.* **2010**, *53*, 123–606.
- [4] *Polyolefins: 50 years after Ziegler and Natta I* in *Advances in Polymer Science*, Vol. 257, (Ed.: W. Kaminsky), Springer, Berlin, **2013**, pp. 1–257.
- [5] G. C. Berry, *Encycl. Mater. Sci. Technol.* **2001**, 7440–7448.
- [6] W. Kaminsky, *J. Polym. Sci. Part A Polym. Chem.* **2004**, *42*, 3911–3921.
- [7] E. Tioni, J. P. Broyer, V. Monteil, T. McKenna, *Ind. Eng. Chem. Res.* **2012**, *51*, 14673–14684.
- [8] T. F. McKenna, *Eur. Polym. J.* **1998**, *34*, 1255–1260.
- [9] T. F. McKenna, A. Di Martino, G. Weickert, J. B. P. Soares, *Macromol. React. Eng.* **2010**, *4*, 40–64.
- [10] E. Tioni, J. P. Broyer, V. Monteil, T. McKenna, *Ind. Eng. Chem. Res.* **2012**, *51*, 14673–14684.
- [11] S. L. Aggarwal, O. J. Sweeting, *Chem. Rev.* **1957**, *57*, 665–742.
- [12] *The Chemistry of Metal-Organic Frameworks: Synthesis, Characterization, and Applications* (Ed.: S. Kaskel), 1<sup>st</sup> ed, Wiley-VCH, Weinheim, **2016**, pp. 1–791.
- [13] J. Gascon, A. Corma, F. Kapteijn, F. X. Llabrés i Xamena, *ACS Catal.* **2014**, *4*, 361–378.
- [14] S. M. Cohen, Z. Zhang, J. A. Boissonnault, *Inorg. Chem.* **2016**, *55*, 7281–7290.
- [15] M. Lammert, S. Bernt, F. Vermoortele, D. E. De Vos, N. Stock, *Inorg. Chem.* **2013**, *52*, 8521–8528.
- [16] F. M. Wisser, P. Berruyer, L. Cardenas, Y. Mohr, E. A. Quadrelli, A. Lesage, D. Farrusseng, J. Canivet, *ACS Catal.* **2018**, *8*, 1653–1661.
- [17] J. N. Hall, P. Bollini, *React. Chem. Eng.* **2019**, *4*, 207–222.
- [18] F. Vermoortele, M. Vandichel, B. Van de Voorde, R. Ameloot, M. Waroquier, V. Van Speybroeck, D. E. De Vos, *Angew. Chem. Int. Ed.* **2012**, *124*, 4971–4974.
- [19] C. Vallés-García, A. Santiago-Portillo, M. Álvaro, S. Navalón, H. García, *Appl. Catal. A Gen.* **2020**, *590*, 117340.
- [20] Y. Lin, C. Kong, L. Chen, *RSC Adv.* **2012**, *2*, 641–6419.
- [21] P. J. Deslauriers, C. Tso, Y. Yu, D. L. Rohlfing, M. P. McDaniel, *Appl. Catal. A Gen.* **2010**, *388*, 102–112.
- [22] M. P. McDaniel, M. M. Johnson, *Macromolecules* **2005**, *20*, 773–778.
- [23] G. A. Martino, C. Barzan, A. Piovano, A. Budnyk, E. Groppo, *J. Catal.* **2018**, *357*, 206–212.
- [24] M. A. Vuurman, I. E. Wachs, D. J. Stukens, A. Oskam, *J. Mol. Catal.* **1993**, *80*, 209–227.
- [25] B. M. Weckhuysen, R. A. Schoonheydt, J. M. Jehng, I. E. Wachs, S. J. Cho, R. Ryoo, S. Kijlstra, E. Poels, *J. Chem. Soc. Faraday Trans.* **1995**, *91*, 3245–3253.
- [26] B. M. Weckhuysen, A. A. Verberckmoes, A. L. Buttiens, R. A. Schoonheydt, *J. Phys. Chem.* **1994**, *98*, 579–584.
- [27] S. M. J. Rogge, A. Bavykina, J. Hajek, H. Garcia, A. I. Olivos-Suarez, A. Sepúlveda-Escribano, A. Vimont, G. Clet, P. Bazin, F. Kapteijn, M. Daturi, E. V. Ramos-Fernandez, F. X. Llabrés i Xamena, V. Van Speybroeck, J. Gascon, *Chem. Soc. Rev.* **2017**, *46*, 3134–3184.
- [28] A. Corma, H. García, F. X. Llabrés i Xamena, *Chem. Rev.* **2010**, *110*, 4606–4655.
- [29] A. Bavykina, N. Kolobov, I. S. Khan, J. A. Bau, A. Ramirez, J. Gascon, *Chem. Rev.* **2020**, *120*, 8468–8535.

- [30] R. J. C. Dubey, R. J. Comito, Z. Wu, G. Zhang, A. J. Rieth, C. H. Hendon, J. T. Miller, M. Dincă, *J. Am. Chem. Soc.* **2017**, *139*, 12664–12669.
- [31] E. D. Metzger, C. K. Brozek, R. J. Comito, M. Dinca, *ACS Cent. Sci.* **2016**, *2*, 148–153.
- [32] R. J. Comito, E. D. Metzger, Z. Wu, G. Zhang, C. H. Hendon, J. T. Miller, M. Dincă, *Organometallics* **2017**, *36*, 1681–1683.
- [33] S. T. Madrahimov, J. R. Gallagher, G. Zhang, Z. Meinhart, S. J. Garibay, M. Delferro, J. T. Miller, O. K. Farha, J. T. Hupp, S. T. Nguyen, *ACS Catal.* **2015**, *5*, 6713–6718.
- [34] A. N. Mlinar, B. K. Keitz, D. Gygi, E. D. Bloch, J. R. Long, A. T. Bell, *ACS Catal.* **2014**, *4*, 717–721.
- [35] S. Liu, Y. Zhang, Y. Han, G. Feng, F. Gao, H. Wang, P. Qiu, *Organometallics* **2017**, *36*, 632–638.
- [36] J. Ye, L. Gagliardi, C. J. Cramer, D. G. Truhlar, *J. Catal.* **2017**, *354*, 278–286.
- [37] R. C. Klet, S. Tussupbayev, J. Borycz, J. R. Gallagher, M. M. Stalzer, J. T. Miller, L. Gagliardi, J. T. Hupp, T. J. Marks, C. J. Cramer, M. Delferro, O. K. Farha, *J. Am. Chem. Soc.* **2015**, *137*, 15680–15683.
- [38] V. Bernales, A. B. League, Z. Li, N. M. Schweitzer, A. W. Peters, R. K. Carlson, J. T. Hupp, C. J. Cramer, O. K. Farha, L. Gagliardi, *J. Phys. Chem. C* **2016**, *120*, 23576–23583.
- [39] T. A. Goetjen, X. Zhang, J. Liu, J. T. Hupp, O. K. Farha, *ACS Sustain. Chem. Eng.* **2019**, *7*, 2553–2557.
- [40] M. I. Gonzalez, J. Oktawiec, J. R. Long, *Faraday Discuss.* **2017**, *201*, 351–367.
- [41] R. J. Comito, K. J. Fritzsching, B. J. Sundell, K. Schmidt-Rohr, M. Dincă, *J. Am. Chem. Soc.* **2016**, *138*, 10232–10237.
- [42] P. Ji, J. B. Solomon, Z. Lin, A. Johnson, R. F. Jordan, W. Lin, *J. Am. Chem. Soc.* **2017**, *139*, 11325–11328.
- [43] M. Rivera-Torrente, P. D. Pletcher, M. K. Jongkind, N. Nikolopoulos, B. M. Weckhuysen, *ACS Catal.* **2019**, *9*, 3059–3069.
- [44] M. J. Vitorino, T. Devic, M. Tromp, G. Férey, M. Visseaux, *Macromol. Chem. Phys.* **2009**, *210*, 1923–1932.
- [45] H. D. Park, R. J. Comito, Z. Wu, G. Zhang, N. Ricke, C. Sun, T. Van Voorhis, J. T. Miller, Y. Román-Leshkov, M. Dincă, *ACS Catal.* **2020**, *10*, 3864–3870.
- [46] T. A. Goetjen, J. Liu, Y. Wu, J. Sui, X. Zhang, J. T. Hupp, O. K. Farha, *Chem. Commun.* **2020**, *56*, 10409–10418.
- [47] B. V. K. J. Schmidt, *Macromol. Rapid Commun.* **2020**, *41*, 1900333–1900361.
- [48] S. Floyd, K. Y. Choi, T. W. Taylor, W. H. Ray, *J. Appl. Polym. Sci.* **1986**, *32*, 2935–2960.
- [49] F. M. McMillan, *Applied Polymer Sciences*, in *ACS Symposium Series*, American Chemical Society, Washington DC, USA, **1985**, 333–361.
- [50] P. Galli, G. Vecellio, *Prog. Polym. Sci.* **2001**, *26*, 1287–1336.
- [51] A. Sonnauer, F. Hoffmann, M. Fröba, L. Kienle, V. Duppel, M. Thommes, C. Serre, G. Férey, N. Stock, *Angew. Chem. Int. Ed.* **2009**, *48*, 3791–3794.
- [52] P. Chowdhury, S. Mekala, F. Dreisbach, S. Gumma, *Micropor. Mesopor. Mater.* **2012**, *152*, 246–252.
- [53] A. Buragohain, S. Couck, P. Van Der Voort, J. F. M. Denayer, S. Biswas, *J. Solid State Chem.* **2016**, *238*, 195–202.
- [54] G. Férey, C. Serre, C. Mellot-Draznieks, F. Millange, S. Surblé, J. Dutour, I. Margiolaki, *Angew.*

- Chem. Int. Ed.* **2004**, *43*, 6296–6301.
- [55] C. Serre, F. Millange, C. Thouvenot, M. Noguès, G. Marsolier, D. Louër, G. Férey, *J. Am. Chem. Soc.* **2002**, *124*, 13519–13526.
- [56] X. Li, J. Zhang, W. Shen, S. Xu, *Mater. Lett.* **2019**, *255*, 126519–126531.
- [57] L. Han, J. Zhang, Y. Mao, W. Zhou, W. Xu, Y. Sun, *Ind. Eng. Chem. Res.* **2019**, *58*, 15489–15496.
- [58] L. J. Murray, M. Dinca, J. Yano, S. Chavan, S. Bordiga, C. M. Brown, J. R. Long, *J. Am. Chem. Soc.* **2010**, *132*, 7856–7857.
- [59] T. Agapie, S. J. Schoffr, J. A. Labinger, J. E. Bercaw, *J. Am. Chem. Soc.* **2004**, *126*, 1304–1305.
- [60] T. Agapie, *Coord. Chem. Rev.* **2011**, *255*, 861–880.
- [61] M. P. McDaniel, *Adv. Catal.* **1983**, *33*, 47–98.
- [62] M. N. Cardoso, A. G. Fisch, *Ind. Eng. Chem. Res.* **2016**, *55*, 9426–9432.
- [63] W. Zhang, Z. Wu, H. Mao, X. Wang, J. Li, Y. Mai, J. Yu, *R. Soc. Open Sci.* **2020**, *7*, 20063–20074.
- [64] A. Alizadeh, T. F. L. McKenna, *Macromol. React. Eng.* **2018**, *12*, 1700024–1700051.
- [65] H. D. Chanzy, J. F. Revol, R. H. Marchessault, A. Lamandé, *Kolloid-Zeitschrift Zeitschrift für Polym.* **1973**, *251*, 563–576.
- [66] Y. Liu, J. Her, A. Dailly, A. J. Ramirez-Cuesta, D. A. Neumann, C. M. Brown, *J. Am. Chem. Soc.* **2008**, *130*, 11813–11818.
- [67] A. V. Neimark, F. X. Coudert, C. Triguero, A. Boutin, A. H. Fuchs, I. Beurroies, R. Denoyel, *Langmuir* **2011**, *27*, 4734–4741.
- [68] R. A. Schoonheydt, *Chem. Soc. Rev.* **2010**, *39*, 5051–5066.
- [69] B. M. Weckhuysen, L. M. De Ridder, R. A. Schoonheydt, *J. Phys. Chem.* **1993**, *97*, 4756–4763.
- [70] B. M. Weckhuysen, A. A. Verberckmoes, A. R. De Baets, R. A. Schoonheydt, *J. Catal.* **1997**, *166*, 160–171.
- [71] B. M. Weckhuysen, R. A. Schoonheydt, *Catal. Today* **1999**, *49*, 441–451.
- [72] K. I. Hadjiivanov, G. N. Vayssilov, *Adv. Catal.* **2002**, *47*, 307–511.
- [73] R. A. Dodson, A. J. Matzger, *ACS Mater. Lett.* **2019**, *1*, 344–349.
- [74] R. A. Dodson, A. G. Wong-Foy, A. J. Matzger, *Chem. Mater.* **2018**, *30*, 6559–6565.
- [75] D. Y. Hong, Y. K. Hwang, C. Serre, G. Férey, J. S. Chang, *Adv. Funct. Mater.* **2009**, *19*, 1537–1552.
- [76] T. Tanasaro, K. Adpakpang, S. Ittisanronnachai, K. Faungnawakij, T. Butburee, S. Wannapaiboon, M. Ogawa, S. Bureekaew, *Cryst. Growth Des.* **2018**, *18*, 16–21.
- [77] J. J. Du, Y. P. Yuan, J. X. Sun, F. M. Peng, X. Jiang, L. G. Qiu, A. J. Xie, Y. H. Shen, J. F. Zhu, *J. Hazard. Mater.* **2011**, *190*, 945–951.
- [78] H. Embrechts, M. Kriesten, M. Ermer, W. Peukert, M. Hartmann, M. Distaso, *RSC Adv.* **2020**, *10*, 7336–7348.
- [79] S. H. Lo, D. Senthil Raja, C. W. Chen, Y. H. Kang, J. J. Chen, C. H. Lin, *Dalt. Trans.* **2016**, *45*, 9565–9573.
- [80] E. Biemmi, S. Christian, N. Stock, T. Bein, *Micropor. Mesopor. Mater.* **2009**, *117*, 111–117.
- [81] F. Wang, H. Guo, Y. Chai, Y. Li, C. Liu, *Micropor. Mesopor. Mater.* **2013**, *173*, 181–188.
- [82] M. Shôâeë, J. R. Agger, M. W. Anderson, M. P. Attfield, *CrystEngComm* **2008**, *10*, 646–648.





# Chapter 6

## Summary, Outlook, and Conclusions

### Abstract

This **Ph.D. Thesis** describes the use of chromium for ethylene polymerization and revolved around the usage of two types of polymerization platforms: conventional Cr/SiO<sub>2</sub> Phillips-type ethylene polymerization catalysts and Cr-based Metal-Organic Framework (MOF) polymerization catalysts. The focus was specifically on using (semi-)batch ethylene polymerization reactions, advanced spectroscopic and microscopic techniques, and polymer characterization techniques, to investigate the effect of metal-alkyl co-catalysts on catalyst performances, active site generation, structure-morphology relationships, and polyethylene (PE) product properties. This **Chapter** summarizes the most important findings of the chapters and gives recommendations for further research avenues into investigating the role of chromium in ethylene polymerization and the critical role that metal-alkyl co-catalysts fulfil in this commercially important reaction.

## 6.1 Summary

This **Ph.D. Thesis** aims to elucidate the role of chromium in ethylene polymerization as well as the critical role of metal-alkyl compounds as co-catalysts in enabling and tailoring the ethylene polymerization reaction. Figure 6.1 provides a schematic illustration of the contents of this **Ph.D. Thesis**.

**Chapter 1** introduces the topic of polymers, starting with describing the concept of polymers and the role that predominantly synthetic polymers nowadays have in everyday life. To that end, an overview of the global annual polymer production is given as well as an overview of the different synthetic polymers that contribute to this, demonstrating that polyolefins have the largest market volume share. Hereafter, the three grand catalytic workhorses that are used in

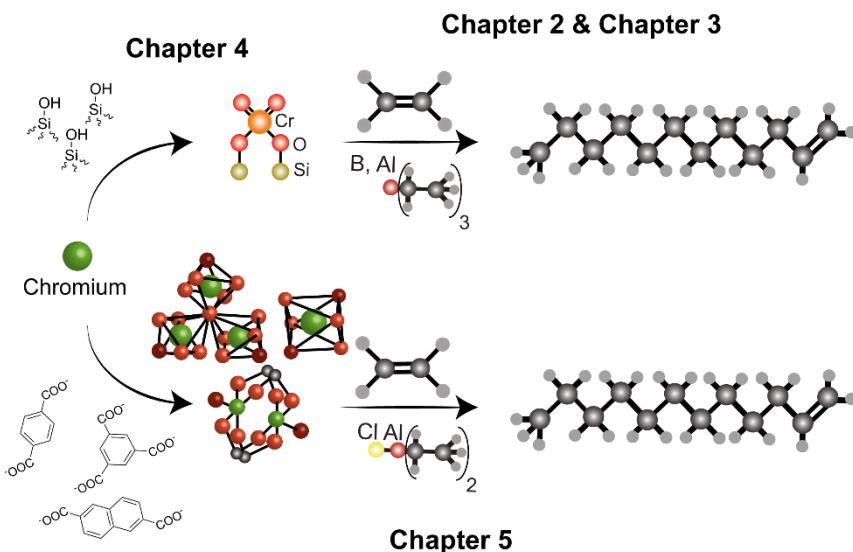


**Figure 6.1.** Schematic illustration of the contents of this **Ph.D. Thesis**. **Chapter 2** describes our investigations towards the effect of tri-ethyl borane and tri-ethyl aluminum as metal-alkyl co-catalysts on the bulk performances and PE densities. The second part of this chapter describes how UV-Vis-NIR diffuse reflectance spectroscopy (DRS) was used to investigate the different redox chemistries, which provided part of the answer for the unique bulk performances. **Chapter 3** describes how the metal-alkyl co-catalysts affect the polyethylene (PE) properties on the bulk scales, after which Scanning Transmission X-ray Microscopy (STXM) was used to investigate whether these differences already existed in the early stages and whether the growth of PE was homogeneous through the catalyst material. In **Chapter 4** we zoom out and use Raman spectroscopy to investigate the Cr<sup>6+</sup> surface structures and discuss the effects of CO, H<sub>2</sub> and H<sub>2</sub> at various temperatures on these surface structures. **Chapter 5** describes an approach in which Cr-based Metal Organic Frameworks (MOFs) were used as ethylene polymerization catalysts. This chapter includes a systematic investigation towards PE properties, the formation of the active sites, structure/morphology relationships and leaching investigations.

the catalytic olefin polymerization are briefly highlighted, with a focus on the Cr/SiO<sub>2</sub> Phillips catalyst since the majority of this **Ph.D. Thesis** revolves around this catalyst system. Subsequently, some of the strengths as well as challenges surrounding the Cr/SiO<sub>2</sub> Phillips catalyst are discussed, so that the reader can appreciate the challenging and delicate nature of this catalyst system. Hereafter, Metal-Organic Frameworks (MOFs) are introduced as Cr-based ethylene polymerization catalysts with a discussion of some of the most relevant and recent examples are discussed. This **Chapter** ends with an outline of this **Ph.D. Thesis** along with a summary of each chapter's contents.

Then we discuss the effect of tri-ethyl borane (TEB) and tri-ethyl aluminum (TEAl) on the performances of an industrial Cr/SiO<sub>2</sub> Phillips catalyst in **Chapter 2**. We found that the induction period, defined as the time between the introduction of ethylene into the reactor and the onset of polymerization, reached a minimum of 8 min regardless of the type and amount of co-catalyst. Both co-catalysts significantly raised the catalytic activity, albeit TEB did so to a larger extent. However, TEB was related to decreasing catalyst activities and slower kinetic profiles at excess amounts, related to deactivation of the catalyst material. In contrast, TEAl enhanced the catalyst activity to a relatively smaller extent, but large usage of larger amounts was not related to decreasing activities and kinetic profiles, indicating the absence of catalyst deactivation at these amounts. This Chapter also demonstrates the ability to tailor the PE density around the benchmark value of a PE produced without any co-catalyst: TEB predominantly raised the density and TEAl decreased the density.

The observed differences in bulk catalyst performances and PE densities inferred that the co-catalysts generated unique active sites. To that end, we have used in-situ UV-Vis-NIR diffuse reflectance spectroscopy (DRS) to investigate the redox chemistry as a function of type and amount of co-catalyst. These experiments revealed that indeed unique activation pathways were enabled by the two co-catalysts. TEAl produced a mixture of Cr sites, specifically mono-grafted Cr<sup>2+</sup>, inaccessible Cr<sup>3+</sup> and bis-alkyl Cr<sup>4+</sup> sites. Activation with TEB produced a combination of Cr<sup>2+</sup> as well as inaccessible Cr<sup>3+</sup> sites, furthermore Cr<sup>4+</sup> cannot be excluded. Furthermore, we also found that increased amounts of TEB resulted in the increased formation of Cr<sup>3+</sup> species, likely explaining the decreasing catalytic activities with increased amounts of TEB. On the other hand, increased amounts of TEAl resulted in a relatively larger number of mono-grafted Cr<sup>2+</sup> sites, which were related to larger numbers of Short-Chain Branches (SCB).

**Chapter 3** builds further on finding that selecting the proper type and amount of co-catalyst can be used as a strategy to attain different PE densities. First, Gel Permeation Chromatography (GPC) experiments were used to investigate the effect of the type and amount of co-catalyst on the Molecular Weight Distribution (MWD) and SCB. This revealed that TEB broadens the MWD to a larger extent than TEAl, the latter co-catalyst only minimally broadening the MWD at lower amounts and slightly more at larger amounts. The amount of SCB was more significant with TEAl than with TEB, unless larger amounts of TEB were used. These findings directly rationalize the

diverging densities: the broader MWD with TEB infers a relatively number of smaller PE chains, which can co-crystallize between larger PE chains, hereby increasing the PE density. In contrast, this was absent with TEAl while this co-catalyst did result in enhanced SCB that hampers efficient crystallization, resulting in the decreased PE density.

The second part of this Chapter focused on understanding if these differences already existed in the early stages of ethylene polymerization, and whether the PE was homogeneously distributed through the catalyst material. To that end, Scanning Transmission X-ray Microscopy (STXM) was exploited to investigate the densities of early-stage PE materials produced with 1.5 and 5.0 molecular equivalents of respectively TEAl and TEB, with limited catalyst yields of 1-2 g<sub>PE</sub>cat<sup>-1</sup>. STXM revealed that the early-stage PE materials were homogeneously distributed in the material and only differed minimally in terms of density, with the materials produced with TEAl arguably demonstrating slightly lower densities. Thus, albeit minor, the differences indeed already exist in the early stages of polymerization. Second, this Chapter revealed that the densities of these early-stage PE materials were lower. This indicates that at low catalyst yields, the PE is still dispersed within the SiO<sub>2</sub> support framework, which restricts free crystallization and results in the lower densities of these early-stage PE materials.

In **Chapter 4** we exploited the Cr<sup>6+</sup>=O bond polarizability to investigate the surface structures of a Cr/SiO<sub>2</sub> Phillips-type ethylene polymerization catalyst and the effect of CO, H<sub>2</sub> and C<sub>2</sub>H<sub>4</sub> as reducing agents at various temperatures. These experiments revealed two types of surface sites, related to the Cr<sup>6+</sup><sub>di-oxo</sub> structure contributing to the Raman spectrum at 985 cm<sup>-1</sup> and the Cr<sup>6+</sup><sub>mono-oxo</sub> structures contributing to the Raman spectrum at 1005 cm<sup>-1</sup>, which was further corroborated by performing in-situ CO/<sup>18</sup>O<sub>2</sub> reduction/re-oxidation experiments. Performing the reductions at various temperatures revealed that H<sub>2</sub> was more proficient at reducing the Cr<sup>6+</sup>=O surface structures than CO up until temperatures of 300 °C, by surpassing this temperature the performances of CO and H<sub>2</sub> converged. Last but not least, we found that C<sub>2</sub>H<sub>4</sub> does not quantitatively remove the Cr<sup>6+</sup>=O Raman signals, suggesting that reduction at 1 atm is insufficient to reduce all Cr<sup>6+</sup> sites.

**Chapter 5** discusses an approach in which three renowned MOFs (MIL-101(Cr)-NDC, MIL-53(Cr), and HKUST-1(Cr)) were used for ethylene polymerization, with Et<sub>2</sub>AlCl as the co-catalyst. These experiments revealed that the catalytic activity strongly depends on the selected MOF, with MIL-101(Cr)-NDC and MIL-53(Cr) demonstrating appreciable catalytic activities and HKUST-1(Cr) demonstrating poor catalytic activity. Investigations into the PE product revealed that only MIL-101(Cr)-NDC produces favorable PE beads, whereas MIL-53(Cr) produced unfavorable worm-like morphologies and HKUST-1(Cr) produced both beads and fibers. Analysis of the MOFs revealed products with broad MWDs, related to PE production over a large variety of active sites rather than one single site.

The second part of this Chapter focused on investigating the activation procedure with a variety of spectroscopic experiments. These experiments revealed that the co-catalyst indeed

produced a variety of active sites, except with HKUST-1(Cr), which appeared to be largely unaltered by the activation procedure with the co-catalyst. On the other hand, MIL-101(Cr)-NDC and MIL-53(Cr) were activated to a larger extent, which coincides with the more appreciable catalyst activities. Thus, these experiments revealed that the propensity of the MOF to react with the co-catalyst is in fact critical for attaining catalytic activity.

However, these findings could also be interpreted as collapse of the MOF due to the co-catalyst. The third part of this Chapter served to answer whether this was the case by means of assessing the effect of the Et<sub>2</sub>AlCl co-catalyst on the surface area, the morphology and the bonds comprising the MOF. Even though the surface area decreased, the MOFs remained porous, even after activation with the co-catalyst, demonstrating that the MOFs do not collapse. These findings were further corroborated by the fact that Scanning Electron Microscopy (SEM) revealed that the morphology of the MOF materials remained intact after activation with the co-catalyst. Furthermore, Diffuse Reflectance Infrared Spectroscopy (DRIFTS) experiments revealed that the chemical bonds comprising the MOF remained intact.

**In summary**, this **Ph.D. Thesis** demonstrates that still new insights are (to be) obtained into the role of chromium in ethylene polymerization, even though this specific element has been at the center of ethylene polymerization for well over half a century. Additionally, the use of chromium-based MOFs revealed an entire new field of opportunities in the use of chromium for ethylene polymerization, which is a field of research in which a wealth of knowledge is to be gained.

## 6.2 Outlook

### 6.2.1 Phillips-type Ethylene Polymerization

A number of ideas and questions have emerged from this **Ph.D. Thesis**. Ethylene polymerization will continue to fulfil a prominent role in our society in the decades to come, and despite being coined as mature research field, great improvements can still be achieved. First, while it is known that co-catalysts affect catalyst performances and PE properties, to date the effects are mainly investigated on a *per case* basis. In line with increased catalyst performances, improved catalyst/product relationships, and e.g., improved resource allocation it is critical to generate libraries with co-catalyst/catalyst relationships in terms of performances and PE product properties. Such research would include systematic investigations into the effect of co-catalysts on the exact active site structure since unique active site/performance relationships proliferate. Collaborations between academia and industrial groups are critical in order to achieve this goal since the former group is often more involved in fundamental research, including synchrotron-based experiments, and the latter group has better access to tools for investigating catalyst performances as well as investigating the PE properties.<sup>[1,2]</sup>

Third, this catalytic system is defined by a large variety of active sites and the knowledge on bulk systems has greatly increased in recent years. However, these investigations are often limited by examining bulk systems rather than trying to disentangle the structure/activity relationships at size dimensions at which the Cr surface structure heterogeneities exist. Recent examples from our group include the usage of correlated ptychography X-ray fluorescence microscopy to investigate the catalyst fragmentation of a MgCl<sub>2</sub> supported Ziegler-Natta catalyst, in which 3D images and videos were produced that visualized the catalyst fragmentation as well as the 3D distribution of catalyst relevant elements and a second study exploiting X-ray Nanotomography to study the fragmentation of a large ensemble of Ziegler-Natta catalysts.<sup>[3,4]</sup> Furthermore, a second example exploited 3-D X-ray Nanotomography to reveal different mechanisms of coke deposition within one single Fluid Catalytic Cracking (FCC) catalyst particle.<sup>[5]</sup> With these techniques, it is possible to disentangle the exact contribution of the different types of Cr surface sites to catalytic performances in terms of e.g. polymerization and fragmentation.

### 6.2.2 Cr-based Metal-Organic Framework Ethylene Polymerization

The recent developments of MOFs in ethylene polymerization predict an exciting future for the application of these materials in the field of polyolefins, with the possibility of providing single-site ethylene polymerization catalysts.<sup>[6–9]</sup> Their performances are understandably not (yet) comparable to those of the optimized three grand workhorses, however these compounds are still in a very early stage of catalyst optimization. To date, assessing the suitability of MOFs is mainly done on a *per case* basis, which would greatly benefit from the possibility to do high-throughput catalytic testing. Such an approach would benefit our understanding into the role of MOFs two-fold. Firstly, one can quickly assess a wide variety of metal-node geometries and pore geometries for ethylene polymerization activity and polymer product properties. Secondly, such an approach simultaneously enables systematic investigations into the effect of the type and amount of co-catalyst on the bulk catalyst performances.<sup>[10]</sup>

Second, understanding the prerequisites for polymerization is critical for understanding the working state of MOFs in ethylene polymerization. Our work has revealed that parameters, such as active site spacing and propensity to react with the co-catalysts, are important to consider for structure/performance relationships. Experience from our group with Atomic Force Microscopy (AFM) could, for example, help in deducing the minimal active site spacing required for favorable PE morphologies. Additionally, this technique could also help in understanding how activation with co-catalysts affects the MOF surface morphology with nanometer scale precision. Completely understanding the role of MOFs would, however, require an interdisciplinary approach, exploiting a broad array of advanced spectroscopic, and microscopic techniques, as well as the ability to model MOFs and compute their interaction with e.g. co-catalysts and ethylene.<sup>[11]</sup> Nevertheless, MOFs show great promise as (potential single site) ethylene

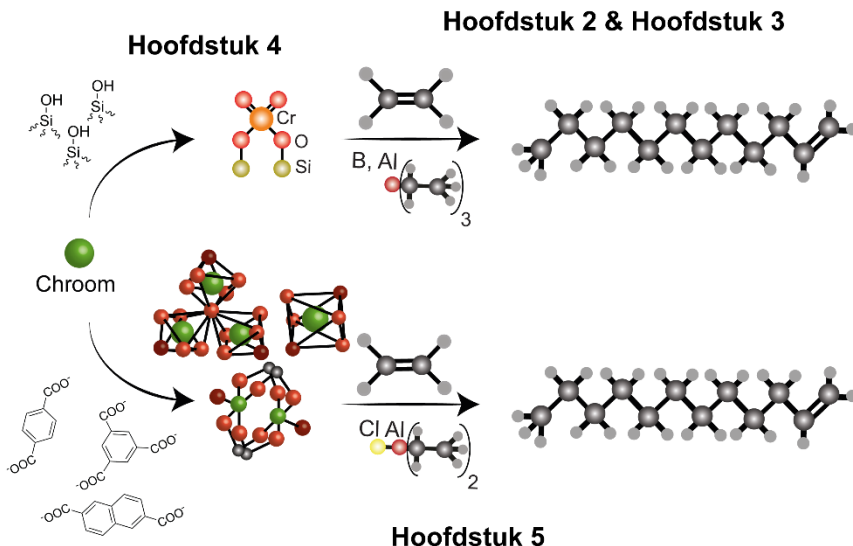
polymerization catalysts. However, owing to the maturity of the polyolefin industry, interdisciplinary research efforts from both industry and academia can aid in MOFs finding their place in the ethylene polymerization reaction.

### 6.3 References

- [1] E. Groppo, G. A. Martino, A. Piovano, C. Barzan, *ACS Catal.* **2018**, *8*, 10846–10863.
- [2] G. A. Martino, A. Piovano, C. Barzan, J. Rabeah, G. Agostini, A. Bruekner, G. Leone, G. Zanchin, T. Monoi, E. Groppo, *ACS Catal.* **2020**, *10*, 2694–2706.
- [3] K. W. Bossers, R. Valadian, S. Zanoni, R. Smeets, N. Friederichs, J. Garrevoet, F. Meirer, B. M. Weckhuysen, *J. Am. Chem. Soc.* **2020**, *142*, 3691–3695.
- [4] K. W. Bossers, R. Valadian, J. Garrevoet, S. van Malderen, R. Chan, N. Friederichs, J. Severn, A. Wilbers, S. Zanoni, M. K. Jongkind, B. M. Weckhuysen, F. Meirer, *JACS Au* **2021**, *1*, 3059–3069.
- [5] M. Veselý, R. Valadian, L. Merten Lohse, M. Toepperwien, K. Spiers, J. Garrevoet, E. T. C. Vogt, T. Salditt, B. M. Weckhuysen, F. Meirer, *ChemCatChem* **2021**, *13*, 2494–2507.
- [6] H. D. Park, R. J. Comito, Z. Wu, G. Zhang, N. Ricke, C. Sun, T. Van Voorhis, J. T. Miller, Y. Román-Leshkov, M. Dincă, *ACS Catal.* **2020**, *10*, 3864–3870.
- [7] R. J. Comito, K. J. Fritzsching, B. J. Sundell, K. Schmidt-Rohr, M. Dincă, *J. Am. Chem. Soc.* **2016**, *138*, 10232–10237.
- [8] P. Ji, J. B. Solomon, Z. Lin, A. Johnson, R. F. Jordan, W. Lin, *J. Am. Chem. Soc.* **2017**, *139*, 11325–11328.
- [9] B. V. K. J. Schmidt, *Macromol. Rapid Commun.* **2020**, *41*, 1900333–1900358.
- [10] T. A. Goetjen, J. Liu, Y. Wu, J. Sui, X. Zhang, J. T. Hupp, O. K. Farha, *Chem. Commun.* **2020**, *56*, 10409–10418.
- [11] L. D. B. Mandemaker, M. Rivera-Torrente, R. Geitner, C. M. Vis, B. M. Weckhuysen, *Angew. Chem. Int. Ed.* **2020**, *59*, 19545–19552.

# Nederlandse Samenvatting

Deze **Ph.D. Thesis** is geschreven om de rol van chroom in etheen polymerisatie te beschrijven, en misschien belangrijker, de rol die metaal-alkyl verbindingen spelen in dit proces. De inhoud van deze **Ph.D. Thesis** is schematische weergegeven in Samenvattend Figuur 1.



**Samenvattend Figuur 1.** Schematische weergave van de inhoud van dit proefschrift. **Hoofdstuk 2** beschrijft het onderzoek naar de invloed van metaal-alkyl verbindingen als co-katalysatoren op de katalytische activiteit, de inductieperiode, en de polyethyleen (PE) dichtheid. Vervolgens werd met behulp van UV-Vis-NIR diffuse reflectance spectroscopy (DRS) de Cr redoxchemie onderzocht en de resultaten verklaarden tot op zekere hoogte de verschillen in de katalytische eigenschappen van de bulk katalysator. **Hoofdstuk 3** beschrijft wat de invloed is van de co-katalysatoren op bulk PE-eigenschappen, zoals moleculaire gewichtsverdeling (MWD) en korte zijketenvertakking. Hierna werd Scanning Transmissie X-ray Microscopie (STXM) gebruikt om te onderzoeken of deze verschillende eigenschappen al bestonden in de vroege stadia van etheen polymerisatie en of de vorming van PE homogeen was in het katalysatordeeltje in deze vroege stadia. In **Hoofdstuk 4** wordt een stap teruggenomen en gebruiken we Raman spectroscopie om de oppervlaktestructuren van  $\text{Cr}^{6+}/\text{SiO}_2$  te onderzoeken, waarna ook het effect van  $\text{CO}$ ,  $\text{H}_2$  en  $\text{C}_2\text{H}_4$  bij verschillende temperaturen op de oppervlaktestructuren werd onderzocht. **Hoofdstuk 5** beschrijft een onderzoek waarin Cr-gebaseerde Metal-Organic Frameworks (MOFs) centraal stonden als etheen polymerisatie katalysatoren. Daarnaast bevat dit hoofdstuk een systematisch onderzoek naar de invloed van het type MOF en co-katalysator op de eigenschappen van het geproduceerde PE, het ontstaan van de actieve katalysator, structuur/morfologie relaties, en de uitloging van de actieve structuur.

**Hoofdstuk 1** geeft een algemene introductie in het onderwerp van polymeren alsook in de rol die synthetische polymeren hebben in onze hedendaagse maatschappij. Daarom wordt de wereldwijde polymeer productie besproken, met als doel de variatie aan verschillende soorten polymeren te laten zien en om te illustreren dat binnen de polymeerchemie de polyolefinen het grootste marktaandeel hebben. Hierna worden de drie katalytische werkpaarden besproken die de grootschalige polyolefine productie mogelijk maken. Gezien deze **Ph.D. Thesis** draait om het gebruik van chroom, wordt de Cr gebaseerde Phillips katalysator uitgebreid besproken, met als doel de gevoeligheid voor bijvoorbeeld zuurstof en de uitdagingen omtrent het gebruik van deze katalysator te illustreren. Vervolgens worden Metal-Organic Frameworks (MOFs) aan de hand van een aantal recente voorbeelden geïntroduceerd als polymerisatiekatalysatoren, met de potentie om als geïmmobiliseerde single-site katalysatoren gebruikt te worden.

Hierna wordt in **Hoofdstuk 2** het effect van tri-ethyl boraan (TEB) en tri-ethyl aluminium (TEAI) als co-katalysatoren op de prestaties van een industriële Cr/SiO<sub>2</sub> Phillips katalysator besproken. Hierin wordt besproken hoe de inductieperiode, gedefinieerd als de tijd tussen het moment van introductie van etheen in de reactor en de daadwerkelijke start van polymerisatie, een minimum van 8 minuten bereikt, ongeacht het type gebruikte co-katalysator. Daarnaast verhoogden beide co-katalysatoren de katalytisch activiteit, maar TEB deed dit sterker dan TEAI. Daartegenover stond wel dat verhoogde hoeveelheden TEB gerelateerd waren aan afnemende katalysatorprestaties, mogelijkerwijs veroorzaakt door deactivatie van de actieve plaatsen. TEAI verhoogde de katalytische activiteit minder, maar had niet als nadeel dat verhoogde hoeveelheden resulteerde in afnemende katalysatorprestaties.

Daarnaast werd ook in dit hoofdstuk besproken hoe het mogelijk is om de PE dichtheid te controleren rondom een benchmark waarde door het selectief toepassen van het juiste type en de juiste hoeveelheid co-katalysator. Hierin verhoogde TEB de PE dichtheid, terwijl TEAI juist de PE dichtheid verlaagde.

De observaties omtrent bulk katalysator prestaties en verschillende PE dichtheden deden vermoeden dat de verschillende co-katalysatoren resulteerden in verschillende manieren waarop de actieve plaats gegenereerd werd. Daartoe werden in-situ UV-Vis-NIR diffuse reflectance spectroscopy (DRS) metingen gebruikt om de redox chemie van de Cr centra als functie van type en hoeveelheid co-katalysator te onderzoeken. Deze experimenten onthulden inderdaad dat de redoxchemie verschilt afhankelijk van het type en hoeveelheid co-katalysator. Bij het gebruik van TEAI werd een variatie aan oppervlaktestructuren gegenereerd, zoals enkelgebonden Cr<sup>2+</sup> structuren, ontoegankelijke Cr<sup>3+</sup> structuren en bis-alkyl Cr<sup>4+</sup> structuren. Daarnaast genereerde TEB actieve plaatsen, die verschilden van de met TEAI gegenereerde actieve plaatsen. Ook onderling was er onderscheid te maken tussen verschillende structuren bij het gebruik van TEB, zoals Cr<sup>2+</sup> structuren alsook Cr<sup>3+</sup> structuren, maar ook Cr<sup>4+</sup> is een mogelijke structuur en kan niet uitgesloten worden. Daarnaast hebben we gevonden dat verhoogde

hoeveelheden co-katalysator gerelateerd zijn aan de verhoogde vorming van Cr<sup>3+</sup>, wat waarschijnlijk een inactieve structuur is.

In **Hoofdstuk 3** wordt verder gebouwd op de bevindingen dat de PE eigenschappen naar wens aangepast kunnen worden door het selecteren van het juiste type en de juiste hoeveelheid co-katalysator. In eerste instantie werd met Gel Permeatie Chromatografie (GPC) onderzocht hoe de verschillende types en hoeveelheid co-katalysator de verdeling van verschillende PE ketens beïnvloeden (MWD, moleculaire gewichtsverdeling). Hier vonden wij dat polymerisatie met TEB resulterde in een bredere verdeling dan polymerisatie met TEAI, tenzij hoge hoeveelheden TEAI gebruikt werden. Vervolgens werden ook de verschillen in de inbouw van zijketens onderzocht met behulp van <sup>13</sup>C kernspinresonantie, wat onthulde dat TEAI een grotere hoeveelheid aan korte zijketens produceerde dan TEB. Deze verschillende eigenschappen verklaarden ook de verschillende PE dichtheden. De hogere dichtheid met TEB werd bewerkstelligd door co-kristallisatie van de kleinere PE ketens tussen de grotere PE ketens. Een soortgelijk proces werd gehinderd bij het gebruik van TEAI doordat hier een relatief kleinere hoeveelheid aan korte PE ketens was als ook door de hogere hoeveelheid korte zijketenvertakking, welke het netjes stapelen van PE ketens verhinderd.

Het tweede deel van dit hoofdstuk beschrijft het gebruik van Scanning Transmissie X-ray Microscopie (STXM) om te onderzoeken of deze verschillende dichtheden al in de vroege stadia van etheen polymerisatie bestonden en of de productie van PE homogeen was door het katalysatordeeltje. Daarom hebben wij polymeermaterialen onderzocht met deze methode waarin de katalysator opbrengsten minimaal waren ( $1\text{-}2 \text{ g}_{\text{PE}}\text{cat}^{-1}$ ), zodat het polymeermateriaal nog nauw verweven zat in de katalysator. Dergelijke experimenten zijn uitgevoerd voor zulke materialen die geproduceerd zijn met respectievelijk 1.5 en 5.0 moleculaire equivalenten van de co-katalysatoren TEB en TEAI. De resultaten lieten zien dat de groei van PE homogeen verdeeld was door het katalysatordeeltje. De materialen geproduceerd met TEAI vertoonden iets lagere dichtheden dan de materialen TEB, desondanks waren de verschillen minimaal. Maar, de resultaten wezen wel uit dat deze materialen beduidend verschilden van bulk referenties. Dit was te verklaren aan de hand van het feit dat het PE materiaal nog grotendeels gevangen zat in het dragermateriaal, waardoor het niet vrij kon kristalliseren. Mocht het polymerisatieproces ongeremd doorgaan, dan zal uiteindelijk het dragermateriaal desintegreeren en zal dit opgelost worden in het groeiende polymeer, vanaf welk moment de kristallisatie van het polymeer niet meer gehinderd wordt.

In **Hoofdstuk 4** is geprofiteerd van de polariseerbaarheid van de Cr<sup>6+</sup>=O verbinding om de Cr oppervlaktestructuren van een Cr/SiO<sub>2</sub> Phillips katalysator te kunnen onderzoeken. Hierin gebruikten wij een Raman microscoop om de invloed van CO, H<sub>2</sub> en C<sub>2</sub>H<sub>4</sub> tijdens reductie en <sup>18</sup>O<sub>2</sub> tijdens oxidatie bij verschillende temperaturen te onderzoeken. Dit leidde tot de mogelijkheid om twee verschillende oppervlaktestructuren te onderscheiden, één die een Raman signaal bij 985 cm<sup>-1</sup> gaf en één die een Raman signaal bij 1005 cm<sup>-1</sup> gaf, die respectievelijk toegeewezen

werden aan Cr<sup>6+</sup><sub>di-oxo</sub> oppervlaktestructuren en Cr<sup>6+</sup><sub>mono-oxo</sub> oppervlaktestructuren. De experimenten met CO en H<sub>2</sub> lieten zien dat de bij het eerste signaal horende oppervlaktestructuren relatief makkelijker reduceren. Daarnaast wezen deze experimenten uit dat H<sub>2</sub> effectiever was in het reduceren van het katalysatormateriaal bij lagere temperaturen dan CO. Maar, naarmate hogere temperaturen gebruikt werden, presteerden beide reductiegassen hetzelfde.

Het gebruik van etheen liet zien dat uitsluitend deels gereduceerde systemen geproduceerd werden, waarbij voornamelijk de oppervlaktestructuren toebehorend aan het eerste Raman signaal gereduceerd werden. Daarnaast lieten deze experimenten zien dat het spectroscopische eindpunt al binnen 6 minuten bereikt is.

In **Hoofdstuk 5** werd een drietal Metal-Organic Frameworks (MOFs) als ethyleen polymerisatiekatalysatoren onderzocht: MIL-101(Cr)-NDC, MIL-53(Cr) en HKUST-1(Cr), met Et<sub>2</sub>AlCl als co-katalysator. In dit hoofdstuk werd duidelijk dat de activiteit sterk afhangt van de geselecteerde MOF, waar de eerste twee MOFs beduidend actiever zijn dan de laatste MOF. Onderzoek naar het PE product liet zien dat uitsluitend MIL-101(Cr)-NDC morfologisch gunstig PE produceerde, terwijl MIL-53(Cr) PE produceerde waarvan de morfologie op wormen leek, en HKUST-1(Cr) PE produceerde waarvan de morfologie zowel gunstige PE ballen als ongunstige PE fibers had. Verder liet analyse van het PE materiaal ook zien dat deze materialen een brede gewichtsspreiding hadden, wat betekende dat deze katalysatoren niet als single-site katalysatoren beschouwd konden worden in hun actieve vorm, terwijl de onaangename materialen juist wel als single-site materialen gedefinieerd zijn. Daarom moet juist de reactie met de co-katalysator een belangrijke parameter zijn in de vorming van de actieve fase, waarin een breed scala aan Cr sites verantwoordelijk is voor de polymerisatie.

In het tweede deel werd deze activatieprocedure onderzocht met een aantal spectroscopische technieken. Deze experimenten wezen inderdaad uit dat de activatie van de MOF gerelateerd was aan de vorming van een breed scala aan Cr structuren, met uitzondering van HKUST-1(Cr). De experimenten wezen uit dat HKUST-1(Cr) vrijwel onaangename was door de co-katalysatoren. Met het oog op de verkregen resultaten, en op de verschillende katalytische activiteiten, konden wij concluderen dat activering van het MOF materiaal door de co-katalysator noodzakelijk is voor het verkrijgen van polymerisatieactiviteit.

De vorming van een breed scala aan actieve centra wees mogelijkwijs op het instorten van het MOF materiaal. De invloed van de co-katalysator op de MOF morfologie, de grootte van het MOF oppervlak en de MOF verbindingen werd onderzocht met respectievelijk Scanning Electron Microscopie (SEM), N<sub>2</sub> fysisorptie en infraroodspectroscopie, en de uitkomsten sloten uiteenvallen van de MOF uit en toonden aan dat polymerisatie daadwerkelijk over de MOF plaats vond.

**Samenvattend**, dit proefschrift laat zien dat ondanks dat chroom al meer dan een halve eeuw wordt gebruikt als actief katalysatorelement in de productie van kunststoffen, er nog steeds

nieuwe aspecten boven tafel komen door het gebruik van geavanceerde microscopische en spectroscopische technieken. Daarnaast laat het gebruik van chroom-gebaseerde MOFs zien dat er nieuwe mogelijkheden zijn bij het gebruik van chroom in etheen polymerisatie, waarin nog een wereld van kennis te vergaren is.



## Appendix A. List of Abbreviations

<b>BET:</b> Brunauer-Emmett-Teller	<b>NEXAFS:</b> Near Edge X-ray Absorption Fine Structure
<b>BTC:</b> 1,3,5-Benzenetricarboxylate (trimesic acid)	<b>NDC:</b> 2,6-Naphthalenedicarboxylate
<b>CT:</b> Charge Transfer	<b>NMR:</b> Nuclear Magnetic Resonance
<b>EPR:</b> Electron Paramagnetic Resonance	<b>OD:</b> Optical Density
<b>E-PS:</b> (expanded-) Polystyrenes	<b>PBD:</b> Powder Bulk Density
<b>FTIR:</b> Fourier Transform Infrared	<b>PCA:</b> Principal Component Analysis
<b>GPC:</b> Gel Permeation Chromatography	<b>PE:</b> Polyethylene
<b>HDPE:</b> High-Density Polyethylene	<b>PET:</b> Polyethylene Terephthalate
<b>HKUST:</b> Hong Kong University of Science and Technology	<b>PP:</b> Polypropylene
<b>ICP-OES:</b> Inductively Coupled Plasma – Optical Emission Spectroscopy	<b>PUR:</b> Polyurethane
<b>LCB:</b> Long-Chain Branching	<b>PVC:</b> Polyvinylchloride
<b>LDPE:</b> Low-Density Polyethylene	<b>pXRD:</b> Powder X-ray Diffraction
<b>LLDPE:</b> Linear Low-Density Polyethylene	<b>SCB:</b> Short-Chain Branching
<b>MAO:</b> Methyl Aluminoxane	<b>SEM:</b> Scanning Electron Microscopy
<b>MDPE:</b> Medium-Density Polyethylene	<b>STXM:</b> Scanning Transmission X-ray Microscopy
<b>MFIR:</b> Melt Flow Index Ratio	<b>TEAI:</b> Tri-ethyl Aluminum
<b>MIL:</b> Matérial Institut Lavoiser	<b>TEB:</b> Tri-ethyl Borane
<b>M<sub>n</sub>:</b> Number-Averaged Molecular Weight	<b>UHMwPE:</b> Ultra-High Molecular Weight Polyethylene
<b>MOFs:</b> Metal Organic Frameworks	<b>UV-Vis-NIR DRS:</b> UV-Vis-NIR Diffuse Reflectance Spectroscopy
<b>MW:</b> Molecular Weight	<b>XANES:</b> X-ray Absorption Near-Edge Structure
<b>MWD:</b> Molecular Weight Distribution	
<b>M<sub>w</sub>:</b> Weight-Averaged Molecular Weight	
<b>M<sub>z</sub>:</b> Z-Averaged Molecular Weight	

## Appendix B. Additional Tables

**Table B1.** An overview of the used parameters for the each of the spectral deconvolutions of the UV-Vis-NIR DRS spectra obtained from the experiments with TEB as co-catalyst. The parameters are provided for the deconvoluted Cr<sup>6+</sup>/SiO<sub>2</sub> UV-Vis-NIR DRS spectra before reduction by TEB and 15 min after pre-contacting the material with TEB.

Material	Bands (HWHM)	Comments
TEB		
Cr <sup>6+</sup> /SiO <sub>2</sub>	15000 (3000), 21500 (3000), 33900 (3000) 20700 (1400), 26400 (2800), 34000 (2000), 37600 (2500) 22000 (1600), 31000 (3000), 35000 (2000), 40000 (3000) 45900 (3500)	Cr <sup>3+</sup> <sub>Oh</sub> Cr <sup>6+</sup> <sub>monochromate</sub> Cr <sup>6+</sup> <sub>dichromate</sub> SiO <sub>2</sub> support
1.50 B:Cr Mole Ratio	9400 (1400), 11900 (2000), 24000 (1500) 16000 (3000), 21500 (3000), 33900 (3000) 21000 (1400), 26900 (2800), 34000 (2000), 37000 (2500) 22300 (1600), 31100 (3000), 35000 (2000), 40200 (3000) 46400 (3500)	Cr <sup>2+</sup> <sub>Oh/Td</sub> Oh = Pseudo-octahedral Cr <sup>3+</sup> <sub>Oh</sub> Cr <sup>6+</sup> <sub>monochromate</sub> Cr <sup>6+</sup> <sub>dichromate</sub> SiO <sub>2</sub> support
Cr <sup>6+</sup> /SiO <sub>2</sub>	15100 (3000), 21500 (3000), 33900 (3000) 20700 (1425), 26400 (2800), 34000 (2000), 37600 (2500) 22100 (1600), 31000 (3000), 35000 (2000), 40200 (3000) 46000 (3500)	Cr <sup>3+</sup> <sub>Oh</sub> Cr <sup>6+</sup> <sub>monochromate</sub> Cr <sup>6+</sup> <sub>dichromate</sub> SiO <sub>2</sub> support
5.0 B:Cr Mole Ratio	9400 (1400), 11900 (2000), 24000 (1500) 15900 (3000), 21500 (3000), 33900 (3000) 21000 (1400), 27200 (2800), 34100 (2000), 37300 (2800) 22400 (1600), 31400 (3000), 35100 (2000), 40600 (3000) 45800 (3500)	Cr <sup>2+</sup> <sub>Oh/Td</sub> Oh = Pseudo-octahedral Cr <sup>3+</sup> <sub>Oh</sub> Cr <sup>6+</sup> <sub>monochromate</sub> Cr <sup>6+</sup> <sub>dichromate</sub> SiO <sub>2</sub> support
Cr <sup>6+</sup> /SiO <sub>2</sub>	15100 (3000), 21500 (3000), 33900 (3000) 20600 (1400), 26300 (2800), 34000 (2000), 37600 (2500) 22100 (1800), 31000 (2850), 35500 (2000), 40600 (3000) 46600 (3500)	Cr <sup>3+</sup> <sub>Oh</sub> Cr <sup>6+</sup> <sub>monochromate</sub> Cr <sup>6+</sup> <sub>dichromate</sub> SiO <sub>2</sub> support
10.0 B:Cr Mole Ratio	9400 (1400), 11900 (2000), 24000 (1500) 16000 (3000), 21500 (3000), 33500 (3000) 21000 (1410), 26900 (2800), 34000 (2000), 37000 (2800) 22300 (1600), 31100 (3000), 35000 (2000), 40200 (3000) 46400 (3500)	Cr <sup>2+</sup> <sub>Oh/Td</sub> Oh = Pseudo-octahedral Cr <sup>3+</sup> <sub>Oh</sub> Cr <sup>6+</sup> <sub>monochromate</sub> Cr <sup>6+</sup> <sub>dichromate</sub> SiO <sub>2</sub> support

**Table B2.** An overview of the used parameters for the each of the spectral deconvolutions of the UV-Vis-NIR DRS spectra obtained from the experiments with TEAI as co-catalyst. The parameters are provided for the deconvoluted Cr<sup>6+</sup>/SiO<sub>2</sub> UV-Vis-NIR DRS spectra before reduction by TEAI and 15 min after pre-contacting the material with TEAI.

Material	Bands (HWHM)	Comments
TEAI		
Cr <sup>6+</sup> /SiO <sub>2</sub>	15000 (3000), 21600 (3000), 33900 (3000) 20700 (1400), 26300 (2800), 33900 (2000), 37100 (2500) 22000 (1600), 31000 (3000), 35000 (2000), 40200 (3000) 46000 (3500)	Cr <sup>3+</sup> <sub>Oh</sub> Cr <sup>6+</sup> <sub>monochromate</sub> Cr <sup>6+</sup> <sub>dichromate</sub> SiO <sub>2</sub> support
1.50 Al:Cr Mole Ratio	11500 (2500), 15200 (2500), 19800 (1500), 22800 (1120)  16000 (3000), 21500 (3000), 33900 (3000) 20800 (1400), 26600 (2800), 34000 (2000), 37000 (2750) 22000 (1600), 30900 (3000), 35000 (2000), 39500 (3000) 45600 (3500)	Cr <sup>2+</sup> <sub>Oh/Td</sub> Oh = Pseudo-octahedral / Cr <sup>3+</sup> <sub>reduced</sub> / Cr <sup>4+</sup> <sub>red</sub> Cr <sup>3+</sup> <sub>Oh</sub> Cr <sup>6+</sup> <sub>monochromate</sub> Cr <sup>6+</sup> <sub>dichromate</sub> SiO <sub>2</sub> support
Cr <sup>6+</sup> /SiO <sub>2</sub>	15000 (3000), 21500 (3000), 33900 (3000) 20700 (1400), 26400 (2800), 34000 (2000), 37300 (2500) 22000 (1600), 31300 (3000), 35000 (2000), 36900 (3000) 46600 (3500)	Cr <sup>3+</sup> <sub>Oh</sub> Cr <sup>6+</sup> <sub>monochromate</sub> Cr <sup>6+</sup> <sub>dichromate</sub> SiO <sub>2</sub> support
5.00 Al:Cr Mole Ratio	11200 (2500), 15200 (2500), 19800 (1500), 24000 (1050)  16000 (3000), 21500 (3000), 33900 (3000) 21000 (1400), 27000 (2800), 34000 (2000), 37000 (2750) 22100 (1600), 31200 (3000), 35000 (2000), 40000 (3000) 46400 (3500)	Cr <sup>2+</sup> <sub>Oh/Td</sub> Oh = Pseudo-octahedral / Cr <sup>3+</sup> <sub>reduced</sub> / Cr <sup>4+</sup> <sub>red</sub> Cr <sup>3+</sup> <sub>Oh</sub> Cr <sup>6+</sup> <sub>monochromat</sub> Cr <sup>6+</sup> <sub>dichromate</sub> SiO <sub>2</sub> support
Cr <sup>6+</sup> /SiO <sub>2</sub>	15000 (3000), 21500 (3000), 33900 (3000) 20800 (1400), 26400 (2800), 34000 (2000), 37400 (2500) 22100 (1680), 31100 (3000), 35000 (2000), 40000 (3000) 46300 (3500)	Cr <sup>3+</sup> <sub>Oh</sub> Cr <sup>6+</sup> <sub>monochromate</sub> Cr <sup>6+</sup> <sub>dichromate</sub> SiO <sub>2</sub> support
10.0 Al:Cr Mole Ratio	11300 (2000), 15200 (2500), 19800 (1500), 24000 (1050)  16000 (3000), 21500 (3000), 33900 (3000) 20900 (1400), 26500 (2800), 34000 (2000), 36900 (2750) 22100 (1600), 31000 (3000), 35300 (2000), 39800 (3000) 46600 (3500)	Cr <sup>2+</sup> <sub>Oh/Td</sub> Oh = Pseudo-octahedral / Cr <sup>3+</sup> <sub>reduced</sub> / Cr <sup>4+</sup> <sub>red</sub> Cr <sup>3+</sup> <sub>Oh</sub> Cr <sup>6+</sup> <sub>monochromate</sub> Cr <sup>6+</sup> <sub>dichromate</sub> SiO <sub>2</sub> support

**Table B3.** An overview of the used parameters for the each of the spectral deconvolutions of the Raman spectra obtained under in-situ conditions with the various reduction gases.

	Bands (HWHM)	Comments
<b>CO</b>		
250 °C	970 (17), 983 (9), 1005 (9)	Partially reduced
300 °C	970 (17), 983 (9), 1005 (9)	Partially reduced
350 °C	970 (17), 983 (9), 1005 (9)	Quantitatively reduced
400 °C	970 (17), 983 (9), 1005 (9)	Quantitatively reduced
<b>H<sub>2</sub></b>		
250 °C	970 (17), 983 (9), 1005 (9)	Partially reduced
300 °C	970 (17), 983 (9), 1005 (9)	Partially reduced
350 °C	970 (17), 983 (9), 1005 (9)	Quantitatively reduced
400 °C	970 (17), 983 (9), 1005 (9)	Quantitatively reduced
<b>C<sub>2</sub>H<sub>4</sub></b>		
90 °C	970 (17), 983 (9), 1005 (9)	Partially reduced
110 °C	970 (17), 983 (9), 1005 (9)	Partially reduced
130 °C	970 (17), 983 (9), 1005 (9)	Partially reduced
150 °C	970 (17), 983 (9), 1005 (9)	Partially reduced

## **Appendix C. List of Scientific Publications and Presentations**

### **C1. Scientific Publications**

1. M. K. Jongkind, M. Rivera-Torrente, N. Nikolopoulos, B. M. Weckhuysen, "Influence of Pore Structure and Metal-Node Geometry on the Polymerization of Ethylene over Cr-Based Metal-Organic Frameworks", *Chem. Eur. J.* **2021**, 27, 5769-5781.
2. M. K. Jongkind, F. Meirer, K. W. Bossers, I. C. ten Have, H. Ohldag, B. Watts, T. van Kessel, N. Friederichs, B. M. Weckhuysen, "Influence of Metal-Alkyls on Early-Stage Ethylene Polymerization over a Cr/SiO<sub>2</sub> Phillips Catalyst: A Bulk Characterization and X-ray Chemical Imaging Study", *Chem. Eur. J.* **2021**, 27, 1688-1699.
3. M. K. Jongkind, M. E. Z. Velthoen, T. van Kessel, N. Friederichs, B. M. Weckhuysen, "Tuning the Redox Chemistry of a Cr/SiO<sub>2</sub> Phillips Catalyst for Controlling Activity, Induction Period and Polymer Properties", *ChemPhysChem* **2020**, 21, 1665-1674.

### **C2. Oral and Poster Presentations at Conferences**

1. "Revealing the Influence of Metal-Alkyls on Early-Stage Cr/SiO<sub>2</sub> Ethylene Polymerization, Poster Presentation, Faraday Discussions e-Conference, London, United Kingdom, February **2021**.
2. "Revealing the Influence of Metal-Alkyls on Early-Stage Cr/SiO<sub>2</sub> Ethylene Polymerization, Poster Presentation, 21<sup>st</sup> NCCC, Noordwijkerhout, the Netherlands, March **2020**.
3. "Tuning the Cr Population in Cr/SiO<sub>2</sub> Philips-type Ethylene Polymerization for Controlling Catalyst Activity and Induction Period, Poster Presentation, BlueSky Conference on Olefin Polymerization, Sorrento, Italy, June **2019**.
4. "Tuning the Cr Population in Cr/SiO<sub>2</sub> Phillips-type Ethylene Polymerization for Controlling the Catalyst Activity, Induction Period and Product Properties", Oral Presentation, 20<sup>th</sup> NCCC, Noordwijkerhout, the Netherlands, March **2019**.

5. "Tuning the Cr<sup>2+</sup>/Cr<sup>3+</sup> Population in Cr/SiO<sub>2</sub> Phillips-type Ethylene Polymerization for Controlling Catalyst Activity and Induction Period", Poster Presentation, Innovative Catalysis and Sustainability School, Bardonecchia, Italy, January **2019**.

### C3. Other Scientific Publications by the Author

1. K. W. Bossers, R. Valadian, J. Garrevoet, R. Chan, N. Friederichs, J. Severn, A. Wilbers, S. Zanoni, M. K. Jongkind, B. M. Weckhuysen, F. Meirer, "Heterogeneity in the Fragmentation of Ziegler Catalyst Particles during Ethylene Polymerization Quantified by X-ray nanotomography", *JACS Au*, **2021**, *1*, 852-864.
2. M. Rivera-Torrente, P. D. Pletcher, M. K. Jongkind, N. Nikolopoulos, B. M. Weckhuysen, "Ethylene Polymerization over Metal-Organic Frameworks and the Influence of Linkers on Their Fracturing", *ACS Catal.* **2019**, *9*, 3059-3069.
3. A. Piovano, P. Pletcher, M. E. Z. Velthoen, S. Zanoni, S-H Chung, K. Bossers, M. K. Jongkind, G. Fiore, E. Groppo, B. M. Weckhuysen, "Genesis of MgCl<sub>2</sub>-based Ziegler-Natta Catalysts as Probed with Operando Spectroscopy", *ChemPhysChem* **2018**, *19*, 2662-2671.
4. J. E. Borger, M. K. Jongkind, A. W. Ehlers, M. Lutz, J. C. Slootweg, K. Lammertsma, "Metalate-Mediated Functionalization of P<sub>4</sub> by Trapping Anionic [Cp\*Fe(CO)<sub>2</sub>(η<sup>1</sup>-P<sub>4</sub>)]<sup>-1</sup> with Lewis Acids", *ChemistryOpen* **2017**, *6*, 350-353.



## Acknowledgements

And here the journey ends, with this Ph.D. Thesis as a final product. I could never have envisioned the way it went back when I started the 1<sup>st</sup> of November in 2016. Yet I do know that I met a lot of great people along the way, some who inspired this work and some who were “just” great company, so I would like to thank everyone who helped me along the way, one way or another.

First and foremost, I would like to thank my professor and supervisor Prof. dr. ir. **Bert Weckhuysen**. Bert, none of this would have been possible without your support and supervision. I would like to thank you for all the scientific discussions we had over the years. The most outstanding and memorable “scientific” discussion being one of the COVID-time progress meetings, where we talked about running a bit too long, only for you to realize that you had to speed off to the next meeting! I think that despite a somewhat rocky start, I embraced all the advice and opportunities you gave me, took them to heart and made them my own. I am happy that this allowed me to collaborate with many great scientists from all over the world, to present my work at national and international conferences, and go to places where I normally would not get easily.

I would also like to thank (former) ICC staff: **Krijn de Jong, Petra de Jongh, Eelco Vogt, Eline Hutter, Freddy Rabouw, Ward van der Stam, and Pieter Bruijnincx**, for providing me with valuable feedback on several occasions as well as for your help in supervising students.

**Florian Meirer**, I think you deserve a special thanks here, your knowledge on X-rays and on programming was invaluable for our work described in Chapter 3. If anything, this has greatly helped me stay motivated on these experiments and seeing it all through. Additionally, I would like to thank you for your help in student supervision, especially during the early-COVID stages this was invaluable, and you smoothly helped both me and Jelle through the final stages of his MSc. Thesis.

I would like to thank my industrial collaborators; without you this work would not have existed **Nic. Friederichs**, I would like to thank you for being my direct industrial contact. Your knowledge on olefin polymerization is astonishing and you greatly helped me out in writing the all the peer-reviewed publications. But not only that, I also greatly enjoyed our scientific and non-scientific talks, including drinks, during the BlueSky and ICS Conferences. **Theo van Kessel**, I remember first meeting you somewhere in the early summer of 2017, where you were introduced as the Cr expert. You have introduced me into the industrial kitchen and revealed a little bit of what goes on there. Also, if I had questions, you were always able to answer these! **Enrico Troisi, Tom**

**Schoffelen, Guillaume Magan**, I would like to thank you for providing me with polyethylene reference materials as well as for doing measurements for, and more importantly, with me.

I would like to thank my synchrotron collaborators; without you Chapter 3 would not have been possible. **Hendrik Ohldag**, thank you for enabling me to perform STXM experiments at the ALS Beamline 11.0.2. More importantly, thank you for always being available for help during these times. I know we have called you at hours we were not supposed to, you were always there for practical support as well as mental support! I always enjoyed measuring at the ALS and will always look back with great pleasure to these trips. **Benjamin Watts**, thank you for allowing us to measure at PolLux as well on several occasions. For some reason we had great weather every time we got to measure. What I will remember the most is you showing us some excellent Australian news channels, I think we must have watched every single available video during the nightshifts.

I would like to thank my colleagues who assisted me during these highly memorable synchrotron beamtrips. **Iris**, I think that you must have been there for most of the trips. You were always reliable and helpful! Furthermore, all the laughing we did made the beamtrips so much more enjoyable. **Silvia**, in addition to being a beamtrip partner, a valued Team-Polymerization member, I do consider you a good friend as well. I am happy that we have managed to align two incredible trips to Banff and Yosemite during some of our joint beamtrips! **Ilse**, in addition to a valued beamtrip colleague, my DDW neighbor, I am happy to have gotten to know you as a great friend! We shared many beamtrips together, which without exception all were very challenging. However, I will happily remember the long nights scouting for trashpandas, and skunks, as well as the many good talks we had. Furthermore, outside our professional life I very much enjoyed the bouldering, the coffees, and the dinners and I hope that we continue to do this!

When I started my Ph.D., you were the only one on polymerization chemistry, **Marjolein**, I want to thank you for showing me around in the first months, for the coffee moments we had, as well as for collaborating with me! **Yuanshuai**, you arrived a little bit later, you are a great and very kind person. You were always helpful, and I most definitely enjoyed all our (scientific) talks! **Max**, I also want to thank you for both scientific and non-scientific discussions! The first thing that jumps to mind is of course Sorrento, I thoroughly enjoyed the food, the weather, the drinks, and the environment and scientific discussions there! **Joren**, unfortunately I did not get to work extensively with you, mostly due to this global pandemic... Yet I am glad that we shared the nightshifts at the DLS, we had great laughs and our nightly walks for sure made time fly by!

**Alessandro**, thank you for always being available for scientific and non-scientific discussions, which certainly helped me get started in the first months of my Ph.D. Additionally, I am also

happy that we got together on the conferences in Bardonecchia and Sorrento, which are very fond memories! I really enjoyed the dinners, drinks, and the skiing. On the last topic, I think you will be a great skier with some more practice! Then, **Elena**, I would very much like to thank you for being available during the conferences for some scientific input, which really helped me at times. Additionally, the skiing, the drinks, and the dinners in both Bardonecchia and Sorrento are moments I still happily think of.

As briefly mentioned, beforehand I was unable to envision how these 4 years would develop. **Miguel**, you are living proof of this since you convinced me to also start working on Cr MOFs. You are amazing and you undeniably made the 5<sup>th</sup> chapter of this Ph.D. Thesis. Thank you for always helping me with questions, even long after your contract ended. I hope that when everything returns to normal, we can go for some beers, since I do believe that I owe you some! **Nikos** also you are a great guy and helped in making the 5<sup>th</sup> chapter into what it is. I want to thank you for your patience when it came to shooting the SEM images, and more importantly, for the great discussions and coffee breaks!

**Thomas**, what can I say? You are a great colleague with a great sense of dry humor, which seemed to particularly come out at the coffee machines. Additionally, I am really amazed by the cover you made and think you did a great job.

**Hans** and **Chris**, thank you for the invaluable help on ultramicrotomy, as well as for the enjoyable talks at times where I had to wait for the machine to do its thing!

I would like to thank all of my amazing colleagues from the DDW 4<sup>th</sup>/5<sup>th</sup> floor for the great working atmosphere: **Ana, Oscar, Xinwei, Yannick, Sebastian, Marianna, Luke, Yadolah, Wirawan, Shiyou, Matteo, Sophie, Michael, Joris, Yannick, Nienke, Rafael, Laura de Kort, Nina, Yaqi, Hongyu, Ina, Kai, Longfei, Lars, Khaled, Carolien, Caroline, Beatriz, Carlos, Lisette, Jeroen, Charlotte, Marisol, Tom, Jessi, Martin, Fabianne, Mark, Romy, Jogchum, Petra, Erik, Guusje, Jelle, Donglong, Yannick, Nynke, Ramon, Stanislav, Katarina, Robert, Egor, Stijn, Anne-Eva, Wouter, Joris, Sander, Jelle**, and others that I forgot mentioning, for which I sincerely apologize.

I had the privilege of supervising a few students over the years. **Albaraa**, thank you for your dedication, you had a challenging road, but you pulled through! Not only that, but you also took the next step in your career and are well on your way. Unfortunately, we were not able to collaborate now that you are also a member of the Polymerization group, but I wish you all the best in the coming years and I hope you will enjoy it! **Jelle**, what can say? You did not take on an easy project, yet you made it your own: you approached it with an analytical mindset and meticulously dissected it, with a very nice outcome. Additionally, I think that the final stage of

your MSc. research was particularly difficult due to COVID regulations. Yet you persevered and delivered a great presentation and great thesis!

Whenever I needed help with practical issues, there were always the ladies of the secretary: **Dymph, Ilonka, Monique, Belén, Sandra** and **Brenda**. Thank you for your availability and the efforts that you put in helping me! You were always available for questions, even when I dropped by outside your regular hours. Whenever there were technical difficulties, I could always fall back on **Oscar, Pascal, Jochem, Joris, Ad, Jan Willem, Dennie** and **Herrick**. I cannot express how much you guys have helped me at times. Keep doing what you do because I am sure that every Ph.D. feels the same!

Then a whole list of people follows who all made work at the DDW so much more enjoyable with the lunches, coffee breaks, regular chats, drinks, and dinners. Thank you, ladies and gentlemen, for making the daily life so much more enjoyable and for your friendships: **Jim, Thimo, Suzan, Remco, Laura, Christa, Kris, Roozbeh, Nathan, Abi, Savannah, Roman, Giorgio, Fouad, Francesco, Christia, and Bas.**

**Johan** and **Sjaak**, the OG VU Lunch group. I want to thank you guys for the moral support. Our Monday lunches were always great and hilarious, I most definitely will miss these, it is time for some drinks (very) soon.

You have been a good friend ever since our studies at the VU, **Lars**. I hope that this will continue to be in the coming years, albeit with more time and flexibility from my side!

**Oscar**, my Lebanese friend. I am happy that you were my neighbor just before everything closed. I enjoyed our burgers and beers. When everything turns a bit more normal, I hope we can go for the Whisky at some point too!

Then I would like to thank **Roozbeh**. I must say even though we were not involved experimentally, you made NIOK and my first ever do-days unforgettable experiences! Additionally, the karaoke during our trips to the DLS and DESY were great fun.

**Katinka**, dear friend, thank you for your friendship and your support through basically the entirety of my Ph.D. I am grateful to have met you early on and I am even more grateful for the friendship that developed, and I am sure that it will continue to grow in the coming years.

**Laurens**, despite no scientific collaborations, I think we did obtain a good friendship from our work together in the DDW. If anything, the memories from NCCC conferences jump out the most,

which all are equally hilarious. Unfortunately, the circumstances made that we could not end our Ph.D. with one last NCCC conference... Yet I am sure that we can continue the fun outside the professional environment.

Then, my running mate (in the literal sense), **Koen Bossers**. I am glad that I got to know you and even more thankful for the friendship that followed. I really enjoyed running with you in these years, and I hope that we will continue to do this more regularly when everything goes back to normal again. Furthermore, I will also happily remember our trips to Bardonecchia and Berkeley! Professionally, we each go our own way now, but I am sure that we will keep in touch!

Dan mijn familie, **Mam**, naast pap ook een zoon in de scheikunde, wat een ellende. Toch was je er altijd, vroeg je hoe het ging en wist ik dat ik alles bij je kwijt kon. Als ik dan aan het laatste jaar denk, dan zijn de momenten dat jullie bij ons in de buurt op vakantie waren en wij langskwamen écht mooie herinneringen, en dan helemaal de zaterdag happen en stappen in Otterlo! Dit is zeker iets wat vaker terug moet komen zodra het weer kan. **Pap**, voor jou toch iets minder erg, een zoon in de scheikunde, jij kon goed meepraten! Ik denk dat ik de afgelopen jaren toch ook veel van onze gesprekken heb geleerd, ook al ben ik soms te eigenwijs om dat toe te geven... Daarnaast ben ik blij dat je me overgehaald hebt om te gaan hardlopen, wat meermaals hielp om alles op een rijtje te zetten, zowel wetenschappelijk als daarbuiten. Ook waren de gezamenlijke hardloopsessies genieten en hoop ik dat we dit vaker mogen doen, misschien toch samen door naar de volle marathon nu? **Jan** en **Sigrid**, ik denk dat ik niet te veel zeg als ik zeg dat onze gezamenlijke vakanties altijd heerlijk waren, of het nou wandelen in de Rockies was of pilsen na het skiën in Italië. Daarnaast was het ook altijd gezellig als jullie spontaan een keertje kwamen wandelen, zeker omdat dit mij dan even uit mijn werk trok. **Marianne, Sorin, Fien, Laura** en **Wessel**: broertjes, zusjes, en ook vrienden, dat we in de komende jaren (nog) meer mogen barbecueën, thee/whisky mogen drinken, spelletjesavonden mogen houden en wat dan ook. Bedankt dat ik altijd over mijn werk kon praten en dat jullie luisterden!

**Lisa**, ik denk dat jouw bijdrage aan dit werk gigantisch is. Ik ben blij dat jij gedurende het hele traject naast mij hebt gestaan. Ik kon altijd mijn verhaal bij je kwijt, en jij wist mij altijd weer op te peppen en te motiveren, of met beide benen op de grond te houden wanneer dit nodig was. We hebben ons allebei op unieke manieren ontwikkeld, maar ik ben vooral blij dat we dit samen hebben gedaan! Gelukkig draaide het de afgelopen vier jaar niet alleen om werk of opleidingen. We hebben ook zo ontzettend veel leuke dingen gedaan samen. Het hardlopen op de zaterdagochtend was altijd een goede afsluiting van de week en tegelijkertijd een goed begin van het weekend. Daarnaast waren de trips in Nederland, Europa, en zelfs Canada geweldig en wisten deze mij altijd weer op te laden om vol energie weer aan de slag te gaan. Lisa, ik ben benieuwd wat de komende jaren voor ons in petto hebben en kijk hier heel erg naar uit!

## About the Author



Maarten Klaas-Jan Jongkind was born on the 18<sup>th</sup> of February 1993 in Amstelveen, the Netherlands. In 2011 he started his Bachelor studies in Chemistry at the Vrije Universiteit in Amsterdam (the Netherlands), where he also performed research on the synthesis of bi-functional Frustrated Lewis Pairs. He graduated in 2014 and started his Master studies the same year at the joint “Molecular Design, Synthesis & Catalysis” program between the Vrije Universiteit and Universiteit van Amsterdam. He did his Master research on the topic of “*Nucleophilic activation of White Phosphorus*” and graduated in the year of 2016. He started his Ph.D. research in

November the same year in the group of Prof. dr. ir. Bert M. Weckhuysen, Utrecht University (the Netherlands) on the topic “*Understanding the working principles of metal-alkyl compounds as co-catalysts in Cr/SiO<sub>2</sub> Phillips Polymerization Catalysis*”. This work was sponsored by the Topconsortium voor Kennis en Innovatieve Chemie (TKI) and SABIC (Geleen). Maarten has collaborated with 4 different research institutions as well as with two students, resulting in scientific articles in peer-reviewed journals. Most of his research findings are described in this Ph.D. Thesis and were presented in both oral and poster presentations at various national and international conferences. In his free time, Maarten is an avid runner and loves to ski. Besides sports, he loves to spend time with friends and family.